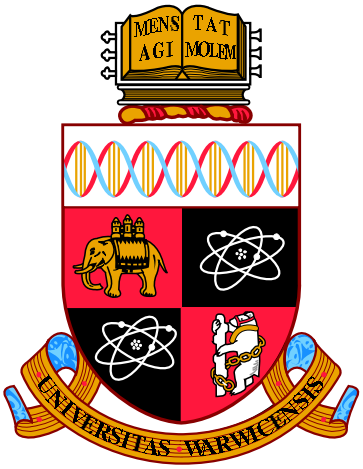

Studies of charmless three-body b-hadron decays at LHCb

by

Rafael Silva Coutinho

Thesis

Submitted to the University of Warwick

for the degree of

Doctor of Philosophy

Physics Department

May 2015

THE UNIVERSITY OF
WARWICK

Contents

Acknowledgments

First and foremost I want to thank my supervisor Tim Gershon for give me this opportunity. For the wisdom, guidance and invaluable support on my unrealistic deadlines and involvements in endless number of analyses. Thanks also to Michal Kreps for all the help and encouragement.

I am especially grateful to Thomas Latham for who have contributed immensely to my personal and professional life. My best wishes to Eugenia and Angelica.

I would like to express my gratitude to all the members of my institute: Paul, Anton, Mark, Matt, Tomas, (potato) Dan, Charlotte and Daniel for the fantastic environment to work. I would like to thank all people I have had the privilege of working with at LHCb, including all members of the Charmless working group and the $K^0_S hh$ μ-group. In special, Stephane, Eli, Diego, Marc, Jan, Marouen and Louis.

I thank my beloved dog Vascão.

I would like to thank my family for all their love and encouragement. For my parents and grandparents who raised me with a passion for science and endless support during these years. For my brother who has been my best friend all my life. Words can not express how grateful I am to my mother, my father, my mother-in law, and father-in-law for all of the sacrifices that you've made on my behalf. I know I always have my family to count on when times are rough. I love you so much.

And most of all for my loving, supportive, encouraging and (in)patient wife Marianna. The best outcome from these years is the certainty that you are not only my best friend, but my soul-mate. There are no words to convey how much I love you.

Declarations

The work presented in this thesis is all my own work, unless it is specifically referenced to the contrary. This thesis has not been submitted, in any form, to this or any other university for another qualification.

Abstract

Studies of charmless three-body decays of either $B^0_{(s)}$ mesons or beauty baryons with a K^0 meson in the final state are presented in this thesis. The analyses are performed using the 2011 and 2012 LHCb dataset, corresponding to an integrated luminosity of 1.0 fb^{-1} and 2.0 fb^{-1} recorded at a centre-of-mass energy of 7 TeV and 8 TeV, respectively. The decays $B^0_s \to {}^{(}\overline{K}{}^{)0} K^\pm \pi^\mp$ and $B^0_s \to K^0 \pi^+ \pi^-$ are observed for the first time, and the decay mode $B^0 \to {}^{(}\overline{K}{}^{)0} K^\pm \pi^\mp$, previously observed by the BaBar experiment, is confirmed. Moreover, the $\Lambda^0_b \to \overline{K}{}^0 p \pi^-$ channel is also observed for the first time and its phase-space integrated *CP* asymmetry measured, which shows no significant deviation from zero. No significant signals are seen for $\Lambda^0_b \to K^0 p K^-$ decays, Ξ^0_b decays to both the $K^0_S p \pi^-$ and $K^0_S p K^-$ final states, and the $\Lambda^0_b \to D^-_s (K^0_S K^-) p$ decay, and upper limits on their branching fractions are reported. Finally, the first untagged decay-time-integrated amplitude analysis of $B^0_s \to K^0_S K^\pm \pi^\mp$ decays has been performed. All branching fraction results obtained from this analysis are either the most precise to date or are first measurements.

1 Introduction

The main theme of this dissertation concerns the phenomenon of symmetry. In particular, experimental evidence suggests that matter dominates the Universe whilst no appreciable primordial antimatter is observed. This baryon asymmetry can be independently confirmed using primordial nucleosynthesis model predictions to estimate the cosmological abundances of light elements or from precise measurements of microwave background. [1] In terms of values of the observed baryon-to-photon ratio in the present day, these are found to be around 10^9 photons for every baryon and no antibaryons. Since the Universe presumably started from a symmetric state of matter and antimatter, the observed baryon asymmetry must have been generated through some dynamical mechanism, referred to as baryogenesis.

Regardless of the cosmological model to explain the production of baryogenesis, the underlying physics must satisfy the conditions stated in the Sakharov criteria [1]: baryon number violation; violation of the charge conjugation and also its combination with parity transformation (hereafter referred to as *CP*); and departure from thermal equilibrium. In the event that all fundamental interactions preserve baryon number, an evolution from an initially baryon-symmetric state would not produce a non-vanishing asymmetry. In addition, invariance under charge-parity transformation implies that processes involving baryons would proceed at precisely the same rate as antibaryons. Finally, since in thermal equilibrium asymmetries are statistically suppressed, the conditions must have changed such that a permanent asymmetry is generated.

Although the main ideas of baryogenesis are accommodated within the Standard Model (SM) of particle physics, additional mechanisms are required to explain the large imbalance between matter and antimatter currently observed. In particu-

[1] Notice that a baryon excess can be in principle explained by a neutrino excess.

lar, among the several features that motivate an extension of the SM, the search for new sources of *CP* violation is of great importance. The investigation of probes of this well known phenomenon, first observed more than five decades ago in the kaon system [2], is the main goal of this work. With the advent of experiments such as BaBar [3] and Belle [4], and more recently LHCb [5], a number of important measurements have been performed, indicating that the dynamics described in the SM seems to be responsible for the *CP* violation observed so far. In this line of research, the study of hadronic b-hadron decays has acquired significant importance in the last few years, since large asymmetries are foreseen in a number of decay channels.

In this thesis, charmless three-body decays of either $B^0_{(s)}$ mesons or beauty baryons with a K^0 meson in the final state are investigated at LHCb. Although some of these modes have been previously observed, both B^0_s and b baryon sectors are almost unexplored. The study of these decays will provide a number of probes to test the SM and novel possibilities to search for *CP* violation effects, which may vary significantly across the phase space (known as the Dalitz plot) [6–8]. Several methods have been proposed to explore these features, and are discussed in this work.

The results presented in this dissertation are based on a data sample corresponding to an integrated luminosity of 3.0 fb^{-1} of pp collisions, collected during 2011 and 2012 at a centre-of-mass energy of respectively 7 TeV and 8 TeV by the LHCb experiment. The remainder of the dissertation is arranged as follows. In Chapter 2, a theoretical introduction to *CP* violation is presented, whilst Chapter 3 describes the main features involving charmless three-body decays. The design and performance of the LHCb spectrometer are discussed in Chapter 4. An overview of the analysis strategy for decays with similar topologies is examined in Chapter 6. Searches for charmless three-body decays of either $B^0_{(s)}$ mesons or beauty baryons with a K^0 meson in the final state are reported Chapter 5, while the first Dalitz-plot analysis of the decays $B^0_s \to K^0_S K^\pm \pi^\mp$ is presented in Chapter 7. Finally, some conclusions are given in Chapter 8. Appendix A and B contain results of a search for $B^0_{(s)} \to J/\psi p\bar{p}$ and $B^+ \to J/\psi p\bar{p}\pi^+$ decays, and sensitivity studies of *CP* violation in $B^0_s \to K^0_S \pi^\pm \pi^\mp$ decays, respectively. Although these studies were performed during my Ph.D. studentship, they are included as Appendices to avoid breaking the narrative flow of the main body of the thesis.

2

CP violation

Symmetry is a *sine qua non* foundation for any underlying physical theory of matter. This is an intuitive notion, recognisable in ideas such as homogeneity, proportionality and balance of any object in the environment. A more sophisticated extension of this philosophy for particle physics is provided through invariant transformations, with remarkable consequences. An important application is the association between the action of continuous symmetry in a system and a corresponding quantity conservation (Nöether's theorem). In terms of relativistic quantum theory, symmetries are represented as operators that transform a state (global transformations in Hilbert space), so that physical observables remain invariant. Symmetries can be manifest in continuous or discrete transformations. In the following the relevant discrete symmetries for the discussion are introduced, in particular charge conjugation (C), parity (P) and, indirectly, time reversal (T) symmetries. The definition and manifestation of asymmetries in these quantities are the main subject of this chapter. Further concepts such as energy conservation and gauge symmetries are also examined in this review.

2.1 Discrete symmetries C, P and T

The evolution of an initial state of any physical system is obtained by either discrete transformations or in the limit of infinite reiterations of infinitesimal discrete steps (continuous). The presence of a symmetry in a system implies the existence of a conserved quantity. Discrete symmetries are implemented by operators with eigenstates with values of ± 1. A necessary and sufficient condition for symmetrical transformations is that the operator is unitary and linear or antiunitary and antilinear. These operators are examined in the following.

Parity invariance

The parity operator of the Poincaré group reverses the sign of all three spatial coordinates in the four-vector form of $(t, \vec{x}) \rightarrow (t, -\vec{x})$, which is equivalent to a mirror-inversion followed by a π radian rotation about the axis perpendicular to the plane of the mirror. Notice that under space inversion the spin component remains unchanged. The representation of this operator in the Hilbert space is unitary and linear, and its symmetry is guaranteed by the invariance of the transition probability. Following the idea that electromagnetic and strong interactions symmetries are preserved under parity transformation, the nature of weak interaction has been initially considered to be likewise invariant.

Parity violation in weak interactions has been first suggested by Lee and Yang [9] to explain the so-called τ-θ puzzle, in response to the absence of evidence of symmetry invariance in reviewing the experimental results to that date. Their proposal originates from the observation that the θ^+ and τ^+ particles, seen decaying respectively to 2π and 3π, were found to have similar masses and lifetimes. The hypothesis that these were different decays of the same particle had been previously excluded in order to preserve parity. The elucidation of this question was experimentally verified using β-nuclei decays of cobalt ${}^{60}\mathrm{Co} \rightarrow {}^{60}\mathrm{Ni}^* + e^- + \bar{\nu}_e$ [10]. From this, and subsequent experiments, it was established that only left-handed chiral electrons e^-_L and right-handed chiral anti-neutrinos $\bar{\nu}_R$ participate in weak interactions in the Standard Model (SM). This experiment provided the first occurrence of parity violation and contributed to the fundamental description of electroweak interactions. The particles θ^+ and τ^+ have been later associated to the same particle, now known as the K^+ meson.

Charge conjugation

Charge conjugation intrinsically transforms a particle into its corresponding anti-particle without changing momentum and spin. Formally this operator negates all internal quantum numbers (*e.g.* electric charge, baryon number, lepton number and strangeness) of the field. Similarly to the parity operator, the charge-conjugation symmetry is invariant for electromagnetic and strong interactions, and is violated in weak interactions.

Time reversal

A Poincaré time reversal interchanges the time component in the four-vector as $(t, \vec{x}) \rightarrow (-t, \vec{x})$, where momenta and spins are flipped whereas energies remain

unchanged. This feature is constrained to the antilinearity (and antiunitarity) representation of this operator that exchanges the initial and final states. One further notable nuance of this symmetry is that the change of $t \to -t$ inverts the boundary conditions of the basis of the Hilbert space. The non-invariance of the time-reversal symmetry has been initially inferred from *CP* violation constraints [11], with a first unambiguous observation recently made in the B^0 system [12].

CP and *CPT* combinations

Although the aforementioned symmetries (C, P) are broken individually due to the chirality of weak interactions, the invariance of the combined symmetry *CP* had been suggested [13] – inspired by the observed conservation of gauge theories such as QED and QCD. An appealing feature of the combined inversion operator is not only the restoration of the left-right symmetry, but also the absence of conflicts with the understanding of the other forces. However, experimental evidence for *CP* violation was later observed in the neutral kaon [2] and B meson [14] systems. A more comprehensive explanation of the manifestation of *CP* violation in the SM is given in the following sections.

In this framework, one of the most fundamental principles to describe nature is the *CPT* theorem, which states the invariance of the Hamiltonian density under the combined operators product. This theorem is of significance importance since it connects to the Lorentz invariance and causality. It is interesting to notice that, in the event of time-reversal violation, *CP* violation is implied in order to preserve the *CPT* symmetry. [1] The combined *CPT* symmetry, until this date, has no experimental evidence of being violated.

2.2 *CP* violation in the Standard Model

The Standard Model is a theory that outlines the interactions of fundamental particles, formalised in a gauge $SU(3)_C \otimes SU(2)_L \otimes U(1)_Y$ Lie symmetry. A local or gauge continuous symmetry is defined as a transformation which can be performed independently at each point in space time. In the framework of quantum field theory (QFT), the properties and interactions of particles are determined by the previously

[1] The equivalence between *CP* and *T* violation has interesting consequences in strong interactions. Although P and T-violation parameters may be introduced in the strong-interaction Lagrangian, experimentally stringent limits on the T-violating neutron electric dipole moment have been imposed [15]. This is referred to in the literature as the "strong *CP* problem". Throughout this work the strong force is assumed to be *CP* conserving.

mentioned Lagrangian density. [2] Under invariant local gauge transformations of the Lagrangian, these properties are described by the aforestated irreducible representations of the group symmetry. The strong sector is associated to the non-abelian SU(3) group and is based on the theory of quantum chromodynamics (QCD). The colour symmetry representation is given by triplets of quarks with the force mediated by massless gluons (gauge bosons), with the Gell-Mann matrices as generators (force carriers related to the interaction) of the group.

The $SU(2)_L \otimes U(1)_Y$ group refers to the unification of quantum electrodynamics (QED) and weak interactions into a single electroweak formulation [16–18]. The abelian electromagnetic interactions are mediated by massless photons, which are accommodated in the form of a Lagrangian invariant under local U(1) phase transformations. Conversely, weak interactions involve massive bosons and are not invariant under *CP*. These features are not predicted in the gauge phenomenology, but can be accommodate through the notion that weak and electromagnetic interactions are manifestations of the same electroweak force, spontaneously broken by the Brout-Englert-Higgs mechanism [19, 20] – which is the foundation of the Standard Model. Particles acquire mass in the SM when a scalar (spin-0 and even parity) field assumes a non-zero vacuum expectation value. In this spontaneous symmetry breaking of the $SU(2)_L \otimes U(1)_Y$ invariance, the required masses for the vector bosons $W^{\pm}$ and Z^0 are generated whilst photons remain massless. One of the most noticeable achievements of this theory is the anticipated existence of a spin-0 particle, so-named the Higgs boson, which only recently has been discovered [21,22].

CP violation is introduced in the SM through the electroweak sector. The underlying Lagrangian is structured in terms of several contributions: gauge-boson kinematics and self-interaction terms; fermion fields; a potential, governed by the scalar field via spontaneous symmetry breaking mechanism; and the gauge invariant Yukawa couplings. All these quantities are constructed as *CP* invariants, except the Yukawa terms that are responsible for the fermion interactions with the scalar field. Fermions are grouped into either left-handed doublets or right-handed singlets for quarks and leptons. Similarly to the bosonic case, fermion masses are prohibited by gauge symmetry, and their masses are generated as a result of their interaction with the Higgs field. The Yukawa Lagrangian is formulated as

$$\mathcal{L}_{\text{Yukawa}} = -Y^u_{ij}\bar{Q}^i_L\phi^c u^j_R - Y^d_{ij}\bar{Q}^i_L\phi d^j_R - Y^l_{ij}\bar{L}^i_L\phi l^j_R + h.c.\,, \tag{2.1}$$

where i and j label the flavour generations, Y_{ij} are complex coupling matrices, the

[2] In quantum field theories, each particle corresponds to an excitation of local quantum field.

L and R subscripts indicate the handedness of the fermion, $Q(L)$ and $u/d(l)$ are respectively the doublets and singlets for quarks (leptons) and ϕ (ϕ^c) is the field (charge conjugate field) of the Higgs doublet. For simplicity, in the following only quarks are considered. Under spontaneous symmetry breaking, the Higgs couplings acquire their vacuum expectation value, which in the unitary gauge choice is

$$\mathcal{L}_{\text{Yukawa}} = -Y^u_{ij}\bar{u}^i_L \frac{v+h(x)}{\sqrt{2}} u^j_R - Y^d_{ij}\bar{d}^i_L \frac{v+h(x)}{\sqrt{2}} d^j_R \tag{2.2}$$

$$= -\sum_{f,i,j} \bar{f}^i_L M^{ij}_f f^i_R \left(1 + \frac{h(x)}{v}\right), \tag{2.3}$$

where M^{ij}_f gathers all information encoded in the Yukawa couplings, v is the vacuum expectation value and $h(x)$ is the real scalar Higgs field. In this schematic representation, the Lagrangian describes the generated mass term of the considered fermion as an interaction between the Higgs field and a fermion-antifermion pair.

Although the M^{ij}_f matrices are in general complex-valued, which naturally introduces the complex phase required for the *CP* violation, this term is non-physical. However, it should be noted that the flavour eigenstates of this coupling matrix are not the same as the mass eigenstates. In order to extract the fermion masses it is necessary to diagonalise this matrix using a unitary transformation

$$M^{\text{diag}}_f = (U^f_L)^\dagger M_f U^f_R \,. \tag{2.4}$$

In this basis, denoted as the mass basis, the elements in the diagonal are real and positive. Therefore, the fermion mass eigenstates and corresponding eigenvalues of the fermion masses are obtained by the transformation $f'^i_{L,R} = (U^f_{L,R})_{ij} f^j_{L,R}$. Finally, the insertion of Eq. 2.4 into Eq. 2.2 relation results in an invariant Lagrangian in the new basis.

The handedness characteristic of the unitary transformation matrix introduces the feature that only charged current interactions, mediated by $W^\pm$ bosons, can cause quark flavour changes. [3] The corresponding Lagrangian before and after the rotation is given in the quark scenario as

$$\mathcal{L}_{\text{CC}} = \frac{g}{\sqrt{2}} \bar{u}_L \gamma^\mu d_L W^+_\mu + h.c. \tag{2.5}$$

$$= \frac{g}{\sqrt{2}} \bar{u}'_L [(U^u_L)^\dagger U^d_R] \gamma^\mu d'_L W^+ + h.c. \,, \tag{2.6}$$

where the quarks of u_L and d_L families are coupled through the expression $(U^u_L)^\dagger U^d_R$,

[3] Note that flavour changing in neutral current interactions is still possible through loop processes.

hereafter referred to as the Cabibbo-Kobayashi-Maskawa (CKM) matrix. The complex phases in the Yukawa couplings are absorbed in the CKM matrix, which is responsible for all *CP* violation effects in the SM.

2.3 The CKM matrix

Historically, the first approach to describe mixing between quark families has been suggested to allow the universality of weak interactions [23]. A simplified quark model was initially proposed by Gell-Mann and Zweig, and subsequently charm quarks were introduced through the formalism of the GIM mechanism [24]. However, the evidence of *CP* violation in the neutral kaon sector indicates the presence of a complex phase in the mixing matrix, which is not possible in a 2×2 matrix. Therefore, Kobayashi and Maskawa generalised the Cabibbo matrix to three generations of quarks, in which case a single arbitrary complex phase exists [25]. This quark-mixing matrix is schematically depicted as

$$V_{\mathrm{CKM}} = \begin{pmatrix} V_{ud} & V_{us} & V_{ub} \\ V_{cd} & V_{cs} & V_{cb} \\ V_{td} & V_{ts} & V_{tb} \end{pmatrix} , \tag{2.7}$$

where the magnitude squared of each element gives the transition probability between quarks with corresponding indices, and represents the already mentioned relation between the mass eigenstates and the eigenstates of charged weak current interactions.

A generic complex $N \times N$ matrix, such as the CKM matrix, is parametrised by $2N^2$ independent parameters. The unitarity condition $\sum_j^N V_{ij} V_{kj}^* = \delta_{ik}$ imposes N^2 constraints on the degrees of freedom. Furthermore, the relative phases between quarks are irrelevant, and can be absorbed into phase redefinitions, reducing another $2N-1$ parameters. The total number of irreducible degrees of freedom of this matrix is given by $(N-1)^2$, and is related to rotational elements and complex phases. A non rigorous interpretation of these numbers is provided by analysing a same dimensional real-valued matrix. In this case, orthogonality implies that only $\frac{1}{2}N(N-1)$ degrees of freedom are independent. Extrapolating this to the complex case it is possible to conclude that there are $\frac{1}{2}(N-1)(N-2)$ possible complex phases. Hence, the CKM matrix is defined by three real parameters related to rotations (Euler angles) and a single complex phase responsible for *CP* violation.

The most standard parametrisation of the flavour mixing matrix is obtained

by the product of three complex rotation matrices as [26]

$$V = \begin{pmatrix} c_{12}c_{13} & s_{12}c_{13} & s_{13}e^{-i\delta} \\ -s_{12}c_{23} - c_{12}s_{23}s_{13}e^{i\delta} & c_{12}c_{23} - s_{12}s_{23}s_{13}e^{i\delta} & s_{23}c_{13} \\ s_{12}s_{23} - c_{12}c_{23}s_{13}e^{i\delta} & -c_{12}s_{23} - s_{12}c_{23}s_{13}e^{i\delta} & c_{23}c_{13} \end{pmatrix}, \tag{2.8}$$

where $s_{ij} = \sin\theta_{ij}$ and $c_{ij} = \cos\theta_{ij}$ with family indices $i, j = 1, 2, 3$, and δ is the *CP*-violating phase. A more convenient representation has been proposed by Wolfenstein [27], which structures the elements in order of magnitudes, defined by

$$\lambda = s_{12}, \quad A = \frac{s_{23}}{s_{12}^2}, \quad \rho = \frac{s_{13}}{s_{12}s_{23}}\cos\delta \quad \text{and} \quad \eta = \frac{s_{13}}{s_{12}s_{23}}\sin\delta, \tag{2.9}$$

where $\lambda \approx 0.22$ (sine of θ_c, the Cabibbo angle). In this approximation, A, ρ and η are real quantities of order of unity, which simplify the expansion. The CKM-matrix elements are written in orders of λ as

$$V = \begin{pmatrix} 1 - \lambda^2/2 & \lambda & A\lambda^3(\rho - i\eta) \\ -\lambda & 1 - \lambda^2/2 & A\lambda^2 \\ A\lambda^3(1 - \rho - i\eta) & -A\lambda^2 & 1 \end{pmatrix} + \mathcal{O}(\lambda^4)\,, \tag{2.10}$$

where it is useful to define $\bar{\rho} = \rho(1 - \lambda^2/2)$ and $\bar{\eta} = \eta(1 - \lambda^2/2)$.

The unitarity of the CKM matrix leads to a number of relations between its elements, which satisfy

$$\begin{aligned} \sum_{i=1}^{3} |V_{ij}|^2 &= \sum_{j=1}^{3} |V_{ij}|^2 = 1\,, \\ \sum_{i=1}^{3} V_{ji}V_{ki}^* &= 0 = \sum_{i=1}^{3} V_{ij}V_{ik}^*\,, \end{aligned} \tag{2.11}$$

where $i = u, c, t$ and $j = d, s, b$ in the first equation, and $i = d, s, b$ and $j, k = u, c, t$ $(j \neq k)$ in the second on the bottom left and reversed in the bottom right. Among these conditions, those in the second system of equations can be interpreted geometrically in the complex plane. Writing these in the explicit form, reads

$$V_{ud}^*V_{us}[\mathcal{O}(\lambda)] + V_{cd}^*V_{cs}[\mathcal{O}(\lambda)] + V_{td}^*V_{ts}[\mathcal{O}(\lambda^5)] = 0\,, \tag{2.12}$$

$$V_{ud}^*V_{ub}[\mathcal{O}(\lambda^3)] + V_{cd}^*V_{cb}[\mathcal{O}(\lambda^3)] + V_{td}^*V_{tb}[\mathcal{O}(\lambda^3)] = 0\,, \tag{2.13}$$

$$V_{us}^*V_{ub}[\mathcal{O}(\lambda^4)] + V_{cs}^*V_{cb}[\mathcal{O}(\lambda^2)] + V_{ts}^*V_{tb}[\mathcal{O}(\lambda^2)] = 0\,, \tag{2.14}$$

$$V_{ud}V_{cd}^*[\mathcal{O}(\lambda)] + V_{us}V_{cs}^*[\mathcal{O}(\lambda)] + V_{ub}V_{cb}^*[\mathcal{O}(\lambda^5)] = 0\,, \tag{2.15}$$

$$V_{ud}V_{td}^*[\mathcal{O}(\lambda^3)] + V_{us}V_{ts}^*[\mathcal{O}(\lambda^3)] + V_{ub}V_{tb}^*[\mathcal{O}(\lambda^3)] = 0\,, \tag{2.16}$$

$$V_{cd}V_{td}^*[\mathcal{O}(\lambda^4)] + V_{cs}V_{ts}^*[\mathcal{O}(\lambda^2)] + V_{cb}V_{tb}^*[\mathcal{O}(\lambda^2)] = 0\,, \tag{2.17}$$

where the approximate size of each term has been indicated. Only 2.13 and 2.16 contain all terms in the same order of λ, which results in triangles with sizeable internal angles in the complex plane (others have squashed representations). Nonetheless, it is noticeable that since four independent parameters are sufficient to describe the CKM matrix, these relations are highly correlated.

The triangle given in Eq. 2.13 is historically known as the unitarity triangle, with the sides normalised to $V_{cd}V_{cb}^*$ and internal angles defined as

$$\alpha = \arg\left(-\frac{V_{td}V_{tb}^*}{V_{ud}V_{ub}^*}\right) = \arg\left(-\frac{1-\rho-i\eta}{\rho+i\eta}\right)\,, \tag{2.18}$$

$$\beta = \arg\left(-\frac{V_{cd}V_{cb}^*}{V_{td}V_{tb}^*}\right) = \arg\left(\frac{1}{1-\rho-i\eta}\right)\,, \tag{2.19}$$

$$\gamma = \arg\left(-\frac{V_{ud}V_{ub}^*}{V_{cd}V_{cb}^*}\right) = \arg\left(\rho+i\eta\right)\,, \tag{2.20}$$

which can be independently measured in different particle decays, providing a direct probe of the *CP* violation mechanism in the SM. Additional correlated observables are also available and are often used to put further constraints on this triangle. In general, these measurements are combined to restrict the possible position of the upper vertex in the unitary triangle. A graphical representation of this triangle along with the status of the global fit measurements for the CKM matrix constraints is shown in Fig. 2.1. Another important angle for the purpose of this analysis is defined by $\arg\left(-V_{cs}V_{cb}^*/V_{ts}V_{tb}^*\right)$, hereafter referred to as β_s. The unitarity triangle angles are related to the single complex phase in the CKM matrix, and thus, to the *CP* violation manifestation. Throughout this work a phase convention is used where, at $\mathcal{O}(\lambda^3)$, the elements $V_{td} = |V_{td}|e^{-i\beta}$ and $V_{ub} = |V_{ub}|e^{-i\gamma}$. In this reference, $t \to d$ and $b \to u$ transitions are the exclusive source of *CP* asymmetries in the SM.

2.4 *CP* violation manifestation

Despite the SM being a remarkable theory in its predictive power, additional sources of *CP* violation are required in New Physics (NP) models. In general, the observation of *CP* violation relies on noticeable differences among processes and their corresponding *CP*-conjugates. The observation of *CP* violation is related to the interference between different amplitudes that contribute to these processes, mani-

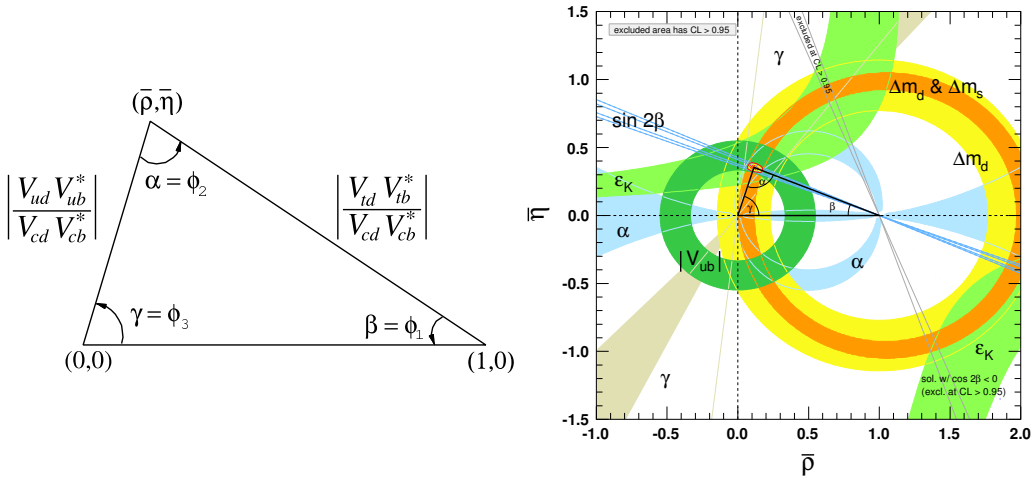

Figure 2.1: Schematic view (left) of the unitarity triangle and a summary (right) of the various measurements that provide constraints on the parameters related to the CKM matrix, compiled by the CKM fitter group [28]. The shaded areas indicate confidence level contours of 95% (68%) by their outer (inner) boundaries.

fested by the complex phase in the coupling that breaks *CP* invariance. The classification of *CP*-violating signatures in the quark sector is discussed in this section.

2.4.1 Neutral mesons mixing

Spontaneous oscillations are a well known property of neutral mesons, that can transit between particle and antiparticle states as time evolves. This phenomenon is characteristic of weak interactions and it has been observed in the K/B system and most recently in D decays.

Consider a generic neutral meson P^0 (which has an antiparticle $\bar{P}^0 \neq P^0$), that evolves into a time-dependent quantum superposition of states. More specifically, an arbitrary state that at $t = 0$ is a linear combination of $|P^0\rangle$ and $|\bar{P}^0\rangle$ eigenstates, evolves acquiring any possible final state component f as

$$|\psi(t)\rangle = \psi_1(t)|P^0\rangle + \psi_2(t)|\bar{P}^0\rangle + \sum_i \psi_i(t)|f_i\rangle\,. \tag{2.21}$$

Ignoring $|f_i\rangle$ terms results in an effective Hamiltonian, with time evolution governed by the Schrödinger equation

$$i\hbar\frac{\partial}{\partial t}\begin{pmatrix}\psi_1(t)\\ \psi_2(t)\end{pmatrix} = \mathcal{H}\begin{pmatrix}\psi_1(t)\\ \psi_2(t)\end{pmatrix} = \begin{pmatrix} M - \frac{i}{2}\Gamma \end{pmatrix}\begin{pmatrix}\psi_1(t)\\ \psi_2(t)\end{pmatrix}, \tag{2.22}$$

where M and Γ denote the mass and decay width Hermitian matrices, and are often referred to as dispersive and absorptive terms, respectively. While absorptive transitions are only described by intermediate processes with sufficient energy for the P^0 particle to decay, dispersive transitions may occur via quantum fluctuations (following Heinsenberg's uncertainty principle). Moreover, the real part of the Hamiltonian is associated with the energy of the system, which in the rest frame of the particle is defined by its own mass. On the other hand, the inclusion of a complex term $i\Gamma/2$ in the Hamiltonian removes its hermiticity and introduces an amplitude proportional to $e^{-\Gamma t}$. Since the particle probability follows an exponential pattern, particles decaying accordingly to $1/\Gamma$ are naturally introduced in the formalism.

Under CPT invariance, the diagonal elements of this matrix are required to satisfy $M_{11} = M_{22}$ and $\Gamma_{11} = \Gamma_{22}$. By diagonalising $\mathcal{H}$, the physical mass eigenstates can be written in terms of linear combinations of flavour eigenstates

$$\begin{aligned} |P_L\rangle &= p|P^0\rangle + q|\bar{P}^0\rangle\,, \\ |P_H\rangle &= p|P^0\rangle - q|\bar{P}^0\rangle\,, \end{aligned} \tag{2.23}$$

where the subscripts L and H refers to the lighter and heavier eigenstates, p and q are the complex mixing parameters that satisfy $|p|^2 + |q|^2 = 1$. The time evolution of these eigenstates is given by

$$|P_{1,2}(t)\rangle = |P_{1,2}\rangle e^{-i\left(M_{1,2} - \frac{i}{2}\Gamma_{1,2}\right)}\,. \tag{2.24}$$

Inverting equation 2.23 and inserting relation 2.24, one can obtain the time evolution of the flavour eigenstates

$$\begin{aligned} |P^0(t)\rangle &= f_+(t)|P^0\rangle + \frac{q}{p} f_-(t)|\bar{P}^0\rangle\,, \\ |\bar{P}^0(t)\rangle &= f_+(t)|\bar{P}^0\rangle + \frac{p}{q} f_-(t)|P^0\rangle\,, \end{aligned} \tag{2.25}$$

where

$$\begin{aligned} f_\pm(t) &= \frac{1}{2}\left(e^{-\left(M_L - \frac{i}{2}\Gamma_L\right)t} \pm e^{-\left(M_H - \frac{i}{2}\Gamma_H\right)t}\right) \\ &= \frac{1}{2}\left(e^{-iMt}e^{-\frac{1}{2}\Gamma t}\left[1 \pm e^{-i\Delta m\, t}e^{-\frac{1}{2}\Delta\Gamma\, t}\right]\right)\,, \end{aligned} \tag{2.26}$$

with $\Delta m \equiv m_H - m_L$, $\Gamma \equiv \frac{1}{2}(\Gamma_L + \Gamma_H)$ and $\Delta\Gamma = \Gamma_L - \Gamma_H$, where $\Delta\Gamma$ can have either sign. The convention is such that $\Delta\Gamma$ is expected to be positive in the SM.

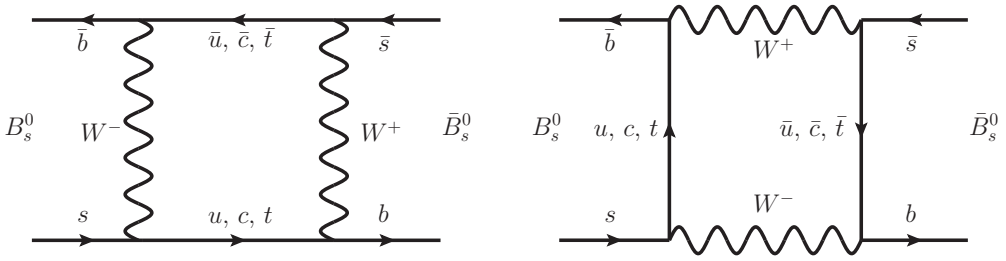

Figure 2.2: Feynman diagrams representing the second order weak interactions that give rise to B_s^0-$\overline{B}_s^0$ mixing. The particles that propagate in the loop correspond to quarks with charge 2/3. Since the t quark dominates these transitions, given the quark-mass hierarchies, $V_{ts}V_{tb}^*$ is the dominant CKM factor in this diagram, introducing the *CP*-violating phase.

Further simplification can be obtained by explicitly expanding the definitions of the eigenstates

$$\Delta m = 2|M_{12}|\left(1 - \frac{1}{8}\frac{|\Gamma_{12}|^2}{|M_{12}|^2}\sin^2\phi\right), \tag{2.27}$$

$$\Delta\Gamma = 2|\Gamma_{12}|\cos\phi\left(1 - \frac{1}{8}\frac{|\Gamma_{12}|^2}{|M_{12}|^2}\sin^2\phi\right), \tag{2.28}$$

where $\phi = \arg\left(-\frac{M_{12}}{\Gamma_{12}}\right)$. Considering only the B_s^0 meson system and given the current experimental measurements $\Delta m_s/\Gamma_s = 26.85 \pm 0.13$ and $\Delta\Gamma_s/\Gamma_s = 0.138 \pm 0.012$ [28], it is a good approximation to consider $\Delta m \gg \Delta\Gamma$, such that [4]

$$\Delta m \approx 2|M_{12}| \quad \text{and} \quad \Delta\Gamma \approx 2|\Gamma_{12}|\cos\phi_s\,. \tag{2.29}$$

Both M_{12} and Γ_{12} matrix elements can be evaluated by interpreting the B_s^0-$\overline{B}_s^0$ mixing through the box diagrams shown in Figure 2.2. [5] Although all intermediate state u, c, t transitions are allowed, the diagrams are dominated by t-quark contributions. Since the CKM dependence of these diagrams relies on the elements V_{tb} and V_{ts}, it is possible to obtain the B_s^0 *CP*-violating mixing phase ϕ_s. Although many NP extensions predict additional complex mixing phases, no convincing experimental evidence has been found to date. The latest measurement is $\phi_s = 0.058 \pm 0.049\,(\text{stat}) \pm 0.006\,(\text{syst})\,\text{rad}$ [29] and is consistent with SM predictions, *e.g.* $\phi_s = 0.037 \pm 0.001$ [30]. Another relevant expression in the context of

[4] Notice that this is also true for B^0 decays, with the values $\Delta m_d/\Gamma_d = 0.774 \pm 0.006$ and $\Delta\Gamma_d/\Gamma_d = (0.1 \pm 1.0) \times 10^{-2}$ [28].

[5] Additional long-distance diagrams required for Γ_{12} are omitted for simplicity.

mixing is the magnitude of the ratio q/p, which in this regime can be written as $|q/p|^2 = 1 - |\Gamma_{12}/M_{12}| \sin\phi_s$. Hence, in the absence of *CP* violation in the mixing (introduced in the following) this parameter is unity.

Consider a decay amplitude $\mathcal{A}_f$ for a given final state f of the meson B_s^0 (or similarly for the antiparticle with $\bar{\mathcal{A}}_f$), defined as $\mathcal{A}_f = \langle f|\mathcal{H}|B_s^0\rangle$. The time-dependent decay rate can be calculated by the modulus squared of this amplitude and replacing equation 2.25 for the mass eigenstates time evolution, such that [31]

$$\begin{aligned}\Gamma_{B_s^0\to f}(t) = \frac{\mathcal{N}_f\, e^{-\Gamma_s t}}{2\tau(B_s^0)}\Big[\cosh\left(\tfrac{\Delta\Gamma_s t}{2}\right) - \\ S_f \sin(\Delta m_s t) + C_f \cos(\Delta m_s t) + A_f^{\Delta\Gamma_s}\sinh\left(\tfrac{\Delta\Gamma_s t}{2}\right)\Big],\end{aligned} \tag{2.30}$$

where $\mathcal{N}_f$ is the normalisation factor, $\tau(B_s^0) = \left(\frac{\Gamma_\mathrm{L}+\Gamma_\mathrm{H}}{2}\right)^{-1}$ is the B_s^0 lifetime and the coefficients of the $\sin(\Delta m_s t)$, $\cos(\Delta m_s t)$ and $\sinh\left(\frac{\Delta\Gamma_s t}{2}\right)$ terms are given as

$$S_f \equiv \frac{2\,\mathcal{I}m(\lambda_f)}{1+|\lambda_f|^2}, \qquad C_f \equiv \frac{1-|\lambda_f|^2}{1+|\lambda_f|^2}, \qquad A_f^{\Delta\Gamma_s} \equiv -\frac{2\,\mathcal{R}e(\lambda_f)}{1+|\lambda_f|^2}, \tag{2.31}$$

where the parameter λ_f encodes information about *CP* violation and is given by $\lambda_f = \frac{q}{p}\frac{\bar{\mathcal{A}}_f}{\mathcal{A}_f}$. Note that, by definition, $(S_f)^2 + (C_f)^2 + (A_f^{\Delta\Gamma_s})^2 = 1$. Similar expression may be obtained for $\langle f|\mathcal{H}|\bar{B}_s^0\rangle$ by changing the sign of the C_f and S_f terms. The interpretation of these terms as different classes of *CP* violation is examined below.

2.4.2 *CP* violation classification

CP violation in the quark sector is commonly classified into three categories which reflect the several manifestations that can be observed in nature. In this section, a brief overview is given of these categories.

CP violation in decay

CP violation in decay can in principle be observed for any heavy flavour hadron. It occurs in the presence of an unequal decay-rate for a particle and its *CP* conjugate. Consider a given process described by several amplitudes, denoting different possible diagrams contributing to the final state. These can also receive different phases, either from strong or weak interactions. The total amplitude can be written as

$$\mathcal{A}_f = \sum_j \mathcal{A}_j e^{i(\delta_j - \phi_j)} \quad \text{and} \quad \bar{\mathcal{A}}_{\bar{f}} = \sum_j \mathcal{A}_j e^{i(\delta_j + \phi_j)}, \tag{2.32}$$

where δ and ϕ are respectively the strong (*i.e. CP*-conserving) and weak (*i.e. CP*-violating) phases. Charge-parity violation in decay occurs when

$$\left|\frac{\bar{\mathcal{A}}_{\bar{f}}}{\mathcal{A}_f}\right| = \left|\frac{\sum_j \mathcal{A}_j e^{i(\delta_j+\phi_j)}}{\sum_j \mathcal{A}_j e^{i(\delta_j-\phi_j)}}\right| \neq 1\,. \tag{2.33}$$

It is particularly notable that, in the case indicated in formulae 2.30, non-zero values for C_f implies $\bar{\mathcal{A}}_{\bar{f}} \neq \mathcal{A}_f$ if $|q/p| = 1$, meaning *CP* violation in decay. It is important to mention that non-vanishing *CP* violation values are observed only when at least two decay amplitudes with different weak and strong phases are contributing. Note that this is the only possible mechanism for *CP* violation in charged mesons and b-baryon decays.

CP violation in mixing

The phenomenon of *CP* violation in mixing has been already introduced, and denotes that the physical states do not corresponding to the *CP* eigenstates. The manifestation of this form is independent of the final state, and is related to the aforementioned difference in the oscillation ratio between the neutral meson and its antiparticle. Therefore, *CP* violation in mixing occurs if

$$\left|\frac{q}{p}\right| \neq 1\,. \tag{2.34}$$

The SM predictions give values that equal unity to one in 10^3. The current experimental measurement in the B_s^0 system is $|q/p| = 1.0039 \pm 0.0021$ [32].

Interference between decay and mixing amplitudes

An alternative genre of *CP* violation is associated to the interference between mixing and decay processes of neutral mesons to the same final state. The parameter that outlines this measurement is encoded in the term S_f from equation 2.30. *CP* violation occurs in the event that the imaginary part of λ takes a non zero value

$$\Im\left(\frac{q}{p}\frac{\bar{\mathcal{A}}_f}{\mathcal{A}_f}\right) \neq 0\,. \tag{2.35}$$

Note that in the absence of *CP* violation in both mixing and decay (*i.e.* $q/p = 1$ and $|\lambda_f| = 1$), this quantity can still assume non-vanishing values in the presence of a phase difference between the mixing and decay amplitudes. A series of processes satisfy these conditions, in particular the $B_s^0 \to K^0 K^{\pm}\pi^{\mp}$ channel.

3

Charmless three-body decays

Description of the nature of hadronic decays requires satisfactory understanding of both weak interactions and strong processes. In this chapter, an overview of the relevant framework for charmless three-body decays is discussed, with particular emphasis on the $B_s^0 \to {}^{(}\overline{K}{}^{)0}K^{\pm}\pi^{\mp}$ decay channel. The underlying structure of multi-body decays is composed of several quasi-two-body states and non-resonant contributions, and therefore, the initial discussion will focus on the elements well established for the two-body case. The formalism to outline the kinematics and dynamics of three-body decays in the so-called Dalitz plot is then defined. Within this picture the decay mode $B_s^0 \to {}^{(}\overline{K}{}^{)0}K^{\pm}\pi^{\mp}$ is examined.

3.1 Quasi-two-body decays

Decays of B^0 and B^+ mesons into two particles have offered for many years a rich environment to probe the mechanisms involved in flavour phenomenology; experimentally explored mainly by the B factory experiments, BaBar and Belle. However, with the recent advent of the LHCb experiment, this programme has been extended to the B_s^0 sector. In this section, the physics potential of this type of decay is examined in detail. In particular, the narrative is based on the $B_s^0 \to K^*K$ decay, which is the most important quasi-two-body contribution for the $B_s^0 \to {}^{(}\overline{K}{}^{)0}K^{\pm}\pi^{\mp}$ channel. A descriptive review of the main theoretical approaches is also provided, in order to establish the fundamental structure that can be extrapolated to the general case of multi-body decays.

3.1.1 Motivation

Searches for new sources of *CP* asymmetries are among the main goals of current particle physics. In particular, flavour changing neutral current processes of B meson decays, predominantly mediated by $b \to s$ amplitudes, are crucial probes of the Standard Model, since as-yet undiscovered particles may contribute to loop diagrams and cause observables to deviate from their predicted values [33–36]. The current experimental measurements indicate good consistency with the SM predictions, however further investigations are required to be sensitive to small deviations.

An interesting decay mode to search for new sources of *CP* violation is the $B_s^0 \to K^*K$ channel, where K^* denotes a kaon resonance such as $K^*(892)$ or $K^*(1430)$. Two charge configurations are present in the final state: $B_s^0 \to \overline{K}^{*0}K^0(K^{*0}\overline{K}^0)$ and $B_s^0 \to K^{*\pm}K^{\mp}$. An interesting feature of these modes is that both final states are accessible to both B_s^0 and $\overline{B}_s^0$ decays, with the amplitudes expected to be comparable in magnitude. These channels have been recently observed by LHCb with inclusive branching fractions of $\mathcal{B}(B_s^0 \to K^{*\pm}K^{\mp}) = (12.7 \pm 1.9 \pm 1.9) \times 10^{-6}$ [37] and $\mathcal{B}(B_s^0 \to \overline{K}^{*0}K^0(K^{*0}\overline{K}^0)) = (10.9 \pm 2.9 \pm 1.2) \times 10^{-6}$ [38]. The dominant decay amplitudes for these modes are shown in Fig. 3.1. The leading diagrams for the charged final state consist of tree $b \to u$ ($V_{ub}^*V_{us} \sim \lambda^4$) and loop ("penguin") $b \to s$ ($V_{tb}^*V_{ts} \sim \lambda^2$) transitions. The neutral mode has a similar penguin contribution but no tree-level amplitude. This latter type of decay is a so-called "pure penguin" decay and it is among the most sensitive probes for new physics. Electroweak penguin (EWP) contributions are, however, not negligible in any of these decays, and these lead to significant uncertainties in the theoretical calculations. Further details on the diagrammatic approach and its implications are given in the next section.

The precise determination of the CKM unitarity triangle phase γ is another important target in flavour physics. The interference between tree and penguin transitions can provide sensitivity to γ. Early propositions explored the ratio and asymmetry in two body decays to extract this weak phase (e.g. $B_{(s)} \to K\pi$ modes) [39–42], however with large uncertainties. Alternative approaches have been proposed to overcome the hadronic uncertainties by studying processes that decay to three-body final states [43,44]. The relative amplitudes and phases of quasi-two-body decays can be measured from the interference pattern in the so-called Dalitz plot (see Section 3.2). The improvement from this method is particularly notable in the case that broad resonances contribute, since interference causes effects to which quasi-two-body approaches have no sensitivity [45–47]. One can exploit the same idea in $B_s^0 \to K^*K$ decays (although uncertainties from EWP amplitudes are

non-negligible) using an isospin analysis [48].

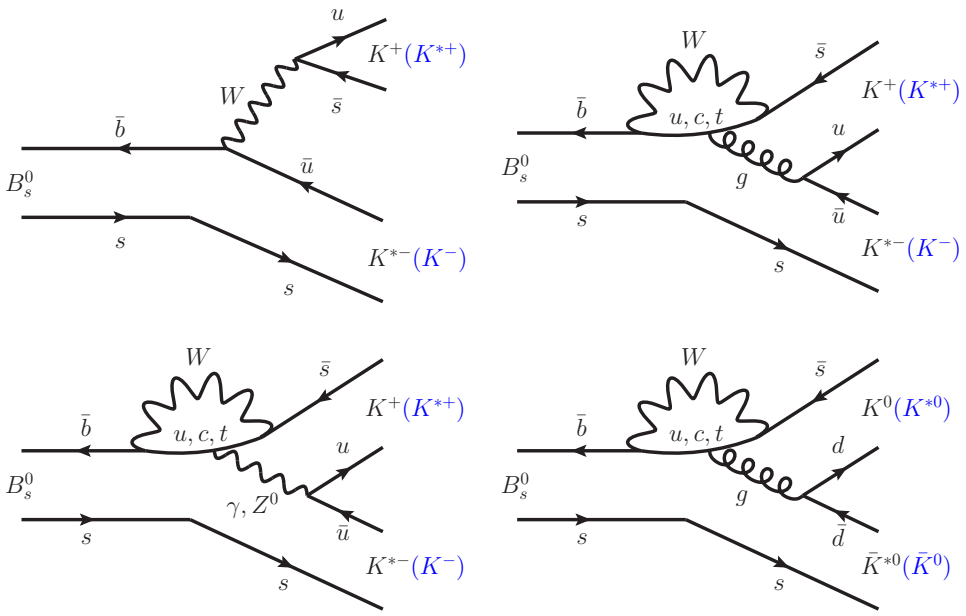

Figure 3.1: Feynman diagrams for (top left) external tree, (top right) gluonic penguin and (bottom left) EWP contributions for $B_s^0 \to K^{*\pm}K^{\mp}$ decays; and (bottom right) gluonic penguin amplitude for the $B_s^0 \to \overline{K}^{*0}K^0(K^{*0}\overline{K}^0)$ decay mode.

Another notable aspect of $B_s^0 \to \overline{K}^{*0}K^0(K^{*0}\overline{K}^0)$ channels is that they are U-spin partners with $B^0 \to K^*K$ neutral final state configuration [49, 50]. The U-spin symmetry is a SU(2) subgroup of flavour SU(3) symmetry, under which a discrete transformation (Weyl reflection) $d \leftrightarrow s$ is performed. [1] Exploiting this symmetry, an extensive number of implications for B_s^0 charmless decays can be investigated. In particular, U-spin multiplets are of great interest as they provide model-independent probes for the SM [51–55]. Similar theoretical approaches can be applied in three-body decays, including recent predictions for $B_s^0 \to {}^{(}\overline{K}{}^{)0}K^{\pm}\pi^{\mp}$ decays [56, 57].

One further noteworthy feature of the B_s^0 system (with regard to *CP* violation searches) is the non-zero width difference $\Delta\Gamma_s$ between the mass eigenstates. Compared to the situation for B^0 decays, the decay-time distribution receives additional terms that do not vanish when integrated over the initial flavour of the B meson. This implies that information about *CP* violation parameters can be obtained from analyses without flavour tagging techniques, through so-called effective lifetime measurements [58, 59]. In section 3.3, an explanation of this concept and

[1] The U-spin symmetry can be interpreted as relating to a doublet (d, s) pair of quarks, similarly to the (u, d) pair in isospin.

discussions about the sensitivity for $B_s^0 \to {}^{(}\overline{K}{}^{)0} K^{\pm}\pi^{\mp}$ decays are presented.

3.1.2 Theoretical framework

The phenomenology of weak decays of hadrons (see Sec. 2) is unavoidably complicated by strong-interaction effects. For example, the simplified picture of the $b \to u$ transition in Fig. 3.1 must be modified to embed gluonic self-energy corrections. Quantum field theory requires the inclusion of all possible virtual states for proper estimation of observables. Since these computations often involve multiple energy scales (due to different particle masses involved in the process), estimations are further impaired. In this section, an Effective Field Theory (EFT) [60, 61] to describe hadronic decays is briefly introduced. In addition, a qualitative overview of the popular theoretical approaches to study the dynamics of these processes is given. Finally, flavour symmetry arguments are discussed with further explanation of the extraction of the CKM phase γ in $B_s^0 \to K^*K$ decays.

Strong interactions parametrisation

Decays of B mesons are associated with phenomena involving distinct energy scales ($M_W \gg m_b \gg \Lambda_{\rm QCD} \gg m_{u,d,s}$),[2] which can often be analysed by separating each relevant domain. These regimes can be classified into short-distance perturbative [3] and non-calculable long-distance effects. The formal framework to describe this methodology is provided by the operator product expansion (OPE) [65]. Considering the tree-level transition in Fig. 3.1 as an example, the amplitude is given by [66, 67]

$$A = i\,\frac{G_F}{\sqrt{2}} V_{ub}^* V_{us} (b^\dagger \gamma^\mu \gamma_L u)(u^\dagger \gamma_\mu \gamma_L s) \frac{M_W^2}{k^2 - M_W^2}\,, \tag{3.1}$$

where $\gamma_L = (1-\gamma_5)$, $G_F/\sqrt{2} = g/8M_W^2$, g is the coupling constant of weak interactions and k is the transferred momentum of the W-boson propagator (typically $k \ll M_W$). Expanding in k^2/M_W^2 terms

$$\begin{aligned} A &= -i\,\frac{G_F}{\sqrt{2}} V_{ub}^* V_{us} (b^\dagger \gamma^\mu \gamma_L u)(u^\dagger \gamma_\mu \gamma_L s) \left[1 + \frac{k^2}{M_W^2} + \dots\right] \\ &\approx -i\,\frac{G_F}{\sqrt{2}} V_{ub}^* V_{us} (\bar{b}u)_{V-A} (\bar{u}s)_{V-A} = -i \frac{G_F}{\sqrt{2}} V_{ub}^* V_{us} Q_2\,, \end{aligned} \tag{3.2}$$

[2] The factor $\Lambda_{\rm QCD} \sim 1$ GeV sets the scale of strong interactions, that is the regime in which the coupling constant becomes large and the physics becomes nonperturbative.

[3] At short-distance (high energies) quarks interact weakly, being considered in an asymptotic freedom, which allows a pertubative calculation [62–64].

where Q_2 is an effective vertex operator. The arguments of the OPE are the products of two charged-current operators expanded into a series of local operators weighted by effective couplings (the so-called Wilson coefficients [68]). Notice that the W-boson degrees of freedom of the theory have been absorbed into the Wilson coefficients.[4] A similar result can be obtained in terms of an effective Hamiltonian, which in this example is simply an alternative convenient parametrisation.

Gluon-exchange contributions can be added to the picture as shown in Fig 3.2. These quantum chromodynamic (QCD) corrections require the introduction of a new operator Q_1, which describes the possibility of colour index exchange in the two colour-singlet weak-current lines when connected to the gluon.[5] The effective Hamiltonian for the tree transition including QCD corrections is given by

$$\mathcal{H}_{\text{eff}} = \frac{G_F}{\sqrt{2}} V_{ub}^* V_{us} (C_1 Q_1 + C_2 Q_2) + H.c.\,, \tag{3.3}$$

where C_i are the Wilson coefficients and Q_i are the effective vertex operators. These terms are non-trivial functions of the energy scale μ (that separates the long/short-distance regimes), the strong coupling α_s and the mass propagator (e.g. t, W, Z and H in the C_i case). Although the choice of the μ value is arbitrary, it is often associated to the order of the mass of the decaying particle, for instance $\mathcal{O}(m_b) \sim$ few GeV [69, 70]. This results in large contributions from $\ln M_W/\mu$ terms ($\mu \ll M_W$) in the calculation of C_i. Using renormalisation group techniques [71, 72], it is possible to evaluate these terms to all orders of the QCD parameter α_s (in a pertubative expansion). One remarkable outcome of this method is that no assumption about the nature of the bound state of the decaying hadron has been made, which results in Wilson coefficients independent of the initial state hadron. Finally, the effective Hamiltonian is given by [73]

$$A(B_s^0 \to K^* K) = \langle K^* K | \mathcal{H}_{\text{eff}} | B_s^0 \rangle = \frac{G_F}{\sqrt{2}} V_{\text{CKM}} \sum_i C_i(\mu) \langle K^* K | Q_i(\mu) | B_s^0 \rangle\,. \tag{3.4}$$

The interpretation of μ as a transition between two physics regimes constrains the full amplitude to be independent of μ. Therefore, any μ dependence of the couplings C_i has to cancel with the Q_i term. This generic approach can be extended to include other transition contributions from QCD penguin ($Q_{3,\ldots,6}$), electroweak

[4] Formally this procedure is discussed using Green's functions in the path-integral formalism, and is referred as "integrating out" the degree of freedom.

[5] This operator is explicitly given by $\sum_{a=1}^{8} [\bar{b}_w \gamma^\mu (1-\gamma_5) \lambda^a_{wz} u_x][\bar{u}_y \gamma_\mu (1-\gamma_5) \lambda^a_{yx} s_x]$, where λ are the Gell-Mann matrices. Using the Fierz transformation it is possible to write this operator as $-(2/3)Q_2 + 2Q_1$, where $Q_1 \equiv (\bar{b}_x u_y)_{V-A} (\bar{u} s)_{V-A}$.

penguin ($Q_{7,\ldots,10}$), and electromagnetic and chromomagnetic dipole ($Q_{7\gamma}$ and $Q_{8\gamma}$) operators [74].

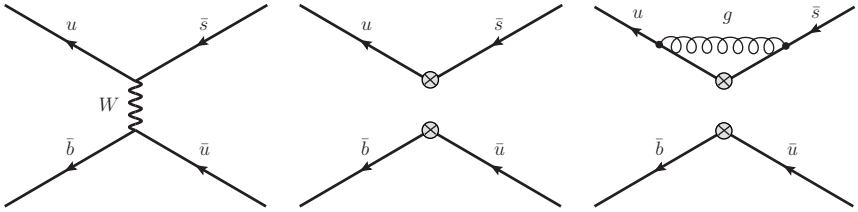

Figure 3.2: Schematic Feynman graphs of the OPE methodology for the $b \to u$ tree-level transition in the case of (left) weak decays, (middle) effective factorisation approach and (right) including possible QCD effects in the effective theory.

Hadronic matrix calculation

Understanding hadronic phenomenology is among the main ambitions of theoretical physics. Many approaches have been proposed to study the dynamics of hadronic processes, among which some of the most popular are QCD factorisation (QCDF) [75], pertubative QCD (pQCD) [76, 77] and soft-collinear effective theory (SCET) [78]. Some of these methods are briefly introduced in this section, preceded by a review of an earlier attempt named "naive" factorisation, which is the foundation of the aforementioned approaches.

The ansatz for factorisation is to describe the weak decay matrix as a product of two current operators $\langle h_1|J^1|0\rangle\langle h_2|J^2|B\rangle$ [79, 80]. The decay is decoupled into two systems, within the *sine qua non* premise that gluon exchanges between these can be neglected. The decomposition for each transition element n for the example of $B_s^0 \to K^{*-}K^+$ is given by

$$\langle K^{*-}K^+|Q_n|B_s^0\rangle = \langle K^+|J_n^1|0\rangle\langle K^{*-}|J_n^2|B_s^0\rangle \;\text{ or }\; \langle K^{*-}|J_n^1|0\rangle\langle K^+|J_n^2|B_s^0\rangle\,, \quad (3.5)$$

where $J_n^{1,2}$ are quark currents. Note that due to the different diagrammatic decomposition for each $K^{*\pm}K^{\mp}$ charge configuration (see Fig. 3.1), distinct factorisation terms are obtained. In this scenario, hadronisation is reduced to non-pertubative hadronic decay form factors and decay constants. This configuration provides a simplified framework, in which observables can be theoretically predicted [6] and even experimentally determined by extrapolating from (semi)leptonic decays. In spite of

[6] Several non-pertubative methods have been used to compute these factors (with some limitations), such as lattice QCD, QCD sum rules, chiral perturbation theory and light-cone amplitudes.

providing reasonable results in specific scenarios, the limitation of this machinery is underlined for instance by the absence of either effects related to rescattering in the final state or strong phase differences between the amplitudes, and a clear dependency on the μ scale.

In order to extend this framework to include non-factorisable strong interaction corrections, the concept of the heavy quark limit (in which $m_b \gg \Lambda_{\rm QCD}$) is introduced. In this kinematic regime, couplings of the light quark h_1 in the $\langle h_1|J_n^i|0\rangle$ systems with soft gluons are suppressed by a power of $\Lambda_{\rm QCD}/m_b$.[7] The QCD factorisation approach relies on this assumption to systematically compute strong final state interactions proportional to m_b. This is satisfied by absorbing non-factorisable gluon exchanges into calculable pertubative couplings that are dependent on the μ scale. An important implication of these couplings is related to the introduction of an imaginary term, which results in accessible strong phases (essential for *CP* violation). Schematically this approach reads [82]

$$\langle K^{*-}K^+|Q_n|B_s^0\rangle = \langle K^+|J_n^1|0\rangle\langle K^{*-}|J_n^2|B_s^0\rangle \left[1 + \sum_n r_n \alpha_s^n + \mathcal{O}(\Lambda_{\rm QCD}/m_b)\right] , \quad (3.6)$$

where radiative α_s^n and power $\Lambda_{\rm QCD}$ corrections are added to the original matrix.

The pQCD approach follows a similar factorisation structure, but with several important distinctions [83]. One of the most important aspects is the description of gluon exchange with the spectator quarks. Instead of assuming that this leads to non-pertubative effects (due to so-called end-point singularities),[8] which can be parametrised through form factors, pQCD introduces the concept of parton transverse momentum, referred to as k_T [85]. In this implementation, singularities are absent due to the pertubative form factor (named Sudakov [86]) suppression near these end-points. Furthermore, annihilation diagram contributions are power-enhanced and strong phases have a significant importance in the pQCD approach [87]. Therefore, significant deviations from the QCDF method in both branching fractions and *CP* violation predictions are expected.

The SCET theory [88, 89] follows the same idea of power expansions in $\Lambda_{\rm QCD}/m_b$ orders, with a caveat of providing a more elegant phenomenological framework to separate the physics at different scales. Instead of describing the dynamics in the full long-distance range, the analysis is performed by expanding into momentum integration regions. In addition to the typical m_b and $\Lambda_{\rm QCD}$ scales, the intermediate

[7] Rigorously this idea is based on the physical concept of colour transparency, where final state interactions are suppressed when high momentum transfer occurs [81].

[8] In the heavy quark limit, singularities appear due to divergences of the integrals, originating from $\sim 1/x^2$ terms, where x is some fraction of the momentum [84].

scale $\sqrt{m_b \Lambda_{\rm QCD}}$ is introduced, corresponding to the interaction between collinear and soft particles. The presence of these distinct scales is systematically examined into a two-step procedure, defined for processes with momentum of $\sqrt{\Lambda_{\rm QCD}/E}$ and $\Lambda_{\rm QCD}/E$, named respectively SCET$_I$ and SCET$_{II}$ theories. These features provide a more robust implementation of the diagrammatic representation, though limitations on the calculation still remain.

Flavour symmetry

An interesting alternative to the model-dependent parametrisation of the strong dynamics in the SM is provided by the flavour symmetry notion. In particular, many simplifications to complex hadronic processes previously discussed can be obtained by imposing or identifying flavour symmetries in the system.

This idea has been briefly introduced within the amplitude decomposition framework, in which the physics pattern of $B_s^0 \to K^*K$ decays is represented by Feynman diagram contributions (Fig. 3.1). In this structure, a conventional approach is to perform a global fit to the flavour-physics parameter space, here denoted in terms of the available vector-pseudoscalar final states.[9] The flavour SU(3) symmetry[10] is investigated through the introduction of a breaking parameter for each generic transition [90]. The results of a such procedure are often extrapolated to perform branching ratio and *CP* violation estimations, assuming conservation of SU(3). Note that factorisable SU(3)-breaking corrections are easily accommodated in these methods. This is the example for the pairs $(B_s^0 \to K^{*+}K^-, B^0 \to \rho^+ K^-)$ and $(B_s^0 \to K^{*-}K^+, B^0 \to K^{*-}\pi^+)$, which are expected to agree under SU(3) symmetry. Furthermore, probes of flavour symmetries can be achieved by comparing related U-spin partners, under which large deviations from predictions may indicate BSM physics.

Although indirect flavour symmetry checks have an important role in the pursuit for new phenomena, potential constraints on the CKM phases are still the most appealing feature. Recently, the use of SU(2) symmetry in the channel $B_s^0 \to K^*K$ has been proposed as a novel method to extract γ [48]. The idea is to decompose each decay configuration in an isospin basis, and build linear combinations of the relevant amplitudes. Mesons such as K and K^* belong to the SU(2) representation, and thus are depicted as isospin $I = 1/2$. The expansion of each state into the

[9] Pseudoscalar are mesons with total spin zero and odd parity, whereas vectors have spin 1 (usual notation refers to $J^P = 0^-, 1^-$).

[10] In extension to the SU(2) symmetry, strange quarks are included in the SU(3) flavour group assuming an approximate symmetry in the triplet (u, d, s).

isospin basis (tensor product of the isospin of each particle) reads

$$\begin{aligned} |K^{*+}K^{-}\rangle &= \sqrt{1/2}|1\,0\rangle + \sqrt{1/2}|0\,0\rangle \\ |K^{*0}\overline{K}^{0}\rangle &= \sqrt{1/2}|1\,0\rangle - \sqrt{1/2}|0\,0\rangle\,, \end{aligned} \tag{3.7}$$

which only allow processes via $\Delta I = 1$ and $\Delta I = 0$ transitions (B_s^0 mesons have $I = 0$). Note that one can obtain identical relations using the final states $K^{*-}K^{+}$ and $\overline{K}^{*0}K^{0}$. The isospin-invariant amplitudes are expanded as

$$\begin{aligned} A_s(K^{*+}K^{-}) &= A_0^1 + A_0^0 \\ A_s(K^{*0}\overline{K}^{0}) &= A_0^1 - A_0^0\,, \end{aligned} \tag{3.8}$$

where the terms $A_{I_z}^{\Delta I}$ include the Clebsch-Gordon coefficients given in Eq. 3.7. Since gluons cannot carry isospin, A_0^0 transitions are associated to QCD penguin operators, whilst other contributions are within A_0^1. Similar relations for the *CP* conjugate final state are obtained, referred to as $A_s^{'}$. The sum of each of these equations results in

$$\begin{aligned} 2A_0^1 &= A_s(K^{*+}K^{-}) + A_s(K^{*0}\overline{K}^{0}) \\ 2A_0^{'1} &= A_s(K^{*-}K^{+}) + A_s(\overline{K}^{*0}K^{0})\,, \end{aligned} \tag{3.9}$$

for the four possible charge final state configurations. Similarly these can be obtained for the $\overline{B}_s^0$ meson. In these combinations, effects of QCD penguins have been cancelled. Therefore, the *CP*-violating weak phase may be extracted through the expression

$$\Phi_0^1 \equiv -\frac{1}{2}\arg\left(\frac{\bar{A}_0^1}{A_0^1}\right) = \gamma\,. \tag{3.10}$$

with analogous independent equation for the $A_s^{'}$ expressions. Note that this method relies on measuring the relative phase between B_s^0 and $\overline{B}_s^0$ amplitudes, which can only be achieved through decays to a final state accessible to both. These relations are however modified by EWP contributions that are CKM-enhanced and involve different weak phases. Recent estimations using SU(3) predict the introduction of large phase shifts and uncertainties up to 70%, which disfavour the method to provide stringent CKM constraints with the current theoretical accuracy [48]. Despite these corrections, the weak phase can be extracted by measuring each magnitude and a set of three relative phases between B_s^0 and its charge-conjugate. This information can be accessed by performing Dalitz plot analyses of $B_s^0 \to K^+K^-\pi^0$ (measures the relative phase between $K^{*+}K^{-}$ and $K^{*-}K^{+}$ final states) as well as

of $B_s^0 \to K_S^0 K^\pm \pi^\mp$ (remaining magnitudes and phases) decays. Further details on the latter process are addressed in the following sections.

Predictions

The prescription aforementioned for the phenomenology of hadronic decays can be used to obtain numerical predictions for the branching ratios and *CP* asymmetries for $B_s^0 \to K^* K$ decays. Tables 3.1 and 3.2 gather the most recent results for the discussed methods. Comparisons of these predictions for the branching ratios indicate fair agreement among the different approaches, with systematically larger mean values and uncertainties for the revised QCDF and SCET methods. Predictions for the *CP*-asymmetries are, however, not all consistent. Since in pure-penguin channels there is a single combination of CKM matrix elements in the regime of t-dominance (absence of interfering diagrams with additional strong phases), *CP* asymmetries vanish in these frameworks. Experimental input for these processes may provide important information for the current theoretical understanding.

3.2 Three-body decay formalism

The features discussed in the domain of two-body decays illustrate the degree of complexity and limitations involved in the phenomenology. Extending this to multibody decay introduces further complications, but also provides additional possibilities for experimental investigation, in particular for three-body decays.

Any particle decay can in general proceed through many intermediate branches. The transition rate in perturbation theory is governed by the Fermi Golden rule, which gives for a particle with mass M decaying into n bodies with masses m_i and four-momenta p_i, the relation

$$\Gamma = \frac{(2\pi)^4}{2M} \int |\mathcal{A}|^2 \delta^4(p - \sum_{i=1}^{n} p_i) \prod_{i=1}^{n} \frac{d^4 p_i}{(2\pi)^3} \delta(p_i^2 - m_i^2)\,, \tag{3.11}$$

where the term $\mathcal{A}$ clusters all the dynamics involved in the process from the kinematic quantities. In this section, this formulation is examined for three-body decays.

3.2.1 Dalitz Plot kinematics

Consider a generic decay of a pseudo-scalar meson at rest, with mass M and four-momentum $P^\mu = (M, 0)$, to three particles with masses m_i, four momenta $p_i^\mu = (E_i, \vec{p}_i)$ and energies E_i, where $i = 1, 2, 3$. Defining Lorentz invariant masses

Table 3.1: Branching ratio predictions (in units of 10^{-6}) for $B_s^0 \to K^* K$ decays. These are evaluated from two QCDF results published respectively in 2003 [91] and 2009 [92], pQCF 2007 [93] and the two solutions for the SCET 2008 [94] and SU(3) 2009 [90] approaches. The uncertainties on Ref. [91] are due to the knowledge of CKM parameters, renormalisation scale and form factors, light-cone expansion and power corrections, respectively. Similarly, for Ref. [90] the first errors are associated to the light-cone expansion and form factors whereas the second to power corrections. Uncertainties on Ref. [93] are related to hadronic quantities, scale dependence and CKM matrix elements, respectively. Finally, in Ref. [94] the errors are given respectively from form factors and CKM matrix elements.

Modes	QCDF	pQCD	SCET	SU(3)
$\overline{B}_s^0 \to K^+ K^{*-}$	$4.1^{+1.7+1.5+1.0+9.2}_{-1.5-1.3-0.9-2.3}$	$6.0^{+1.7+1.7+0.7}_{-1.5-1.2-0.3}$	$8.4^{+4.4+1.6}_{-3.4-1.3}$	7.45 ± 0.93
	$10.3^{+3.0+4.8}_{-2.2-4.2}$		$9.5^{+3.2+1.2}_{-2.8-1.1}$	7.79 ± 0.86
$\overline{B}_s^0 \to K^{*+} K^-$	$5.5^{+1.3+5.0+0.8+14.2}_{-1.4-2.6-0.7-\ 3.6}$	$4.7^{+1.1+2.5+0.0}_{-0.8-1.4-0.0}$	$9.8^{+4.6+1.7}_{-3.7-1.4}$	8.16 ± 0.70
	$11.3^{+7.0+8.1}_{-3.5-5.1}$		$10.2^{+3.8+1.5}_{-3.2-1.2}$	8.79 ± 0.66
$\overline{B}_s^0 \to K^0 \overline{K}^{*0}$	$3.9^{+0.4+1.5+1.3+10.4}_{-0.4-1.4-1.4-\ 2.8}$	$7.3^{+2.5+2.1+0.0}_{-1.7-1.3-0.0}$	$7.9^{+4.4+1.6}_{-3.4-1.3}$	5.21 ± 0.68
	$10.5^{+3.4+5.1}_{-2.8-4.5}$		$9.3^{+3.2+1.2}_{-2.8-1.0}$	5.74 ± 0.63
$\overline{B}_s^0 \to K^{*0} \overline{K}^0$	$4.2^{+0.4+4.6+1.1+13.2}_{-0.4-2.2-0.9-\ 3.2}$	$4.3^{+0.7+2.2+0.0}_{-0.7-1.4-0.0}$	$8.7^{+4.4+1.6}_{-3.5-1.4}$	9.11 ± 0.70
	$10.1^{+7.5+7.7}_{-3.6-4.8}$		$9.4^{+3.7+1.4}_{-3.1-1.2}$	9.54 ± 0.66
$B_s^0(\overline{B}_s^0) \to K^+ K^{*-}$	–	–	$16.5^{+6.4+3.2}_{-4.9-2.6}$	–
			$17.5^{+5.0+2.5}_{-4.4-2.1}$	
$B_s^0(\overline{B}_s^0) \to K^{*+} K^-$	–	–	$19.8^{+6.9+3.4}_{-5.6-2.9}$	–
			$21.8^{+5.4+2.8}_{-4.7-2.4}$	
$\overline{B}_s^0 \to K^{*\pm} K^{\mp}$	–	–	$18.2^{+6.3+3.3}_{-5.0-2.7}$	–
			$19.7^{+5.0+2.6}_{-4.2-2.2}$	
$\overline{B}_s^0 \to K^{*0} \overline{K}^0, \overline{K}^{*0} K^0$	–	–	$16.6^{+6.2+3.2}_{-4.9-2.7}$	–
			$18.7^{+4.9+2.6}_{-4.2-2.2}$	

Table 3.2: *CP* asymmetry predictions (in %) for $B_s^0 \to K^* K$ decays. The value are extracted from the same publications used for the branching ratio predictions: QCDF [91, 92], pQCF [93], SCET [94] and SU(3) [90]. Refer to Table 3.1 for details on the uncertainties.

Modes	QCDF	pQCD	SCET	SU(3)
$\overline{B}_s^0 \to K^+ K^{*-}$	$2.2^{+0.6+8.4+5.1+68.6}_{-0.7-8.0-5.9-71.0}$	$-36.6^{+2.3+2.8+1.3}_{-2.3-3.5-1.2}$	$-11.2^{+19.1+1.3}_{-16.2-1.3}$	8.5 ± 8.4
	$-11.0^{+0.5+14.0}_{-0.4-18.8}$		$-12.3^{+11.4+0.8}_{-11.3-0.8}$	7.3 ± 7.9
$\overline{B}_s^0 \to K^{*+} K^-$	$-3.1^{+1.0+3.8+1.6+47.5}_{-1.1-2.6-1.3-45.0}$	$55.3^{+4.4+8.5+5.1}_{-4.9-9.8-2.5}$	$7.1^{+11.2+0.7}_{-12.4-0.7}$	-4.1 ± 7.2
	$25.5^{+9.2+16.3}_{-8.8-11.3}$		$9.6^{+13.0+0.7}_{-13.5-0.9}$	-1.8 ± 5.4
$\overline{B}_s^0 \to K^0 \overline{K}^{*0}$	$1.7^{+0.4+0.6+0.5+1.4}_{-0.5-0.5-0.4-0.8}$	0	0	0
	$0.49^{+0.08+0.09}_{-0.07-0.12}$			
$\overline{B}_s^0 \to K^{*0} \overline{K}^0$	$0.2^{+0.0+0.2+0.1+0.2}_{-0.1-0.3-0.1-0.1}$	0	0	0
	$0.10^{+0.08+0.05}_{-0.07-0.02}$			

(hereafter referred to as Dalitz variables) with the available 4-momenta as

$$\begin{aligned} m_{ij}^2 = (p_i^\mu + p_j^\mu)^2 &= m_i^2 + m_j^2 + 2E_iE_j - 2\vec{p}_i \cdot \vec{p}_j \\ &= (P^\mu - p_k^\mu)^2 = M^2 + m_k^2 - 2ME_k \,, \end{aligned} \tag{3.12}$$

where the relation $m_{12}^2 + m_{13}^2 + m_{23}^2 = M^2 + m_1^2 + m_2^2 + m_3^2$ constrains the system to two independent values of m_{ij}^2.

Three-body final states are specified initially by a system with twelve degrees of freedom. The conservation of total four-momenta, the relation $E^2 = m^2 + \vec{p}^2$ and defined masses of final state particles reduce the dimension of the decay to five. Furthermore, in the case that the initial and final particles are all spinless, the absolute orientation in space is arbitrary (isotropic process). Therefore, two independent variables are sufficient to describe this system, in which each event can be described by a point in the bi-dimensional phase space. The Dalitz plot (DP) [6] is defined as this physical plane constructed from two of the m_{ij}^2 variables.

The conservation of four-momentum of the reaction restricts the events into a closed region of the phase space. The contours of the DP for three-body decays are defined from equation 3.11 as

$$\Gamma = \frac{1}{2(2\pi)^5 M} \int |\mathcal{A}|^2 \delta^4(p - p_1 - p_2 - p_3) \frac{d\vec{p}_1}{2E_1} \frac{d\vec{p}_2}{2E_2} d^4p_3 \delta(p_3^2 - m_3^2) \,, \tag{3.13}$$

which is constrained by the four-dimensional δ^4 function. On the other hand, the $\delta(p_3^2 - m_3^2)$ term enforces real (on-shell) particles in the final state, in contrast to the possible virtual particles involved in intermediate states. In the centre-of-mass (CM) reference frame, fixing the direction of $\vec{p}_1$ and integrating initially in d^4p_3, gives

$$\Gamma = \frac{\pi^2}{2(2\pi)^5 M} \int |\mathcal{A}|^2 \delta_{\cos\theta_{12}} dE_1 dE_2 d\cos\theta_{12} \,, \tag{3.14}$$

where θ_{12} is the angle between $\vec{p}_1$ and $\vec{p}_2$. [11] Integrating this expression in the cosine and using Eq. 3.12 results in the description of the decay rate as

$$\Gamma = \frac{1}{256\pi^3 M^3} \int |\mathcal{A}|^2 \, dm_{ij}^2 \, dm_{jk}^2 \,. \tag{3.15}$$

The kinematic boundaries of the Dalitz plot are constrained by the points

[11] Note that $\delta_{\cos\theta_{12}}$ is defined as $\delta\left(\cos\theta_{12} - \frac{M^2 + m_1^2 + m_2^2 - m_3^2 - 2M(E_1+E_2) + 2E_1E_2}{2\vec{p}_1\vec{p}_2}\right)$ and $E_3 = \sqrt{p_1^2 + p_2^2 + 2p_1p_2\cos\theta_{12} + m_3^2}$.

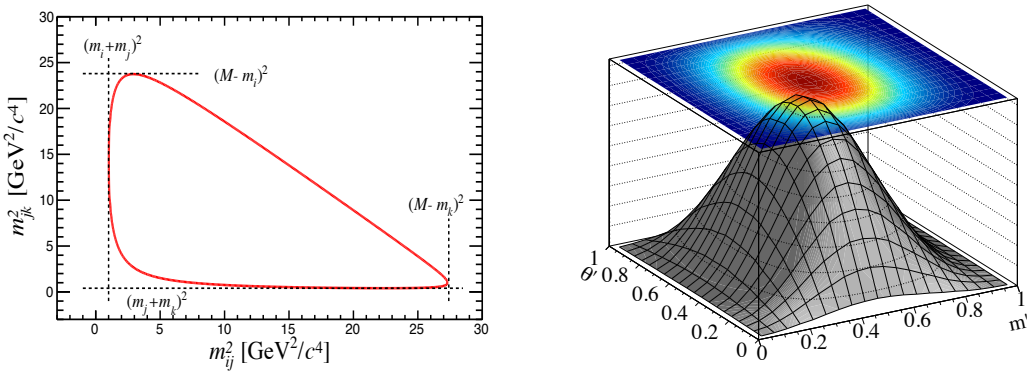

Figure 3.3: Schematic view of the (left) Dalitz plot boundaries and the (right) corresponding square Dalitz plot Jacobian transformation. Four-momentum conservation is underlined by red line contours.

where $\cos^2\theta_{12} = 1$. The extrema of this relation within the physical region are underlined in each invariant axis as

$$(m_i + m_j)^2 \leq m_{ij}^2 \leq (M - m_k)^2 \,. \tag{3.16}$$

Figure 3.3 summarises the phase-space momentum distribution constraints in the CM frame for $B_s^0 \to \overset{(-)}{K}{}^0 K^\pm \pi^\mp$ decays. Accordingly to Eq. 3.12, the minimum of m_{ij}^2 is attained with $\cos\theta_{ij} = 1$, which implies $\theta_{ij} = 0$ and $\theta_{ik} = \theta_{jk} = \pi$. In this regime, the momenta of particles i and j are collinear and opposite to particle k, which receives its largest possible momentum due to momentum conservation. Likewise, the maximum of m_{ij}^2 occurs with $\cos\theta_{ij} = -1$, and hence, $\theta_{ij} = \pi$ and $\theta_{ik} = \theta_{jk} = 0$, where the particle k is at rest and i and j are flying back-to-back.

Finally, a point at the centre of the Dalitz plane correspond to the three particles having the same momentum. The DP gives a uniform representation of the phase space, and therefore, non-uniform structures in the Dalitz plot are indicative of dynamic effects in the matrix element. The following sections will examine the representation of this phenomenon.

Three-body charmless decays signal events often populate regions close to the kinematic boundaries of the Dalitz plot, which reflects the large Q value available in the process. In addition, combinatorial backgrounds dominantly accumulate at the edges of the phase space, which further complicates a possible empirical binned modelling of these contributions. An alternative to the conventional parametrisation of the phase space can be obtained by a transformation to a rectangular plane (hereafter referred to as the square Dalitz plot (sqDP) [95])

$dm_{ij}^2\, dm_{jk}^2 \longrightarrow |\det J|\, dm'\, d\theta'$, where

$$\begin{aligned} m' &\equiv \frac{1}{\pi} \arccos\left(2\frac{m_{ij} - m_{ij}^{\min}}{m_{ij}^{\max} - m_{ij}^{\min}} - 1 \right), \\ \theta' &\equiv \frac{1}{\pi}\theta_{ij}, \end{aligned} \tag{3.17}$$

where m_{ij} is the invariant mass of the particles i and j, $m_{ij}^{\max} = M - m_k$ and $m_{ij}^{\min} = m_i + m_j$ are the boundaries of Eq. 3.16, θ_{ij} is the helicity angle of a given ij system (*i.e.* the angle between k and i in the ij rest frame) and J is the Jacobian of the transformation. The new variables have validity ranges between 0 and 1. The determinant of the Jacobian is given by

$$|J| \;=\; 4\,|\mathbf{p}_{i,j}^*||\mathbf{p}_k^*| \cdot \frac{\partial m_{ij}}{\partial m'} \cdot \frac{\partial \cos\theta_{ij}}{\partial \theta'} \tag{3.18}$$

where $|\mathbf{p}_{i,j}^*| = \sqrt{E_{i,j}^{*} - m_{i,j}^2}$ and $|\mathbf{p}_k^*| = \sqrt{E_k^{*} - m_k^2}$ are defined in the ij rest frame. This expression can be visualised in Fig. 3.3. The partial derivatives read

$$\frac{\partial m_{ij}}{\partial m'} = -\frac{\pi}{2}\sin(\pi m')\left(m_{ij}^{\max} - m_{ij}^{\min}\right) \quad \text{and} \quad \frac{\partial \cos\theta_{ij}}{\partial \theta'} = -\pi \sin(\theta'\pi)\,. \tag{3.19}$$

3.2.2 Isobar model

One comprehensive approach to describe the dynamics in the hadronic matrix elements for multibody decays is known as the Isobar Model [96–98]. The total amplitude $\mathcal{A}$ is approximated as a sum of coherent isobar terms, with individual couplings and propagators, from resonant or nonresonant decay channels as

$$\mathcal{A}(m_{ij}^2, m_{jk}^2) = \sum_{l=1}^{N} c_l F_l(m_{ij}^2, m_{jk}^2)\,, \tag{3.20}$$

where F_l are dynamical amplitudes that contain the lineshape and spin-dependence of the hadronic part of the amplitude labelled by l evaluated at the point in the phase space (m_{ij}^2, m_{jk}^2), and c_l are complex coefficients describing the relative magnitude and phase of the different isobars. Since the F_l terms describe strong dynamics only, they are *CP* conserving. By contrast, the c_l terms can be *CP* violating, which is manifested when the complex conjugate isobar term differs from c_l in either magnitude or phase – as previously mentioned this can occur when the amplitude l has contributions from both tree and penguin amplitudes.

Lorentz invariance of the decay matrix is satisfied under the condition that

its elements depend exclusively on products of four-vectors. In particular, with the available four-momentum and polarisation information, the amplitude is interpreted in terms of energies and momenta of the particles involved in the process. In the following sections, these concepts are explored in the view of building a phenomenological amplitude for three-body decays.

Properties of an amplitude analysis

Multibody decays can, in general, proceed through intermediate quasi-two-body and nonresonant amplitudes. The appearance of structures in the topology of the phase space is related to the nature of the transition amplitude. The formal representation of this phenomenon is described by $\mathcal{S}$-matrix theory, which binds the physical observables of the initial and final states. The scattering amplitude for the state transition $|i\rangle$ to $|f\rangle$ is connected to the unitary $\mathcal{S}$-matrix by a scattering amplitude $\mathcal{M}$ as

$$\mathcal{S}_{fi} = \langle f|i\rangle - 2\pi i\langle f|\mathcal{M}|i\rangle = \mathbb{1} - 2\pi i\langle f|\mathcal{M}|i\rangle\,, \tag{3.21}$$

which is the superposition of the collapse of the initial to the final state and a interaction transition amplitude. The distinction between the decay amplitude $\mathcal{A}$ and the scattering amplitude $\mathcal{M}$ is fundamentally defined by the constraints imposed due to unitarity of the $\mathcal{S}$-matrix. At low energy, scattering is dominated by resonances, that in the absence of significant overlaps, are identified as distinct enhancements in the cross-section. Furthermore, the properties of mass, width and spin translate into characteristic distributions. The determination of these properties relies on the underlying scattering amplitude formalism.

Consider the elastic scattering of two particles, here assumed to behave independently of the third particle in the decay. In this illustration, it is convenient to describe the $\mathcal{M}$-matrix elements in terms of Mandelstam variables [99]. The Lorentz-invariance in these terms reflects the dependence of only two kinematic variables s (total energy in the CM system) and t (four-momentum transferred) to describe this process (or any other non-redundant combination). An interesting feature of these quantities is the physical region constraints imposed in the complex plane domain, as shown in Fig. 3.4. Each of these regions are disconnected and belong to different physics processes. Nonetheless, any arbitrary (or convenient) choice of coordinates in this Mandelstam plane is sufficient. One further notable aspect in this visualisation is the fourth physical intersection region in the event that $M > m_1 + m_2 + m_3$. In this case the boundaries recover the previous contours obtained for the Dalitz plot shown in Eq. 3.16.

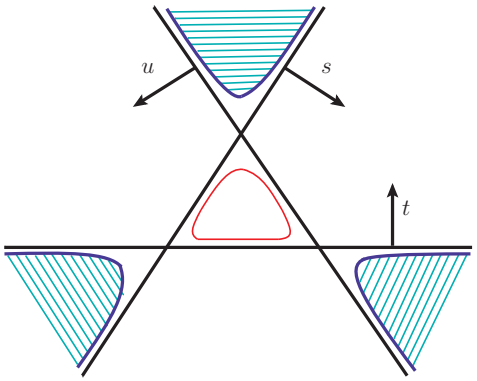

Figure 3.4: Physical boundary regions of the Mandelstam plane. The red line contours represent the fourth hidden boundaries in the event that $M > m_1 + m_2 + m_3$.

The differential cross-section for elastic two-body scatterings using the Fermi Golden rule is given by

$$\frac{d\sigma_{\text{elastic}}}{d\Omega} = \frac{1}{64\pi^2 s} \left|\mathcal{M}(s,z)\right|^2 , \tag{3.22}$$

where $z = \cos\theta$, defined from $t = 2p^2(\cos\theta - 1)$. It is convenient to expand the scattering amplitude in a series of partial waves as [12]

$$|\mathcal{M}(s,z)| = 16\pi \sum_{l=0}^{\infty} (2l+1) f_l(s) P_l(z) , \tag{3.23}$$

where l is the angular momentum, $f_l(s)$ are the partial wave $\mathcal{M}$-matrix elements and $P_l(z)$ are the Legendre polynomials. The value of σ_{elastic} is obtained by performing an angular integration using the property that the Legendre functions are a complete basis for $-1 \leq z \leq 1$, to be

$$\sigma_{\text{elastic}}(s) = \frac{16\pi}{s} \sum_{l=0}^{\infty} (2l+1) |f_l(s)|^2 . \tag{3.24}$$

The unitarity of the $\mathcal{S}$-matrix imposes important restrictions on the scattering amplitude. Culminating from this constraint is the optical theorem [100], that connects the imaginary part of the elastic amplitude to the cross-section of all processes evaluated at $z = 1$. In the regime of elastic unitarity, $\sigma_{\text{tot}}(s) = \sigma_{\text{elastic}}(s)$,

[12] An heuristic argument to motivate this expansion is that at low energies, only lowest order $f_l(s)$ are non-vanishing. The rigorous justification relies on the conservation of angular momentum l, that enables the formulation of the scattering into independent partial waves.

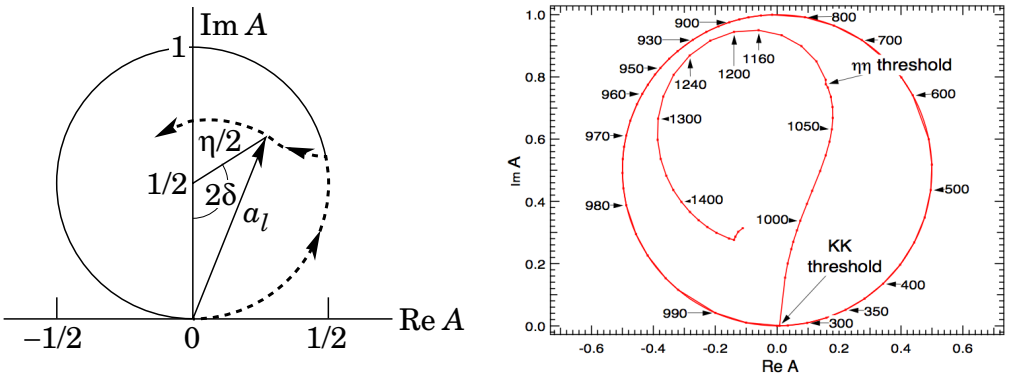

Figure 3.5: Argand diagram visualisation of the partial wave amplitude as a function of the energy. A schematic view of the trajectory evolution is shown on the left [28], whereas the right plot shows the $\pi\pi$ fit results reported in [101].

and hence, for each partial wave the following relation is valid

$$\Im\left[f_l(s)\right] = \frac{2p}{\sqrt{s}}|f_l(s)|^2 = \rho(s)|f_l(s)|^2\,, \tag{3.25}$$

where $\rho(s)$ is hereafter referred to as the Mandelstam phase-space factor. Above the inelastic threshold, this expression receives an additional term $\frac{1}{4\rho(s)}[1-\eta_l^2(s)]$, where η_l is the inelasticity parameter. Notice that the elastic scenario is recovered with $\eta_l = 1$. This methodology formulates elastic scattering as a physical phase shift δ_l in the partial wave, originating from the transmission through the interaction region. The general solution for partial wave amplitudes using Eq. 3.21 reads

$$f_l(s) = \frac{1}{\rho(s)}\frac{\eta_l e^{2i\delta_l(s)} - 1}{2i}\,. \tag{3.26}$$

The evolution of this complex number with energy can be visualised as a trajectory in the Argand plane shown in Figure 3.5. It is important to realise that in the elastic region the amplitude path rotates around the unit circle, with phase δ.

Another relevant feature in the understanding of the amplitude structure is the imaginary dependence on the Mandelstam phase-space factor. The natural discontinuity of this function can be well-defined by connecting continuously two planes (referred to as Riemann sheets). This structure appears whenever a threshold energy is reached, in the so-called channel opening. The singularities on the first Riemann sheet (known as physical region) correspond to the zeros of the $\mathcal{S}$-matrix whilst the poles on the second sheet are associated to resonances. Due to this, the

mass and width measured in different processes can differ but still be associated to the same pole.

One final remark is related to the interpretation of the resonant states, characterised as short-lived particles similar to excited spectral lines of atoms. The relativistic wave function of unstable particle is proportional to $e^{-iMt}e^{-\Gamma t/2}$, where the Γ dependence is justified by the large uncertainty on the energy associated to the short lifetime. The propagator for these particles is obtained through a Fourier transformation into the energy space, which results in the so-named Breit-Wigner formula (BW). In the partial wave representation, the amplitude reads

$$f_l(s) \sim \frac{1}{(M^2 - s) - i\rho\Gamma}\,, \tag{3.27}$$

which is independently obtained by constraints on the unitarity of the imaginary part. The Γ term is a function of the channel and angular momentum, which is further examined in the next section. This approximation is valid in the region near the pole at $s = M^2 - i\rho\Gamma$, particularly for a single channel and small values of Γ. A formal generalisation for multiple overlapping resonances (not covered in this work) is available in the context of the K-matrix description [102].

Mass lineshapes

A large number of dynamic models are proposed in the literature to parametrise various resonances. The aforementioned modelling of single-channel single-pole resonances through the Breit-Wigner form is often the most appropriate and/or convenient mass lineshape. The explicit relativistic (RBW) expression is given by

$$R(s) = \frac{1}{(m_0^2 - s) - im_0\Gamma}\,, \tag{3.28}$$

where m_0 is the nominal resonance pole mass and the mass-dependent decay width reads

$$\Gamma = \Gamma_0 \left(\frac{q}{q_0}\right)^{2L+1} \left(\frac{m_0}{\sqrt{s}}\right) X_L^2(|\vec{q}|r)\,, \tag{3.29}$$

where q is the momentum of either daughter in the rest frame of the resonance, L is the orbital angular momentum between the resonance and the bachelor particle (hereafter defined as the third particle not contained in the resonance) and $X_L(z)$, where $z = |\vec{q}|\,r$ with resonance radius r taken to be $4.0\,\mathrm{GeV}^{-1} \approx 0.8\,\mathrm{fm}$, is the

empirical Blatt-Weisskopf penetration barrier factor [103]

$$\begin{aligned} X_{L=0}(z) &= 1\,, \\ X_{L=1}(z) &= \sqrt{\frac{1+z_0^2}{1+z^2}}\,, \\ X_{L=2}(z) &= \sqrt{\frac{z_0^4+3z_0^2+9}{z^4+3z^2+9}}\,, \end{aligned} \tag{3.30}$$

where z_0 represents the value of z when the invariant mass is equal to the pole mass of the resonance. The introduction of this term preserves the angular momentum distribution by modulating the amplitude near threshold. In this formulation, the BW function can be expressed as $1/\cot\delta - i$ or $\sin\delta e^{i\delta}$, where $\cot\delta = \frac{m_0^2-s}{m_0\Gamma}$. Note that this indicates a variation in the phase of 90° at the pole mass but also that the phase goes from zero at the threshold to 180° far above the pole, which is consistent with the scattering-pole description.

This parametrisation is well established for narrow and well-isolated resonances such as the $K^{*0}(892)$ contribution. However, in the event that there is more than one overlapping resonance in the same partial wave or a significant interference with a nonresonant component, this discussion is not valid since the sum of the contributions in the isobar model violates unitarity. An example is seen in $K\pi$ scatterings, where a spin-0 resonance interferes strongly with a nonresonant (or "slowly varying") term. The so-called LASS lineshape [104] has been suggested to model this scalar amplitude $(K\pi)_0^*$ as a nonresonant effective range form together with a $K_0^*(1430)$ resonance. The modified version of this parametrisation for B decays reads

$$R_j(s) = \frac{\sqrt{s}}{q\cot\delta_B - iq} + e^{2i\delta_B}\frac{m_0\Gamma_0\frac{m_0}{q_0}}{(m_0^2-s) - im_0\Gamma_0\frac{q}{\sqrt{s}}\frac{m_0}{q_0}}\,, \tag{3.31}$$

where $\cot\delta_B = \frac{1}{aq} + \frac{rq}{2}$, and a and r are the scattering length and the effective range parameters, respectively.[13] It is important to notice that this approximation is curtailed at 1.8 GeV/c^2 (around the charm mass), above which no data from the LASS experiment is available and, therefore, the application is not valid.

Angular distribution

Prior to the discussion of the most general expression for the isobar model, it is essential to incorporate systematically the angular information into the amplitude.

[13] These values are measured by the LASS experiment to to be $a = 1.95 \pm 0.09\,(\,\mathrm{GeV}/c^2)^{-1}$ and $r = 1.76 \pm 0.36\,(\,\mathrm{GeV}/c^2)^{-1}$.

In contrast to scalar resonances which have no preferential direction for the daughters, vector and higher spin states present non-trivial angular distributions. The Lorentz-invariant decay amplitudes in the spin-1 case are defined as

$$\begin{aligned} \mathcal{A}(R \to P_i P_j) &= X_L^R \epsilon_\mu(m)(p_j - p_i)^\mu \,, \\ \mathcal{A}(B \to R P_k) &= X_L^B \epsilon_\nu(m) p_k^\nu \,, \end{aligned} \tag{3.32}$$

where X_L^R and X_L^B are Blatt-Weisskopf form factors and ϵ^μ is the polarisation vector of the resonance, with $\epsilon^\mu(p_i + p_j)_\mu = 0$ due to the absence of time-dependence in the rest frame of the resonance. Examining the product of these amplitudes and summing over the polarisation[14] leads to the amplitude $X_L^R X_L^B(-2\vec{p}_i \cdot \vec{p}_k)$. The generalisation of this angular term for arbitrary integer spin has been developed by Zemach [105] in terms of Legendre polynomials, giving $(-2|p_i| \cdot |p_k|)^J P_J(\cos\theta_{ik})$.

The angle θ_{ik} is known as the helicity angle, defined as the angle between the momentum vector of one of the daughters in the rest frame of the resonance and the axis defined by the momentum of the resonance in the B rest frame. The polynomial dependence of the amplitude yields distinct patterns in the phase space. Scalar resonances reveal uniform distributions whilst vectors are populated accordingly to $\cos^2\theta_{ik}$. The helicity angle definition in terms of invariant masses is

$$\cos\theta_{ik} = \frac{(m_{ik}^2)_{\max} + (m_{ik}^2)_{\min} - 2m_{ik}^2}{(m_{ik}^2)_{\max} - (m_{ik}^2)_{\min}} \,. \tag{3.33}$$

Interference effects

The dynamics described in the previous sections can be summarised as an interplay of poles and zeros in the Mandelstam plane. In dominant single-channels, the distribution of events in the Dalitz plot is well-defined in certain energy regions. However, in most scenarios the decay amplitude is more complicated and consists of many overlapping/interfering resonances.

An important related pattern is associated to the nature of quantum mechanics, that imposes interference between intermediate processes that give a common final state. This mechanism is illustrated by analysing a simple amplitude compound of two resonances that overlap in a region of the Dalitz plot. The distribution of

[14] Polarisation vectors satisfy the following relation $\sum_m \epsilon^\mu(m)\epsilon^\nu(m) = -g^{\mu\nu} + \frac{p_R^\mu p_R^\nu}{p_R^2}$.

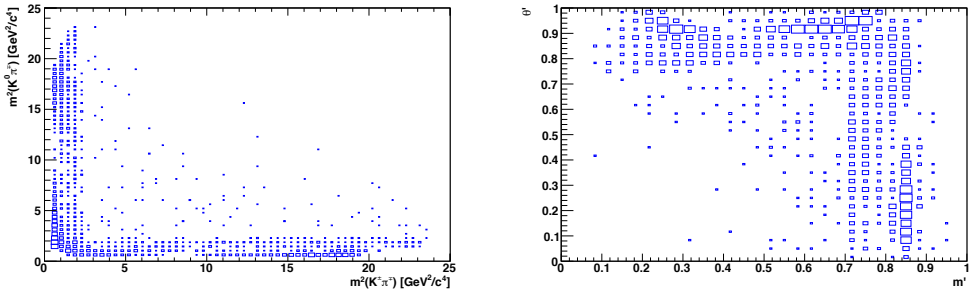

Figure 3.6: Simulated distributions for the (left) standard and (right) square Dalitz plot for $B_s^0 \to {}^{(}\overline{K}{}^{)0} K^{\pm}\pi^{\mp}$ decays.

events for this process follows

$$\begin{aligned} |\mathcal{A}|^2 &= |a_1 e^{i\delta_1} F_1(m_{ij}^2) + a_2 e^{i\delta_2} F_2(m_{jk}^2)|^2 \\ &\propto |F_1|^2 + r^2|F_2|^2 + 2r\,\mathrm{Re}\,(F_1 F_2^*)\cos\delta - 2r\Im\,(F_1 F_2^*)\sin\delta\,, \end{aligned} \tag{3.34}$$

where $r = a_2/a_1$ and $\delta = \delta_2 - \delta_1$. An obvious implication is the potential destructive or constructive interference in regions of the phase space. Although the orthogonality of Legendre polynomials ensures that the interference between resonances in the same invariant mass pair with different spins integrates to zero, interference patterns are still accessible in an amplitude analysis. This remarkable feature permits all relative phases to be experimentally obtained as long as there are overlapping resonances. An illustration of the typical population of events in a Dalitz plot for $B_s^0 \to {}^{(}\overline{K}{}^{)0} K^{\pm}\pi^{\mp}$ decays is shown in Figure 3.6. Note that there are clear overlapping regions in the low ${}^{(}\overline{K}{}^{)0}\pi^{\mp}$ and $K^{\pm}\pi^{\mp}$ invariant masses that can interfere. The techniques involved in the extraction of the Dalitz-plot observables are examined in later chapters.

3.3 The $B_s^0 \to K^0 K^{\pm}\pi^{\mp}$ decay

In recent years, there has been an increasing interest in B_s^0 meson decays, primarily motivated by exciting results reported by LHCb [106, 107]. The main purpose of the current research is to provide valuable insights in this topic, by performing the first Dalitz plot analysis of a hadronic charmless three-body B_s^0 decay, using the decay channel $B_s^0 \to K^0 K^{\pm}\pi^{\mp}$. The first observation of this inclusive mode has been reported in Ref. [108] giving $\mathcal{B}(B_s^0 \to K^0 K^{\pm}\pi^{\mp}) = (73.6 \pm 5.7 \pm 7.5) \times 10^{-6}$ (further details are given in Section 6). There is fair agreement between the

current predictions summarised in Table 3.3 and this measurement. In addition, the dynamics of this process has clear intriguing features, such as the non-trivial predictions for the $K_0^*(1430)$ resonance branching fractions, which depend on the charge configuration. The understanding of this signature can be addressed by the Dalitz-plot analysis performed in this research.

Table 3.3: Branching fraction predictions (in units of 10^{-6}) for resonant and nonresonant Dalitz-plot contributions, for each $B_s^0 \to K^0 K^\pm \pi^\mp$ final state [56, 57].

$\overline{B}_s^0 \to \overline{K}^0 K^+ \pi^-$		$\overline{B}_s^0 \to K^0 K^- \pi^+$	
$K^{*0}\overline{K}^0$	$1.5^{+0.0+2.4+0.0}_{-0.0-0.9-0.0}$	$\overline{K}^{*0}K^0$	$3.8^{+0.0+0.8+0.0}_{-0.0-0.7-0.0}$
$K^{*-}K^+$	$3.5^{+0.0+0.7+0.1}_{-0.0-0.7-0.1}$	$K^{*+}K^-$	$2.6^{+0.0+2.7+0.1}_{-0.0-1.1-0.1}$
$K_0^{*0}(1430)\overline{K}^0$	$0.6^{+0.0+0.9+0.0}_{-0.0-0.4-0.0}$	$\overline{K}_0^0(1430)K^0$	$14.5^{+0.0+3.3+0.0}_{-0.0-2.9-0.0}$
$K_0^{*-}(1430)K^+$	$14.5^{+0.0+3.2+0.1}_{-0.0-2.9-0.1}$	$K_0^{*+}(1430)K^-$	$1.0^{+0.0+1.0+0.0}_{-0.0-0.4-0.0}$
NR	$23.8^{+0.2+9.9+0.0}_{-0.1-6.7-0.0}$	NR	$24.2^{+0.0+7.9+0.0}_{-0.0-5.1-0.0}$
Total [56]	$35.3^{+0.3+15.7+0.0}_{-0.2-\ 9.8-0.0}$	Total	$36.7^{+0.2+14.9+0.1}_{-0.2-\ 9.0-0.1}$
$\overline{B}_s^0 \to \overline{K}^0 K^+ \pi^-$		$\overline{B}_s^0 \to K^0 K^- \pi^+$	
$K^{*0}\overline{K}^0$	$0.7^{+0.0+1.7+0.0}_{-0.0-0.5-0.0}$	$\overline{K}^{*0}K^0$	$2.3^{+0.0+0.6+0.0}_{-0.0-0.5-0.0}$
$K^{*-}K^+$	$2.3^{+0.0+0.6+0.0}_{-0.0-0.5-0.0}$	$K^{*+}K^-$	$1.3^{+0.0+2.0+0.0}_{-0.0-0.7-0.0}$
$K_0^{*0}(1430)\overline{K}^0$	$0.5^{+0.0+1.2+0.0}_{-0.0-0.4-0.0}$	$\overline{K}_0^0(1430)K^0$	$16.6^{+0.0+5.1+0.0}_{-0.0-4.3-0.0}$
$K_0^{*-}(1430)K^+$	$15.5^{+0.0+4.5+0.0}_{-0.0-3.9-0.0}$	$K_0^{*+}(1430)K^-$	$0.9^{+0.0+1.4+0.0}_{-0.0-0.5-0.0}$
NR	$12.3^{+0.2+12.6+0.0}_{-0.3-6.3-0.0}$	NR	$12.9^{+0.3+13.2+0.0}_{-0.4-6.6-0.0}$
Total [57]	$33.7^{+0.1+20.9+0.0}_{-0.2-12.0-0.0}$	Total	$34.2^{+0.2+21.1+0.1}_{-0.3-12.0-0.1}$

While the main features of this mode have been reviewed in previous sections, further discussions are required to accommodate the implications of both final state charge configurations being accessible, *a priori*, of similar rates for both B_s^0 and $\overline{B}_s^0$ decays. The decay-time distribution for $\overline{B}_s^0$ and B_s^0 meson decays to a final state f (e.g. $\overline{K}^0 K^+ \pi^-$) can be written in the general formula of Eq. 2.30 as

$$\frac{d}{dt}\Gamma_{\overline{B}_s^0 \to f}(t) = \frac{\mathcal{N}_f\, e^{-t/\tau(B_s^0)}}{2\tau(B_s^0)} \Big[\cosh\left(\tfrac{\Delta\Gamma_s t}{2}\right) + S_f \sin(\Delta m_s t) - C_f \cos(\Delta m_s t) + A_f^{\Delta\Gamma_s} \sinh\left(\tfrac{\Delta\Gamma_s t}{2}\right) \Big], \tag{3.35}$$

and

$$\frac{d}{dt}\Gamma_{B_s^0 \to f}(t) = \frac{\mathcal{N}_f\, e^{-t/\tau(B_s^0)}}{2\tau(B_s^0)} \Big[\cosh\left(\tfrac{\Delta\Gamma_s t}{2}\right) - S_f \sin(\Delta m_s t) + C_f \cos(\Delta m_s t) + A_f^{\Delta\Gamma_s} \sinh\left(\tfrac{\Delta\Gamma_s t}{2}\right) \Big]. \tag{3.36}$$

In the remainder of this work, it will be assumed that $|q/p| = 1$ (*i.e.* absence of *CP*

violation in mixing), so that

$$\lambda_f = R_f e^{i\left(\phi_s^f + \delta_f\right)}\,, \tag{3.37}$$

where $R_f = \left|\frac{\bar{\mathcal{A}}_f}{\mathcal{A}_f}\right|$, δ_f is the strong (*i.e. CP* conserving) contribution to the relative phase between $\bar{\mathcal{A}}_f$ and $\mathcal{A}_f$ and ϕ_s^f is the sum of the weak (*i.e. CP* violating) part of the phase difference and $\arg\left(\frac{q}{p}\right)$.

By requiring that the integral over t from zero to infinity of the sum of Eqs. 3.35 and 3.36 is equal to $|A_f|^2 + \left|\bar{A}_f\right|^2$, the normalisation factor is found to be

$$\mathcal{N}_f = \left(|A_f|^2 + \left|\bar{A}_f\right|^2\right) \frac{1-y^2}{1+yA_f^{\Delta\Gamma_s}}\,, \tag{3.38}$$

where $y = \tau(B_s^0)\Delta\Gamma_s/2$. The correction involving y is the origin of the difference between branching fractions calculated at $t = 0$ or after integration over decay time [109]. It is relevant for the discussion that follows that the current world average is $y = 0.061 \pm 0.005$ [32].

In the case of $B_s^0 \to {}^{(}\overline{K}{}^{)}{}^0 K^\pm \pi^\mp$ decays, the final state f in Eqs 3.35 and 3.36 refers to a single point in the phase space. Specifically, if f is the point in the $\overline{K}{}^0 K^+\pi^-$ Dalitz plot with $(m^2(\overline{K}{}^0\pi^-), m^2(K^+\pi^-)) = (s,t)$ then $\bar{f}$ is the point in the $K^0K^-\pi^+$ Dalitz plot with $(m^2(K^0\pi^+), m^2(K^-\pi^+)) = (s,t)$. Expressions equivalent to Eqs 3.35 and 3.36 but for the final state $\bar{f}$ are obtained simply by replacing f with $\bar{f}$, with

$$S_{\bar{f}} \equiv \frac{2\,\Im(\lambda_{\bar{f}})}{1+\left|\lambda_{\bar{f}}\right|^2}\,, \qquad C_{\bar{f}} \equiv \frac{1-\left|\lambda_{\bar{f}}\right|^2}{1+\left|\lambda_{\bar{f}}\right|^2}\,, \qquad A_{\bar{f}}^{\Delta\Gamma_s} \equiv -\frac{2\,\mathrm{Re}(\lambda_{\bar{f}})}{1+|\lambda_{\bar{f}}|^2}\,, \tag{3.39}$$

where $\lambda_{\bar{f}} = \frac{q}{p}\frac{\bar{\mathcal{A}}_{\bar{f}}}{\mathcal{A}_{\bar{f}}}$ where $\bar{\mathcal{A}}_{\bar{f}}$ and $\mathcal{A}_{\bar{f}}$ have obvious definitions. If there is no *CP* violation in decay, then $\left|\bar{\mathcal{A}}_{\bar{f}}\right| = |\mathcal{A}_f|$ and $\left|\mathcal{A}_{\bar{f}}\right| = \left|\bar{\mathcal{A}}_f\right|$, so that

$$\lambda_{\bar{f}} = R_f^{-1} e^{i\left(\phi_s^f - \delta_f\right)}\,, \tag{3.40}$$

and $C_f = -C_{\bar{f}}$. It is interesting to note that, since $\mathcal{N}_{\bar{f}} = \left(\left|A_{\bar{f}}\right|^2 + \left|\bar{A}_{\bar{f}}\right|^2\right)\frac{1-y^2}{1+yA_{\bar{f}}^{\Delta\Gamma_s}}$, in general $\mathcal{N}_f \neq \mathcal{N}_{\bar{f}}$ even in absence of *CP* violation in decay, in contrast to the situation for the B^0 system [30] where $y = 0$ to a good approximation. However,

since the ratio of normalisation factors is

$$\begin{aligned}\frac{\mathcal{N}_{\bar{f}}}{\mathcal{N}_f} &= \frac{\left(\left|A_{\bar{f}}\right|^2+\left|\bar{A}_{\bar{f}}\right|^2\right)}{\left(\left|A_f\right|^2+\left|\bar{A}_f\right|^2\right)}\frac{\left(1-y^2\right)/\left(1+yA_{\bar{f}}^{\Delta\Gamma_s}\right)}{\left(1-y^2\right)/\left(1+yA_f^{\Delta\Gamma_s}\right)}\,,\\ &= \frac{1+yA_f^{\Delta\Gamma_s}}{1+yA_{\bar{f}}^{\Delta\Gamma_s}}\,,\\ &= \frac{1+R_f^2-2yR_f\cos\left(\phi_s^f+\delta_f\right)}{1+R_f^2-2yR_f\cos\left(\phi_s^f-\delta_f\right)}\,,\end{aligned} \tag{3.41}$$

where the second and third equalities assume absence of *CP* violation in decay, the asymmetry between $\mathcal{N}_f$ and $\mathcal{N}_{\bar{f}}$ cannot be larger than $2yR_f/(1+R_f^2)$ (moreover since, without loss of generality, $R_f \leq 1$, it must be less than y). If, in addition, $\cos\left(\phi_s^f+\delta_f\right) = \cos\left(\phi_s^f-\delta_f\right)$ then $A_{\bar{f}}^{\Delta\Gamma_s} = A_f^{\Delta\Gamma_s}$ and $\mathcal{N}_f = \mathcal{N}_{\bar{f}}$ – this is realised in the case that $\phi_s^f = 0$ (absence of *CP* violation in the interference between mixing and decay) when also $S_f = -S_{\bar{f}}$.

The above discussion makes clear how different forms of *CP* violation may be manifest in different types of analysis

i. Untagged, decay-time-integrated Dalitz-plot analysis:
In the absence of all forms of *CP* violation, there is a symmetry between the $\overline{K}^0K^+\pi^-$ and $K^0K^-\pi^+$ distributions. In essence, this arises from the relation between $\mathcal{N}_{\bar{f}}$ and $\mathcal{N}_f$. This symmetry can be broken by either *CP* violation in the interference between mixing and decay or by *CP* violation in decay, as seen in Eq. 3.41. However, in the former case the asymmetry cannot be larger than y, so if significantly larger effects are seen this would be an unambiguous signature of *CP* violation in decay. In general one would expect to find larger asymmetries in some local regions of the phase space, and either model-dependent or model-independent methods could be used to search for such effects. In a model-dependent approach, the distinction between *CP* violation in the interference between mixing and decay and *CP* violation in decay becomes heuristic: the fit determines the isobar complex coefficients, and if *CP* is violated both categories of effects will in general occur.

ii. Untagged, decay-time-dependent Dalitz-plot analysis:
The $A_{\bar{f}}^{\Delta\Gamma_s}$ and $A_f^{\Delta\Gamma_s}$ terms can be determined separately, and therefore more information is obtained compared to the decay-time-integrated case.

iii. Tagged, decay-time-dependent Dalitz-plot analysis:

The C_f, $C_{\bar{f}}$, S_f and $S_{\bar{f}}$ parameters can be determined. This provides additional sensitivity to the underlying model parameters.

One important feature to emphasise is that there are four amplitudes to consider, named both B_s^0 and $\overline{B}_s^0$ decays to both final states f and $\bar{f}$. Even if the absence of *CP* violation in decay is assumed, there are still two independent amplitudes, $\mathcal{A}_f$ and $\bar{\mathcal{A}}_f$. In an untagged analysis it is in general impossible to disentangle the two components, coming from B_s^0 and $\overline{B}_s^0$ decays. This situation has never previously been considered in any B decay Dalitz plot. In cases that have been studied where the final state is not self-conjugate, such as $B^0 \to K^+\pi^-\pi^0$ [110], the decay amplitudes are assumed to be flavour-specific, so that one of the two possible contributions vanishes. In the time-integrated Dalitz-plot analysis of $B^0 \to K^0_S\pi^+\pi^-$ [111], resonance contributions are either flavour-specific (*e.g.* $K^{*+}\pi^-$) or self-conjugate (*e.g.* $K^0_S\rho^0$), so in both cases there is only a single amplitude in the absence of *CP* violation in decay.

This limitation can be seen by examining the untagged decay-time-integrated Dalitz-plot analysis approach [i]. In the $\overline{K}^0K^+\pi^-$ final state, summing Equations 3.35 and 3.36 gives

$$\Gamma_{\overline{B}_s^0\to f}(t) + \Gamma_{B_s^0\to f}(t) = \frac{\mathcal{N}_f e^{-t/\tau(B_s^0)}}{\tau(B_s^0)}\left[\cosh\frac{\Delta\Gamma_s t}{2} - A_f^{\Delta\Gamma_s}\sinh\frac{\Delta\Gamma_s t}{2}\right]. \quad (3.42)$$

After integrating over time and inserting the definitions of $\mathcal{N}_f$ and $A_f^{\Delta\Gamma_s}$, the signal probability density function that can be used in a fit is determined to be

$$\mathcal{P}_f^{\rm sig}(s,t) = \frac{|\mathcal{A}_f|^2 + |\bar{\mathcal{A}}_f|^2 - 2\mathcal{D}\,{\rm Re}(\mathcal{A}_f^*\bar{\mathcal{A}}_f)}{\int\int_{DP}\ |\mathcal{A}_f|^2 + |\bar{\mathcal{A}}_f|^2 - 2\mathcal{D}\,{\rm Re}(\mathcal{A}_f^*\bar{\mathcal{A}}_f)\ ds\,dt}, \quad (3.43)$$

with a similar expression for the conjugate final state $\bar{f}$. The factor $\mathcal{D}$ is given by the ratio

$$\mathcal{D} = \frac{\int_0^\infty \epsilon(t)e^{-\Gamma_s t}\sinh\frac{\Delta\Gamma_s t}{2}dt}{\int_0^\infty \epsilon(t)e^{-\Gamma_s t}\cosh\frac{\Delta\Gamma_s t}{2}dt}, \quad (3.44)$$

where non-uniform experimental decay-time acceptance $\epsilon(t)$ has been included. In the limit of uniform acceptance, this reduces to $y_s = \Delta\Gamma_s/(2\Gamma_s) = (6.9\pm0.6)\%$ [28]. This factor is responsible for the difference between the $t = 0$ branching fraction and the time-integrated branching fraction, and must be considered when results are interpreted.

Several symmetries can be seen from Eq. 3.43, including $\mathcal{A}_f \leftrightarrow \bar{\mathcal{A}}_f$ and $\mathcal{A}_f \to e^{i\phi}\mathcal{A}_f$, $\bar{\mathcal{A}}_f \to e^{-i\phi}\bar{\mathcal{A}}_f$. This demonstrates that an untagged analysis cannot

determine $\mathcal{A}_f$ and $\bar{\mathcal{A}}_f$ unambiguously and independently. The main conclusion is that either time dependent or independent analyses cannot be performed without the need of tagging for ${}^{(}\overline{K}{}^{)}{}^0 K^\pm\pi^\mp$ final states. For decay channels like $B_s^0 \to K^0\pi^+\pi^-$, the K^* resonances populate different regions of the Dalitz plot. Therefore, there is a self-tagging feature to these decays, allowing the implementation of any of the different types of analysis discussed above. Studies have been performed to address how much additional sensitivity is obtained as the analysis is made increasingly more complex, as reported in Appendix B.

Although a full tagged, time-dependent analysis can resolve all amplitudes, also allowing for *CP* violation in decay, the data sample currently available makes this approach unattractive. Note that the flavour-tagging power for hadronic final states in LHCb is typically of 5% [112, 113]. Instead, an effective Dalitz-plot model is obtained, in which a single amplitude, containing resonances added in the isobar approach, is used to describe each final state. This model is used to fit the data and is shown to give good estimates of the resonance branching fractions. By fitting the $\overline{K}{}^0 K^+\pi^-$ and $K^0 K^-\pi^+$ final states simultaneously, the presence of *CP* violation can be investigated by allowing for differences in the two distributions. Due to the approximations in this model, however, the complex coefficients obtained, in particular the relative phases, cannot be straightforwardly interpreted.

4

The LHCb detector

In an ideal visualisation of the interaction between elementary particles (*e.g.* $pp \to b\bar{b}$, $\bar{b} \to B_s^0 Y$, $B_s^0 \to {}^{(\overline{)}}\overline{K}{}^0 K^{\pm}\pi^{\mp}$), the information in each stage of the process would be available. In reality the only tangible knowledge that can be obtained from LHC collisions is that of the final state products. Therefore, in order to describe the properties and mechanisms involved in these interactions, it is compulsory to reconstruct the process from these quantities. The manner in which particles are detected is through their interaction with matter. Charged and neutral particles have distinct interactions and also particular behaviours are expected for different energy domains. Any detector design is structured to interpret these processes, and thus, reconstruct a picture of the event by gathering information about the momentum, mass/energy and the trajectory of each final state particle. The detection techniques used in LHCb are reviewed in this chapter, in which a general description of the LHC accelerator is given together with an overview and specification of the LHCb experiment.

4.1 The LHC

The Large Hadron Collider (LHC) [114] is a particle accelerator and collider, located near the Franco-Swiss border (Geneva surrounding area) at the *Centre Européenne pour la Recherche Nucléaire*, CERN. This synchrotron machine has been placed in the same tunnel as the former Large Electron Positron Collider (LEP) [115], ranging between 50 to 170 meters deep underground and 27 km in circumference. Proton beams are operated in two concentric and opposite paths, accelerated by 8 (per beam) radio-frequency oscillator cavities and intercalated by 1232 segments of dipole magnet and 392 quadrupole magnets that keep the particles confined to the accelerator. A magnetic field of 8.3 T to bend the beams is produced by LHC dipoles

made of niobium-titanium (NbTi) cables, which present superconductive properties if cooled down to 20 K (−253.15°C).

At nominal conditions, the LHC experiment is designed to collide protons at a centre-of-mass energy of 14 TeV, with each beam carrying 7 TeV. The beam is structured in bunch periods of 24.95 ns with each bunch containing 1.1×10^{11} protons, generating up to 600 million collisions per second. [1] Collisions take place in the event of a bunch crossing (each proton beam is composed of 2808 bunches), with a frequency of 40 MHz. Prior to the injection at LHC, protons are passed through a complex chain of acceleration. Figure 4.1 shows the many layers involved in reaching high energies, as follows

i. Protons are created in duoplasmatron ion sources through the ionisation (electron removal) of hydrogen gas. These beams are then accelerated to 50 MeV by a linear accelerator, LINAC2;

ii. Beams are transferred to the Proton Synchrotron Booster (PSB) which splits the beam in four bunches. The booster ring accelerates the protons to an energy of 1.4 GeV;

iii. Next, protons are injected into the Proton Synchrotron (PS) that accelerates them up to 25 GeV. The required proton bunch structure (24.95 ns spacing) of the LHC is addressed in the PS by applying another beam separation;

iv. The pre-LHC final acceleration is provided by the Super Proton Synchrotron (SPS), which collects the proton bunches and brings them to 450 GeV;

v. The beams are finally injected in the LHC at approximately 130 m from Point 2 and 160 m from Point 8. Inside the LHC storage ring, the beams are accelerated up to their desired energy.

The proton beams interact simultaneously in four detector points in the LHC ring, ATLAS (Point 1), CMS (Point 5), LHCb (Point 8) and ALICE (Point 2). ATLAS (A Toroidal LHC ApparatuS) [117] and CMS (Compact Muon Solenoid) [118] are general purpose experiments with physics programmes ranging from the confirmation and measurements of the observables of the Standard Model (*e.g.* Higgs boson) to searches for New Physics at the TeV scale. The LHC Beauty (LHCb) experiment [5] is designed to investigate heavy flavour physics phenomena, including searches for indirect signatures of New Physics in quantum loop processes and

[1] For practical reasons the bunch pattern is non uniform, which provide a larger buffer between crossings. On average, this corresponds to a frequency of 31.6 MHz.

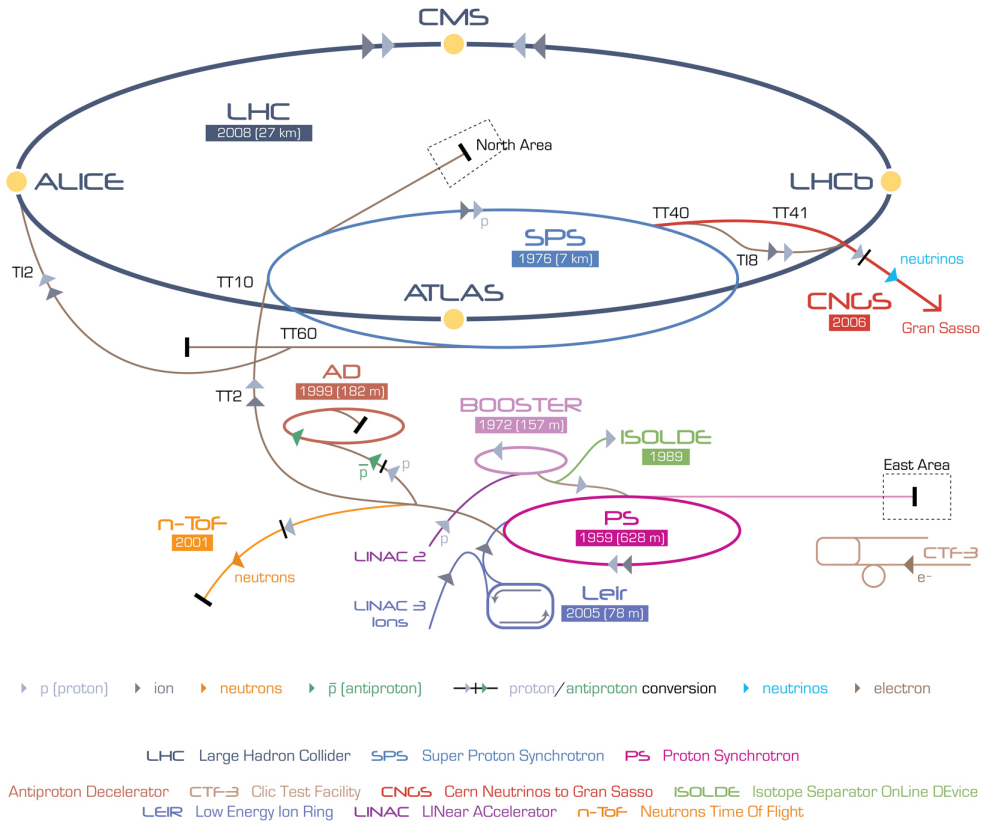

Figure 4.1: Schematic view of the CERN accelerator complex [116] with the location of the four main experiments at the LHC.

precise measurements of *CP* violation in the heavy quark sector. ALICE (A Large Ion Collider Experiment) [119] is specifically designed to study quark-gluon plasma processes through heavy ion collisions (Pb-Pb).

The number of events expected in LHC depends on the cross-section of the process and the delivered luminosity, which can be approximated as

$$\mathcal{L} = \frac{N_b^2 n_b f_{\text{rev}} \gamma_r}{4\pi \epsilon_n \beta^*} F \,, \tag{4.1}$$

where N_b and n_b are respectively the number of particles per bunch and bunches per beam, f_{rev} the revolution frequency, γ_r the relativistic factor, ϵ_n the normalised emittance, β^* quantifies the amount of focusing of the beam and F is a geometric luminosity reduction factor. At the design specifications, the LHC is constructed to reach an instantaneous luminosity of up to 10^{34} cm^{-2} s^{-1}, which allows access to phenomena in the TeV scale. During the 2011 and 2012 operation, data have been collected at a centre-of-mass energies of 7 TeV and 8 TeV, respectively, with up to

1368 bunches at 50 ns spacing. These are the datasets used in the remainder of this work.

4.2 The LHCb experiment

LHC collisions provide the world's most intense source of B mesons. Indeed, proton-proton collisions at high energies produce all species of b hadrons, including B^+, B^0, B_s^0, B_c^+ mesons and b-baryons (*e.g.* Λ_b^0 and Ξ_b^0). The typical mechanisms that contribute to $b\bar{b}$ pair production are given in Figure 4.2, corresponding to $q\bar{q}$ annihilation, gluon splitting and gluon fusion. In all these diagrams there are interactions between the parton constituents of both protons. At the LHC energy scale, in general the two incoming partons have dissimilar momenta. Since the mass of the $b\bar{b}$ pair is negligible in comparison to the centre-of-mass energy of the parton, gluons are radiated at low angle to the beam directions. Among the distinct features resulting from this characteristic is the angular correlation in the production of the b and $\bar{b}$ quarks. This outgoing system predominantly produces a pair of b hadrons, both of which travel forward (or both backward) along the beam axis direction. The polar angle distribution and the LHCb acceptance are shown in Figure 4.2.

This angular correlation influenced the design of the LHCb experiment, as a single-arm forward spectrometer. The geometry covers a forward angular range of 15 mrad to 300 (250) mrad in the bending (non-bending) plane of the magnet, or equivalently in the pseudorapidity[2] range of $2 < \eta < 5$. The main goal of LHCb is to be able to reconstruct particles within this acceptance with high efficiency. For this purpose, information from the various sub-detectors are combined. A schematic side view of the LHCb spectrometer and its constituent sub-detectors is shown in Figure 4.3. A right-handed coordinate system is defined with the z-axis parallel to the beam axis in the direction from the VELO towards the muon stations, and the y-axis pointing upwards. In this arrangement the magnetic field bends trajectories in the xz plane.

LHCb has been planned to operate at nominal luminosity of 2×10^{32} cm^{-2} s^{-1}, which is lower than the maximum that can be provided by LHC. At the maximum LHC conditions, bunch crossings typically involve multiple proton-proton inelastic interactions, with the number of interactions given by a Poisson distribution dependent on the cross-section. In events with multiple pp interactions, there is a higher detector occupancy, which degrades the performance of the reconstruction.

[2]Pseudorapidity is defined as $\eta = -\ln(\tan\theta/2)$, where θ is the polar angle with respect to the beam axis.

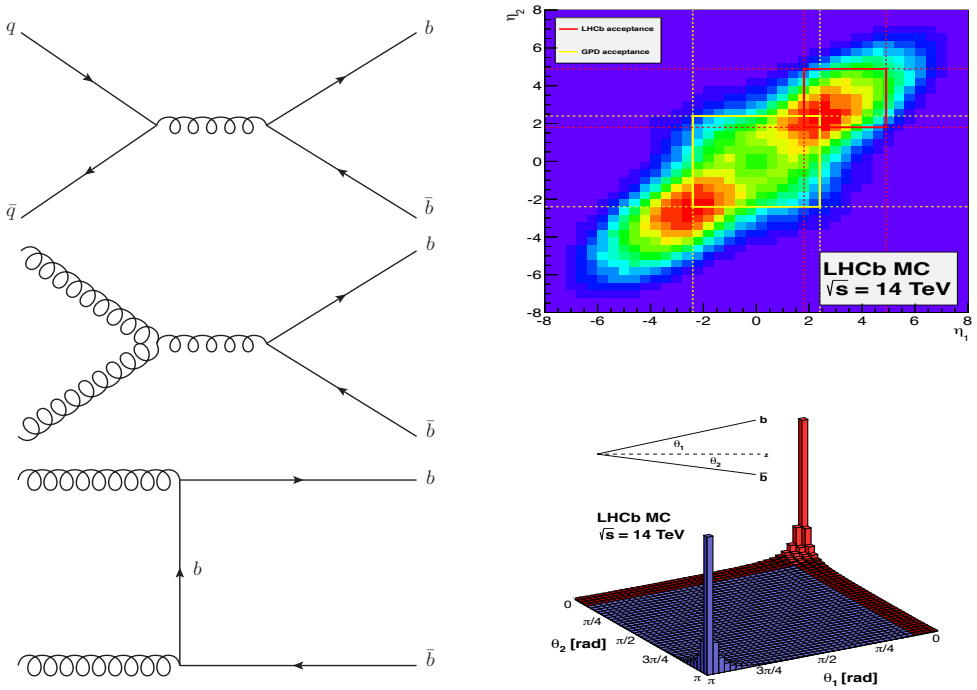

Figure 4.2: (left) Dominant Feynman diagrams for $b\bar{b}$ production at LHCb (from top to bottom): $q\bar{q}$ annihilation; gluon separation; and gluon fusion. The correlation of the $b\bar{b}$ pair angle is shown from simulation (top right) in terms of pseudorapidity of the b and $\bar{b}$, including a comparison between the LHCb and ATLAS/CMS acceptance and (bottom right) in terms of the polar angle [120].

Hence, this harsh environment compromises the sensitivity of many precision measurements. Figure 4.4 indicates the correlation between the number of proton-proton interactions and the luminosity. Notice that the probability of a single pp collision is maximised approximately at 3×10^{32} cm^{-2} s^{-1}. However, additional factors (radiation damage in the electronics and detector occupancy) motivated the choice for a design luminosity of 2×10^{32} cm^{-2} s^{-1}. The luminosity reduction, known as "levelling", is provided by mis-aligning the beams (transverse beam offset [122]) around the interaction point at LHCb.

While LHCb is primarily dedicated to study *CP*-violation effects and rare decays in the beauty and charm sectors, it has an extensive physics programme that depends on several key features

i. Many analyses rely significantly on the vertex resolution, where is essential to achieve a precise measurement of the distance with which tracks approach the primary vertex, separation of primary and secondary vertices, and decay time resolution (the limiting feature to resolve B_s^0 flavour oscillation);

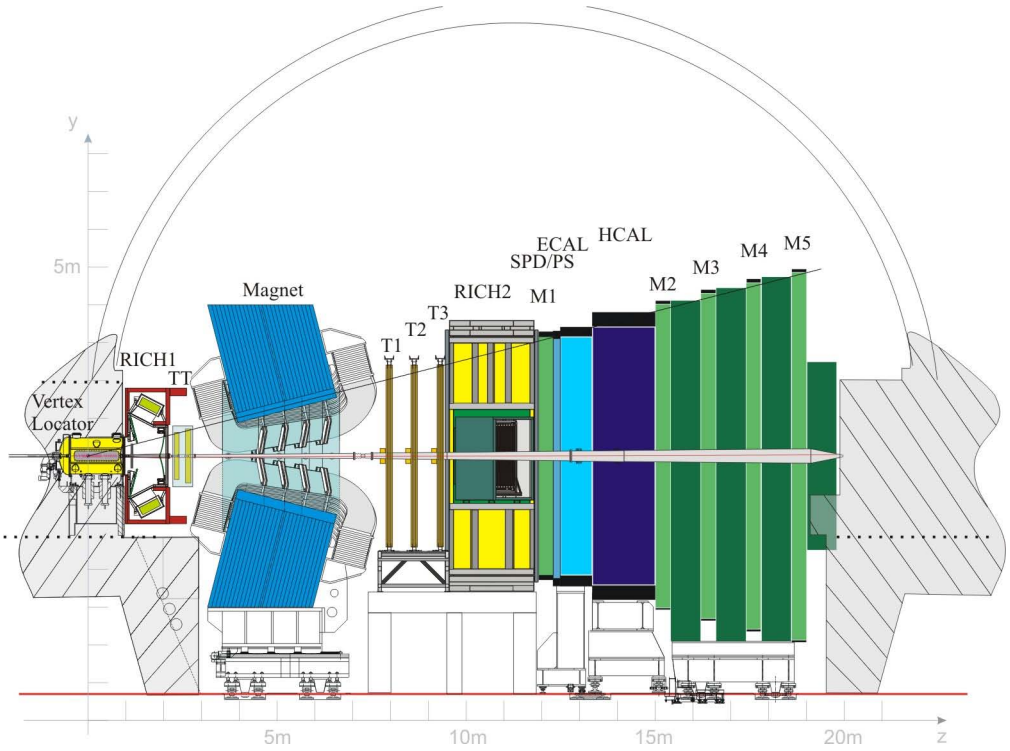

Figure 4.3: Schematic view of the LHCb spectrometer layout in the right-handed coordinate system with the z-axis along the beam, and the y-axis along the vertical [121].

ii. Decays with similar topologies are foreseen. The discrimination of competing channels by distinguishing the particles that make up the final state (*i.e.* K, π and protons) is fundamental;

iii. The rejection of various sources of background is enabled by precise mass resolution, which is naturally linked to high resolution on the track momenta;

iv. The frequency of visible interactions expected at LHCb is $\sim$ 10 MHz, which from these interactions only 15 kHz are $b\bar{b}$ events. Therefore, the ability to select interesting physics events with a fast and reliable trigger system is essential.

The LHCb spectrometer can be described in terms of three main systems: tracking, particle identification and trigger. The main specifications and performance of these are discussed in the next sections.

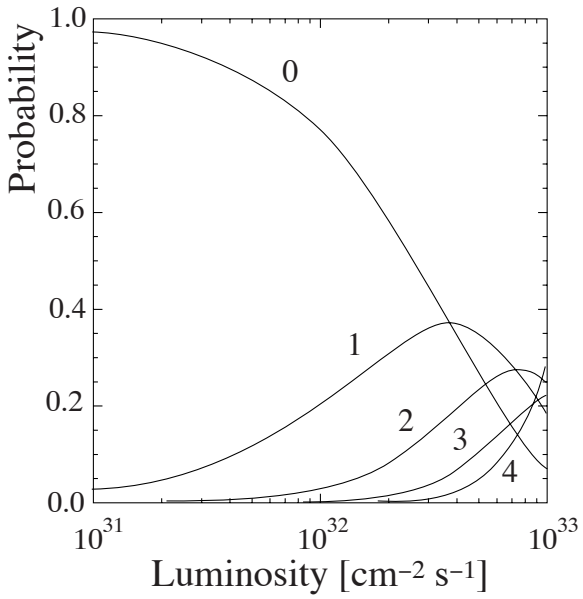

Figure 4.4: Probability of number of proton-proton interactions per bunch crossing as a function of luminosity, at the inelastic cross-section of 80 mb at LHCb [123].

4.3 Tracking system

Tracking at LHCb is performed by a series of systems coherently synchronised to accurately determine both decay vertices and track trajectories. Although information from most subdetectors is used in the reconstruction of these signatures, the precision obtained comes predominantly from the dedicated systems: the Vertex Locator (VELO), Tracker Turicensis (TT) and additional inner (IT) and outer (OT) layers of tracking stations, in conjunction with the dipole magnet.

4.3.1 Magnet

The LHCb dipole magnet [124] is located between the TT and tracking stations. In the presence of a magnetic field, charged particles experience a perpendicular force that enables, from the degree of curvature, the momentum of the particles to be determined. In order to achieve a precision on resolution of $\delta p/p \approx 0.5\%$ for momenta up to 200 GeV/c, an integrated bending power of 4 Tm is maintained by the magnetic field. The apparatus consists of two trapezoidal coils (saddle-shaped), with an iron yoke window-frame inside, as indicated in Figure 4.5. An important feature of the LHCb magnet is the ability to invert the polarity of the field in order to control potential charge detection asymmetries that could lead to systematic biases on *CP* violation observables [125].

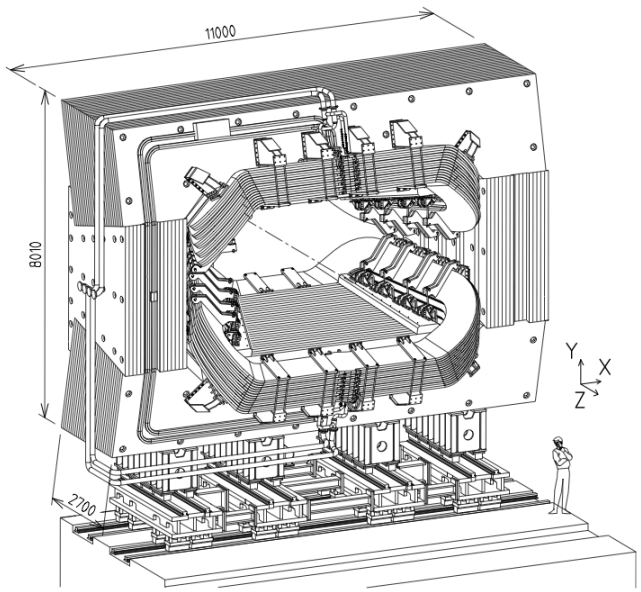

Figure 4.5: Schematic view of the LHCb dipole magnet with the saddle-shaped coil and the window-frame yoke which guides the field lines [124].

4.3.2 Vertex Locator

The VELO is the closest sub-detector to the interaction point and is composed of two retractable halves [5]. During beam injection and energy ramping, the aperture required by the LHC machine increases, and therefore, the two detectors halves are retracted to a distance of 29 mm from the beam axis in order to avoid beam-induced damage to the sensors. When the beams are stable, the two halves are automatically closed around the beam, providing a sensitive area 8 mm from the beam. Each VELO half is composed of 21 modules each with two back-to-back semi-circular 300 μm oxygenated n^+-on-n silicon sensors (n-type implant in an n-type bulk with a back p-type implant) that provide radial and azimuthal hit coordinates (Fig. 4.6). The modules have three basic functions: maintain the sensors in a fixed position relative to the support; provide and connect the electrical readout to the sensors; and thermally manage the operation in the vacuum. The sensor readout is performed by 16 analog ASICs (Beetle version 1.5 [126]) chips. The mapping of the strips to the Beetle chips has been chosen such that each Beetle reads out 4 links with 32 channels each, and per sensor there are 64 links. This results in a total of 2048 strips for each sensor. Two oxygenated n^+-on-p silicon sensors are also installed at the end of the VELO which allows comparison with the performance of the n^+-on-n sensors. Finally, two additional Pile-Up stations are located in the most upstream

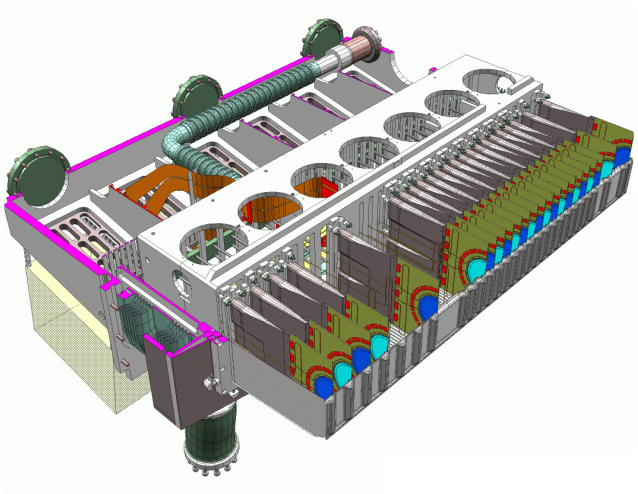

Figure 4.6: Schematic view of one VELO detector half. The (21+2) aligned sensor modules indicated in the picture operate in the secondary vacuum provided by the aluminum foil (RF foil), that separates the sensors from the primary vacuum of the LHC.

positions.

Each n^+ implant requires a first metal layer to capacitively couple to the sensor strips and a second metal layer (routing line) to carry the collected charge to the readout electronics. In R sensors the routing lines are designed perpendicularly to the sensors strips, whilst for the ϕ sensors they are parallel to the strips. Figure 4.7 displays the orientation of the sensors and metal layers. The proximity of the silicon sensors to the LHC beam results in a highly non-uniform particle fluence that goes up to 5×10^{13} 1 MeV $\mathrm{n_{eq}}/\,\mathrm{cm}^2$ (for 1 fb^{-1} [127]). Therefore, radiation damage effects that may cause degradation of the sensor performance are monitored on a regular basis. Scans of the cluster efficiency [3] have shown an unexpected inefficiency for R-sensors due to particles that pass close to a second metal layer that may induce a signal on the routing lines; however, no significant effect on the physics performance has been seen. The VELO sensors are operated at a nominal temperature of $-8°\mathrm{C}$ that minimises radiation induced effects. The temperature is controlled by a bi-phase CO_2 cooling system maintained at $-30°\mathrm{C}$. Moreover, sensors are operated in a secondary vacuum with respect to the beam volume, which is made possible by a 300 μm thick aluminium foil responsible for shielding the modules, referred to as the RF-foil.

The performance of the VELO system is directly related to a number of

[3] A cluster is defined as one or more adjacent silicon strips with charge above a particular threshold.

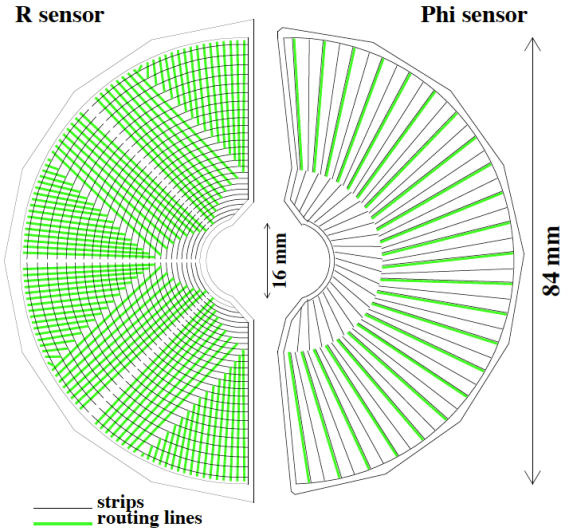

Figure 4.7: Schematic design of VELO R (left) and ϕ (right) sensors. Both strips and routing lines are shown.

physics parameters [128]. By simultaneously investigating its response in data and simulated events, the good quality of the data under consideration is ensured. Among the variables to evaluate the detector performance, the primary vertex (PV) and impact parameter (IP) resolutions are key parameters. Figure 4.8 shows the PV resolution as a function of the number of tracks for 2012 data. For a primary vertex with 25 tracks associated (typical LHCb event), a resolution of 13.5 μm (x), 12.5 μm (y) and 90 μm (z) is found. Furthermore, the resolution of IP_x as a function of the inverse of transverse momentum for 2012 data and simulation is shown. An approximately linear dependence of the resolution on $1/p_{\mathrm{T}}$ is observed (at high p_{T} tending to $\approx 12\,\mu$m), with excellent agreement with the expectation from simulation.

4.3.3 Tracking stations

In addition to the information obtained in the VELO, a system of four tracking stations are positioned (TT) upstream and (T1-T3) downstream of the dipole magnet. The detector acceptance coverage is ensured by the use of two technologies in the downstream stations, the inner (IT) and outer (OT) trackers.

Tracker Turicensis

The Tracker Turicensis (TT) [129,130] detector is manufactured using silicon microstrip technology similar to that used in the VELO, with a strip pitch of 183 µm and 500 µm thick p^+-on-n sensors. This station is composed of four planar layers 150 cm

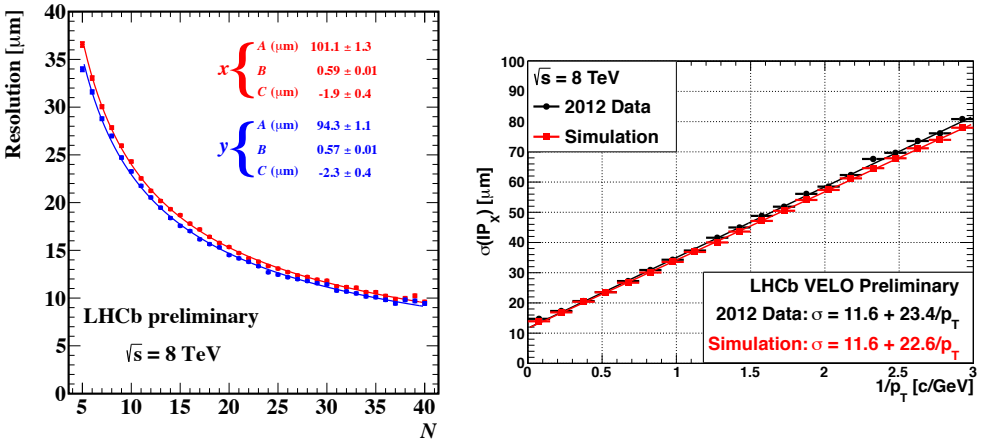

Figure 4.8: (left) Primary vertex resolution of events with one PV from 2012 data, as a function of track multiplicity for (red) x and (blue) y positions, and (right) impact parameter resolution in x as a function of the inverse of the transverse momentum for 2012 data and simulation [128]. The PV resolution is fitted using the function $A/N^B + C$, where A is a constant, B accounts for the track multiplicity and C is the best possible resolution.

wide and 130 cm high, covering an active area of $8.4\,\mathrm{m}^2$. These layers are arranged in a "x-u-v-x" layout, with vertical (x-layers) and rotated by stereo angles of $+5°$ and $-5°$ (u/v-layers) readout strips. The structure of these planes is illustrated in Figure 4.9. This layout enables sufficient resolution to resolve the transverse momentum. An approximate 59 μm single-hit resolution is observed, which is comparable to the nominal design of 50 μm [131]. Note that the reconstruction efficiencies of low momentum tracks as well as long-lived particles that decay downstream of the VELO are constrained by the performance of the TT.

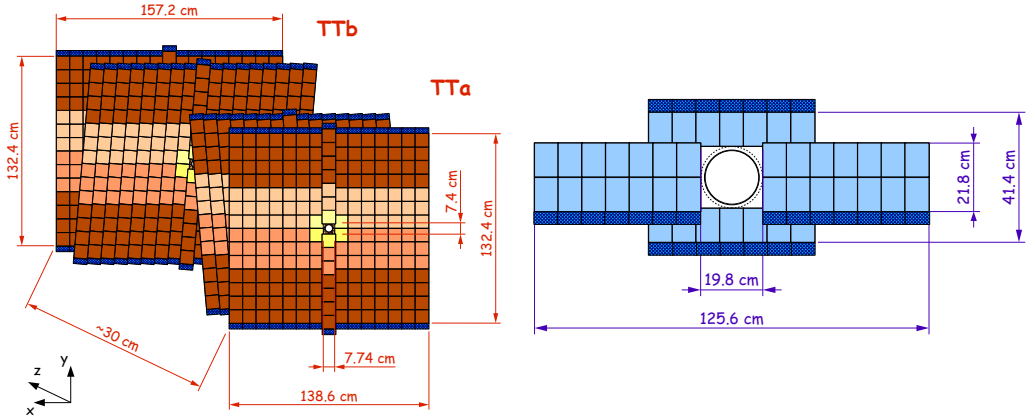

Figure 4.9: Schematic view of the (left) four TT layers with internal tilts rotated by ±5° and (right) an inner IT layer. Notice the two-layers pair arrangement with a 27 cm separation between the layers, centred at $z = 232$ cm (TTa) and $z = 262$ cm (TTb) [132].

Inner Tracker

The Inner Tracker [133] is positioned in three downstream tracking stations T1-T3, each consisting of four boxes arranged around the beam pipe. A detector box contains four detector layers separated into single and double lines of seven staggered silicon ladders. In order to avoid uncovered regions in the acceptance, the top and bottom modules are staggered 4 mm in the z-axis and 3 mm in the x-axis, with respect to the lateral ladders. Furthermore, in each of the boxes the silicon layers are orientated analogously to the TT layout, with an observed single-hit resolution of 50 μm.

Outer Tracker

In contrast to the innermost region that features a high particle flux, the remaining area has a significant reduction in the occupancy, enabling a coarser granularity. Therefore, the Outer Tracker detector [134] covers this large acceptance (total area of $5{\times}6\,\mathrm{m}^2$) utilising a drift-tube technology. The OT acceptance extends from the outer boundaries of the inner tracker up to coincide with the nominal LHCb coverage. Moreover, the aforementioned strategy of misalignment of the stereo angles of the inner layers is also used in the OT. This is designed in four layers of arrays of gaseous straw tubes 2.4 m long and 4.9 mm in diameter. Each of these modules contains two monolayers of drift tube as shown in Figure 4.10. The gas is composed of a mixture of Ar (70%) and CO_2(30%). Both these characteristics enable the detector to achieve a fast drift-time across the drift-tubes under 50 ns, which is the performance required for the tracking algorithm. Although harsher conditions (*i.e.* higher occupancy) than the designed specifications have been seen, a typical hit resolution of 205 μm has been obtained [135].

4.3.4 Tracking reconstruction

The LHCb tracking reconstruction combines information obtained from all the various tracking stations to recreate the trajectory of a charged particle. Both optimal reconstruction efficiency and momentum resolution are compromised in order to guarantee the robustness in the rejection of fake and cloned tracks. The reconstruction algorithm is based on a two-stage procedure, in which hits identified as being correlated to the same track by the pattern recognition software, are re-fitted to enhance the quality of the track. In the tracking finding scheme, the method is initialised by searching for straight lines joining clusters (referred to as track seeds) in the VELO detector. Thresholds of three R-sensor and three ϕ-sensor clusters are

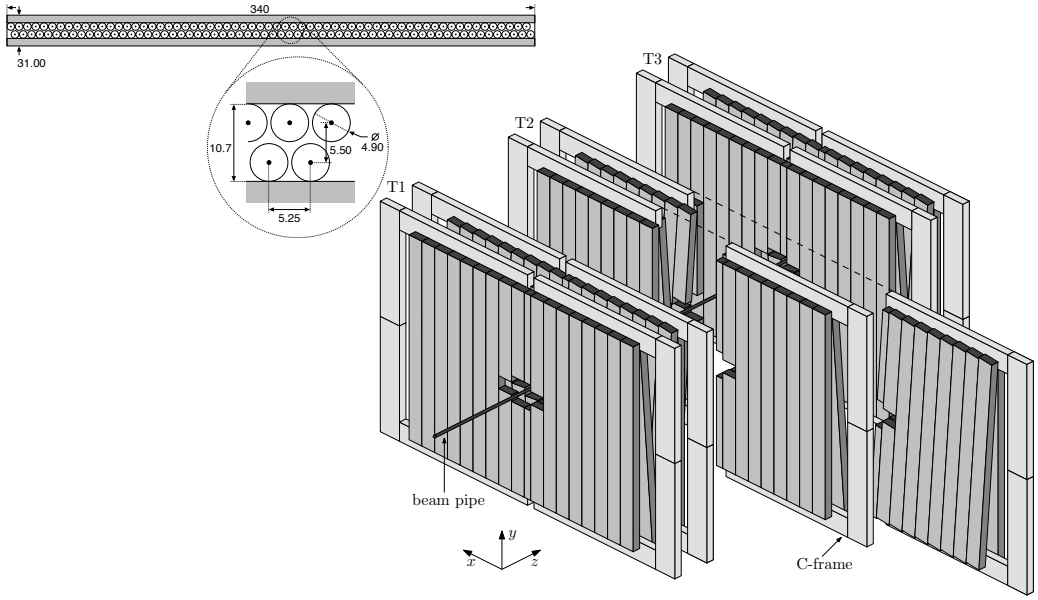

Figure 4.10: Schematic overview of the outer tracker (top left) module bi-monolayers approach and (right) detector layout [135]. Notice that each station is separated into two halves and retractable on both sides of the beam x-axis.

required to initiate the process. The algorithm verifies the consistency of trajectories from the interaction point constructed from only R-clusters, with the ϕ-sensor information. These are sequentially extrapolated to each tracking station to reconstruct the complete track. Tracks are fitted using a Kalman filter [136] method, which provides fast estimation and precision on the track parameters whilst including corrections, such as multiple scattering, energy loss and the residual magnetic field in the VELO.

According to the nature of the charged particle's trajectories in the spectrometer, there are many possible pattern recognition categories (Figure 4.11): "VELO tracks" are formed exclusively from hits in the VELO modules that afterwards exit the detector acceptance; "Upstream tracks" traverse in addition the TT stations, and are typically low momentum particles; "Long tracks" are made with the combined information of the full tracking system, resulting in the most precisely determined momenta; "Downstream tracks" traverse only the TT and T stations; and "T-tracks" that are only measured in the T stations. In addition to "Long tracks", tracks classified as Downstream are of great relevance for this dissertation, since they can be used to reconstruct long-lived particles (*e.g.* K^0_S mesons) that decay outside the VELO acceptance. However, the mass resolution is expected to be degraded,

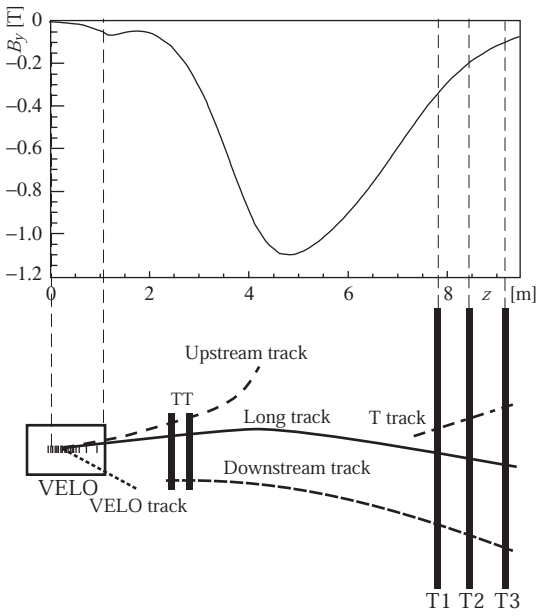

Figure 4.11: Illustration of the various LHCb tracking pattern algorithms alongside with with the magnetic field representation as a function of z-axis.

since the track resolution is worse in the absence of the VELO information. Note that about two-third of the K_S^0 decays are reconstructed from downstream tracks, indicating their importance [137].

4.4 Particle Identification

LHCb employs a dedicated particle identification (PID) system to distinguish different types of charged particles over a $[2, 100]$ GeV momentum range. The distinctions between particle species for each track are achieved by combining information obtained separately from three subdetectors, which are examined in the following.

4.4.1 RICH detectors

Positioned either side of the dipole magnet, the Ring Imaging Cherenkov (RICH) detectors [138] are designed to identify charged particles, in association with the tracking system, using Cherenkov radiation. A charged particle, travelling faster than the velocity of light in a medium with refractive index n, emits a characteristic cone of electromagnetic radiation. Since all Cherenkov photons are emitted at the same angle θ_c with respect to the particle trajectory, it is possible to determine the

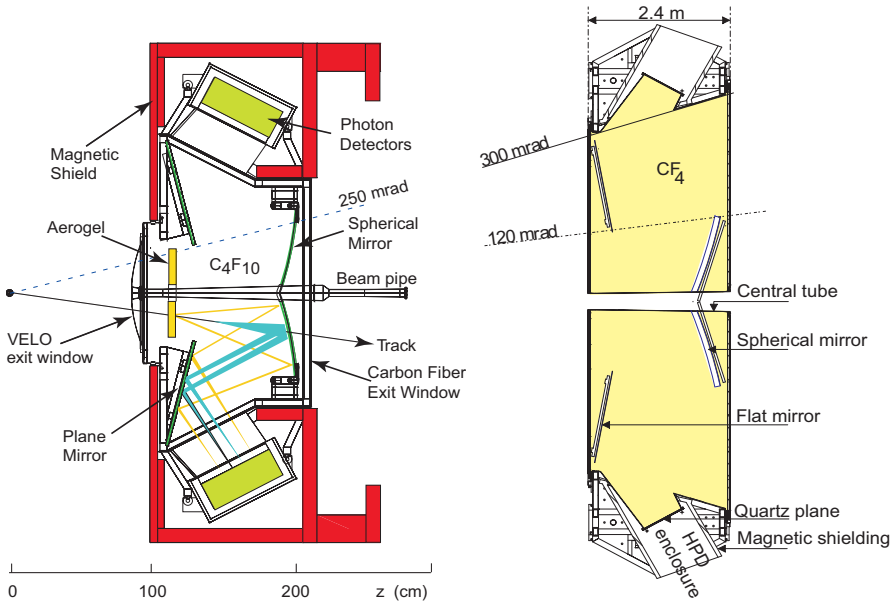

Figure 4.12: Schematic side view of the (left) RICH-1 and (right) RICH-2 layout [129].

particle velocity using the relation

$$\cos\theta_c = \frac{1}{n\beta}\,, \tag{4.2}$$

where β is the ratio between the particle velocity and the speed of light in the vacuum. In the event that the momentum of the charged particle and the Cherenkov angle are known, the rest-mass of a particle is determined using $p = \gamma m_0 \beta c$.

The detector topology influenced the design specification. The coverage of the full momentum range is achieved by the use of two separate RICH counters, as shown in Figure 4.12. In the domain close to the interaction point, low momentum particles associated to a large angular aperture are covered by the RICH-1 detector [2-60 GeV], which is placed upstream of the TT station. Higher rapidity ranges with larger momentum particles are the responsibility of a second counter downstream of the T1-T3 stations, RICH-2 [15-100 GeV]. The concept of both detectors is the same; the differences are in the dimension and the radiator gas utilised. RICH-1 contains two radiators, an aerogel (SO_2) material with $n = 1.03$ and fluorobutane (C_4F_{10}) with $n = 1.0014$. In contrast, RICH-2 operates with a single gas radiator (CF_4) with $n = 1.0005$. The motivation for the radiator choice for different momentum ranges is indicated in Figure 4.13. In both cases, the Cherenkov light is detected with Hybrid Photon Detectors (HPDs), which measure the spatial positions of the emitted photons.

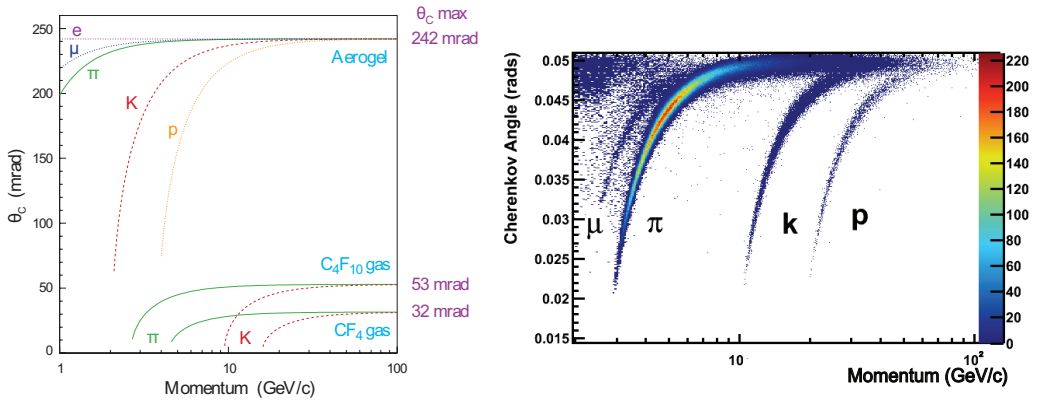

Figure 4.13: (left) Cherenkov angle distribution as a function of the track momentum for the radiators RICH1 and RICH2. Note the good distinction between π/K in the low momentum region for the Aerogel and in the high momentum region for CF_4, which justifies the respective choice of the radiators for RICH1 and RICH2. (right) Reconstructed Cherenkov angle as a function of momentum in the C_4F_{10} radiator for isolated tracks [139].

4.4.2 Calorimeter

The LHCb calorimeter is designed to obtain measurements of the energy and position of electrons, photons and hadrons, alongside providing crucial information for the hardware trigger decisions. Placed downstream of the RICH-2 counter, it is formed of a canonical sequence of electromagnetic (ECAL) and hadronic (HCAL) calorimeters. Additional information for the detection of neutral particles (*i.e.* π^0 and prompt photons) is provided by two scintillator layers (PS and SPD) situated upstream of the ECAL. Calorimetry is based on absorption of the energy of a particle in the material bulk, followed by the measurement of the deposited energy. Energy loss in a medium is inversely proportional to the radiation length, X_0. Incoming particles can interact with the medium producing secondary particles, which eventually lead to a shower (or cascade). Calorimeters are designed to absorb all or almost all of the energy of the incident particles. Note that the showers induce the generation of light in the scintillators, and the emitted photons are collected by photomultipliers. This allows the deposited energy to be measured.

SPD/PS

The Scintillating Pad Detector and Preshower are the first active material of the calorimeter system and are designed to determine the nature of the particles prior to entering the ECAL. Both systems consist of planes of scintillator pads which are separated by a 15 mm lead converter layer ($\approx 2.5X_0$), with the same segmentation of the ECAL. The lead converter thickness is specifically designed to initiate

electromagnetic showers as well as optimise the separation between pions and electrons with a good energy resolution. Whilst the SPD assists in the identification of charged particles, in particular separating electrons from photons, backgrounds from charged pions are reduced by the association of the electromagnetic shower in the PS detector with the information in the ECAL.

ECAL

The LHCb electromagnetic calorimeter is designed with a Shashlik technology, structured in 66 layers of 2 mm of lead alternated by planes of scintillator pads of 4 mm thickness (corresponding to a total of 25 X_0), orientated perpendicularly to the beam direction. The highly non-uniform occupancy over the calorimeter surface leads to a design in which the calorimeter is segmented into inner, middle and outer sections with increasing cell size, as shown in Figure 4.14. Note that the correspondence between SPD/PS and ECAL is guaranteed by the implementation of the same cell-scheme. The scintillator light readout is connected by multianode photomultiplier tubes with single wavelength-shifting (WLS) fibres. The ECAL achieved an energy resolution of $(0.8/\sqrt{E} \oplus 0.9)\%$, where E is the energy in GeV and the uncertainties are summed in quadrature [140].

HCAL

The hadronic calorimeter is responsible for measuring the energies of hadrons and providing a fast-reponse on high-energy signals for the trigger. Unlike the ECAL planes, the device consists of 26 modules of alternating layers of iron and scintillator tiles orientated parallel to the beam axis, inspired by the design of the ATLAS TileCal [117]. The substantial area of the detector combined with the moderate segmentation constraints imposed by the reduced collimation topology of hadronic showers, lead to an optimal layout with a larger cell size than the ECAL and consists of only two sections (inner and outer zones). Figure 4.14 depicts the lateral segmentation of the HCAL cell. The HCAL provides an energy resolution of $(69/\sqrt{E} \oplus 0.9)\%$, where E is in GeV [140].

4.4.3 Muon System

The LHCb muon chambers are located at the downstream region of the spectrometer and consist of five stations (M1-M5) responsible for the identification of muons and providing a standalone fast-response on high-p_{T} muons to the trigger (Figure 4.15). The first muon station is positioned upstream of the calorimeters in order to avoid

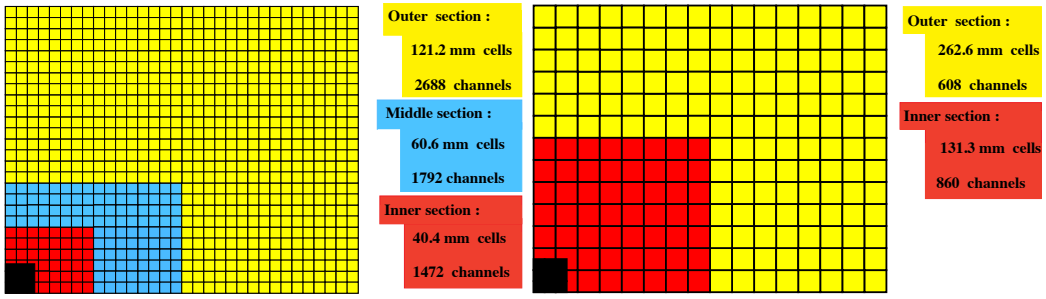

Figure 4.14: Schematic view of the calorimeter segmentation for (left) SPD/PS/ECAL and (right) HCAL [141].

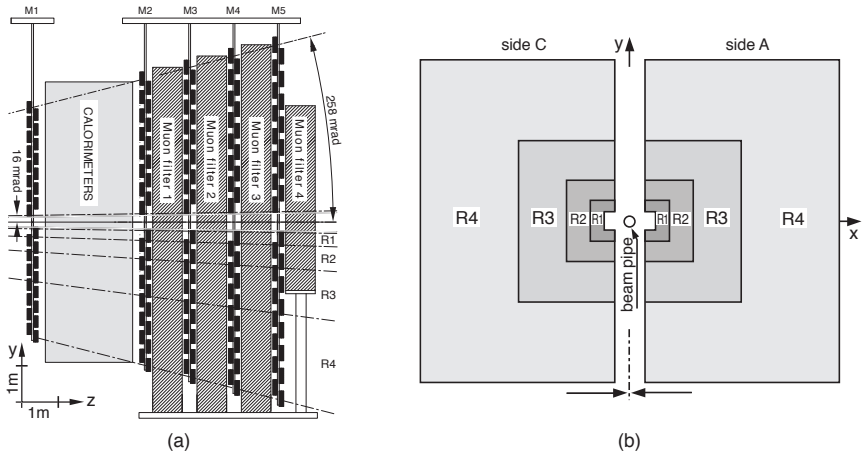

Figure 4.15: Schematic view of the (left) side of the LHCb muon detector and the (right) two mechanically independent station halves with the four regions (R1-R4) indicated.

multiple scattering processes originating from hadronic cascades. This approach extends the muon tracking map, resulting in an enhancement in the purity of the sample. However, the irradiation in the innermost region is significantly increased. Therefore, this central region is specifically equipped with triple gas electron multiplier (GEM) detectors that are robust against radiation. In the outer regions and in all other stations (M2-M5), Multi Wire Proportional Chamber (MWPC) technologies are utilised. Notice that additional iron absorbers plates (80 cm thick) are interleaved between stations M2-M5 and also after M5 to reduce backgrounds.

The geometric design of the detector combines the required radial segmentation with projective scaling. Each station is subdivided into four regions with dimension and granularity scaled to maintain a near homogeneous occupancy and resolution. Figure 4.15 depicts the ratio $1:2:4:8$ implemented in the apparatus.

4.4.4 Particle identification methods

The information independently acquired in the RICH, calorimeters and muon detectors are utilised in profiling charged particles. Information on neutral particles is obtained from the SPD/PS/ECAL. Whilst charged pions/kaons and protons are separated by the RICH detectors, electrons are identified by combining the track momentum and assigned ECAL cluster energy. Additional improvement is achieved by considering the energy deposited in the PS and the extrapolated trajectory in the HCAL. Photons are reconstructed from clusters in the ECAL which are not associated to any track in the event and are further refined with information collected by the SPD and PS. Neutral pions are built either from two photons or a single cluster in the ECAL, referred to as resolved and merged categories, respectively. Finally, muons are identified through the extrapolated trajectories in the muon chambers. For the purpose of this dissertation two combinations of these pieces of information are considered: the difference in the log likelihood of the particle hypothesis under consideration with respect to the pion hypothesis using information only from the RICH detectors; or a more sophisticated method in which additional sub-detector information is introduced and evaluated in a multivariate technique, resulting into a single probability. Both approaches are further examined in the next sections.

4.5 Trigger System

The LHCb Trigger is among the most fundamental components for good performance of the experiment. At the nominal LHC conditions, the bunch crossing frequency of the LHC can reach up to 40 MHz, which corresponds to an average visible frequency of 10 MHz at LHCb. In these events, there is an estimated average of 100 kHz of $b\bar{b}$ pairs produced, of which only 15 % decay within the angular acceptance. Given the elevated bunch crossing frequency and the limited capability in storage, the trigger system is designed to reduce the event rate to manageable levels whilst selecting the physics of interest. This is implemented in a two-stage system, with hardware and software levels, as discussed in the following. The details of the criteria imposed in these stages are postponed to the next chapter.

4.5.1 Hardware Trigger

The first stage of the trigger, hereafter referred to as Level-0 (L0), is a set of hardware constraints maintained synchronously with the LHC clock. Utilising only partial detector information, the L0 is designed to reduce the event rate to 1.1 MHz, which

corresponds to the upper limit imposed by the front-end electronics. The decision is based on the kinematics of b-hadron decays, in which decay products are typically produced with large momentum and transverse energy.[4] In each bunching crossing, the information collected from the calorimeters and muon stations are transmitted to the L0 global decision unit, which evaluates the boolean response of the event.

There are two main approaches used to select interesting events in L0: the highest E_T cluster from the calorimeter is inspected against the relevant threshold; the transverse momentum of single/di-muon candidates in the muon chambers are compared to a given requirement. Notice that the multiple hypotheses in the calorimeter essentially create different overlapping L0 classes. One further notable aspect is related to the fixed total L0 bandwidth. The non-flexibility on the rate results in a compulsory compromise between the threshold of each individual decision. The nominal output rate is split approximately as 400 kHz, 490 kHz and 150 kHz for muons, hadrons and photons/electrons, respectively. The correponding E_T/p_{T} thresholds are given in Sec. 5.1.1.

4.5.2 Software Trigger

The High Level Trigger (HLT) is designed as a series of C++ algorithms which reduces the output rate to approximately 2 kHz, corresponding to the nominal event rate for being permanently stored. Given the large data flow and limited computational resources, the HLT architecture is divided in two stages: fast partial event reconstruction with an inclusive selection (HLT1) in order to reduce the rate to 40 and 80 kHz for 2011 and 2012, respectively [142,143]; complete event reconstruction with final trigger selection (HLT2).

With the additional information available, the strategy of a single track trigger is implemented in HLT1 using information on the quality of the track and the displacement from the primary vertex. In this simplified model, track segments in the VELO detector are identified and compared to calorimeter clusters or hits in the muon chambers. Further improvements on the tracking search are obtained by reducing the phase-space boundaries to consider only tracks with transverse momentum above the required threshold conditions. In particular, an inclusive approach for beauty decays has been designed, which comprises a large fraction of the output bandwidth.

At the last stage of the software trigger, the full tracking reconstruction can

[4] The transverse energy is calculated in clusters of 2×2 cells, and is defined as $E_T = \sum_{i=1}^{4} E_i \sin\theta_i$, where E_i is the energy deposited in a given cell i and θ_i is the angle of the mean cell position with respect to the z-axis.

be employed. Since more refined methods are available, there are a great number of exclusive selections implemented in the code. However, for the purpose of this dissertation, the generic multibody beauty line is of particular relevance. A dedicated discussion regarding the main settings and implications attributed to this topological trigger is presented in the next chapter.

4.5.3 Trigger convention

The set of unique configurations that defines the software version, sequence of algorithms and selection filters used in the L0 and HLT is referred to as the Trigger Configuration Key (TCK). The TCK is identified as a 32-bit value (with the initial 16 bits reserved for the L0 settings), encoded for every event in the raw data, which labels the corresponding entry in the trigger configuration database. This hexadecimal representation provides a simplified access to the parameters used in the trigger at the time the data were recorded, as well as ensuring the reproducibility in the simulation. Considering datasets with more than 10 pb^{-1} of integrated luminosity, a total of 6 and 13 configurations have been used in 2011 and 2012 data taking, respectively [144].

Another important consideration is the association of a trigger object with a signal track. An event is classified as TOS (Trigger on Signal) if the signal under study triggers the event, whereas TIS (Trigger Independent of Signal) categorises the trigger objects not associated to the signal. The non-exclusive classification in TOS and TIS allows data-driven determinations of the trigger efficiency, which are obtained by $\epsilon^{\text{TOS(TIS)}} = N^{\text{TIS\&TOS}}/N^{\text{TIS(TOS)}}$ for signal-like (independent) events. Further details on the nuances of this definition are given in the next chapters.

5

$K^0_S hh$ generalities

The study of charmless three-body decays of neutral B mesons and beauty baryons to final states containing K^0 mesons is of great interest for improving the understanding of hadronic interactions and in the search for CP violation effects. Of the two physical eigenstates of the K^0-$\overline{K}^0$ system, only the K^0_S meson can be detected at LHCb, where it is reconstructed in the $\pi^+\pi^-$ final state and classified into two categories. Candidates decaying within the VELO are hereafter referred to as "Long-Long" or LL, whilst those that have information only from the tracking stations are named "Down-Down" or DD.

The remaining chapters discuss the results of investigations performed on the dataset collected by the LHCb experiment, corresponding to an integrated luminosity of 1.0 fb^{-1} and 2.0 fb^{-1} for 2011 and 2012, respectively. In particular, branching ratio measurements of b-hadron decays to $K^0_S h^\pm h'^\mp$ final states are described in Chapter 6, while the amplitude analysis of $B^0_s \to K^0_S K^\pm \pi^\mp$ decays is discussed in Chapter 7. Whilst high-energy proton-proton collisions provide unprecedented production of b hadrons, significant developments in data analysis techniques have also been achieved. Therefore, it is essential to revise the implementations and nuances of these various approaches. In the following, a series of common tools and techniques utilised in these analyses are examined.

5.1 Trigger settings

The topology of three-body hadronic decays provides a distinctive signature in the detector. Some features are however modified due to the presence of a neutral long-lived particle in the final state. In particular, the momentum shared among the tracks and the characteristic displacement of the K^0_S decay vertex reflect a distinct event topology. This affects both the performance of the trigger and the variation

of efficiency over the phase space. These effects are examined in each stage of the trigger in the following.

Although various TCK settings have been introduced at different periods of data taking [143, 144], pronounced distinctions are observed for two transitions: the beam energy increase in 2012 and the introduction of Downstream tracks in HLT2 during the technical stop at the end of June of the same year. The inclusion of long-lived particles constructed from Downstream tracks results in a significantly higher absolute efficiency and in a prominent change of the efficiency variation over the Dalitz plot for this category. It is therefore necessary for the 2012 data and simulated samples to be divided into two running periods, hereafter referred to as the pre-June and post-June or more simply 2012a and 2012b periods. In order to simulate the various trigger conditions correctly, samples have been produced using TCKs, recommended by the trigger group, that are representative of the three periods, given by the hexadecimal identifiers `0x40760037` (2011), `0x4097003d` (2012a) and `0x409f0045` (2012b) and corresponding to integrated luminosities of 339.9 pb^{-1}, 272.8 pb^{-1} and 27.6 pb^{-1}, respectively. Notice that although the later configuration does not correspond to a large portion of the delivered luminosity, differences with respect to the most contributing TCK `0x40990042` (555.3 pb^{-1}) are expected to be marginal.

5.1.1 L0 settings

The trigger lines are generally optimised using representative channels with appropriate high-p_{T} tracks in the final state. In particular, the baseline figure-of-merit is driven by the maximisation of absolute efficiencies, which overlooks possible effects due to variations across the phase space. Whilst this approach is suitable for a broad range of analyses, multibody decays often have a rich intermediate structure, which can be significantly affected by this choice. This is addressed in the analyses by examining the population of events throughout the Dalitz plane at each stage of the trigger. A notable aspect of these processes is that although *a priori* these distributions are unknown (and are determined from the data), the interesting physics is clustered on the boundaries of the phase space, as indicated in Figure 3.6. This provides a global benchmark for three-body decays, which favours selection requirements that enhance the sensitivity on the corners and edges of the plane (*e.g.* by producing an uniform efficiency distribution over the Dalitz plot).

The L0 requirements used in this analysis are the logical "or" of the `L0Hadron TOS` and `L0Global TIS` decisions. This combined criterion is designed to select at least one trigger object originating from the signal or an object that has no associated

overlap with the signal, following the convention described in Sec. 4.5.3. Although most of the trigger settings were kept reasonably stable throughout the years, unavoidable changes were imposed to adjust to the running conditions. `L0Hadron TOS` candidates are selected if the measured hadronic E_{T} is greater than nominal thresholds 3500, 3620 and 3740 MeV, for the TCK configurations implemented in 2011, 2012a and 2012b, respectively. In addition, a common upper limit on the number of SPD hits of 600 is enforced. Figure 5.1 indicates the expected efficiency variation over the square Dalitz plot. Notice that for the `L0Hadron TOS` line the efficiency is enhanced in the corners of the DP, resulting from the effect of triggering on a single high-p_{T} track. Recall that in the corners of the DP, one particle is at rest while the other two carry their maximum momentum values. No similar structure is observed in the `L0Global TIS`, which indicates an approximately unbiased nature over the phase-space of interest. Due to the similarity of the chosen thresholds, a consistent figure is seen for all data taking conditions and K^0_{S} categories. Nonetheless, Down-Down efficiencies are found to be systematically larger than the corresponding Long-Long ones by a few percent, due to the larger boost of B candidates in this category.

5.1.2 HLT1 hadronic line

Similarly to the L0 decision, an inclusive approach is implemented at HLT1 [145]. In particular, the conceptual design of a single track trigger coincides at a good level with the expected topology of the event. Candidates have been selected using the `Hlt1TrackAllL0 TOS` line, whose requirements are listed in Table 5.1. While there are differences in the p and p_{T} criteria between the three running periods, only the variation in the requirement for the χ^2/ndf on the track fit has a significant effect on the efficiency. This is most pronounced for the 2012a conditions, with a typical loss of five percent in the efficiency.

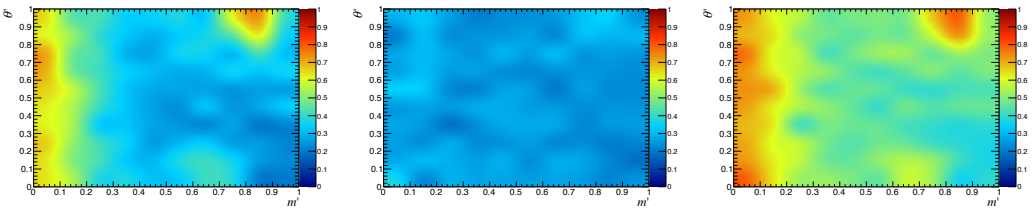

Figure 5.1: L0 efficiency variation as a function of the $B^0_s \to K^0_{\mathrm{S}} K^+ \pi^-$ square Dalitz plot position for (left) `L0Hadron TOS`, (middle) `L0Global TIS` and (right) `L0Hadron TOS` or `L0Global TIS` decisions.

However, the most notable feature of the HLT1 stage relies on the partial forward tracking algorithm utilised. Since the initialisation of the method is based on the identification of track segments in the VELO detector, only Long tracks are considered in this approach. Hence, the absence of high-p_{T} Downstream tracks results in an appreciable degradation of the efficiency for regions of the Dalitz plot where both h^+ and h'^- tracks have low momentum. Figure 5.2 depicts this effect as a function of the phase-space position, separated by K^0_{S} category and year. These non-uniformities for the Down-Down category reinforce the need to separate the analysis into the K^0_{S} types in order to ensure an accurate modelling of the efficiency.

Table 5.1: Requirements applied on the triggering track in the `Hlt1TrackAllL0` line for the nominal `0x40760037`, `0x4097003d` and `0x409f0045` TCKs.

	`Hlt1TrackAllL0` thresholds					
Year	VELO hits	VELO missing hits	hits	χ^2/ndf	$p\,[\mathrm{GeV}/c]$	$p_{\mathrm{T}}\,[\mathrm{GeV}/c]$
2011	> 9	< 3	> 16	–	> 10.0	> 1.7
2012a	> 9	< 3	> 16	< 1.5	> 10.0	> 1.7
2012b	> 9	< 3	> 16	< 2.0	> 3.0	> 1.6

5.1.3 Generic multibody HLT2 beauty line

The capability to perform a similar reconstruction to the offline tracking at the HLT2 stage, *a priori* introduces the feasibility of exclusive selections. However,

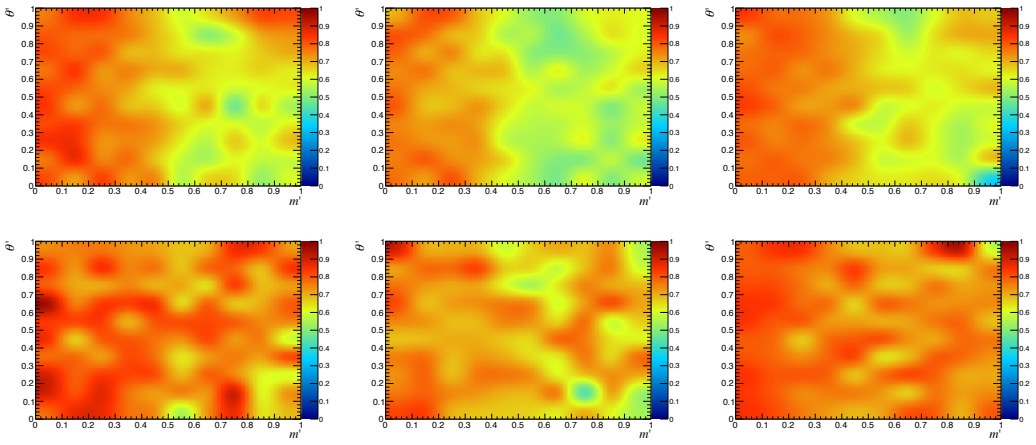

Figure 5.2: HLT1 efficiency variation as a function of the $B^0_s \to K^0_{\mathrm{S}} K^+ \pi^-$ square Dalitz plot position for the `Hlt1TrackAllL0` decision for the (left) 2011, (middle) 2012a and (right) 2012b conditions, separated by the (top) Down-Down and (bottom) Long-Long K^0_{S} category.

the option of an inclusive approach is still preferred due to the performance of the generic topological multibody beauty line [146], referred to as the "n-body line". The concept is based on the two-, three- or four-body topology. Candidates are reconstructed by combining a $(n-1)$-body candidate and a particle ($n \geq 2$), which is used successively as input to each following associated multibody line. The inclusive configuration is accommodated by the absence of quantities related, *e.g.*, to the impact parameter with respect to the primary vertex, stringent constraints on the quality of the vertices and, most importantly, of the mass of the candidate. In the event that only a subset of all daughter particles is considered in the b-hadron mass calculation, an offset with respect to the nominal value is observed. Since both the precise number of missing daughters and to which type of particles they correspond are unknown, it is convenient to use the concept of corrected mass inspired by neutrino experiments, and defined as [147]

$$m_{\rm corr} = \sqrt{m^2 + \left|p_{\rm T}^{\rm miss}\right|^2} + p_{\rm T}^{\rm miss}\,, \tag{5.1}$$

where $p_{\rm T}^{\rm miss}$ is the component of the momentum of the missing particle transverse to the direction of flight of the B candidate. The direction of flight is obtained from the vector between the primary and secondary vertices. Notice that this corresponds to the transverse momentum loss of a massless particles, in other words, the minimum correction to the candidate mass if a daughter particle is missing.

In order to understand the importance of the n-body line for the analyses under discussion, Figure 5.3 demonstrates the concept through the three- and two-body selection efficiency for $B^0_{(s)} \to K^0_{\rm S} h^{\pm} h'^{\mp}$ decays. It is noticeable that the criterion applied in the 3-body line reduces the population of events in the corners of the Dalitz plane. However, these candidates may still be recovered in the two-body line (*i.e.* in the event that there are missing daughters), since the $m_{\rm corr}$ variable is distributed near the B meson mass. This interesting pattern indicates the suitability of this inclusive approach for multibody decays.

Another important aspect of the n-body topological lines is the definition of the requirements utilised during the data taking. These lines are constructed in a two-stage process, where initially mild cuts are applied in order to reduce further background and enhance the quality of the $(n-1)$-body objects. Summaries of the requirements for filtering $K^0_{\rm S}$ candidates and for constructing the multibody objects are given in Tables 5.2 and 5.3, respectively. In addition, charged particles are selected with $p > 5000$ MeV/c, $p_{\rm T} > 500$ MeV/c, $\chi^2_{\rm IP} > 4$ and track $\chi^2/{\rm ndf} < 3\,(2.5)$ for the 2011/2012a (2012b) configuration. The most prominent effect due to the

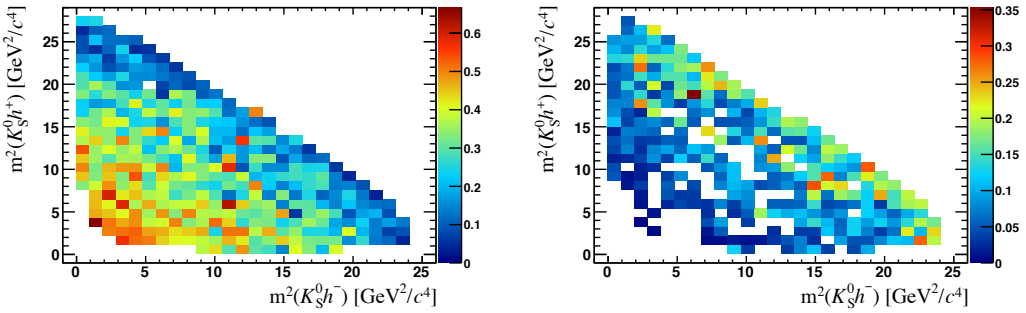

Figure 5.3: `Hlt2Topo(n)Body TOS` efficiency variation as a function of the $B^0_{(s)} \to K^0_S h^\pm h'^\mp$ K^0_S DD Dalitz-plot position for (left) 2-Body and (right) 3-Body decisions.

changes in these generic multibody beauty lines is related to the aforementioned absence of Downstream tracks as input to the method. Figure 5.4 shows the apparent non-uniform phase-space efficiency distribution in the Down-Down K^0_S category caused by this implementation. Although a significant enhancement in the DD efficiency is observed after the 2012 technical stop, further improvements are required in order to achieve similar levels to the LL case. It is worth mentioning that the introduction of a minimum K^0_S lifetime criterion for LL during 2012 does not cause significant differences in efficiency, unlike for other analyses such as $B^0_{(s)} \to K^0_S K^0_S$ and $B^\pm \to K^0_S h^\pm$ [148].

One further notable feature of the HLT2 topological lines concerns the exis-

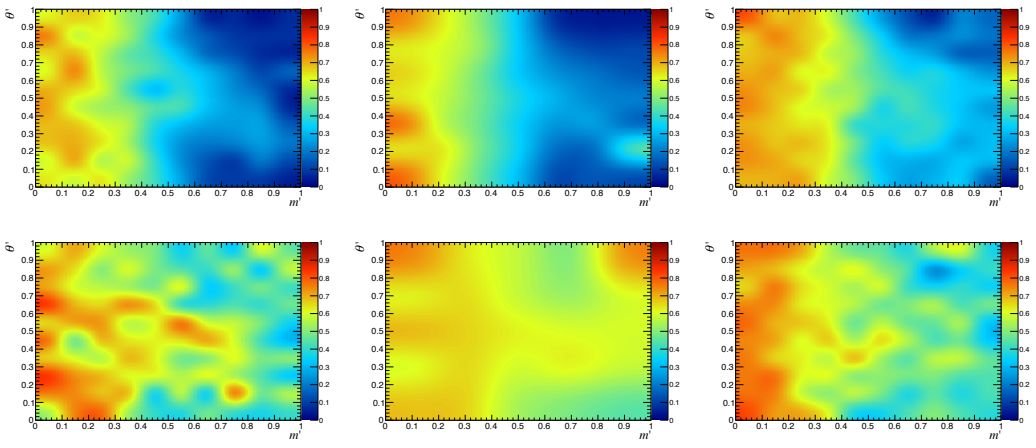

Figure 5.4: HLT2 efficiency variation as a function of the $B^0_s \to K^0_S K^+ \pi^-$ square Dalitz plot position for the `Hlt2Topo(2,3,4)Body TOS` decision for the (left) 2011, (middle) 2012a and (right) 2012b conditions, separated by the (top) Down-Down and (bottom) Long-Long K^0_S category.

Table 5.2: Requirements applied on the K^0_S input particles used in the HLT2 n-body algorithm for the different period of the year. The notation refers to: χ^2_{IP} is defined as the difference in χ^2 of a given PV reconstructed with and without the considered track; DIRA is the cosine of the angle between the reconstructed momentum of the B meson and its direction of flight (pointing angle); and χ^2_{VS} is the square of the separation distance between the K^0_S vertex and the associated PV divided by its uncertainty squared.

Particle container	Variable	Input track category		
		Long		Downstream
		2011	2012a/2012b	2012b
$\pi^{\pm}$-K^0_S daughter	Track χ^2/ndf	< 3	< 3	< 4
	χ^2_{IP}	> 16	> 36	–
	p	> 5000 MeV/c	–	> 3000 MeV/c
	p_T	> 500 MeV/c	–	> 175 MeV/c
K^0_S candidate	χ^2_{vtx}/ndf	< 10	< 30	< 30
	p	> 5000 MeV/c	–	–
	p_T	> 500 MeV/c	–	–
	DIRA	> 0	–	–
	χ^2_{IP}	> 4	–	–
	τ	–	> 2 ps (2012b)	–
	SV_z	–	–	> 400 mm
	χ^2_{VS}	> 1000	–	–
	$\lvert M - m_{K^0_S}\rvert$	< 45 MeV/c^2	< 35 MeV/c^2	< 64 MeV/c^2

tence of two forms of selection, either in a cut-based (named `Simple`) or multivariate classifier approach. The concept of the multivariate approach (hereafter referred to as Bonsai Boosted Decision Tree or `BBDT` [147]) is to perform a multi-dimensional classification of the variables for a given response of interest. Further details of this methodology are given in Sec. 5.3.4. The introduction of this algorithm was in-

Table 5.3: Requirements applied on the n-track objects in the topological HLT2 lines. Conditions exclusive to given year configurations are given in the parenthesis. In addition to the definitions in Tab. 5.2, DOCA refers to the distance of closest approach.

Selection stage	Variable	`Hlt2Topo(n)Body` line		
		$n = 2$	$n = 3$	$n = 4$
Input $(n-1)$-object	χ^2_{vtx}/ndf	–	< 10	–
	M	–	< 6000 MeV/c^2	< 6000 MeV/c^2
n-track object	$M(\sum p^\mu)$	< 7000 MeV/c^2		
	Max DOCA	< 0.2 mm		
	DIRA	> 0		
	χ^2_{VS}	< 100		
	Smallest child χ^2_{IP} (2012)	> 16 or at least one V^0		
n-body line (2011 only)	$\sum p_T$(MeV/c)	> 3000	> 4000	> 4000
	Smallest track χ^2/ndf	< 2.4		

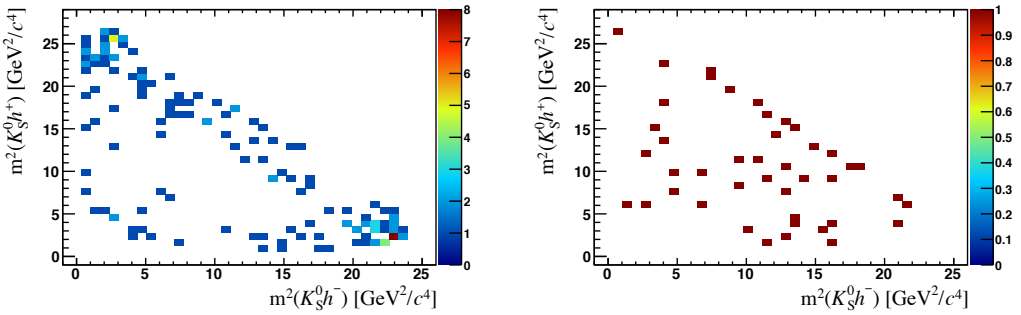

Figure 5.5: Additional events recovered by the (left) `Hlt2Topo2BodySimple TOS` and `Hlt2Topo3BodySimple TOS` decisions for Down-Down and Long-Long K^0_S categories, respectively. Notice that many of these events populate the boundaries of the Dalitz plot, and therefore, are of great interest for this analysis.

tended to supersede the `Simple` decision, by exploiting the discrimination power of the trigger using as input the variables: $\sum |p_{\rm T}|$, $p_{\rm T}^{min}$, $m_{\rm corr}$, DOCA, the candidate $\chi^2_{\rm IP}$ and flight distance χ^2. However, the slightly different set of variables between the `BBDT` and `Simple` lines results in additional events that are recovered by the latter decision, as indicated in Figure 5.5. Since this behaviour was not anticipated, the `Simple` lines were removed in 2012 data taking, which introduces another complication for this analysis. The implementation of the HLT2 topological multivariate selection is under revision for Run 2 in order to address this issue.

5.2 Stripping selection

In order to reduce the size of the stored data and also to simplify the interface with users for data analysis, the `Stripping` environment is introduced as a framework in which sets of exclusive (or inclusive) selections prior to the data manipulation are applied. These algorithms (hereafter referred to as `Stripping` lines) are designed to be run during periodic campaigns that accommodate improvements to the reconstruction software and selections. Charmless three-body neutral B meson and b-baryon decays containing K^0_S mesons have been studied within the `StrippingB2KShh` line builder, produced in either the so-called `Stripping17b` or `Stripping20` campaigns. The main settings used in these configurations are examined in the following.

5.2.1 Stripping framework

Although an inclusive stripping for $K^0_S h^{\pm} h'^{\mp}$ final states has been pursued in both selection revisions, noticeable conceptual differences are seen in the methodology implemented. Among these, the approach of considering either a single or multiple

particle species hypotheses in the invariant mass calculation is the most prominent distinction. A representation of the inclusive capability for these channels is shown in Figure 5.6. Whilst in `Stripping17b` the charged particles were reconstructed under multiple hypotheses and selected in a narrow window around the B^0-B_s^0 mass regions, an inclusive approach is used in `Stripping20`. Since there is a large overlap, the main limitation on the exclusive design is related to the exclusion of contributions from $B^0_{(s)} \to K^0_S p\bar{p}$ decays, which populate the lower region of the mass window.

Similar to the trigger technical requirements, all stripping lines are constrained to upper limits on both the minimum bias retention rate of 5×10^{-4} and a processing time of 1 ms per event. An effective way to reduce the timing is to remove high-multiplicity events, which is achieved by limiting the number of `Long` tracks per event to 250. In addition, a sanity criterion of the number of primary vertices per event to be ≥ 1 is imposed. Moreover, only mild cuts on the momenta and impact parameters of individual daughter particles can be made to obtain an unbiased Dalitz plane of the decay modes. As a consequence, cuts on topological variables such as flight distance of the B candidate or its pointing angle are instead used as the main discriminative information.

5.2.2 Stripping criteria

Within the `B2KShh` stripping, B meson or b-baryon candidates are formed by combining a K^0_S candidate with two oppositely charged tracks. While pion candidates are drawn from the so-called `StdLoosePions` container, kaons are obtained from the corresponding `StdLooseKaons` list. The requirements on these are detailed in Table 5.4, including additional requirements made for this analysis that the χ^2 per degree of freedom of the track fit be less than 4 and that in `Stripping20` the ghost

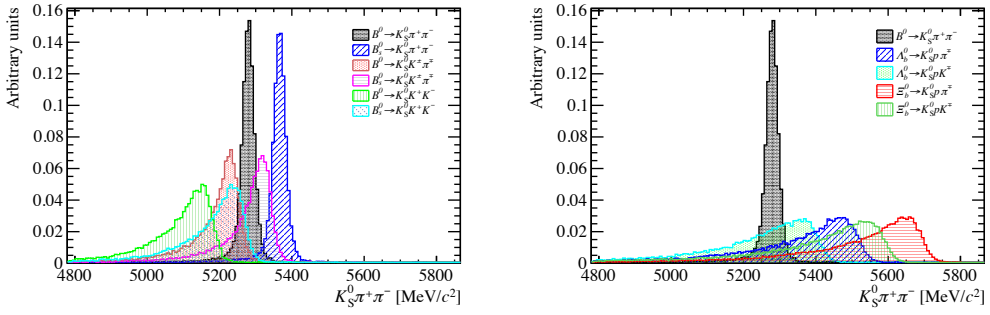

Figure 5.6: Simulated invariant mass distributions of the various signal channels of interest reconstructing both of the charged hadron daughters as pions as representative of the inclusive `Stripping20` approach, and separated for (left) $B^0_{(s)}$ and (right) $\Lambda^0_b(\Xi^0_b)$ decays.

Table 5.4: Standard particle configurations defined for track candidates in the Stripping. Notice that a loose particle identification cut based on the difference in the log likelihood of the kaon hypothesis with respect to the pion is applied in the `StdLooseKaons` container. The track ghost probability is obtained from a multivariate classifier that separates misreconstructed tracks (ghost tracks) from good tracks, combining information from different stages of the track reconstruction and from global event properties [149]. Clone distance is the Kullback-Liebler distance to the closest track [150].

Variable Definition	Selection Requirement
`StdLoose(Pions,Kaons)`	
Track fit χ^2 per degree of freedom	$\chi^2_{\text{trk}}/\text{ndof} < 4$
"Clone distance"	CloneDist > 5000
Track ghost probability	GhostProb < 0.5
Transverse momentum	$p_{\text{T}} > 250\,\text{MeV}/c$
Minimum impact parameter χ^2 wrt PVs	$\chi^2_{\text{IP}} > 4$
Particle identification (Kaons)	$\Delta \ln \mathcal{L}_{K\pi} > -5.0$

probability be less than 0.5.

The K^0_{S} candidates are reconstructed in their decay to $\pi^+\pi^-$ and are drawn from both the `StdLooseKsLL` and `StdLooseKsDD` lists. The former list takes its pion candidates from the `StdLoosePions`, which are formed only from `Long` tracks. The latter list uses pion candidates from the `StdNoPIDsDownPions`, which are formed from `Downstream` tracks, *i.e.* those which do not have hits in the VELO as discussed in Sec. 4.3.4. Details of the selection requirements placed on the K^0_{S} candidates, both by the list definitions and by the `StrippingB2KShh` algorithms are given in Table 5.5. The b-hadron candidates are formed from simple four-momentum addition and some loose combination cuts are applied to reduce the number of candidates that undergo a full vertex fit. Selection requirements, common to both the Down-Down and Long-Long K^0_{S} categories, are mainly based on the topology and kinematics of the b-hadron candidate. Following the vertex fit further quality cuts are made on these objects. Details on both sets of criteria are given in Tables 5.6 and 5.7.

5.3 Selection

Further separation of the signal from all sources of background is essential in order to enhance the sensitivity to the observables of interest. Both multivariate (MVA) and particle classification criteria have been developed in order to achieve this. In particular, the multivariate selection is designed to reduce background contributions whilst maintaining an approximately uniform efficiency over the phase space. This

Table 5.5: Stripping selection requirements for the K^0_S candidates separated in the Down-Down and Long-Long K^0_S categories.

Variable Definition	Selection Requirement
`StdLooseKsLL` plus additional requirements	
K^0_S daughter track fit χ^2/ndof	$\chi^2_{\pi\text{trk}}/\text{ndof} < 4$
K^0_S daughter track ghost probability (`Stripping20`)	GhostProb < 0.5
K^0_S daughter track momentum	$p_{K^0_S\text{daug}} > 2\,\text{GeV}/c$
K^0_S daughter minimum impact parameter χ^2 wrt PVs	$\chi^2_{\text{IP}} > 9$
Mass difference wrt nominal K^0_S mass	$\left\lvert m_{\pi^+\pi^-} - m_{K^0_S}\right\rvert < 20\,\text{MeV}/c^2$
χ^2 of K^0_S vertex fit	$\chi^2_{K^0_S\,\text{vtx}} < 12$
χ^2 separation of K^0_S vertex and associated PV	$\chi^2_{K^0_S-\text{PV VD}} > 80$
`StdLooseKsDD` plus additional requirements	
K^0_S daughter track momentum	$p_{K^0_S\text{daug}} > 2\,\text{GeV}/c$
K^0_S daughter minimum impact parameter χ^2 wrt PVs	$\chi^2_{\text{IP}} > 4$
Mass difference wrt nominal K^0_S mass	$\left\lvert m_{\pi^+\pi^-} - m_{K^0_S}\right\rvert < 30\,\text{MeV}/c^2$
χ^2 of K^0_S vertex fit	$\chi^2_{K^0_S\text{vtx}} < 12$
χ^2 separation of K^0_S vertex and associated PV	$\chi^2_{K^0_S-\text{PVVD}} > 50$
K^0_S momentum	$p_{K^0_S} > 6\,\text{GeV}/c$

is obtained by the preferential use of topological quantities (*i.e.* variables related to the daughter particles' kinematics are avoided).

Similarly to the trigger and stripping stages of the selection, the strategy is based on the subdivision of the dataset between the three trigger operation conditions and the Down-Down and Long-Long K^0_S categories. A generic approach is adopted, which is not dependent on either the final state or the initial particle under investigation. This allows $B^0 \to K^0_S\pi^+\pi^-$ decays to be used as the baseline channel in a common optimisation.

5.3.1 Preselection

In addition to the trigger criteria examined in Section 5.1, high signal-efficiency cuts are applied on top of the stripping to reduce the number of unwanted candidates. Events with a clearly isolated B vertex are retained by requiring $\Delta\chi^2_{\text{isol}} > 4$. This quantity is computed by comparing the difference between the χ^2 of the vertex formed with the B daughters tracks only and that formed when adding also the most consistent track in the event. Partially reconstructed B decays where a charged track is missed, together with a fraction of the combinatorial background, are removed by this criteria. A further requirement on the separation of the B and K^0_S vertices in the z-direction is also applied, removing events where the long-lived particle is

Table 5.6: Stripping selection requirements for the Long-Long K^0_S line for both `Stripping17b` and `Stripping20` campaigns.

	Selection Requirement	
Variable Definition	`Stripping17b`	`Stripping20`
Combination cuts		
Transverse momentum of the B candidate	$p_T > 1000\,\text{MeV}/c$	
Sum of the daughters' transverse momenta	$\sum_{\text{daug}} p_T > 3000\,\text{MeV}/c$	
p_T of at least 2 B daughters	$p_T > 800\,\text{MeV}/c$	
Upper candidate mass limit	$m_{K^0_S h^+h^-} < 5866\,\text{MeV}/c^2$	$m_{K^0_S h^+h^-} < 6200\,\text{MeV}/c^2$
Lower candidate mass limit	$m_{K^0_S h^+h^-} > 4779\,\text{MeV}/c^2$	$m_{K^0_S h^+h^-} > 4000\,\text{MeV}/c^2$
IP wrt PV of highest p_T B daughter	IP $> 0.05\,\text{mm}$	
Maximum DOCA χ^2 of any 2 daughters	$\chi^2(\text{DOCA})_{\text{max}} < 5$	
Post-vertex fit criteria		
Transverse momentum of the B candidate	$p_T > 1500\,\text{MeV}/c$	
χ^2 of B vertex fit	$\chi^2_{B\,\text{vtx}} < 12$	
Cosine of B pointing angle	$\cos(\text{DIRA}_B) > 0.9999$	
Minimum B IP χ^2 wrt PVs	$\chi^2_{\text{IP}} < 8$	
Minimum vertex distance wrt PVs	$\lvert B_{\text{vtx}} - PV\rvert_{\text{min}} > 1\,\text{mm}$	
χ^2 separation of B vertex and associated PV	$\chi^2_{B-\text{PV VD}} > 50$	

reconstructed upstream of the B vertex. The chosen values are analysis dependent, and are discussed appropriately in the corresponding sections. Finally, candidate events having one or more tracks that are consistent with being a muon are rejected. This makes use of the binary `isMuon` criterion, evaluated by a threshold number of muon stations with hits in a given field of interest [151].

5.3.2 Datasets for the MVA training

The main multivariate method utilised in this analysis is based on a Boosted Decision Tree (BDT) [152] approach, with the AdaBoost algorithm [153]. Further details on this machine learning technique are given in Section 5.3.4. While simulated $B^0 \to K^0_S\pi^+\pi^-$ signal events produced under the same conditions as the data are used as the signal sample, the high sideband of the $K^0_S\pi^+\pi^-$ mass spectrum in data, $m \in [5425, 6000]\,\text{MeV}/c^2$, is utilised as a background sample. The left-hand sideband is removed in order to avoid potential contamination from partially reconstructed backgrounds. Additionally, contributions from b-baryon decays are removed from the data by explicitly vetoing the combinations of $pK^0_S\pi$ and pK^0_S consistent with the Λ^0_b and Λ^+_c masses, respectively. Since the topological properties of $K^0_S\pi^+\pi^-$ and the other signal modes are observed to be essentially the same, this training is used for all decay modes in the analysis. However, the optimal point at which to place a cut has to be determined separately for each spectrum since the level of combinatorial background varies.

Table 5.7: Stripping selection requirements for the Down-Down K^0_S line for both `Stripping17b` and `Stripping20` campaigns.

	Selection Requirement	
Variable Definition	`Stripping17b`	`Stripping20`
Combination cuts		
Transverse momentum of the B candidate	$p_T > 1000\,\text{MeV}/c$	
Sum of the daughters' transverse momenta	$\sum_{\text{daug}} p_T > 3000\,\text{MeV}/c$	$\sum_{\text{daug}} p_T > 4200\,\text{MeV}/c$
p_T of at least 2 B daughters	$p_T > 800\,\text{MeV}/c$	
Upper candidate mass limit	$m_{K^0_S h^+h^-} < 5866\,\text{MeV}/c^2$	$m_{K^0_S h^+h^-} < 6200\,\text{MeV}/c^2$
Lower candidate mass limit	$m_{K^0_S h^+h^-} > 4779\,\text{MeV}/c^2$	$m_{K^0_S h^+h^-} > 4000\,\text{MeV}/c^2$
IP wrt PV of highest p_T B daughter	IP $> 0.05\,\text{mm}$	
Maximum DOCA χ^2 of any 2 daughters	$\chi^2(\text{DOCA})_{\max} < 5$	
Pos-vertex fit criteria		
Transverse momentum of the B candidate	$p_T > 1500\,\text{MeV}/c$	
χ^2 of B vertex fit	$\chi^2_{B\,\text{vtx}} < 12$	
Cosine of B pointing angle	$\cos(\text{DIRA}_B) > 0.9999$	$\cos(\text{DIRA}_B) > 0.999$
Minimum B IP χ^2 wrt PVs	$\chi^2_{\text{IP}} < 8$	$\chi^2_{\text{IP}} < 6$
Minimum vertex distance wrt PVs	$\lvert B_{\text{vtx}} - PV\rvert_{\min} > 1\,\text{mm}$	$\lvert B_{\text{vtx}} - PV\rvert_{\min} > 1.7\,\text{mm}$
χ^2 separation of B vertex and associated PV	$\chi^2_{B-\text{PV VD}} > 50$	
Sum of the daughters' impact parameter χ^2	–	$\sum_{\text{daug}} \chi^2_{\text{IP}} > 50$

In order to increase the useful background sample statistics for the training of the MVA, without biasing the classification of the events, a set of two BDTs is constructed. The full training samples are arbitrarily separated into two equal datasets by using a reproducible pseudo-random number, lying in the range $[0, 1]$. This quantity is evaluated for each event as a function of the run and event number according to the algorithmic sequence given by $[(134 \times \text{eventNumber} + \text{runNumber})\%531241]/531241$. The sample of events with random number greater than 0.5 is used to train the first BDT (denoted in the following $\texttt{BDT}_1$) and the response is validated on the other half of the sample. The reciprocal procedure is used to train the second BDT (denoted $\texttt{BDT}_2$), yielding the very same statistics in the test and training samples. The use of two independent BDTs ensures that no bias is induced in the analysis.

5.3.3 Discriminating variables

In the process of pursuing improvements in performance, two sets of selections have been considered. These correspond to the criteria utilised in the branching ratio measurement and in the amplitude analysis, hereafter referred to as `SelBR` and `SelDP`, respectively. Notice that while the `SelBR` criteria are applied only to 2011 data, the `SelDP` requires the trigger operation subdivision.

To prevent the introduction of bias on the Dalitz plane, the discriminating

Table 5.8: List of variables used as inputs of the $K^0_S h^+ h^-$ BDT discriminant and corresponding importance ranking $[0, 1]$ for the 2011 condition, as obtained for Down-Down and Long-Long K^0_S. A similar hierarchical order is seen for the 2012a and 2012b settings.

	SelBR				SelDP			
	Rank DD		Rank LL		Rank DD		Rank LL	
Variable Definition	$\texttt{BDT}_1$	$\texttt{BDT}_2$	$\texttt{BDT}_1$	$\texttt{BDT}_2$	$\texttt{BDT}_1$	$\texttt{BDT}_2$	$\texttt{BDT}_1$	$\texttt{BDT}_2$
B flight distance significance w.r.t PV	0.173	0.174	0.239	0.240	0.151	0.156	0.096	0.106
Sum of the hadrons IP χ^2 w.r.t PV	0.168	0.164	0.230	0.230	0.159	0.160	0.175	0.190
B pointing angle (DIRA)	0.166	0.164	0.224	0.219	0.069	0.070	0.113	0.097
B pseudorapidity	0.154	0.151	0.171	0.181	0.140	0.138	0.120	0.116
B transverse momentum	0.147	0.146	0.171	0.166	0.051	0.049	0.075	0.049
B vertex fit χ^2	0.086	0.082	0.095	0.100	0.143	0.144	0.073	0.061
B IP significance w.r.t PV	0.069	0.064	0.026	0.034	0.051	0.055	0.051	0.054
B transverse momentum asymmetry	–	–	–	–	0.160	0.162	0.097	0.137
Isolation of the B vertex	–	–	–	–	0.074	0.070	0.082	0.074
K^0_S vertex fit χ^2	0.020	0.016	–	–	–	–	–	–
K^0_S IP significance w.r.t PV	–	–	0.192	0.188	–	–	–	–
K^0_S flight distance significance w.r.t PV	–	–	0.068	0.079	–	–	0.117	0.117

variables are chosen to be exclusively topological in nature, regarding the final state particles. The impact parameter of a b-hadron daughter is known to bias the DP of the decay through its correlation with the kinematic properties. It has therefore been chosen to consider instead the sum of the individual impact parameters of all daughters of the b hadron. In addition, B candidate vertex reconstruction properties, pointing estimators and lifetime-related observables are used. The p_T and η of the B meson complete the set of common B-related discriminating variables.

Additional discriminating variables related to the isolation of the B candidate vertex are considered in the SelDP scenario: the estimator of the difference of the quality of the vertex $\Delta\chi^2_{\text{isol}}$ (used likewise in the preselection); and the so-called p_T asymmetry. This is constructed according to

$$p_T^{\text{asym}} = \frac{p_T(B) - \sum_n p_T(n)}{p_T(B) + \sum_n p_T(n)}, \tag{5.2}$$

where $p_T(B)$ is the transverse momentum of the B candidate and the scalar sum is over the tracks contained in the cone with half-angle 1.5 units in the plane of pseudorapidity (dimensionless) and azimuthal angle (rad) around the B candidate flight direction, excluding those associated with the signal B candidate. Moreover, some of the variables related to the K^0_S properties are removed due to the marginal effect on the training response. Table 5.8 indicates the importance of these discriminants in the BDT decision process for 2011 conditions. Similar patterns are observed for the other configurations.

Compatibility of simulation with data

In order to verify the data and simulation consistency of the discriminating variables, the *s$\mathcal{P}$lot* technique [154] is used on the data with the b-hadron candidate invariant mass as the discriminating variable. A discussion about the implementation of this statistical tool to unfold the data into signal and background components is given in Section 5.4. The distributions of each of the considered variables for 2011 conditions are shown superimposed for both data and simulation in Figure 5.7. A Kolmogorov-Smirnov test [1] is computed for each comparison. A satisfactory agreement is observed for all variables in each sample except for the $p_{\mathrm{T}}^{\mathrm{asym}}$. Although this discrepancy results in a slightly sub-optimal performance of the BDT and affects the efficiency calculation, the noticeable improvement on the training response including this variable compensates for such effects.

In addition, combinatorial background candidates appear to be kinematically softer than the signal, making both the transverse momentum and pseudorapidity of the B candidate powerful discriminators. Notice that the range of some of the topological variables covers a few orders of magnitude; hence the logarithm of their value is used both in the optimisation and in the plotting of the variables.

Correlations between discriminants

Among the various interesting features of multivariate techniques, the possibility to exploit the strength of the correlations between variables is of great importance. While cut-based approaches ignore correlation effects, the full potential of the phase space is explored in the multivariate method. Figure 5.8 indicates the linear correlation coefficients between the discriminants for 2011 condition. Although there is a strong correlation between p_{T} and η, it has been seen that the inclusion of both discriminators provides a better performance for the method. Notice that linear correlations for a given variable do not represent all possible correlations that might exist. For instance, the non-linear correlations between topological variables (and to a lesser extent kinematic ones) justifies the use of the BDT technique. Likewise, the different observed correlations which exist for background and signal events again act to favour a selection based on a multivariate approach.

[1] The Kolmogorov-Smirnov nonparametric test evaluates the probability that the datasets are drawn from the same parent distribution.

5.3.4 BDT training process

The introduction of multivariate algorithms in particle physics experiments enables enhanced sensitivity to various observables. The usage of these is primarily related to the capability to provide classification from an apparent undistinguishable sample. In particular, a decision tree is an example of this class of algorithms, consisting of a non-parametric supervised learning method.

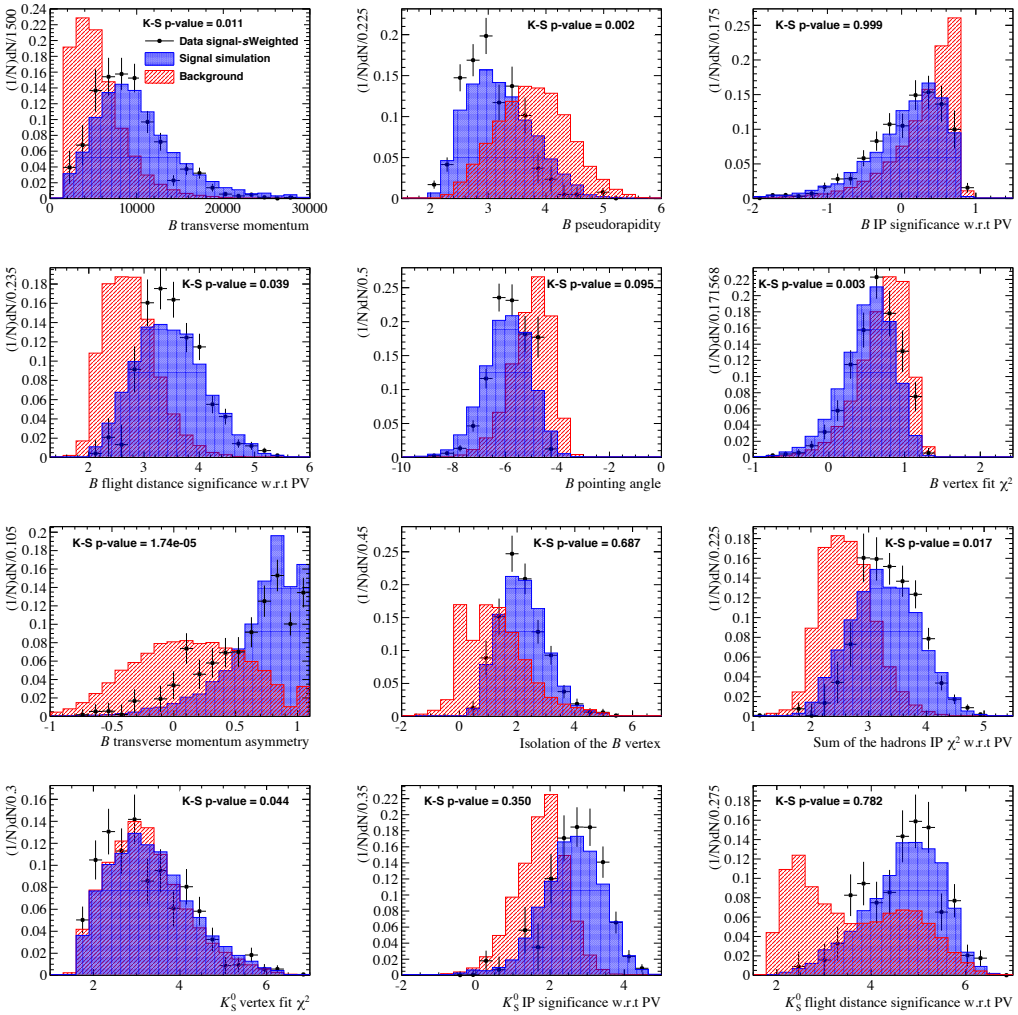

Figure 5.7: Distribution of the BDT training variables from 2011 simulated signal events (blue), background (red) and signal $s\mathcal{W}$eights (black). There is a relatively good agreement between signal like variables. Notice that the variables minimum B IP χ^2 wrt PVs, χ^2 separation of B vertex and associated PV, cosine of B pointing angle, χ^2 of B vertex fit, isolation of the B vertex, χ^2 separation of K^0_S vertex and associated PV, sum of the hadrons IP χ^2 w.r.t PV and K^0_S IP χ^2 wrt PVs are shown in log scale.

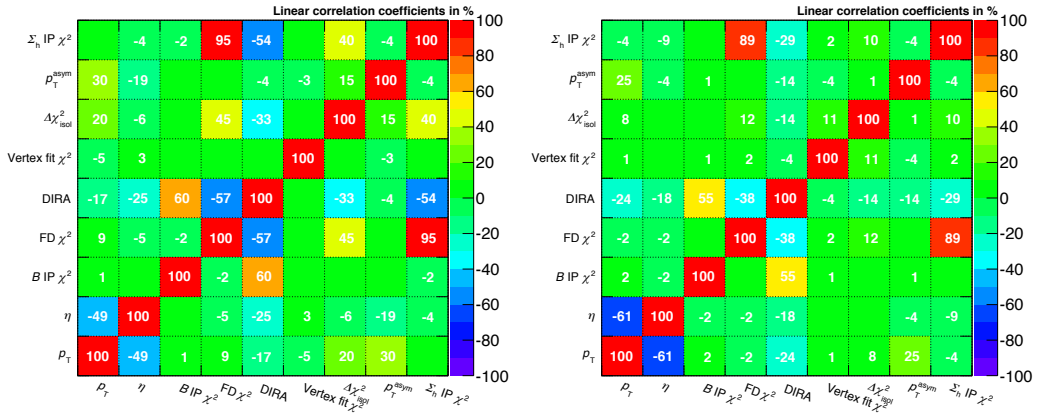

Figure 5.8: Correlations between training variables for (left) simulated $B^0 \to K^0_S \pi^+ \pi^-$ decays and (right) background from high mass sideband.

The concept of these classifiers is based on the construction of a prediction model for a target observable, obtained by a set of decision rules inferred from input information. Decision trees categorisations [155] are based on a branch-like segmentation, decided by the signal-like or background-like classification of the event. Each of these univariate tree tests is obtained by identifying the optimal separation value between signal and background from a given input variable. This process is repeated for all discriminants until a certain node has reached either a minimum number of events or a minimum/maximum signal purity. The response of the algorithm is obtained from the labelled signal/background leaves, containing weights associated to the corresponding signal purity fraction. Since this method is structured in layers of branches and leaves, the inspiration for the decision tree name is clear.

Although decision trees provide a popular learning technique with a simple implementation, the training is often unstable and small fluctuations in the dataset can produce significant changes in the response. An improvement in the robustness of the training is achieved using a boosting method – here represented by the AdaBoost algorithm [156]. Misclassified events, *i.e.* signal-like candidates that are associated to a background leaf or vice-versa, receive an increased weight (boosted) than the corrected identified node, and a new decision tree is formed. This boosting procedure is applied several times, typically $\mathcal{O}(10^3)$, combining all set of decision trees to obtain a more reliable classifier.

The discriminant response histograms for both `SelBR` and `SelDP` 2011 Down-Down conditions are displayed in Figure 5.9 for $\texttt{BDT}_1$ and $\texttt{BDT}_2$, respectively. Al-

though the details of the training of the BDTs in each run period are different, there is an overall similarity of the shapes. However, appreciable distinctions are observed between the K^0_S categories, resulting from the different variables used in the classification. Kolmogorov-Smirnov statistic tests have been computed in each case and did not indicate the presence of any overtraining. The distributions of $\texttt{BDT}_1$ and $\texttt{BDT}_2$ for training and testing are also compatible. In order not to bias the analysis towards one given training, the final selection variable, denoted BDT in the following, is arbitrarily taken as $\texttt{BDT}_1$ or $\texttt{BDT}_2$ for the events which were not used in the training procedure.

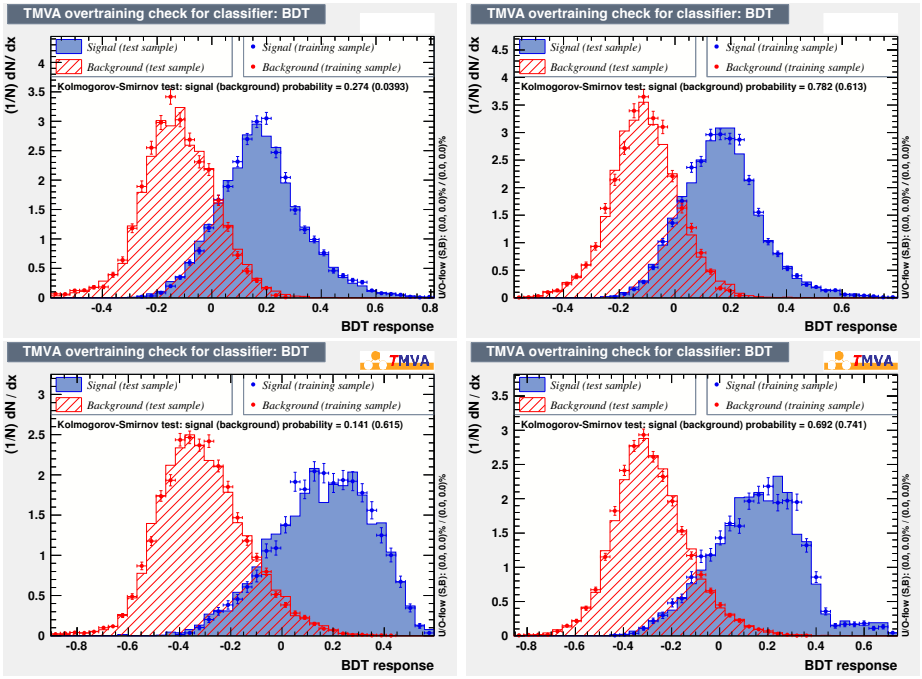

Figure 5.9: Training and validation samples response for the $\texttt{BDT}_1$ (left) and $\texttt{BDT}_2$ (right) discriminants separated between the (top) SelBR and (bottom) SelDP scenario, for the Down-Down K^0_S category. The histograms are normalised to the same number of entries.

5.3.5 PID methodology

The primary purpose of particle identification (PID) in LHCb is to distinguish between charged particle species that give otherwise identical final states. Although PID requirements are mainly intended to reduce such so-called cross-feed contributions, combinatorial backgrounds are also impacted. The particle identification routines introduced in Sec. 4.4.4 are hereafter referred to as $\Delta \log \mathcal{L}_{hh'}$ and $\texttt{ProbNN}_{h^{(\prime)}}$, where $h^{(\prime)}$ stands for the particle hypothesis under consideration. These correspond

to the differences in the likelihoods of the different mass categories and a Bayesian neural network-based probability approach, respectively. Notice that the `ProbNN` parameters range between 0 and 1 and can be treated as probabilities. Both classifiers are used extensively throughout this dissertation.

An important feature of particle identification is the observed disagreement between the distributions in simulation and the actual detector response. Therefore, it is essential to have a data-driven technique to measure the performance, particularly for the efficiency calculations. A common practice to achieve this in LHCb is with the `PIDCalibTool` package, which uses kinematic characteristics (*e.g.* momentum and transverse momentum) of a data calibration sample to re-weight the simulated distributions. This procedure can also take into account the correlations amongst the tracks, in the case of multibody decays. Furthermore, since pronounced non-trivial variations of the PID efficiency over the phase space are foreseen, this calibration method is performed as a function of the Dalitz-plot position. Details on this are given in Sec. 6.3.5.

5.3.6 Selection optimisation technique

The choice of the optimal cut on both `BDT` response and PID criteria can be driven by several figures-of-merit (FoM), each appropriate for a certain situation. For instance, the standard choice of the maximal significance of the signal (S) with respect to background (B) is given by

$$\texttt{FoM}_1 = \frac{S}{\sqrt{(S+B)}}\,, \tag{5.3}$$

and is suitable for a branching fraction measurement, where there is already a measurement or very reliable prediction, such that the value of S can be calculated given the efficiency of the selection criteria. Another important relation is defined by

$$\texttt{FoM}_2 = \frac{S^2}{(S+B)^{\frac{3}{2}}}\,, \tag{5.4}$$

and is referred to as the "significance $\times$ purity" figure-of-merit.

In the search for previously unobserved modes, an appropriate alternative figure-of-merit based on a frequentist ansatz [157] reads

$$\texttt{FoM}_{\mathrm{Punzi}} = \frac{\epsilon_{\mathrm{sig}}}{a/2 + \sqrt{B}}\,, \tag{5.5}$$

where the signal efficiency (ϵ_{sig}), which can be obtained by counting the simulated

events that pass the multivariate/particle identification selection, is used instead of the expected signal yield. The expected number of background events can be estimated from an exponential fit of the high mass sideband of the data [2] and extrapolating to obtain the number of combinatorial background in the signal region. The parameter a corresponds to the aimed-for significance (in units of Gaussian standard deviations σ), typically chosen to be 3 or 5.

Dalitz-plot FoM optimisation

The aforementioned FoM approaches are either based on the maximisation of the signal significance or sensitivity. However, it is unclear which FoM, if any, provides more sensitivity to the magnitudes and phases that are the observables of interest for the Dalitz-plot analysis.

In order to determine which response is more suitable to minimise the uncertainties in the foreseen amplitude analysis, a series of toy simulation studies have been performed [158]. The basic idea is to estimate the statistical and most significant systematic effects on the determination of the magnitude and phase of the isobar parameters introduced in Sec. 3.2.2. A simplified model has been implemented for $B_s^0 \to K_S^0 K^\pm \pi^\mp$ decays utilising the resonances $K^{*(\pm,0)}(892)$ and $K_0^{*(\pm,0)}(1430)$, parametrised by the relativistic BW and LASS lineshapes, respectively. All magnitudes are set to unity and the phases are set to zero. The coefficients are measured relative to the resonance contribution $K^{*\pm}(892)$, which is used as the reference amplitude. The expected yields and combinatorial background shape are obtained from the 2011 dataset with the `SelBR` selection, as discussed in Section 6. Finally, efficiency variations over the phase space are also considered using simulated samples. The generation and fit of the Dalitz-plot distributions are implemented through the `Laura++` framework [159]. Further details about this routine are given in Chapter 7.

This procedure is repeated for each MVA value, simultaneously for Down-Down and Long-Long K_S^0 categories, in order to determine the statistical uncertainties in each observable. In addition, two sources of systematic uncertainties are considered: the nominal combinatorial background model is replaced by the background distribution obtained with the *sPlot* technique; and the efficiency maps are varied within their uncertainties. The uncertainty on each isobar parameter is evaluated individually and summed in quadrature. Figure 5.10 shows the magnitude and phase uncertainties combined for all resonances. Notice that both parameters have reasonable agreement on the `SelBR` cut-value region that minimises the un-

[2] Only events satisfying $m_{K_S^0 hh'} > 5550\ (5530)\,\mathrm{MeV}/c^2$ are considered in order to avoid the Λ_b^0 veto region in the Down-Down (Long-Long) categories.

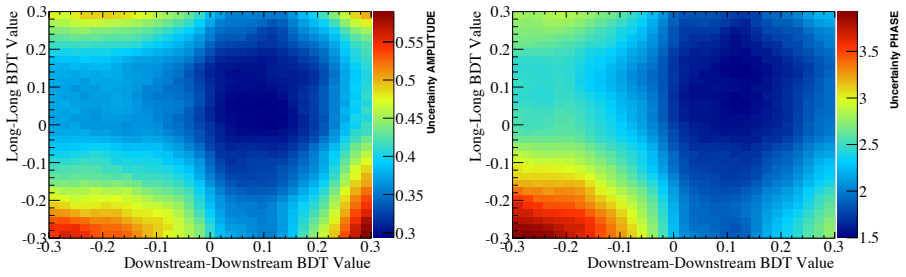

Figure 5.10: Combined uncertainties on the (left) magnitude and (right) phase isobar parameters for $B_s^0 \to K_S^0 K^{\pm}\pi^{\mp}$ as a function of the `SelBR` cut-value.

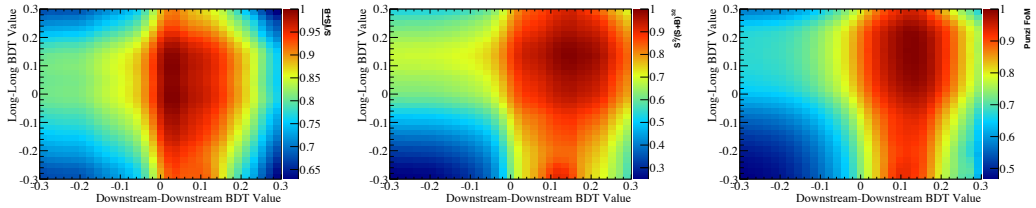

Figure 5.11: Figures-of-merit corresponding to (left) $\texttt{FoM}_1$, (centre) $\texttt{FoM}_2$ and $\texttt{FoM}_{\text{Punzi}}$ for the Toy simulated studies, as a function of the `SelBR` cut-value.

certainties of the measurement, however, slightly tighter cuts are clearly preferred to minimise the uncertainty on the phase parameter. This is a reflection of the large background contributions near the boundaries of the Dalitz plot that limits the determination of the interference pattern.

In order to evaluate which optimisation FoM responds more closely to these results, the aforementioned figures-of-merit are shown in Figure 5.11. These indicate that the $\texttt{FoM}_2$ is the most suitable approach for the amplitude analysis foreseen in this dissertation.

5.3.7 Multiple candidates

The fraction of selected events that contain more than one candidate is found to be typically less than $\mathcal{O}(10^{-3})$. The retained candidate is randomly chosen by applying an algorithmic, hence reproducible, sequence from the run number information. The candidate is selected which is identified by the integer part of the expression $N_{\text{cands}} \times |\sin n| + 0.999$, where N_{cands} is the number of candidates in the event and n the ranking of this event in the initial ntuple (before selection).

5.4 Fitting framework

Prior to the determination of the physical observables of interest, it is important to introduce the main concepts and methods employed in the estimation of parameters. In the remainder of this section these principles are examined. Further details can be found in Refs. [160, 161].

5.4.1 Maximum likelihood fitting

Assuming that the observables of interest are continuous variables (although similar principles hold for the discrete case), the notion of a Probability Density Function (PDF) is introduced as the normalised representation of its distribution. An estimator attempts to determine the unknown parameters of a PDF from some function of the data. In the event that multiple experiments are performed, an unbiased estimator of each measurement follows a distribution centred at the true parameter value. Suppose an experiment provides measurements of $x\colon\ x_1\,,\ldots\,,x_n$, then the probability of this observation as a function of the unknown parameter θ is the so-called likelihood function of the sample. If the x_i are independent observations, the most general formula for the likelihood is obtained as

$$\mathcal{L}(x;\theta) = \prod_{i=1}^{n} f(x_i;\theta)\,. \tag{5.6}$$

Notice that θ-values close to the nominal figures correspond to large likelihoods. The maximum likelihood (ML) estimator, $\hat{\theta}$, is therefore the parameter value for which the likelihood is maximised [162], *i.e.* any other value satisfies $\mathcal{L}(x;\theta) \leq \mathcal{L}(x;\hat{\theta})$. The determination of the ML is simplified if the function of θ is differentiable, which allows the maximum to be obtained from the roots of $\mathcal{L}'(\vec{x};\theta) = \partial\mathcal{L}(\vec{x};\theta)/\partial\theta = 0$. Alternatively, it is is common to use the logarithmic version as it satisfies

$$-\frac{\partial}{\partial\theta}\ln\mathcal{L} = -\frac{\partial}{\partial\theta}\sum_{i=1}^{n}\ln f(x_i;\theta) = 0\,. \tag{5.7}$$

Hereafter $-\ln\mathcal{L}$ is referred to as the negative log-likelihood (NLL).

Although in a single-species PDF the normalisation to unity can be imposed, in the case of multiple contributions the total number of events is usually regarded as a free parameter. This is associated by a Poisson distributed random variable

with mean value ν, modifying the formalism as

$$\mathcal{L}(\nu,\theta) = \frac{\nu^n}{n!}e^{-\nu}\prod_{i=1}^{n} f(x_i;\theta)\,. \tag{5.8}$$

This is known as an extended maximum likelihood (EML) and is extensively used in particle physics. Furthermore, the similarity between the various $K^0_S h^{\pm}h'^{\mp}$ final states investigated provides a number of possible constraints between the parameters to be incorporated in the fit. Improvement on the fitting robustness is naturally expected with a reduced set of parameters. In addition, penalty terms to the likelihood using external information provide another technique to make the fit more stable. These can be introduced as

$$-\frac{\partial}{\partial\theta}\sum_{i=1}^{n}\ln\mathcal{L} + \sum_j \frac{(\theta_j - \theta_j^{\text{const}})^2}{2\sigma_j^2} = 0\,, \tag{5.9}$$

hereafter referred to as Gaussian constraint. This is analogous to imposing a Gaussian *prior* on the parameter, which is often favoured in contrast to fixing it.

5.4.2 The *sPlot* method

The *sPlot* technique [154] is a likelihood-based background subtraction approach designed to resolve different fit components. Assuming that a set of unknown control variables x is uncorrelated to a discriminating variable y, the so-called *sWeights* for species n for each event e are given as

$${}_s\mathcal{P}_n(y_e) = \frac{\sum_{j=1}^{N_s}\mathbf{V}_{nj}f_j(y_e)}{\sum_{k=1}^{N_s}N_k f_k(y_e)}\,, \tag{5.10}$$

where $N_{(j,k)}$ are the component yields, $f_{(j,k)}$ are the PDFs and $\mathbf{V}_{nj}$ is the covariance matrix obtained from the fit of the species yields. The distributions of the control variables are deduced from

$$N_n\bar{M}_n(\bar{x})\delta x = \sum_{e\subset\delta x}{}_s\mathcal{P}_n(y_e)\,, \tag{5.11}$$

where the $\sum_{e\subset\delta x}$ is evaluated over $N_{\delta x}$ events, and each interval is centred on $\bar{x}$ and has width δx. Notice that $N_n\bar{M}_n(\bar{x})\delta x$ can be interpreted as the unfolded true x-distribution from histogramming ${}_s\mathcal{P}_n(y_e)$. Therefore, this is a valuable technique for unfolding signal/background structures.

5.5 Efficiency evaluation

The efficiency for multibody decays requires careful estimation. Since these decays are comprised of several quasi-two-body and nonresonant contributions, all of them possibly interfering, the population of events throughout the phase space is driven by its dynamical structure. *A priori* this distribution is unknown and must be determined from the data.

Generally the efficiency is not uniform across the Dalitz plane, and therefore, it is necessary to consider the non-trivial variations across the phase space. Note that for the amplitude analyses these features are naturally considered. The strategy implemented in this dissertation for branching fraction measurements consists of calculating the efficiencies in bins of the phase space $[\theta', m']$ and weighting these with data-driven $s\mathcal{W}$eights in order to correct for non-uniformities. The applicability of this procedure is ensured by verifying the absence of correlations between the Dalitz-plot position and the variables that enter the likelihood fit, *i.e.* the reconstructed mass of the b-hadron candidate. Figure 5.12 shows the mean and RMS of the $K^0_S h^\pm h'^\mp$ distribution for $B^0_s \to K^0_S K^\pm \pi^\mp$ signal simulated events as a function of the Dalitz plot. No significant trends are observed (neither in any companion mode), which indicates the suitability of the technique. The efficiency-corrected yield is then given by

$$N_{\text{sig.(corr.)}} = \sum \frac{w_i}{\varepsilon_i}\,, \tag{5.12}$$

where ε_i is the efficiency in the square Dalitz-plot bin containing the event i and w_i is the event-by-event signal $s\mathcal{W}$eight. Note that the average efficiency is therefore obtained from

$$\bar{\varepsilon} = \frac{N_{\text{sig.}}}{N_{\text{sig. (corr.)}}}\,, \tag{5.13}$$

where $N_{\text{sig.}} = \sum w_i$.

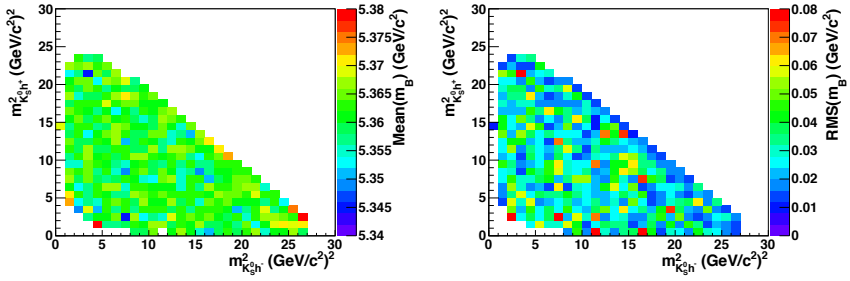

Figure 5.12: The mean (left) and RMS (right) of the reconstructed mass of the b-hadron candidate as a function of the Dalitz-plot position for $B^0_s \to K^0_S K^\pm \pi^\mp$ simulated events for the `SelBR` criteria.

6 Branching fractions

Searches for charmless three-body decays of either $B^0_{(s)}$ mesons or beauty baryons with a K^0_S meson in the final state have been performed using the pp collision data collected in 2011, corresponding to an integrated luminosity of 1.0 fb^{-1}. In this section the results of these studies, as reported in Refs. [108] and [163], are detailed.

6.1 General considerations

Similarities between the $K^0_S h^\pm h'^\mp$ final states allow several strategies to be shared among these analyses, including the dataset and selection. Moreover, generalities regarding the branching fraction extraction are discussed in the following.

6.1.1 Master formulae for the extraction

Measurements of branching fraction ratios are made for several $K^0_S h^\pm h'^\mp$ final states with respect to the normalisation channel $B^0 \to K^0_S \pi^+ \pi^-$. These are expressed as

$$\frac{\mathcal{B}\left(H^0_q \to K^0_S h^\pm h'^\mp\right)}{\mathcal{B}\left(B^0 \to K^0_S \pi^+ \pi^-\right)} = \frac{\epsilon^{\text{Sel.}}_{B^0 \to K^0_S \pi^+ \pi^-}}{\epsilon^{\text{Sel.}}_{H^0_q \to K^0_S h^\pm h'^\mp}} \times \frac{\epsilon^{\text{PID}}_{B^0 \to K^0_S \pi^+ \pi^-}}{\epsilon^{\text{PID}}_{H^0_q \to K^0_S h^\pm h'^\mp}} \times \frac{N_{H^0_q \to K^0_S h^\pm h'^\mp}}{N_{B^0 \to K^0_S \pi^+ \pi^-}} \times \frac{f_d}{f_q}\,, \quad (6.1)$$

where H^0_q stands for the b-hadron under consideration, the selection efficiency reads

$$\epsilon^{\text{Sel.}}_{H^0_q \to K^0_S h^\pm h'^\mp} = \epsilon^{\text{Gen.}}_{H^0_q \to K^0_S h^\pm h'^\mp} \times \epsilon^{\text{Reco\&Strip}}_{H^0_q \to K^0_S h^\pm h'^\mp} \times \epsilon^{\text{Trig.}}_{H^0_q \to K^0_S h^\pm h'^\mp} \times \epsilon^{\text{MVA}}_{H^0_q \to K^0_S h^\pm h'^\mp}\,,$$

where the upper index of the ϵ indicates the selection stage and $\epsilon^{\text{Sel.}}$ denotes the overall selection efficiency. N stands for the number of signal events observed in a given decay mode and $f_{(d,q)}$ is the probability for a b quark to fragment into the hadron under investigation.

The efficiency factorisation is useful to understand the different systematic effects that can affect the measurement. However, the final estimation of $\epsilon^{\text{Sel.}}$ is given by combining the intermediate steps into an overall efficiency. Indeed, as explained in Section 5.5, these are in general determined as a function of the phase-space position and averaged appropriately. Note that the PID efficiency is computed separately with a data-driven method to address the disagreements indicated in Sec. 5.3.5.

6.1.2 Signal significance evaluation

An important concept to be formalised in this context is the statistical framework to quantify the signal significance. The strategy is inspired by Wilks' theorem [164]

i. Perform mass fit scans fixing the signal yield to a wide range of values, including the nominal result and the null hypothesis. The statistical significance of each signal is computed as $\sqrt{2\ln(\mathcal{L}_{\text{sig}}/\mathcal{L}_0)}$, where $\mathcal{L}_{\text{sig}}$ and $\mathcal{L}_0$ are the likelihoods from the nominal fit and from the fit omitting the signal component, respectively;

ii. Plot $\ln(\mathcal{L}(N_j)/\mathcal{L}_{\text{sig}})$, where $\mathcal{L}(N_j)$ is the likelihood from the fit where the signal yield is fixed to a given value, N_j;

iii. Convert the negative log likelihood to the likelihood;

iv. Convolve the likelihood with a Gaussian of width equal to the total systematic uncertainty on the signal yield (*i.e.* the fit model systematic uncertainties);

v. Sum the Down-Down and Long-Long $-\Delta\ln\mathcal{L}$ values. This can then be interpreted as a χ^2 for two degrees of freedom and the corresponding p-value calculated. The significance is then defined as the square root of the χ^2 for one degree of freedom that gives the same p-value.

This procedure is used in any signal significance evaluation in this document, where the negative log-likelihood profile will also be given. A very similar approach is also used for upper limit setting, as discussed in the following.

6.1.3 Combining K^0_{S} branching ratio results

Since it is a general feature of these analyses to separate the two K^0_{S} candidate categories, it is important to define a clear strategy for combining these results. Notice that although the relative branching fractions in Eq. 6.1 are given in terms of final states containing K^0_{S} mesons, the final results are converted to be given in terms of final states containing K^0 or $\overline{K}^0$ mesons, following the convention of the PDG and HFAG.

The calculation of the relative branching fraction for each configuration is extracted by the master formula given in Eq. 6.1. The combined DD and LL central value is obtained by summing the log-likelihood scans for the two K^0_S categories, where each has been convoluted with a Gaussian in order to account for all sources of systematic uncertainties that are not correlated between these two types. The combined uncertainties on the measurement are determined using a variation of the Best Linear Unbiased Estimate (BLUE) method [165, 166]. From the branching ratio values obtained, the weights to be used in a linear combination of the input uncertainties are determined as

$$\begin{aligned} \bar{\mathcal{B}} &= \alpha\mathcal{B}_{\rm DD} + (1-\alpha)\mathcal{B}_{\rm LL} \\ \therefore\ \alpha &= \left(\bar{\mathcal{B}} - \mathcal{B}_{\rm LL}\right) / \left(\mathcal{B}_{\rm DD} - \mathcal{B}_{\rm LL}\right) . \end{aligned} \tag{6.2}$$

Each set of uncertainties is then combined using these α-values in the error propagation. Although most uncertainties are treated as uncorrelated, in the event of correlations between K^0_S types, a conservative fully correlated approach is preferred, in which these shared systematics are added after the convolution.

6.1.4 Upper limits

Any search for previously unobserved modes is susceptible to the absence of a significant signal, hereafter demarcated by a $3\,\sigma$ threshold. In order to place confidence limits on the branching fraction for each mode of interest, either Bayesian or frequentist approaches are utilised.

The negative log-likelihood profile routine can be adapted to set upper limits following a Bayesian-like procedure

i. Repeat all previous steps of the significance calculation indicated in Sec. 6.1.2, but convolute the likelihood considering all sources of systematic uncertainties that are not correlated between DD and LL. These scans are presented as functions of branching fraction values;

ii. Sum the Down-Down and Long-Long $-\Delta\ln\mathcal{L}$ scans;

iii. Convolute the combined likelihood considering the correlated systematics, which are considered to be fully correlated in this approach;

iv. Integrate the likelihood multiplied by a Bayesian prior that is uniform in the positive branching fraction region;

v. Find the value of the branching fraction such that the integral from 0 to this value corresponds to 90% or 95% of the integral from 0 to infinity, in other words, the credibility levels placed in these measurements.

An alternative methodology is provided by Feldman-Cousins (FC) confidence belts [167], which express the results in terms of an interval with a given confidence limit (CL). This approach is independent of any *prior* assumption of the result, and produces either two-sided bounds or an upper limit on the unknown of interest.

Assume $P(x;\mu)$ as the probability density function, similarly to Sec. 5.4, relating the observed quantity x (*i.e.* the observed yield) to the unknown parameter μ (*i.e.* relative branching fraction) on which it is desired to obtain the limit. Confidence levels are determined as

i. Evaluate the ratio of likelihoods $R = \dfrac{P(x;\mu)}{P(x;\mu_{\rm best})}$, where $\mu_{\rm best}$ is taken to be that corresponding to the measured value x when the yield is positive, otherwise it is set to zero.

ii. The probability $P(x;\mu)$ is defined by a Gaussian function, with a resolution given by the sum in quadrature of statistical and systematic uncertainties, obtained individually for the DD and LL categories.

iii. Acceptance regions are numerically constructed by adding x-values in decreasing order of R, until the integrated probability in the band exceeds the required confidence limit, for each value of μ.

iv. This procedure is repeated for a range of branching fraction values in order to construct upper and lower belts.

v. CL belts for the combined $K^0_{\rm S}$ categories are derived by the same ordering principle, as the product of likelihoods of the two reconstruction categories.

This strategy is independent of the observed likelihood function, which avoids the possibility of under-coverage of the measurement, where the negative log-likelihood is no longer parabolic for small event numbers.

6.2 Study of $B^0_{(s)} \to K^0_{\rm S} h^\pm h'^\mp$ decays

6.2.1 Introduction

Charmless $B^0_{(s)} \to K^0_{\rm S} h^\pm h'^\mp$ three-body decays, where $h^{(\prime)}$ stands for pions or kaons, can be used for a number of physics goals in addition to the ones introduced in Sec. 3.

The decay channels $B^0 \to K^0_S\pi^+\pi^-$ and $B^0 \to K^0_S K^+K^-$ allow for measurements of the weak phase (2β) in B^0-$\overline{B}^0$ mixing using $b \to q\bar{q}s$ transitions, which can be obtained by time-dependent analyses of the three-body Dalitz planes. The comparison of the weak phase extractions in $b \to q\bar{q}s$ and $b \to c\bar{c}s$ transitions are important probes for New Physics contributions in the $b \to s$ decay, under the assumption that the $b \to c\bar{c}s$ transition is dominated by Standard Model processes. Although the results from B-factories for $K^0_S\pi^+\pi^-$ [168, 169] and $K^0_S K^+K^-$ [170, 171] final states indicate fair agreement, the uncertainties are still large and further sensitivity can be obtained by studying these process at LHCb.

Another relevant mode is the previously unobserved $B^0_s \to K^0_S\pi^+\pi^-$ decay. The ratio of the amplitudes of the isospin-related mode $B^0_s \to K^-\pi^+\pi^0$ and its charge conjugate exhibits a direct dependence on the weak phase ($\beta_s + \gamma$). The particular interest in these modes lies in the absence of electroweak penguins, yielding a theoretically clean extraction [44] of γ provided that the strong phase between $B^0_s \to K^-\pi^+\pi^0$ and its charge conjugate can be fixed elsewhere. The shared intermediate states between $B^0_s \to K^-\pi^+\pi^0$ and $B^0_s \to K^0_S\pi^+\pi^-$ (explicitly $K^{*-}\pi^+$) offers that possibility, requiring an analysis of the $B^0_s \to K^0_S\pi^+\pi^-$ Dalitz plane.

The first step towards these physics searches is to establish the signals with the LHCb spectrometer and measure their branching fractions. Table 6.1 summarises the experimental knowledge of the branching fractions of the B^0 modes prior to this work. In particular, the decay modes $B^0_s \to K^0_S h^+h^-$ were all unobserved and the observation of $B^0 \to K^0_S K^\pm\pi^\mp$ by BaBar [172] had not been confirmed. This section reports the results of this exploratory study relative to the already precisely measured $B^0 \to K^0_S\pi^+\pi^-$ decay.

6.2.2 Selection optimisation

The main features of the selection have been introduced in Section 5. Nonetheless, it is important to revise the choice of the `SelBR` BDT response for each K^0_S category

Table 6.1: Experimental results for $K^0_S h^\pm h'^{(*)\mp}$ branching fractions [32] prior to this work.

	Branching fraction (10^{-6})		
Decay mode	BaBar	Belle	World average
$B^0 \to K^0\pi^+\pi^-$	50.2 ± 2.3	47.5 ± 4.4	49.6 ± 2.0
$B^0 \to K^0 K^\pm\pi^\mp$	6.4 ± 1.2	< 18	6.4 ± 1.2
$B^0 \to K^0 K^+K^-$	23.8 ± 2.6	28.3 ± 5.2	24.7 ± 2.3

and final state of interest. In order to obtain the best precision on the measured branching fraction, two optimisation strategies have been performed depending on whether the decay mode has been previously observed or not. This is achieved by using the figures-of-merit, defined in Sec. 5.3.6, $\texttt{FoM}_1$ and $\texttt{FoM}_{\text{Punzi}}$, hereafter referred to as `Loose` and `Tight` selections, respectively. Notice that both $B^0 \to K^0_S K^\pm \pi^\mp$ and $B^0_s \to K^0_S K^\pm \pi^\mp$ decays are classified as discovered modes, since preliminary studies at LHCb reported significant signals [173].

The $\texttt{FoM}_1$ is calculated from the expected background extrapolated from an exponential fit in the right side-band to the B^0 and B^0_s mass regions, while the expected signal is estimated using the known branching fractions and efficiencies. For the previously undiscovered channels the $\texttt{FoM}_{\text{Punzi}}$ is utilised with $a = 5$. Figures 6.1 and 6.2 show the corresponding optimisation distributions for $\texttt{FoM}_1$ and $\texttt{FoM}_{\text{Punzi}}$, respectively. The optimal BDT criteria and corresponding signal/background efficiencies are summarized in Table 6.2. For the normalisation $B^0 \to K^0_S \pi^+ \pi^-$ channel no dedicated optimisation is performed, instead the values chosen for $B^0_s \to K^0_S K^\pm \pi^\mp$ decays are used. Although aligned BDT cut-values for the normalisation with respect to the mode of interest could potentially reduce systematics effects, it has been observed that these are negligible due to the approximately flat Dalitz-plot acceptance resulting from the BDT selection.

Furthermore, particle identification criteria have been imposed to separate the various final states. A common requirement has been placed in each particle category (either pion or kaon) independently of the decay channel under consideration, as listed in Table 6.3. Since the performance of the PID calibration on high momentum tracks above 100 GeV is degraded, only hadrons with momentum below this threshold are considered. The charged pion tracks from the K^0_S decay and the tracks from the B meson are required to be inconsistent with muons (`isMuon` false) following the criteria imposed in the BDT training process.

6.2.3 Background

The structure of the backgrounds to charmless $B^0_{(s)} \to K^0_S h^\pm h'^\mp$ decays is rich. In order to simplify the classification of possible background sources, four main categories are identified

i. Fully reconstructed backgrounds are vetoed by removing candidates where the invariant mass of two of the final-state daughters corresponds either to an intermediate charm or misidentified charmonium state. The possible J/ψ, $\psi(2S)$, χ_c, D and Λ_c^+ intermediate states are reconstructed and excluded by vetoing

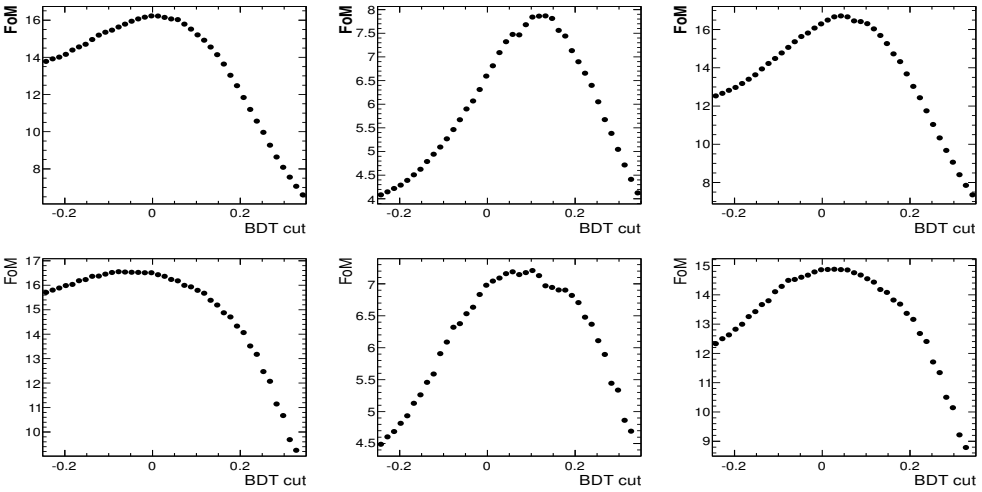

Figure 6.1: Figures-of-merit computed as $\texttt{FoM}_1$ for the observed modes (left) $B^0 \to K^0_S K^+ K^-$, (middle) $B^0 \to K^0_S K^\pm \pi^\mp$ and (right) $B^0_s \to K^0_S K^+ K^-$, separated in the (top) Down-Down and (bottom) Long-Long K^0_S categories.

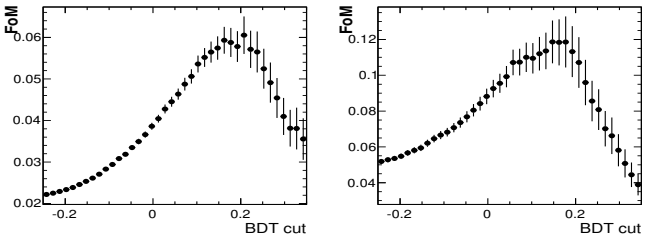

Figure 6.2: Figures-of-merit computed as $\texttt{FoM}_{\text{Punzi}}$ for the undiscovered modes (left) $B^0_s \to K^0_S \pi^+ \pi^-$ and (right) $B^0_s \to K^0_S K^+ K^-$, in the Down-Down K^0_S category.

their reconstructed mass using $|m_{\text{rec}} - m_{\text{PDG}}| < 48\,\text{MeV}/c^2$ and $|m_{\text{rec}} - m_{\text{PDG}}| < 30\ \text{MeV}/c^2$ for charmonia and D (or Λ_c^+) transitions, respectively. The complete list of vetoed contribution is

- $J/\psi \to \pi^+\pi^-$, $J/\psi \to \mu^+\mu^-$ and $J/\psi \to K^+K^-$;
- $\chi_{c0} \to \pi^+\pi^-$, $\chi_{c0} \to \mu^+\mu^-$ and $\chi_{c0} \to K^+K^-$;
- $D^0 \to K^-\pi^+$, $D^0 \to \pi^+\pi^-$, $D^0 \to K^+K^-$;
- $D^+ \to K^0_S K^+$, $D^+ \to K^0_S \pi^+$;
- $D^+_s \to K^0_S K^+$, $D^+_s \to K^0_S \pi^+$;
- $\Lambda_c^+ \to p K^0_S$.

ii. Partially-reconstructed backgrounds are from four-body final states in which the four momentum of the lost particle is relatively "soft". Note however that

Table 6.2: BDT discriminant optimal cut and efficiencies as determined from the training samples for the different $K^0_S h^\pm h^{(\prime)\mp}$ modes.

K^0_S category	Decay mode	BDT cut	ϵ Signal	ϵ Background
Down-Down	$B^0_s \to K^0_S \pi^+ \pi^-$	0.17	0.51	0.02
	$B^0_s \to K^0_S K^+ K^-$	0.14	0.59	0.02
	$B^0 \to K^0_S K^+ K^-$	-0.03	0.91	0.22
	$B^0 \to K^0_S K^\pm \pi^\mp$	0.10	0.70	0.05
	$B^0_s \to K^0_S K^\pm \pi^\mp$	0.03	0.83	0.11
Long-Long	$B^0_s \to K^0_S \pi^+ \pi^-$	0.14	0.79	0.01
	$B^0_s \to K^0_S K^+ K^-$	0.14	0.74	0.01
	$B^0 \to K^0_S K^+ K^-$	-0.06	0.96	0.13
	$B^0 \to K^0_S K^\pm \pi^\mp$	0.04	0.90	0.07
	$B^0_s \to K^0_S K^\pm \pi^\mp$	0.04	0.90	0.07

Table 6.3: PID criteria applied to each track originating from the B meson.

	Hypothesis disfavoured	
Track Category	Kaon/Pion	Proton
Pion	$\Delta \ln \mathcal{L}_{K\pi} < 0$	$\Delta \ln \mathcal{L}_{p\pi} < 10$
Kaon	$\Delta \ln \mathcal{L}_{K\pi} > 5$	$(\Delta \ln \mathcal{L}_{p\pi} - \Delta \ln \mathcal{L}_{K\pi}) < 10$

contributions from decays with missing charged particles are suppressed by the use of vertex isolation information in the selection. Since a series of individual backgrounds can contribute to the signal spectra, canonical representations of the nature of the particle which is not reconstructed are utilised in the mass fit model.

iii. Possible cross-feeds between the $B^0_{(s)} \to K^0_S h^\pm h^{\prime\mp}$ decays are a natural source of background in this exploratory search. None of the selected candidates can enter, by the definition of the particle identification criteria employed, in two distributions. Selected but misidentified decays, however, can appear in a companion spectrum.

iv. Unlike the previous contributions, combinatorial background are made out of random combinations of tracks that happen to fake a signal decay. The LL and DD categories are very different in this respect, the latter receiving a higher level of fake combinations. Although a large fraction of this is reduced by using the multivariate selection, it is expected to be the largest background under the potential signal peaks.

6.2.4 Fit model and results

An accurate description of the possible contributions to the mass spectrum is crucial for an unbiased branching fraction measurement. This section details the mass fitting framework as well as the corresponding data fit results.

Fitting machinery

Due to the plurality of possible $K^0_S h^\pm h^{(\prime)\mp}$ final state configurations and related backgrounds, a dedicated mass fit machinery has been designed. The fit contains a total of six mass spectra corresponding to the final states $K^0_S\pi^+\pi^-$, $K^0_S K^\pm\pi^\mp$ and $K^0_S K^+K^-$, and the DD and LL K^0_S categories. These are parametrised in the mass fit framework and the relevant yields are simultaneously determined from an extended unbinned fit. The probability density function in each spectrum is defined as the sum of several components (*i.e.* signal, backgrounds and signal cross-feeds). The fit has been commissioned by means of pseudo-experiments, which have indicated the constraints on the model parameters that are necessary to ensure the stability of the fit. During the analysis review process, the mass fit regions of the previously undiscovered modes were not inspected, but for simplicity only the unblinded results are discussed here.

Signal parametrisation

For each of the $B^0_{(s)} \to K^0_S h^\pm h^{\prime\mp}$ modes asymmetric tails that result from a combination of the effects of final state radiation and stochastic tracking imperfections are expected. The chosen model for the signal is the sum of two Crystal Ball (CB) functions [174], that share common values for the peak position and width, but have independent power law tails on opposite sides of the peak. Alternative models have also been studied, and this choice is found to provide the most accurate description for a given number of parameters.

The CB function is defined in terms of $t = m-\mu$, where m is the reconstructed mass and μ is the mean value of the Gaussian, as

$$CB(t) = \mathcal{N}\cdot\begin{cases} \exp(-t^2/2\sigma^2) & \text{if } t/\sigma > -\alpha \\ (\frac{n}{|\alpha|})^n \exp(-\alpha^2/2)(\frac{n-\alpha^2}{|\alpha|} - \frac{t}{\sigma})^{-n} & \text{if } t/\sigma \leq -\alpha, \end{cases} \tag{6.3}$$

where σ is the resolution of the Gaussian part of the function and $\mathcal{N}$ is the normalization of the function. The sign of the α parameter governs the right-handed or left-handed location of the tail and the parameter n drives the power law associated to the decrease of the tail.

The B^0 and B_s^0 peak positions are free in the fit to allow for tracking systematics. Four parameters related to the widths of the double-CB function are also not constrained in the fit: the common width of the $B^0 \to K_S^0\pi^+\pi^-$ and $B_s^0 \to K_S^0\pi^+\pi^-$ signals; the relative widths of $K_S^0K^\pm\pi^\mp$ and $K_S^0K^+K^-$ to $K_S^0\pi^+\pi^-$, which are the same for B^0 and B_s^0 decay modes; and the ratio of Long-Long over Down-Down widths, which is the same for all decay modes. These assumptions are made necessary by the otherwise poor determination of the width for the suppressed mode of each spectrum. The turnover point and power tail parameters are fixed in the data fit, which are obtained from simulation independently for each reconstruction mode but universal for B^0 and B_s^0 means, and the K_S^0 categories. In particular, the right-hand side parameters are shared between all modes due to the common nature of the effect. The fraction of the second CB is universal and is left free in the fit to the simulation but is fixed in the fit to data.

Signal cross-feed model

Any $B_{(s)}^0 \to K_S^0h^\pm h'^\mp$ decay can form a background in a companion spectrum through the misidentification of the final-state charged meson. These so-called signal cross-feeds must also be accounted for in the fit model and the yields appropriately parametrised. It has been found that these lineshapes are satisfactorily modelled by single CB functions. Most of the CB parameters are constrained to be the same for the B^0/B_s^0 mesons and K_S^0 categories in the fit to the simulation, apart from the mean values that are floated independently. All parameters obtained from the simulation are subsequently fixed in the fit to data.

Only contributions from the decays $B^0 \to K_S^0\pi^+\pi^-$ and $B^0 \to K_S^0K^+K^-$ reconstructed and selected as $K_S^0K^+\pi^-$, or the decays $B_s^0 \to K_S^0K^\pm\pi^\mp$ and $B^0 \to K_S^0K^\pm\pi^\mp$ reconstructed and selected as either $K_S^0K^+K^-$ or $K_S^0\pi^+\pi^-$ are considered. The yield of each misidentified decay is given in terms of the yield of the corresponding correctly identified decay multiplied by the relative selection efficiency. This is Gaussian constrained to the values obtained from the simulation. Note that the particle identification efficiencies and misidentified rates are again extracted using the `PIDCalib` method.

Partially-reconstructed backgrounds

In order to reduce the number of components in the fit, only four generic categories of partially reconstructed backgrounds are considered in each final state. Contributions from radiative decays (*e.g.* $B^0 \to \eta'(\rho^0\gamma)K_S^0$ decays) are studied separately and

included only in the $K^0_S\pi^+\pi^-$ final state. These backgrounds are not included in the $K^0_S K^+K^-$ and $K^0_S K^\pm\pi^\mp$ channels, since they are expected to contribute a negligible number of events. On the other hand, charmless and charmed B decays with a missing pion are parameterised in all cases.

These decays are modelled by means of a generalised ARGUS function [175] convolved with a Gaussian to address the experimental resolution, as

$$A(m; m_t, c, p) = \frac{2^{-p}c^{2(p+1)}}{\Gamma(p+1) - \Gamma(p+1, c^2/2)} \cdot \frac{m}{m_t^2}(1 - \frac{m^2}{m_t^2})^p \exp\left[-\frac{1}{2}c^2(1 - \frac{m^2}{m_t^2})\right], \quad (6.4)$$

where $\Gamma(n)$ stands for the Gamma function, $\Gamma(n, l)$ the upper incomplete Gamma function, m_t is a threshold mass value (cutoff), c governs the curvature and p controls the falling of the slope. The cutoff parameters of each contribution are fixed to the physical threshold of the partially-reconstructed nature, named the mass difference between the B meson and the missing particle. All remaining parameters are determined from the simulation and fixed in the data fit, except the width of the Gaussian function which is constrained to the signal mode resolution. The normalisation of all such contributions is Gaussian constrained using the ratio of efficiencies from the simulation and the ratio of branching fractions with respect to the signal. Relative uncertainties on these ratios of 100%, 20% and 10% are considered for charmless, charmed and radiative decays, respectively.

Combinatorial background

The combinatorial background is modelled by an exponential function, where the slope parameter is fitted for each of the two K^0_S reconstruction categories. Although initially three scale factors have been introduced to allow for different slopes in $K^0_S K^\pm\pi^\mp$ and $K^0_S K^+K^-$ with respect to $K^0_S\pi^+\pi^-$, these are taken to be unity in order to provide greater stability to the fit.

Data fit results

The results of the simultaneous fits to the `Loose` and `Tight` selections are shown respectively in Figs. 6.3 and 6.4, and a summary of the fitted yields of each mode is gathered in Table 6.4. Notice that there is overall good agreement between the fit model and the data in the whole mass range. An unambiguous first observation of $B^0_s \to K^0_S K^\pm\pi^\mp$ decays and a clear confirmation of the BaBar observation [172] of $B^0 \to K^0_S K^\pm\pi^\mp$ decays are obtained, where the latter has a statistical significance of $9.6\,\sigma$. Significant yields for the $B^0_s \to K^0_S\pi^+\pi^-$ decays are also observed, with the likelihood profiles shown in Fig. 6.5 for DD and LL K^0_S samples separately.

Table 6.4: Yields obtained from the simultaneous fit corresponding to the chosen optimisation of the selection for each mode, where the uncertainties are statistical only. The average total selection efficiencies are also given for each decay mode, where the uncertainties are due to the limited simulation sample size.

		Down-Down		Long-Long	
Mode	BDT	Yield	Efficiency (%)	Yield	Efficiency (%)
$B^0 \to K^0_S \pi^+ \pi^-$	`Loose`	845 ± 38	0.0336 ± 0.0010	360 ± 21	0.0117 ± 0.0009
$B^0 \to K^0_S K^+ K^-$	`Loose`	256 ± 20	0.0278 ± 0.0008	175 ± 15	0.0092 ± 0.0016
$B^0_s \to K^0_S K^\pm \pi^\mp$	`Loose`	283 ± 24	0.0316 ± 0.0007	152 ± 15	0.0103 ± 0.0008
$B^0 \to K^0_S K^\pm \pi^\mp$	`Tight`	92 ± 15	0.0283 ± 0.0009	52 ± 11	0.0133 ± 0.0005
$B^0_s \to K^0_S \pi^+ \pi^-$	`Tight`	28 ± 9	0.0153 ± 0.0013	25 ± 6	0.0109 ± 0.0006
$B^0_s \to K^0_S K^+ K^-$	`Tight`	6 ± 4	0.0150 ± 0.0021	3 ± 3	0.0076 ± 0.0016

The $B^0_s \to K^0_S \pi^+ \pi^-$ decays are observed with a combined statistical significance of $6.2\,\sigma$, which becomes $5.9\,\sigma$ including fit model systematic uncertainties. For the $B^0_s \to K^0_S K^+ K^-$ signal only hints are seen, with a statistical significance of $2.1\,\sigma$.

s$\mathcal{P}$lotting extraction

In order to evaluate the average efficiency as a function of the phase space, the *s*$\mathcal{P}$*lot* technique is used to recover the signal Dalitz-plot distribution. However, the constraints in the likelihood with Gaussian priors on both cross-feed and partially-reconstructed background yields are a scenario not foreseen or examined by the *s*$\mathcal{P}$*lot* authors. The correct implementation is recovered if these yield parameters are either freely varied or fixed. Although the latter is the favoured option, it assumes that the Dalitz-plot distribution of each background is known, which introduces large uncertainties in the efficiency determination.

To overcome this limitation, the fit framework is modified according to the following prescription. Partially-reconstructed decays are reduced to a negligible amount by cutting away events with invariant mass below 5.192 GeV. Cross-feeds are however non-reducible contributions, but their true phase-space distributions can be extracted from the *s*$\mathcal{W}$eights obtained independently in each corresponding spectrum. Multiple fixed known contributions can be included in the *s*$\mathcal{P}$*lot* approach, which preserves the main properties relevant for this work.

6.2.5 Efficiencies

The previously introduced strategy for a data-corrected efficiency determination consists of binning the simulated efficiency over the Dalitz plane and re-weighting according to the *s*$\mathcal{P}$lot and `PIDCalibTool` information. The calibration of the sim-

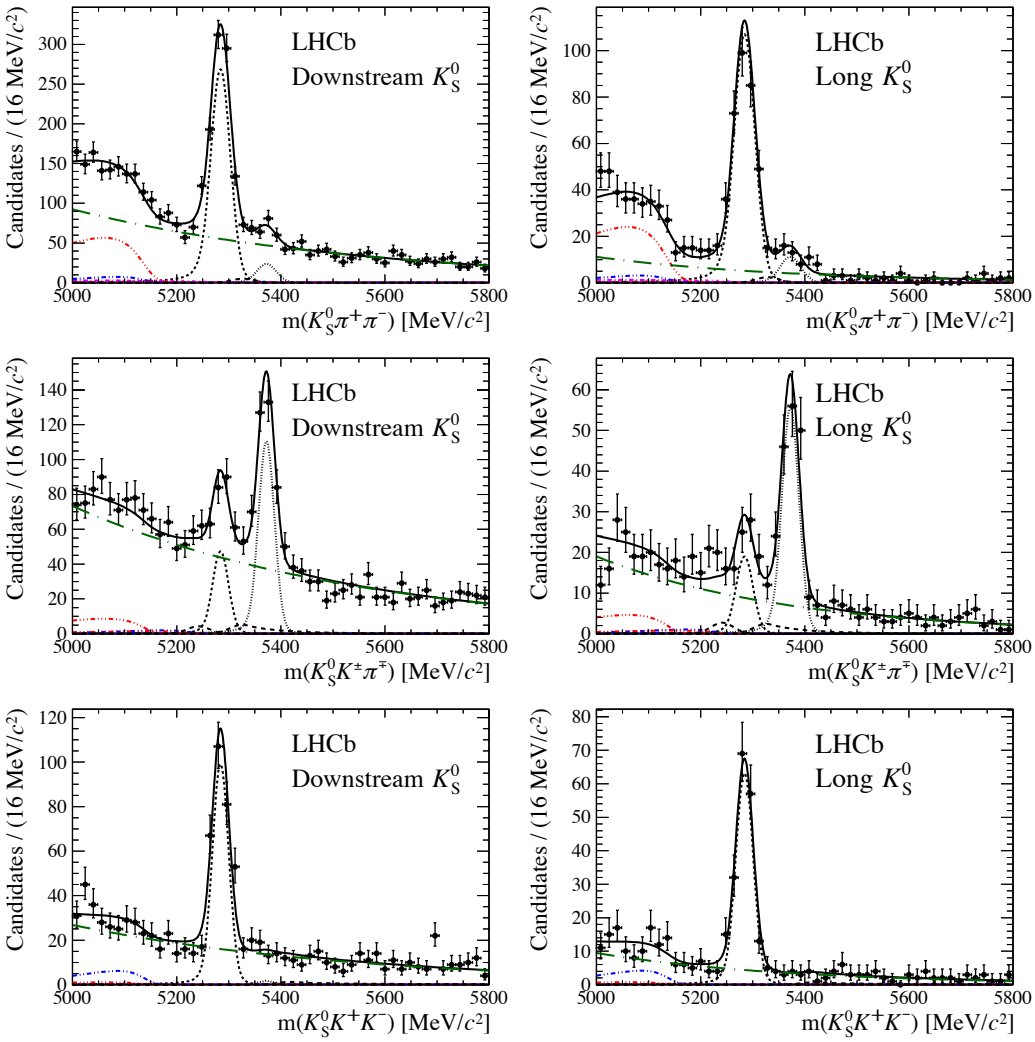

Figure 6.3: Invariant mass distributions for (top) $K^0_S\pi^+\pi^-$, (middle) $K^0_S K^\pm\pi^\mp$ and (bottom) $K^0_S K^+K^-$ candidates for the `Loose` selection, separated in the (left) Down-Down and (right) Long-Long K^0_S categories. Each component of the fit model is displayed: the B^0 (B^0_s) signal components are the black short-dashed (dotted) lines; misidentified decays are the black dashed lines; partially reconstructed contributions from B to open charm decays (red dash triple-dotted), charmless hadronic decays (blue dash double-dotted), $B^0 \to \eta' K^0_S$ (violet dash single-dotted) and charmless radiative decays (pink short-dash single-dotted lines); and combinatorial background (green long-dash dotted line).

ulated particle identification performance utilises high-purity data control samples, *e.g.* $D^* \to D^0(K^+\pi^-)\pi$ and $\Lambda \to p\pi^-$ decays, to tabulate two-dimensional efficiency histograms for the different track species as a function of momentum and $p_{\rm T}$. These histograms are constructed separately for the different charges, particle categories and magnet polarities. For each simulated signal event, the kinematics of each track

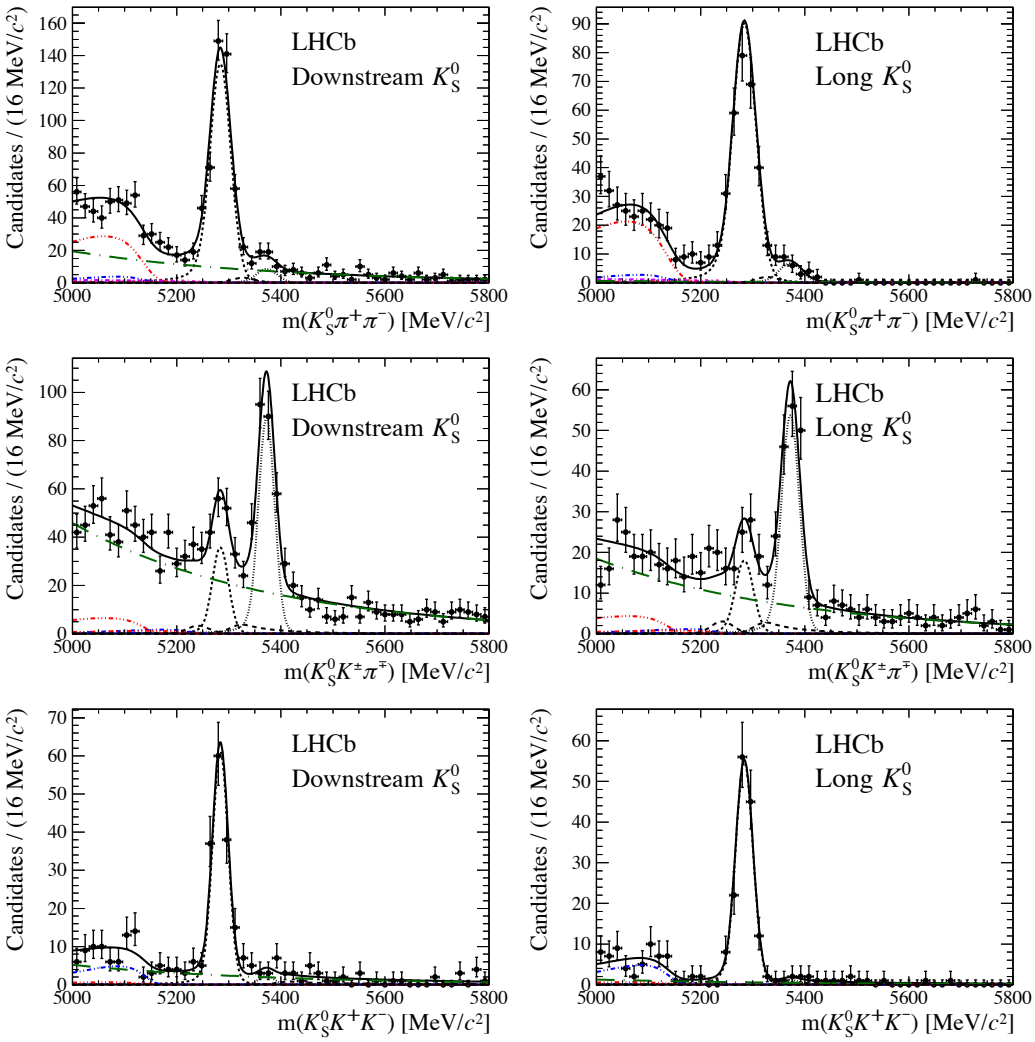

Figure 6.4: Invariant mass distributions for (top) $K^0_S\pi^+\pi^-$, (middle) $K^0_S K^\pm\pi^\mp$ and (bottom) $K^0_S K^+K^-$ candidates for the `Tight` selection, separated in the (left) Down-Down and (right) Long-Long K^0_S categories. Refer to Fig. 6.3 for components details.

is compared to the associated histogram to obtain the appropriate efficiency. These per-event values can then be used to form Dalitz-plot maps, which are added to the general weighting procedure.

The harmonic averaged total efficiency for each mode is given in Table 6.4. Notice that in general Long-Long candidates have a significantly lower efficiency with respect to the Down-Down configuration, resulting mainly from the geometry of the detector. Moreover, the efficiency-corrected Dalitz-plot distributions of the decay modes $B^0_s \to K^0_S\pi^+\pi^-$, $B^0_s \to K^0_S K^\pm\pi^\mp$, and $B^0 \to K^0_S K^\pm\pi^\mp$ are displayed in Figure 6.6. Some structure is evident at low $K^0_S\pi^\pm$ and $K^\pm\pi^\mp$ invariant masses

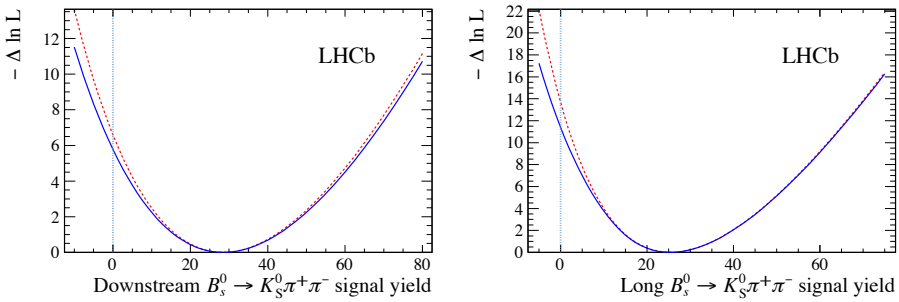

Figure 6.5: Likelihood profile of the $B_s^0 \to K_S^0\pi^+\pi^-$ signal yield for the (left) Down-Down and (right) Long-Long categories. The dashed red line is the statistical-only profile, while the solid blue line also includes the systematic uncertainties.

in the $B_s^0 \to K_S^0 K^\pm\pi^\mp$ decay mode, while in the $B^0 \to K_S^0 K^\pm\pi^\mp$ decay the largest structure is seen in the low $K_S^0 K^\pm$ invariant mass region. The non-trivial dynamics of $B_s^0 \to K_S^0 K^\pm\pi^\mp$ decays is further explored in the following chapter.

6.2.6 Systematics

The choice of the normalisation channel $B^0 \to K_S^0\pi^+\pi^-$ is designed to minimise or eliminate most of the possible systematic uncertainties in the branching fraction determination. The remaining sources of systematic effects and the methods used to estimate the corresponding uncertainties are described in this section. A summary of these contributions separated for each signal mode and K_S^0 type is given in Table 6.5.

Table 6.5: Systematic uncertainties on the ratio of branching fractions for Down-Down and Long-Long K_S^0 reconstruction. All uncertainties are relative and are quoted as percentages.

Down-Down	Fit	PID	Selection	Trigger	Total	f_s/f_d
$\mathcal{B}\left(B^0 \to K_S^0 K^\pm\pi^\mp\right) / \mathcal{B}\left(B^0 \to K_S^0\pi^+\pi^-\right)$	5	1	6	3	8	—
$\mathcal{B}\left(B^0 \to K_S^0 K^+K^-\right) / \mathcal{B}\left(B^0 \to K_S^0\pi^+\pi^-\right)$	1	1	5	3	6	—
$\mathcal{B}\left(B_s^0 \to K_S^0\pi^+\pi^-\right) / \mathcal{B}\left(B^0 \to K_S^0\pi^+\pi^-\right)$	8	1	16	2	18	8
$\mathcal{B}\left(B_s^0 \to K_S^0 K^\pm\pi^\mp\right) / \mathcal{B}\left(B^0 \to K_S^0\pi^+\pi^-\right)$	2	1	5	1	6	8
$\mathcal{B}\left(B_s^0 \to K_S^0 K^+K^-\right) / \mathcal{B}\left(B^0 \to K_S^0\pi^+\pi^-\right)$	1	1	18	3	18	8
Long-Long						
$\mathcal{B}\left(B^0 \to K_S^0 K^\pm\pi^\mp\right) / \mathcal{B}\left(B^0 \to K_S^0\pi^+\pi^-\right)$	5	1	10	1	11	—
$\mathcal{B}\left(B^0 \to K_S^0 K^+K^-\right) / \mathcal{B}\left(B^0 \to K_S^0\pi^+\pi^-\right)$	3	1	20	1	20	—
$\mathcal{B}\left(B_s^0 \to K_S^0\pi^+\pi^-\right) / \mathcal{B}\left(B^0 \to K_S^0\pi^+\pi^-\right)$	5	1	10	1	11	8
$\mathcal{B}\left(B_s^0 \to K_S^0 K^\pm\pi^\mp\right) / \mathcal{B}\left(B^0 \to K_S^0\pi^+\pi^-\right)$	3	1	12	2	13	8
$\mathcal{B}\left(B_s^0 \to K_S^0 K^+K^-\right) / \mathcal{B}\left(B^0 \to K_S^0\pi^+\pi^-\right)$	2	1	22	1	22	8

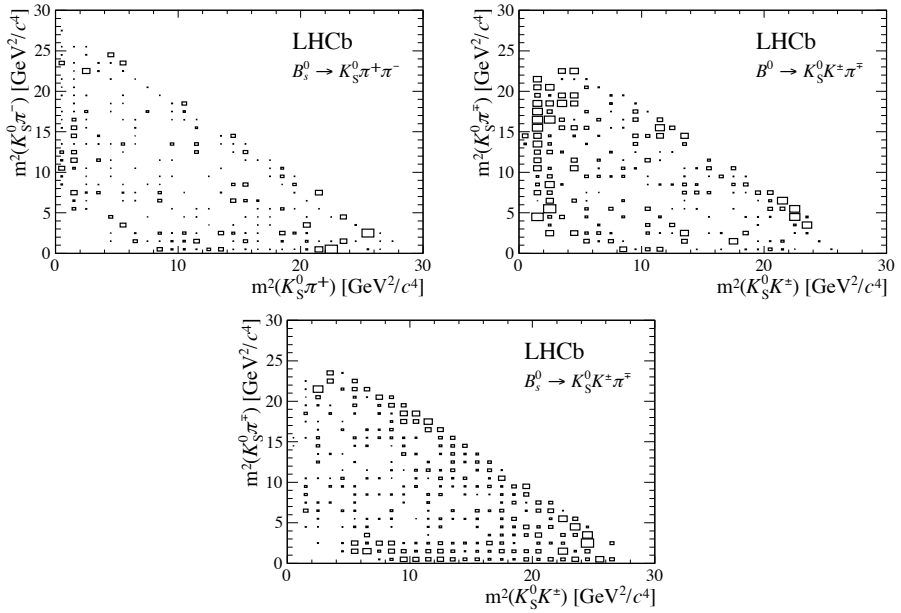

Figure 6.6: Efficiency-corrected Dalitz-plot distributions, produced using the $s\mathcal{P}$lot procedure for (top left) $B_s^0 \to K_S^0\pi^+\pi^-$, (top right) $B^0 \to K_S^0K^\pm\pi^\mp$ and (bottom) $B_s^0 \to K_S^0K^\pm\pi^\mp$ decays. Bins with negative content appear empty.

Fit model

The systematics related to the fit model reflect directly in the measured yields, and therefore, a detailed estimation is required. Two sources of uncertainties are considered: parameters constrained to the values determined from simulated events and the choice of the models used in the nominal fit. These are evaluated as following

i. A series of pseudo-experiments are generated from the nominal fit which are fitted by varying all of the fixed parameters according to their correlation matrix. The yields difference between the toy and baseline fits ensembles are then fitted with a Gaussian function. The systematic uncertainty is assigned as the linear sum of the absolute value of the corresponding mean and resolution.

ii. Datasets are generated according to an alternative model and the baseline fit is performed on these ensembles. Similarly to above, the sum of the resulting bias and resolution of the yields difference distribution gives the value of the uncertainty. The choice of the signal shape is examined by removing the right-tail of the mass distribution (*i.e.* replacing the shape with a single CB function). For the combinatorial background, the effect of floating independently the slopes for each spectrum and replacing the exponential by a linear model are evaluated.

It is worth mentioning that pseudo-experiments were also used to investigate possible biases induced by the fit machinery, however no significant biases were found. The total fit model systematic uncertainty is given by the sum in quadrature of all contributions. These are mostly dominated by the uncertainties on the combinatorial background. Note that the statistical uncertainties are obtained directly from the fit results without the use of pseudo-experiment ensembles.

PID efficiency calculation

The `PIDCalib` procedure used to evaluate the data-driven particle identification efficiencies utilises calibrated proxy modes that are kinematically different from the signal channels. While the binning routine attempts to mitigate these discrepancies, there could be some remaining systematic effects. To quantify any bias inherent to this approach, the calibration procedure is repeated with simulated samples of the control modes, such that the uncertainties are evaluated as

$$\Delta_{\text{sys,calib}} = \left| \frac{\epsilon_{\text{MC,sig}} - \epsilon_{\text{MC,cal}}}{\epsilon_{\text{MC,sig}} + \epsilon_{\text{MC,cal}}} \times \epsilon_{\text{data,cal}} \right| , \tag{6.5}$$

where $\epsilon_{\text{MC,sig}}$ stands for the efficiency extracted directly from simulation of the signal decay, $\epsilon_{\text{MC,cal}}$ is the efficiency determined from the simulated calibration sample and $\epsilon_{\text{data,cal}}$ is the efficiency determined from the data calibration sample calculated previously. These are found to be below the percent level and are assigned as systematic uncertainties. In addition, uncertainties due to the finite size of both calibration and simulated signal samples are considered. While the first is found to be negligible, the latter is evaluated using the bootstrap technique. Total systematic uncertainties are obtained by combining these errors in quadrature. Note that the uncertainties on the ratio of branching fractions due to the PID procedure are considered fully correlated.

Selection efficiency

Although branching fraction measurements are determined using relative efficiencies that are often well described by the simulation, some possible systematic effects mainly related to data/simulation discrepancies remain. In order to estimate these contributions a series of procedures have been performed as following

i. Uncertainties related to the finite size of the simulated signal samples are propagated as a systematic uncertainty.

ii. Effects related to the binning choice for the square Dalitz plot are estimated by repeating the efficiency extraction with binning schemes with different granularities, and extracting the average and RMS of these figures. Systematic uncertainties are assigned by combining in quadrature the relative statistical uncertainty and the RMS divided by the average. These are the dominant uncertainties on the statistically limited channels. It is worth mention that this can be affected by (negligible) double counting of the statistical errors.

iii. Disagreements between data and simulation at the hardware stage trigger are addressed with large calibration $D^{*+} \to D^0(\to K^-\pi^+)\pi_s^+$ data samples, which are examined for differences between pions and kaons, separated by positive and negative hadron charges, as a function of $p_{\rm T}$ [142]. Noticeable discrepancies are only observed at high $p_{\rm T}$, with a slightly higher efficiency for pions. Uncertainties are propagated by re-weighting the simulated samples by these data-driven calibration curves.

iv. The ageing of the calorimeters during the data taking period can induce changes in the absolute scale of the trigger efficiencies. While this was mostly mitigated by periodic recalibration, relative variations occurred of order 10%. Since the kinematics vary from one mode to the other, albeit only marginally, a systematic effect on the ratio of efficiencies arises. This is fully absorbed by increasing the trigger efficiency systematic uncertainty by 10%.

6.2.7 Results

The branching fraction for each mode is obtained from the signal yields and efficiencies gathered in Table 6.4 and the averaged f_s/f_d, here taken from hadronic and semileptonic measurements $f_s/f_d = 0.256 \pm 0.020$ [176].

$B_s^0 \to K_{\rm S}^0 K^\pm \pi^\mp$ results

The relative branching fractions for the two $K_{\rm S}^0$ categories are determined to be

$$\begin{aligned}
\frac{\mathcal{B}(B_s^0 \to K_{\rm S}^0 K^\pm \pi^\mp)}{\mathcal{B}(B^0 \to K_{\rm S}^0 \pi^+\pi^-)}_{\rm DD} &= 1.39 \pm 0.13\ (\text{stat.})\ \pm 0.08\ (\text{syst.})\ \pm 0.11\ (f_s/f_d)\,, \\
\frac{\mathcal{B}(B_s^0 \to K_{\rm S}^0 K^\pm \pi^\mp)}{\mathcal{B}(B^0 \to K_{\rm S}^0 \pi^+\pi^-)}_{\rm LL} &= 1.87 \pm 0.21\ (\text{stat.})\ \pm 0.23\ (\text{syst.})\ \pm 0.15\ (f_s/f_d)\,,
\end{aligned}$$

and their combination reads

$$\frac{\mathcal{B}(B_s^0 \to K_{\rm S}^0 K^\pm \pi^\mp)}{\mathcal{B}(B^0 \to K_{\rm S}^0 \pi^+\pi^-)} = 1.48 \pm 0.11\ (\text{stat.})\ \pm 0.08\ (\text{syst.})\ \pm 0.12\ (f_s/f_d)\,.$$

A satisfactory agreement is obtained for Down-Down and Long-Long categories, with a compatibility within two standard deviations.

$B^0 \to K^0_S K^\pm \pi^\mp$ results

The BaBar observation is confirmed with the relative branching fractions given by

$$\begin{aligned}
\frac{\mathcal{B}(B^0 \to K^0_S K^\pm \pi^\mp)}{\mathcal{B}(B^0 \to K^0_S \pi^+ \pi^-)}_{\rm DD} &= 0.129 \pm 0.022\ (\text{stat.}) \ \pm 0.011\ (\text{syst.})\,, \\
\frac{\mathcal{B}(B^0 \to K^0_S K^\pm \pi^\mp)}{\mathcal{B}(B^0 \to K^0_S \pi^+ \pi^-)}_{\rm LL} &= 0.127 \pm 0.028\ (\text{stat.}) \ \pm 0.014\ (\text{syst.})\,,
\end{aligned}$$

and their combination reads

$$\frac{\mathcal{B}(B^0 \to K^0_S K^\pm \pi^\mp)}{\mathcal{B}(B^0 \to K^0_S \pi^+ \pi^-)} = 0.128 \pm 0.017\ (\text{stat.}) \ \pm 0.009\ (\text{syst.})\,.$$

Note the good agreement with the BaBar relative measurement of 0.131 ± 0.025 [172].

$B^0_s \to K^0_S \pi^+ \pi^-$ results

The relative branching fractions for this previously unobserved state are given as

$$\begin{aligned}
\frac{\mathcal{B}(B^0_s \to K^0_S \pi^+ \pi^-)}{\mathcal{B}(B^0 \to K^0_S \pi^+ \pi^-)}_{\rm DD} &= 0.28 \pm 0.09\ (\text{stat.}) \ \pm 0.05\ (\text{syst.}) \ \pm 0.02\ (f_s/f_d)\,, \\
\frac{\mathcal{B}(B^0_s \to K^0_S \pi^+ \pi^-)}{\mathcal{B}(B^0 \to K^0_S \pi^+ \pi^-)}_{\rm LL} &= 0.29 \pm 0.07\ (\text{stat.}) \ \pm 0.03\ (\text{syst.}) \ \pm 0.02\ (f_s/f_d)\,,
\end{aligned}$$

and their combination reads

$$\frac{\mathcal{B}(B^0_s \to K^0_S \pi^+ \pi^-)}{\mathcal{B}(B^0 \to K^0_S \pi^+ \pi^-)} = 0.29 \pm 0.06\ (\text{stat.}) \ \pm 0.03\ (\text{syst.}) \ \pm 0.02\ (f_s/f_d)\,.$$

Consistent results are again obtained between the two K^0_S categories.

$B^0 \to K^0_S K^+ K^-$ results

The measurement for the well established $B^0 \to K^0_S K^+ K^-$ mode is obtained as

$$\begin{aligned}
\frac{\mathcal{B}(B^0 \to K^0_S K^+ K^-)}{\mathcal{B}(B^0 \to K^0_S \pi^+ \pi^-)}_{\rm DD} &= 0.366 \pm 0.033\ (\text{stat.}) \ \pm 0.023\ (\text{syst.})\,, \\
\frac{\mathcal{B}(B^0 \to K^0_S K^+ K^-)}{\mathcal{B}(B^0 \to K^0_S \pi^+ \pi^-)}_{\rm LL} &= 0.618 \pm 0.065\ (\text{stat.}) \ \pm 0.126\ (\text{syst.})\,,
\end{aligned}$$

consistent results are obtained between the two determinations and their combination reads

$$\frac{\mathcal{B}(B^0 \to K^0_S K^+ K^-)}{\mathcal{B}(B^0 \to K^0_S \pi^+ \pi^-)} = 0.385 \pm 0.030 \text{ (stat.)} \pm 0.025 \text{ (syst.)}\,.$$

This result is in agreement with the B-factories measurement of 0.506 ± 0.057.

$B^0_s \to K^0_S K^+ K^-$ results

Since a hint of a $B^0_s \to K^0_S K^+ K^-$ signal has been observed, the results are expressed in terms of limits on the branching fraction at 90 % CL, following the Feldman-Cousins approach. Figure 6.7 displays the confidence belts for Down-Down and Long-Long K^0_S categories, which numerically read

$$\begin{aligned} \frac{\mathcal{B}(B^0_s \to K^0_S K^+ K^-)}{\mathcal{B}(B^0 \to K^0_S \pi^+ \pi^-)}_{\text{DD}} &\in [0.002; 0.066] \text{ at } 90\% \text{ C.L.}\,, \\ \frac{\mathcal{B}(B^0_s \to K^0_S K^+ K^-)}{\mathcal{B}(B^0 \to K^0_S \pi^+ \pi^-)}_{\text{LL}} &< 0.13 \text{ at } 90\% \text{ C.L.} \end{aligned}$$

and therefore, a double-sided interval is obtained for the combination

$$\frac{\mathcal{B}(B^0_s \to K^0_S K^+ K^-)}{\mathcal{B}(B^0 \to K^0_S \pi^+ \pi^-)} \in [0.004; 0.068] \text{ at } 90\% \text{ C.L.}$$

Absolute branching fractions

Absolute branching fractions are calculated using the average value measured by the B-factory experiments $\mathcal{B}(B^0 \to K^0\pi^+\pi^-) = (4.96 \pm 0.20) \times 10^{-5}$ [28]. The measured time-integrated branching fractions for the modes of interest are

$$\begin{aligned} \mathcal{B}\left(B^0 \to {}^{(}\overline{K}{}^{)0} K^\pm \pi^\mp\right) &= (6.4 \pm 0.9 \pm 0.4 \pm 0.3) \times 10^{-6}\,, \\ \mathcal{B}\left(B^0 \to K^0 K^+ K^-\right) &= (19.1 \pm 1.5 \pm 1.1 \pm 0.8) \times 10^{-6}\,, \\ \mathcal{B}\left(B^0_s \to K^0 \pi^+ \pi^-\right) &= (14.3 \pm 2.8 \pm 1.8 \pm 0.6) \times 10^{-6}\,, \\ \mathcal{B}\left(B^0_s \to {}^{(}\overline{K}{}^{)0} K^\pm \pi^\mp\right) &= (73.6 \pm 5.7 \pm 6.9 \pm 3.0) \times 10^{-6}\,, \\ \mathcal{B}\left(B^0_s \to K^0 K^+ K^-\right) &\in [0.2; 3.4] \times 10^{-6} \text{ at } 90\% \text{ CL}\,, \end{aligned}$$

where the first uncertainty is statistical, the second systematic and the last due to the uncertainty on $\mathcal{B}(B^0 \to K^0\pi^+\pi^-)$. These observations are an important milestone towards more detailed studies of these transitions.

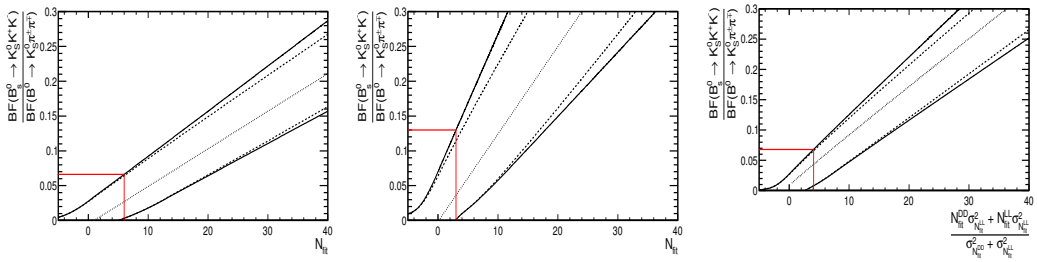

Figure 6.7: CL belts for (left) DD, (centre) LL and (right) combined K^0_S categories. The dashed line corresponds to the 90% CL belt with statistical uncertainty only, solid line the overall constraint including systematics and the red lines indicate the results of the fit. Note that not all systematic uncertainties are included in the individual K^0_S CL belts, since common sources are accounted for in the combination.

6.3 Searches for $\Lambda_b^0(\Xi_b^0) \to K^0_S p h^-$ decays

6.3.1 Introduction

The study of beauty baryon decays is still at an early stage. Among the possible ground states with spin-parity $J^P = \frac{1}{2}^+$ [28], no hadronic three-body charmless decays had been observed prior to this work. Even the charm intermediate states suffer from large uncertainties on their measurements. For the states other than the Λ_b^0, the knowledge is even more limited since fundamental properties, such as masses and widths, are poorly known. LHCb has excellent potential to improve the understanding of these b baryons.

One exciting motivation for b baryons is the search for CP asymmetries in the decays. In contrast to the neutral B meson decays, there is no mixing, and hence no CP violation from mixing, since it does not conserve baryon number. Therefore, all CP violation studies in baryonic modes search for CP violation in decay. Finally, it has been noted that hyperons produced in hadron-hadron collision could be polarized [177]. This feature represents a challenging issue for QCD, and can be further exploited in the studies of these decays.

In this section, the results of a search for Λ_b^0 and Ξ_b^0 baryon decays to final states containing a K^0_S meson, a proton and either a kaon or a pion (denoted $\Lambda_b^0(\Xi_b^0) \to K^0_S p h^-$ where $h = \pi, K$) are reported. No published theoretical prediction or experimental limit exists for their branching fractions. Intermediate states containing charmed hadrons are excluded from the signal sample and studied separately: the $\Lambda_b^0 \to \Lambda_c^+(pK^0_S)\pi^-$ decay is used as a control channel, while the $\Lambda_b^0 \to \Lambda_c^+(pK^0_S)K^-$ and $\Lambda_b^0 \to D_s^-(K^0_S K^-)p$ decays are also searched for. The $\Lambda_b^0 \to \Lambda_c^+(pK^-\pi^+)K^-$ decay has recently been observed [178], while the $\Lambda_b^0 \to D_s^- p$

decay has been suggested as a source of background to the $B_s^0 \to D_s^{\mp} K^{\pm}$ mode [179]. All branching fractions are measured relative to that of the well-known control channel $B^0 \to K^0 \pi^+ \pi^-$ [28], used likewise in Section 6.2.

6.3.2 Selection optimisation

Analogously to the companion non-baryonic state, this search is based on the `SelBR` selection and a similar dataset, defined in Section 5. The only difference is a looser preselection criteria: the separation between the K_S^0 and b hadron candidate vertices must be positive in the z direction; and the K_S^0 flight distance must be greater than 15 mm. Otherwise, the discussion in the previous sections is applicable to this case.

Since intermediate charmed states are also investigated, it is important to define the invariant mass regions that are chosen to ensure the veto/collection of these events. First, b hadron candidates are selected within the ranges $5469 < m(K_S^0 p h^-) < 5938\,\mathrm{MeV}/c^2$ and $4779 < m(K_S^0 \pi^+ \pi^-) < 5866\,\mathrm{MeV}/c^2$. Whilst $\Lambda_b^0 \to \Lambda_c^+ (p K_S^0) h^-$ candidates from the $\Lambda_b^0 \to K_S^0 p h^-$ superset are selected within $\pm 30\,\mathrm{MeV}/c^2$ of the nominal Λ_c^+ mass in the $m(K_S^0 p)$ region, *i.e.* $[2256, 2316]\,\mathrm{MeV}/c^2$, $\Lambda_b^0 \to D_s^- (K_S^0 K^-) p$ decays are collected by requiring $m(K_S^0 K) \in [1938, 1998]\,\mathrm{MeV}/c^2$.

The $\mathtt{FoM}_{\mathrm{Punzi}}$ ansatz for unobserved modes is again utilised to determine the optimal BDT cut value for each mode and K_S^0 category. The results of the optimisation are summarised in Table 6.6. An alternative optimisation approach, which minimises the expected upper limit on the branching fraction, is also investigated, hereafter referred to as $\mathtt{FoM}_{\mathrm{UL}}$. A series of background-only pseudo-experiments is generated in order to determine the expected statistical uncertainty on the signal yield, σ_{Sig}, for the null hypothesis. The $\mathtt{FoM}_{\mathrm{UL}}$ is defined as $\frac{1.64\,\sigma_{\mathrm{Sig.}}}{\epsilon_{\mathrm{Sel.}}}$, where the factor 1.64 is used to give an approximation of the 90 % CL upper limit on the signal yield. Although a fair agreement is found between the two figures-of-merit, $\mathtt{FoM}_{\mathrm{UL}}$ prefers slightly tighter criteria and it is used only as a cross-check of the chosen $\mathtt{FoM}_{\mathrm{Punzi}}$ value. The $\mathtt{FoM}_{\mathrm{Punzi}}$ optimisation for the intermediate charmed transitions has been also performed. For favoured $\Lambda_b^0 \to \Lambda_c^+ (p K_S^0) \pi^-$ decays the selection defined for $\Lambda_b^0 (\Xi_b^0) \to K_S^0 p \pi^-$ is used. The normalisation channel $B^0 \to K_S^0 \pi^+ \pi^-$ follows the same selection as the mode under consideration.

Remaining backgrounds are further suppressed using particle identification criteria. Baryon number conservation restricts the potential background sources after applying a stringent constraint on the proton identification. Nonetheless, the choice of the most appropriate PID requirements is still optimised using the $\mathtt{FoM}_{\mathrm{Punzi}}$, simultaneously for the two charged tracks. Notice that in order to avoid data/simulation disagreements in the efficiency estimation, the actual detector re-

Table 6.6: Figures-of-merit optimal cut values for the `SelBR` and particle identification discriminants determined for the different $K^0_S ph^-$ final states.

Decay mode	K^0_S type	`SelBR`		$\texttt{FoM}_{\text{Punzi}}$ PID	
		$\texttt{FoM}_{\text{Punzi}}$	$\texttt{FoM}_{\text{UL}}$	h_1	h_2
$\Lambda_b^0(\Xi_b^0) \to K^0_S p\pi^-$	DD	0.08	0.16	$\Delta\ln\mathcal{L}_{p\pi} > 12$	$\Delta\ln\mathcal{L}_{K\pi} < -1$
	LL	0.10	0.14	$\Delta\ln\mathcal{L}_{p\pi} > 12$	$\Delta\ln\mathcal{L}_{K\pi} < -1$
$\Lambda_b^0(\Xi_b^0) \to K^0_S pK^-$	DD	0.08	0.12	$\Delta\ln\mathcal{L}_{p\pi} > 5$	$\Delta\ln\mathcal{L}_{K\pi} > 8$
	LL	0.10	0.12	$\Delta\ln\mathcal{L}_{p\pi} > 5$	$\Delta\ln\mathcal{L}_{K\pi} > 8$
$\Lambda_b^0 \to \Lambda_c^+(pK^0_S)K^-$	DD	-0.02	–	$\Delta\ln\mathcal{L}_{p\pi} > -4$	$\Delta\ln\mathcal{L}_{K\pi} > 7$
	LL	-0.02	–	$\Delta\ln\mathcal{L}_{p\pi} > -4$	$\Delta\ln\mathcal{L}_{K\pi} > 7$
$\Lambda_b^0 \to D_s^-(K^0_S K^-)p$	DD	-0.10	–	$\Delta\ln\mathcal{L}_{p\pi} > 1$	$\Delta\ln\mathcal{L}_{K\pi} > 4$
	LL	-0.10	–	$\Delta\ln\mathcal{L}_{p\pi} > 1$	$\Delta\ln\mathcal{L}_{K\pi} > 4$

sponse is obtained again using the `PIDCalibTool`. The results for this optimisation are given in Table 6.6, where the anticipated preference for a tight requirement on the proton is seen. For $B^0 \to K^0_S\pi^+\pi^-$ decays no special optimisation has been made, and the criteria are identical to those from the $B^0_{(s)} \to K^0_S h^\pm h'^\mp$ analysis.

6.3.3 Background

There is limited prior knowledge of the branching fractions of b-baryon decays that may form backgrounds to the current search. Numerous modes are investigated with simulation in order to have a comprehensive representation of potential sources

i. Final states including charmonia and charmed states, *e.g.* $\Lambda_b^0 \to J/\psi ph^-$ and $\Lambda_b^0 \to D^0 ph^-$, respectively, are potential peaking backgrounds. However, no structure has been observed when examining the appropriate two-body mass region. These backgrounds are therefore not explicitly modelled.

ii. Mis-identified backgrounds from B mesons decays are found to be marginal due to the large separation between the $\Lambda_b^0(\Xi_b^0)$ and B masses and tight proton PID.

iii. Topologically similar decays such as the unobserved $\Lambda_b^0 \to \Lambda h^+h^-$ channel are investigated and no clear structure is seen.

iv. Similar baryonic final states such as $\Lambda_b^0 \to \Lambda_c^+(pK^-\pi^+)h^-$ decays, where the kaon is misidentified as a pion, and the πK pair can form a K^0_S candidate, are found to peak under the signal region. To suppress this background, candidates that have $pK^-\pi^+$ masses within $30\,\text{MeV}/c^2$ of the known Λ_c^+ mass are vetoed.

v. No significant structure has been observed that could be associated to partially-reconstructed backgrounds, *e.g.* $\Lambda_b^0 \to \Lambda_c^+(K^0_S p\pi^0)h^-$ and $\Lambda_b^0 \to \eta'(\rho\gamma)\Lambda$.

6.3.4 Fit model and results

Similarly to the $B^0_{(s)} \to K^0_S h^\pm h'^\mp$ searches, a dedicated fitting framework is designed to determine simultaneously all signal and background yields through an unbinned extended maximum likelihood fit to the b-hadron candidate invariant mass distributions. There are sixteen contributions of interest, corresponding to $\Lambda^0_b(\Xi^0_b) \to K^0_S p h^-$, $\Lambda^0_b \to \Lambda^+_c(pK^0_S)h^-$, $\Lambda^0_b \to D^-_s(K^0_S K^-)p$ and $B \to K^0_S \pi^+\pi^-$ decays, separated into the Down-Down and Long-Long K^0_S reconstruction categories. In the following, further details on the fitter architecture and data fit results are given.

Signal parametrisation

In contrast to the non-baryonic channels, the signal mass distributions are modelled by the sum of a core Gaussian and a bifurcated Gaussian function, that share the same mean value. Whilst the core resolution is allowed to be different for each K^0_S category, the two widths of the bifurcated Gaussian are common to DD and LL types. Alternative shapes such as double-CB are studied using simulation, and this choice is found to provide the most stable and accurate description for this search.

Since the regions of ± 50 MeV/c^2 (*cf.* the typical resolution of 15 MeV/c^2) around both the Λ^0_b and Ξ^0_b known masses were not examined until the selection criteria were finalised, the possibility of a signal observation could not be ensured. In order provide a more robust framework, the significant decay $\Lambda^0_b \to \Lambda^+_c(pK^0_S)\pi^-$ is utilised as a proxy mode, allowing a subset of fit parameters common to the unobserved b baryon decays to be determined from data. The core width and the relative fraction between the Gaussian and bifurcated Gaussian component are therefore expressed in terms of the parameters obtained from the fit to $\Lambda^0_b \to \Lambda^+_c(pK^0_S)\pi^-$ candidates, with deviations from those values allowed within ranges as seen in the simulation. The function used for each unobserved channel j and K^0_S type c is

$$\mathrm{PDF}(m;\mu,\sigma^c_{\mathrm{core}},\sigma_{\mathrm{R}},\sigma_{\mathrm{L}}) = s^{c,j}_f f^c G(m;\mu,s^{c,j}_\sigma\sigma^c_{\mathrm{core}}) + (1 - s^{c,j}_f f^c)B(m;\mu,\sigma_{\mathrm{L}},\sigma_{\mathrm{R}})\,, \quad (6.6)$$

where m is the invariant mass of the b hadron candidate and G and B represent the Gaussian and bifurcated Gaussian distributions respectively. The parameters σ_{L} and σ_{R} are respectively the left and right widths of the bifurcated Gaussian function, σ^c_{core} and f^c are the width and the fraction of the core Gaussian for $\Lambda^0_b \to \Lambda^+_c(pK^0_S)\pi^-$ candidates, while $s^{c,j}_\sigma$ and $s^{c,j}_f$ are the corresponding scale factors for the channel j, determined from simulation. The peak position μ for Λ^0_b decays is shared among all modes, while that for Ξ^0_b decays is fixed to the measured Λ^0_b and Ξ^0_b mass difference, $m_{\Xi^0_b} - m_{\Lambda^0_b} = 168.6 \pm 5.0\,\mathrm{MeV}/c^2$ [28]. The scale factors for Λ^0_b and Ξ^0_b signal shapes

are allowed to differ but are found to be consistent.

Signal cross-feeds

The most appropriate lineshape for signal cross-feeds is found to be a double Crystal Ball function, defined previously, except here the means and widths of the two functions are allowed to differ. In this approach, all possible decays of Λ_b^0 and Ξ_b^0 baryons with misidentification of a final-state charged meson are modelled. Each cross-feed yield is Gaussian constrained to be equal to the number of signal candidates in its corresponding true spectrum, multiplied by the relevant misidentification efficiency.

Combinatorial background

An exponential shape is used to describe the combinatorial background, which is treated as independent for each decay mode and K_S^0 type. Note that this is contrary to the $K_S^0 h^\pm h'^\mp$ case where a single slope was required to ensure the fit stability.

Normalisation channel

The modelling of the signal and background contributions for the normalisation channel $B^0 \to K_S^0 \pi^+ \pi^-$ is identical to the description discussed in Sec. 6.2.4 for the $B^0_{(s)} \to K_S^0 h^\pm h'^\mp$ analysis.

Data fit results

The results of the fit to data are shown in Figures 6.8 and 6.9 for $\Lambda_b^0(\Xi_b^0) \to K_S^0 p h^-$ and charmed $\Lambda_b^0 \to \Lambda_c^+(pK_S^0)h^-$ and $\Lambda_b^0 \to D_s^-(K_S^0 K^-)p$ candidates, respectively. Due to similarities to the results reported in Sec. 6.2.4, the mass fits for the normalisation channel $B^0 \to K_S^0 \pi^+ \pi^-$ are omitted. The fitted yields are gathered in Table 6.7. The total combined significance is found to be $8.6\,\sigma$ for $\Lambda_b^0 \to K_S^0 p \pi^-$ decays, as indicated in the negative log-likelihood profiles shown in Fig. 6.10. This corresponds to the first observation of a charmless hadronic three-body decay of a b baryon. Moreover, the statistical significance for the $\Lambda_b^0 \to \Lambda_c^+(pK_S^0)K^-$ decay is found to be respectively $9.4\,\sigma$ and $8.0\,\sigma$ for Down-Down and Long-Long categories, confirming the recent observation of this channel [178]. Whilst the significance for $\Lambda_b^0 \to K_S^0 p K^-$ is $2.1\,\sigma$, all other channels are below $2\,\sigma$.

In order to obtain $s\mathcal{W}$eights for the phase-space efficiency corrections, similar modifications to those used in the $B^0_{(s)} \to K_S^0 h^\pm h'^\mp$ measurements are required to ensure the applicability of the *s*$\mathcal{P}$*lot* method. In this approach, cross-feeds from $\Lambda_b^0 \to K_S^0 p K^-$ decays and the companion Ξ_b^0 modes are neglected for the extraction

Table 6.7: Fitted yields and efficiency for each channel, separated by K^0_S type. Yields are given with both statistical and systematic uncertainties, whereas for the efficiencies only the uncertainties due to the limited simulated sample sizes are given. The three rows for the $B^0 \to K^0_S\pi^+\pi^-$ decay correspond to the different BDT selections for charmless signal modes and the channels containing Λ_c^+ or D_s^- hadrons.

Mode	Down-Down		Long-Long	
	Yield	Efficiency ($\times 10^{-4}$)	Yield	Efficiency ($\times 10^{-4}$)
$\Lambda_b^0 \to K^0_S p\pi^-$	$106.1 \pm 21.5 \pm 3.7$	5.40 ± 0.12	$90.9 \pm 14.6 \pm 1.0$	2.26 ± 0.06
$\Lambda_b^0 \to K^0_S pK^-$	$11.5 \pm 10.7 \pm 1.2$	5.34 ± 0.11	$19.6 \pm 8.5 \pm 0.8$	2.87 ± 0.07
$\Xi_b^0 \to K^0_S p\pi^-$	$5.3 \pm 15.7 \pm 0.7$	5.35 ± 0.10	$6.4 \pm 8.5 \pm 0.5$	2.67 ± 0.07
$\Xi_b^0 \to K^0_S pK^-$	$10.5 \pm 8.8 \pm 0.5$	6.12 ± 0.10	$6.3 \pm 5.6 \pm 0.4$	2.91 ± 0.07
$\Lambda_b^0 \to \Lambda_c^+(pK^0_S)\pi^-$	$1391.6 \pm 39.6 \pm 24.8$	4.85 ± 0.09	$536.8 \pm 24.6 \pm 3.5$	1.71 ± 0.05
$\Lambda_b^0 \to \Lambda_c^+(pK^0_S)K^-$	$70.0 \pm 10.3 \pm 3.3$	4.69 ± 0.07	$37.4 \pm 7.1 \pm 2.7$	1.66 ± 0.03
$\Lambda_b^0 \to D_s^- p$	$6.3 \pm 5.1 \pm 0.6$	2.69 ± 0.05	$6.5 \pm 3.7 \pm 0.2$	0.89 ± 0.03
$B^0 \to K^0_S\pi^+\pi^-$ ($K^0_S ph$)	$913.5 \pm 45.0 \pm 12.2$	5.57 ± 0.09	$495.7 \pm 31.8 \pm 7.5$	2.86 ± 0.06
$B^0 \to K^0_S\pi^+\pi^-$ ($\Lambda_c^+ h$)	$1163.8 \pm 60.7 \pm 18.8$	7.38 ± 0.11	$589.0 \pm 33.3 \pm 17.3$	3.27 ± 0.06
$B^0 \to K^0_S\pi^+\pi^-$ ($D_s^- p$)	$1317.8 \pm 77.1 \pm 25.7$	7.76 ± 0.11	$614.1 \pm 38.3 \pm 14.8$	3.47 ± 0.07

of the $\Lambda_b^0 \to K^0_S p\pi^-$ signal. Note that this procedure is only available for the observed charmless decays. An alternative for undiscovered channels is discussed in the following section.

6.3.5 Efficiencies

Although b-baryon decays introduce further complexity to the phase space compared to the B^0 meson case, where the two-dimensional Dalitz plane covers all degrees of freedom, due to the presence of initial and final states with spin, the conventional phase space can still be used if spin effects are neglected.[1] In addition to the harmonic average data-driven method discussed in Sec. 5.5, it is necessary to consider two alternative scenarios. In the absence of a significant b-hadron signal, it is not possible to determine the true phase-space distribution of the signal events. Instead, the efficiency corresponding to a uniform distribution across the square Dalitz plot is used as the nominal value, and an uncertainty is assigned due to the variation across the phase space. Note that variations of the efficiency over the phase space are quite pronounced, and this results in a correspondingly large systematic uncertainty. Another relevant distinction is related to the intermediate charmed states. Since these populate narrow bands in the Dalitz plot, it is not relevant to consider variations within the phase space. Instead, the efficiency for that particular two-body decay is used. The efficiencies extracted for all modes are reported in Table 6.7.

The Dalitz plot distribution for $\Lambda_b^0 \to K^0_S p\pi^-$ decays is shown in Fig. 6.11,

[1] Note that Λ_b^0 baryons produced in pp collisions at $\sqrt{s} = 7\,\text{TeV}$ have been measured to have only a small degree of polarisation [180].

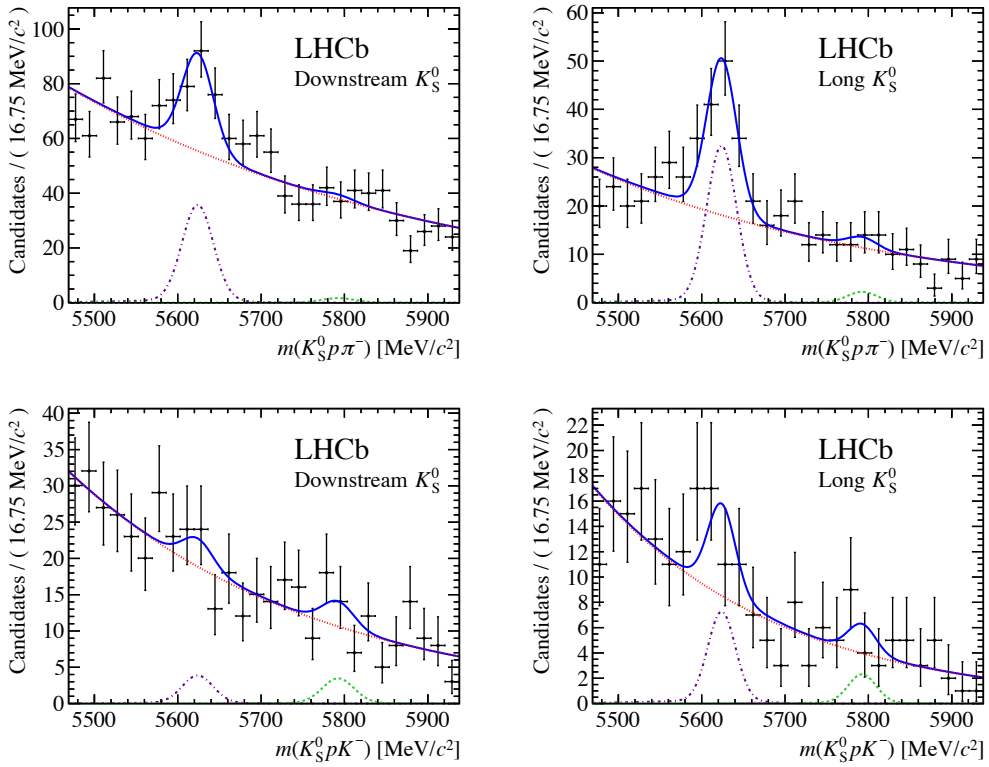

Figure 6.8: Invariant mass distribution of (top) $K^0_S p\pi^-$ and (bottom) $K^0_S pK^-$ candidates for the (left) Down-Down and (right) Long-Long K^0_S categories. Components of the fit model are displayed: Λ^0_b signal (violet dot-dashed), Ξ^0_b signal (green dashed) and combinatorial background (red dotted). The overall fit is given by the solid blue line. Contributions with very small yields are not shown.

which is obtained using the $s\mathcal{P}$lot technique and applying event-by-event efficiency corrections based on the position of the decay in the square Dalitz plot. A structure at low $p\pi^-$ invariant mass, which may originate from excited nucleon states, is apparent but there are no clear structures in the other two invariant masses.

6.3.6 Systematics

Analogously to the $K^0_S h^\pm h'^\mp$ case, most of the systematics uncertainties on the branching fraction are conveniently minimised by utilising $B^0 \to K^0_S \pi^+\pi^-$ as a normalisation channel. Nonetheless, some additional considerations are necessary in order to address the different b-hadron species examined in the ratio. Table 6.8 summarises these contributions individually, as discussed in the following.

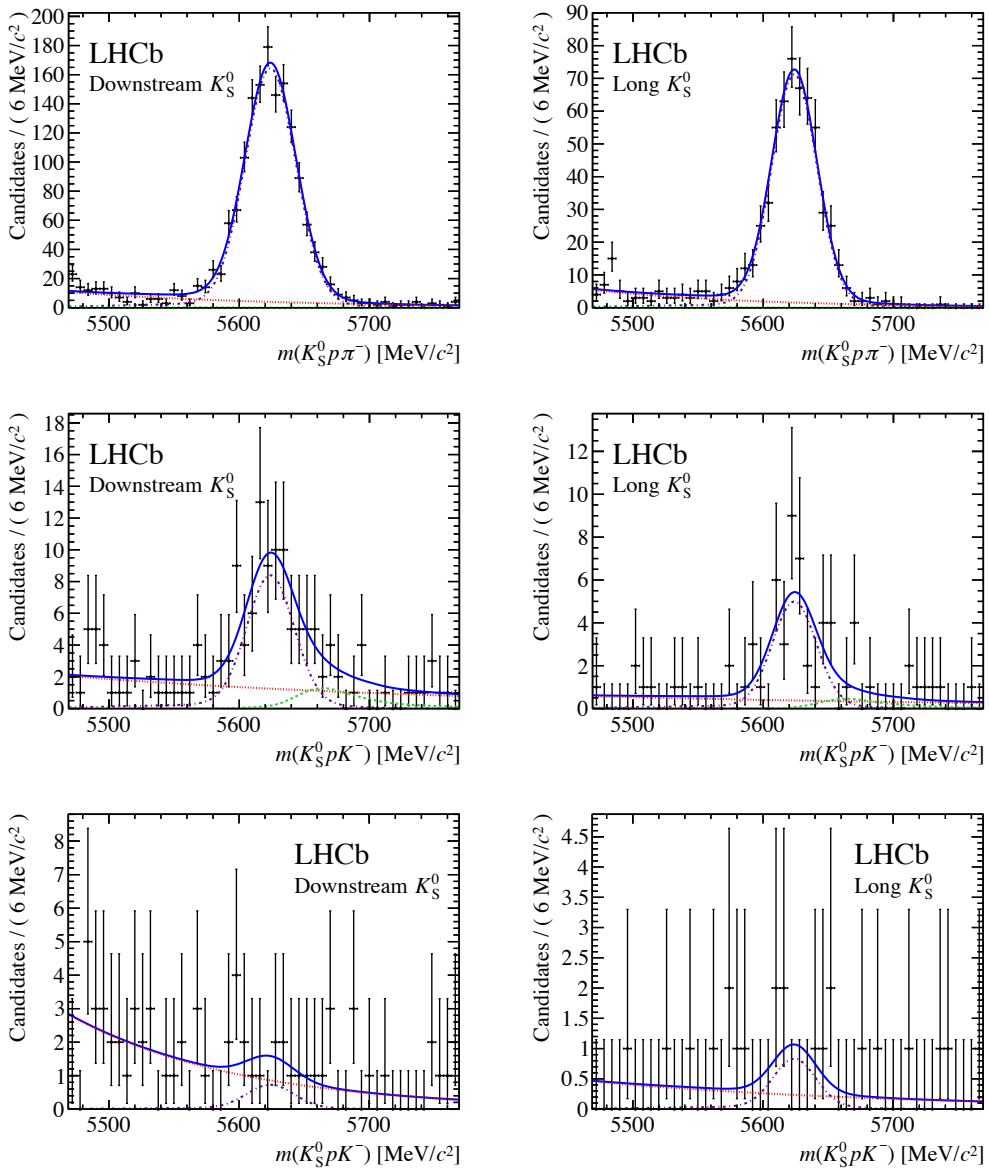

Figure 6.9: Invariant mass distribution of (top) $\Lambda_b^0 \to \Lambda_c^+(pK_S^0)\pi^-$, (middle) $\Lambda_b^0 \to \Lambda_c^+(pK_S^0)K^-$ and (bottom) $\Lambda_b^0 \to D_s^-(K_S^0K^-)p$ candidates for the (left) Down-Down and (right) Long-Long K_S^0 categories. Refer to Fig. 6.8 for components details.

Fitting model

A series of pseudo-experiments are used to determine possible uncertainties related to the description of the signal and background shape

i. Alternative models are considered to verify the stability of the fit. The nominal signal shapes are replaced with a double CB and the background model is

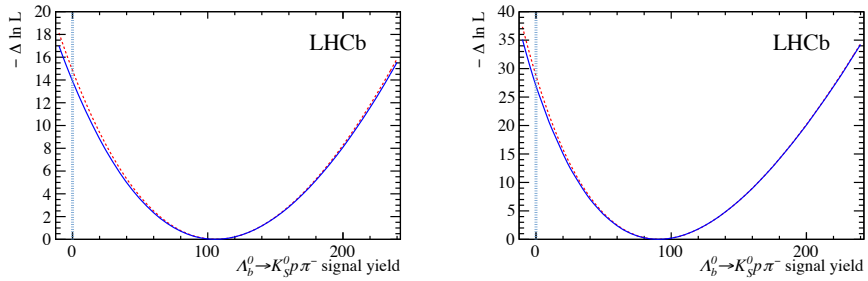

Figure 6.10: Likelihood profile of the $\Lambda_b^0 \to K_S^0 p\pi^-$ signal yield for the (left) Down-Down and (right) Long-Long categories. The dashed red line is the statistical-only profile, while the solid blue line also includes the systematic uncertainties.

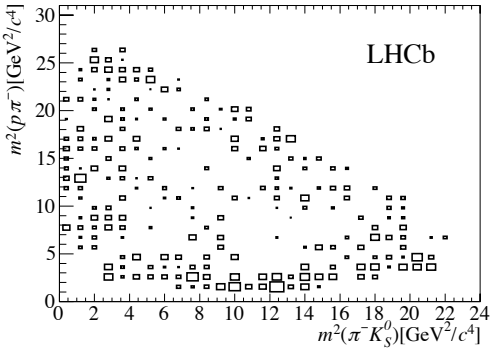

Figure 6.11: Background-subtracted, efficiency-corrected Dalitz plot distribution of $\Lambda_b^0 \to K_S^0 p\pi^-$ decays for Down-Down and Long-Long K_S^0 categories combined. Some bins have negative entries (consistent with zero) and appear empty.

changed to a second-order polynomial function. The uncertainties are evaluated from the yield variation between the baseline and the model under investigation.

ii. Possible biases induced by the fit machinery are investigated; no significant biases are found, and uncertainties are assigned according to the ensemble size.

The total fit model systematic uncertainty is given by the sum in quadrature of all these contributions. For the normalisation channel the same set of variations described in Sec. 6.2.6 are considered.

Particle identification

The uncertainties inherent to the particle identification efficiency determination are treated identically to the description in Sec. 6.2.6. Notice however that these are more pronounced than for $B \to K_S^0 h^\pm h'^\mp$ decays, due to the larger disagreement observed between the detector response and simulation for the proton identification.

Table 6.8: Relative systematic uncertainties on the branching fraction ratios (%) with respect to $B^0 \to K^0_S \pi^+ \pi^-$ decays. The total is obtained from the sum in quadrature of all contributions except that from knowledge of the fragmentation fractions.

Down-Down	Fit model	Fit bias	Simulation	$\Delta_{\rm PHSP}$	PID	Vetoes	Total	$f_{\Lambda_b^0}/f_d$
$\mathcal{B}(\Lambda_b^0 \to K^0_S p\pi^-)$	1	<1	6	4	6	3	10	27
$\mathcal{B}(\Lambda_b^0 \to K^0_S pK^-)$	8	4	6	58	2	4	59	27
$\mathcal{B}(\Xi_b^0 \to K^0_S p\pi^-)$	12	7	4	64	6	–	66	–
$\mathcal{B}(\Xi_b^0 \to K^0_S pK^-)$	4	3	4	47	2	–	47	–
$\mathcal{B}(\Lambda_b^0 \to \Lambda_c^+(pK^0_S)\pi^-)$	2	<1	5	–	6	<1	8	27
$\mathcal{B}(\Lambda_b^0 \to \Lambda_c^+(pK^0_S)K^-)$	5	<1	5	–	4	1	8	27
$\mathcal{B}(\Lambda_b^0 \to D_s^-(K^0_S K^-)p)$	7	6	6	–	6	–	12	27
Long-Long								
$\mathcal{B}(\Lambda_b^0 \to K^0_S p\pi^-)$	2	1	6	3	4	<1	8	27
$\mathcal{B}(\Lambda_b^0 \to K^0_S pK^-)$	4	1	6	42	4	1	43	27
$\mathcal{B}(\Xi_b^0 \to K^0_S p\pi^-)$	8	2	5	47	5	–	49	–
$\mathcal{B}(\Xi_b^0 \to K^0_S pK^-)$	6	4	5	37	5	–	39	–
$\mathcal{B}(\Lambda_b^0 \to \Lambda_c^+(pK^0_S)\pi^-)$	3	<1	6	–	4	<1	8	27
$\mathcal{B}(\Lambda_b^0 \to \Lambda_c^+(pK^0_S)K^-)$	8	1	5	–	6	<1	11	27
$\mathcal{B}(\Lambda_b^0 \to D_s^-(K^0_S K^-)p)$	4	2	6	–	8	–	11	27

Selection

An understanding of discrepancies in the selection and efficiency determination is crucial to the interpretation of the branching fraction results. The determination of these sources of uncertainties is given by a series of independent studies that are added in quadrature

i. Statistical uncertainties related to the limited simulation sample.

ii. Data/simulation discrepancies are foreseen in a number of variables, *e.g.* in the $\Lambda_b^0(\Xi_b^0)$ transverse momentum. The $p_{\rm T}$ distribution for $\Lambda_b^0 \to \Lambda_c^+\pi^-$ decays in data is obtained with the *s$\mathcal{P}$lot* technique, and compared to that in the simulation. The corresponding possible bias in the efficiency is assigned as systematic uncertainty to each decay mode.

iii. The Λ_b^0 lifetime value used in the simulation, $\tau(\Lambda_b^0) = 1.380$ ps, differs significantly from the most precise measurement at the time of $1.482 \pm 0.018 \pm 0.012$ ps [181]. A re-weighting procedure for the efficiency is performed to address these differences. Note that the Ξ_b^0 lifetime was not measured at the time, and no uncertainty was assigned to the value used in the simulation.[2]

iv. The distribution of events across the phase space may vary significantly due to the selection as well as the actual dynamics of the decay. Whilst the uncertain-

[2] Although no measurements of the Ξ_b^0 lifetime existed, isospin predicts a similar value to the Ξ_b^- lifetime, which was measured to be at the time 1.56 ± 0.26 ps [182].

ties for the observed and normalisation channels are examined by varying the square Dalitz-plane binning scheme, the spread of the per-bin efficiency over the phase space (labelled Δ_{PHSP}) is assigned as the systematic uncertainties for the unobserved modes. Note that this source of uncertainty does not affect channels with intermediate charmed states.

Vetoes

The effect of the vetoes applied to remove charmed intermediate states in the phase space needs to be corrected for, and this introduces an additional source of systematic uncertainty. This is estimated by varying the size of the veto windows and repeating the analysis.

Hadronisation probability

The fragmentation fraction of Λ_b^0 baryons ($f_{\Lambda_b^0}$) with respect to those of B^+ and B^0 mesons (f_u and f_d, respectively) has been measured by LHCb [183] to be

$$f_{\Lambda_b^0}/(f_u + f_d) = (0.404 \pm 0.110) \times [1 - (0.031 \pm 0.005) \times p_{\text{T}}(\text{GeV}/c)]\,, \qquad (6.7)$$

where the statistical, systematic and $\mathcal{B}(\Lambda_c^+ \to pK^-\pi^+)$ uncertainties are summed in quadrature, and the linear dependence is found to apply up to $p_{\text{T}} = 14\,\text{GeV}/c$. In the case of Ξ_b^0 baryons, there is no measurement of the fragmentation fraction, and therefore the results quoted include this factor.

The p_{T} dependence of the fragmentation fraction ratio is obtained using semileptonic decays, and therefore is given in terms of the combined p_{T} of the charmed hadron and the muon in the final state. A correction due to the undetected neutrino is obtained from simulation, so that the appropriate fragmentation fraction ratio corresponding to the mean p_{T} for each signal mode can be determined ($f_u = f_d$ is assumed) [184]. For channels with significant signal the mean p_{T} (not event-by-event) is determined from data with the *sPlot* technique; otherwise the value from reconstructed simulated events is used. Systematic uncertainties arise due to the parametrisation of $f_{\Lambda_b^0}/f_d$ versus p_{T} and possible inaccuracy in the mean p_{T} determination.

6.3.7 Branching fractions

The branching fraction for each mode is obtained from the signal yields and efficiencies gathered in Table 6.7 as indicated in the following.

Relative branching fraction and limits

The relative branching fraction measurements and upper limits placed at both 90 % and 95 % confidence level using the Bayesian uniform prior are obtained as

$$\begin{aligned}
\frac{\mathcal{B}(\Lambda_b^0 \to K_S^0 p\pi^-)}{\mathcal{B}(B^0 \to K_S^0\pi^+\pi^-)} &= 0.25 \pm 0.04\,(\text{stat}) \pm 0.02\,(\text{syst}) \pm 0.07\,(f_{\Lambda_b^0}/f_d)\,, \\
\frac{\mathcal{B}(\Lambda_b^0 \to K_S^0 pK^-)}{\mathcal{B}(B^0 \to K_S^0\pi^+\pi^-)} &< 0.07\ (0.08)\ \text{ at }\ 90\,\%\ (95\,\%)\ \text{CL}\,, \\
f_{\Xi_b^0}/f_d \times \frac{\mathcal{B}(\Xi_b^0 \to K_S^0 p\pi^-)}{\mathcal{B}(B^0 \to K_S^0\pi^+\pi^-)} &< 0.03\ (0.04)\ \text{ at }\ 90\,\%\ (95\,\%)\ \text{CL}\,, \\
f_{\Xi_b^0}/f_d \times \frac{\mathcal{B}(\Xi_b^0 \to K_S^0 pK^-)}{\mathcal{B}(B \to K_S^0\pi^+\pi^-)} &< 0.02\ (0.03)\ \text{ at }\ 90\,\%\ (95\,\%)\ \text{CL}\,, \\
\frac{\mathcal{B}(\Lambda_b^0 \to \Lambda_c^+(pK_S^0)\pi^-)}{\mathcal{B}(B^0 \to K_S^0\pi^+\pi^-)} &= 2.83 \pm 0.13\,(\text{stat}) \pm 0.16\,(\text{syst}) \pm 0.77\,(f_{\Lambda_b^0}/f_d)\,, \\
\frac{\mathcal{B}(\Lambda_b^0 \to \Lambda_c^+(pK_S^0)K^-)}{\mathcal{B}(B^0 \to K_S^0\pi^+\pi^-)} &= 0.17 \pm 0.02\,(\text{stat}) \pm 0.01\,(\text{syst}) \pm 0.05\,(f_{\Lambda_b^0}/f_d)\,, \\
\frac{\mathcal{B}(\Lambda_b^0 \to D_s^-(K_S^0K^-)p)}{\mathcal{B}(B^0 \to K_S^0\pi^+\pi^-)} &< 0.07\ (0.08)\ \text{ at }\ 90\,\%\ (95\,\%)\ \text{CL}\,.
\end{aligned}$$

Satisfactory agreement is obtained for Down-Down and Long-Long categories, with compatibility within two standard deviations for all measurements. The relative branching fraction of $\Lambda_b^0 \to \Lambda_c^+ K^-$ and $\Lambda_b^0 \to \Lambda_c^+ \pi^-$ decays is

$$\frac{\mathcal{B}(\Lambda_b^0 \to \Lambda_c^+ K^-)}{\mathcal{B}(\Lambda_b^0 \to \Lambda_c^+ \pi^-)} = 0.059 \pm 0.007\,(\text{stat}) \pm 0.004\,(\text{syst})\,.$$

This result is in agreement with a recent, more precise measurement [178], from which it is independent, up to a negligible correlation in the systematic uncertainty due to particle identification efficiencies.

Absolute results

The absolute branching fractions are calculated using the measured branching fraction of the normalisation channel $\mathcal{B}(B^0 \to K^0\pi^+\pi^-) = (4.96 \pm 0.20) \times 10^{-5}$ [28]

$$\begin{aligned}
\mathcal{B}(\Lambda_b^0 \to \overline{K}^0 p\pi^-) &= (1.26 \pm 0.19 \pm 0.09 \pm 0.34 \pm 0.05) \times 10^{-5}\,, \\
\mathcal{B}(\Lambda_b^0 \to K^0 pK^-) &< 3.5\ (4.0) \times 10^{-6} \ \text{ at } \ 90\,\%\ (95\,\%)\ \text{CL}\,, \\
f_{\Xi_b^0}/f_d \times \mathcal{B}(\Xi_b^0 \to \overline{K}^0 p\pi^-) &< 1.6\ (1.8) \times 10^{-6} \ \text{ at } \ 90\,\%\ (95\,\%)\ \text{CL}\,, \\
f_{\Xi_b^0}/f_d \times \mathcal{B}(\Xi_b^0 \to \overline{K}^0 pK^-) &< 1.1\ (1.2) \times 10^{-6} \ \text{ at } \ 90\,\%\ (95\,\%)\ \text{CL}\,, \\
\mathcal{B}(\Lambda_b^0 \to \Lambda_c^+(p\overline{K}^0)\pi^-) &= (1.40\ \pm 0.07\ \pm 0.08\ \pm 0.38\ \pm 0.06) \times 10^{-4}\,, \\
\mathcal{B}(\Lambda_b^0 \to \Lambda_c^+(p\overline{K}^0)K^-) &= (0.83\ \pm 0.10\ \pm 0.06\ \pm 0.23\ \pm 0.03) \times 10^{-5}\,, \\
\mathcal{B}(\Lambda_b^0 \to D_s^-(K^0K^-)p) &< 3.5\ (3.9) \times 10^{-6} \ \text{ at } \ 90\,\%\ (95\,\%)\ \text{CL}\,,
\end{aligned}$$

where, for the Λ_b^0 decays, the uncertainties are respectively statistical, systematic, from $f_{\Lambda_b^0}/f_d$ and due to the uncertainty on $\mathcal{B}(B^0 \to K^0\pi^+\pi^-)$. For the Ξ_b^0 decays the unknown ratio of fragmentation fractions $f_{\Xi_b^0}/f_d$ is factored out, and the normalisation channel uncertainty is negligible.

The $\Lambda_b^0 \to \Lambda_c^+ h^-$ absolute branching fractions can be determined more precisely than the product branching fractions with $\Lambda_c^+ \to p\overline{K}^0$, since $\mathcal{B}(\Lambda_c^+ \to p\overline{K}^0)/\mathcal{B}(\Lambda_c^+ \to pK^-\pi^+)$ is known to better precision [28] than the absolute value of $\mathcal{B}(\Lambda_c^+ \to pK^-\pi^+)$ that dominates the uncertainty on $f_{\Lambda_b^0}/f_d$. Dividing the product branching fractions quoted above by $\mathcal{B}(\Lambda_c^+ \to pK^-\pi^+)$ and by the ratio of Λ_c^+ branching fractions gives

$$\begin{aligned}
\mathcal{B}(\Lambda_b^0 \to \Lambda_c^+\pi^-) &= (5.97\ \pm 0.28\ \pm 0.34\ \pm 0.70\ \pm 0.24\,) \times 10^{-3}\,, \\
\mathcal{B}(\Lambda_b^0 \to \Lambda_c^+ K^-) &= (3.55\ \pm 0.44\ \pm 0.24\ \pm 0.41\ \pm 0.14\,) \times 10^{-4}\,.
\end{aligned}$$

Similarly, the known value of $\mathcal{B}(D_s^- \to K_S^0 K^-)$ [28] can be used to obtain

$$\begin{aligned}
\mathcal{B}(\Lambda_b^0 \to D_s^- p) &= (2.7\ \pm 1.4\ \pm 0.2\ \pm 0.7\ \pm 0.1\ \pm 0.1) \times 10^{-4}\,, \\
&< 4.8\ (5.3) \times 10^{-4} \ \text{ at } \ 90\,\%\ (95\,\%)\ \text{CL}\,,
\end{aligned}$$

where the last uncertainty is due to the uncertainty on $\mathcal{B}(D_s^- \to K_S^0 K^-)$.

6.3.8 $\mathcal{A}_{CP}$ measurement

The significant signal observed for the $\Lambda_b^0 \to K_S^0 p\pi^-$ channel allows a measurement of its *CP* asymmetry integrated over phase-space. The simultaneous extended maximum likelihood fit is modified to determine the raw asymmetry, defined as

$$\mathcal{A}_{CP}^{\rm RAW} = \frac{N_{\bar{f}} - N_f}{N_{\bar{f}} + N_f}\,, \tag{6.8}$$

where $N_{\bar{f}/f}$ is the observed yield for $\Lambda_b^0/\overline{\Lambda}_b^0$ decays. To obtain the physical *CP* asymmetry, this has to be corrected for small detection ($\mathcal{A}_{\rm D}$) and production ($\mathcal{A}_{\rm P}$) asymmetries, $\mathcal{A}_{CP} = \mathcal{A}_{CP}^{\rm RAW} - \mathcal{A}_{\rm P} - \mathcal{A}_{\rm D}$. This can be conveniently achieved with $\Lambda_b^0 \to \Lambda_c^+(pK_S^0)\pi^-$ decays, which share the same final state as the mode of interest, and have negligible expected *CP* violation.

The measured inclusive raw asymmetry for $\Lambda_b^0 \to \Lambda_c^+(pK_S^0)\pi^-$ decays is found to be $\mathcal{A}_{CP}^{\rm RAW} = -0.047 \pm 0.027$, where the uncertainty is statistical only, indicating that the combined detection and production asymmetry is at the most at few percent level. Similarly, the fitted raw asymmetry for $\Lambda_b^0 \to K_S^0 p\pi^-$ decays is $\mathcal{A}_{CP}^{\rm RAW} = 0.17 \pm 0.13$. The raw asymmetry for each of the background components is found to be consistent with zero, as expected.

Several sources of systematic uncertainties are considered. The uncertainty on $\mathcal{A}_{\rm P}+\mathcal{A}_{\rm D}$ comes directly from the result of the fit to $\Lambda_b^0 \to \Lambda_c^+(pK_S^0)\pi^-$ decays. The effect of variations of the detection asymmetry with the decay kinematics, which can be slightly different for reconstructed $\Lambda_b^0 \to K_S^0 p\pi^-$ and $\Lambda_b^0 \to \Lambda_c^+(pK_S^0)\pi^-$ decays, is negligible. The possible variation of the *CP* asymmetry across the phase-space of the $\Lambda_b^0 \to K_S^0 p\pi^-$ decay, and the non-uniform efficiency results in a systematic uncertainty that is evaluated by weighting events using the *sPlot* technique and obtaining an efficiency-corrected value of $\mathcal{A}_{CP}^{\rm RAW}$. The 0.003 difference with respect to the nominal value is assigned as uncertainty. Effects related to the choices of signal and background models, and possible intrinsic fit biases, are evaluated in a similar way as for the branching fraction measurements, leading to an uncertainty of 0.001. These uncertainties are summed in quadrature to yield the total systematic uncertainty.

The phase-space integrated *CP* asymmetry is found to be

$$\mathcal{A}_{CP}(\Lambda_b^0 \to K_S^0 p\pi^-) = 0.22 \pm 0.13\,({\rm stat}) \pm 0.03\,({\rm syst})\,,$$

which is consistent with zero.

7

$B_s^0 \to K_S^0 K^\pm \pi^\mp$ Dalitz plot analysis

In this chapter, the first Dalitz-plot analysis of the decays $B_s^0 \to K_S^0 K^\pm \pi^\mp$ is presented, where the two charge-conjugate final states are studied separately but simultaneously. The analysis is based on 3.0 fb^{-1} of data collected by LHCb during 2011 and 2012. In addition to the compulsory nuances related to the trigger conditions, these studies reflect the improvements foreseen for the amplitude analysis anticipated in Chapter 5. Note that these results are under internal review with the LHCb collaboration and share several features to the ongoing analysis aiming to update the $K_S^0 h^\pm h'^\mp$ branching fractions [185].

7.1 Selection revision

An amplitude analysis of $B_s^0 \to K_S^0 K^\pm \pi^\mp$ decays is a natural extension of the first observation of this mode. The revised selection strategy for the LHC Run I data sample is based on the `B2KShh Stripping20` campaign and the MVA `SelDP` criterion described previously.

The optimal selection on the `BDT` response is determined by examining separately each invariant mass spectrum (*i.e.* $B_{(s)}^0 \to K_S^0 h^\pm h'^\mp$ mode, trigger operation condition and K_S^0 category), given the distinct variations in the combinatorial background level. Notice that the anticipated $\texttt{FoM}_2$ is used, since it favours the minimisation of the uncertainties on the isobar parameters. The distributions of the figures-of-merit for the example of $B_s^0 \to K_S^0 K^\pm \pi^\mp$ decays are shown in Fig. 7.1, with the optimal `SelDP` values for all modes and benchmark signal/background efficiencies determined on the test samples gathered in Table 7.1. It should be noted that in the event that no clear peak is observed, the working point is chosen at the beginning of the plateau in order to maximize the signal efficiency (*i.e.* 2012a and 2012b DD $B_s^0 \to K_S^0 \pi^+ \pi^-$ decays and 2011 LL $B^0 \to K_S^0 K^+ K^-$ decays).

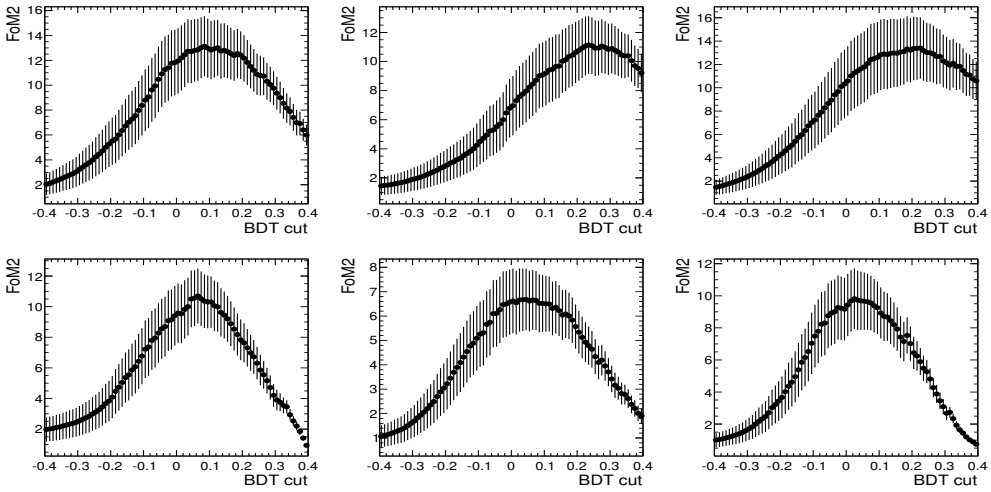

Figure 7.1: Figures-of-merit computed as $\texttt{FoM}_2$ for $B_s^0 \to K_S^0 K^\pm \pi^\mp$ decays for (left) 2011, (centre) 2012a and (right) 2012b, separated in the (top) DD and (bottom) LL K_S^0 categories.

Table 7.1: Figures-of-merit optimal cut values for the `SelDP` discriminants determined for the different final states, trigger operations and K_S^0 categories.

		2011			2012a			2012b		
Final state	K_S^0 type	$\texttt{FoM}_2$	ϵ Signal	ϵ Bkg	$\texttt{FoM}_2$	ϵ Signal	ϵ Bkg	$\texttt{FoM}_2$	ϵ Signal	ϵ Bkg
$K_S^0\pi^+\pi^-$	DD	0.03	0.706	0.033	0.15	0.700	0.038	0.13	0.592	0.017
	LL	−0.04	0.914	0.069	0.00	0.796	0.016	−0.02	0.808	0.022
$K_S^0 K^\pm \pi^\mp$	DD	0.08	0.640	0.024	0.23	0.595	0.019	0.22	0.472	0.012
	LL	0.06	0.790	0.032	0.04	0.726	0.032	0.02	0.742	0.023
$K_S^0 K^+ K^-$	DD	−0.04	0.815	0.061	0.11	0.764	0.008	0.04	0.716	0.056
	LL	−0.06	0.934	0.114	0.02	0.773	0.028	−0.10	0.912	0.060

Unlike the previous $K_S^0 h^\pm h'^\mp$ analysis, the particle identification criteria rely on the neural network-based `ProbNN` approach, since for this measurement it provides a better performance in comparison to $\Delta \log \mathcal{L}_{hh'}$ method. The strategy follows a cut-combination $\texttt{ProbNN}_h \times (1 - \texttt{ProbNN}_{h'})$, which requires that the particle has a given threshold probability of being a given h-ID hypothesis and not the h'-ID. Hereafter such criteria are referred to as $\texttt{ProbNN}_{hh'}$. [1] The PID optimisation has been designed to reject both combinatorial and cross-feed backgrounds. Whilst combinatorial yields are obtained identically to the procedure for the BDT optimisation, misidentified contributions are estimated by extrapolating the yields for the given `PIDCalib`-corrected efficiencies. Notice that in this procedure the criteria for both charged tracks are simultaneously optimised. The chosen values for each track hypothesis are found to be $\texttt{ProbNN}_{\pi K} > 0.40$ for $K_S^0\pi^+\pi^-$ and $\texttt{ProbNN}_{\pi K(K\pi)} > 0.30$

[1] It is also possible to impose cuts on $\texttt{ProbNN}_h$ alone, without multiplying by $(1 - \texttt{ProbNN}_{h'})$. However, the combination is found to be effective in this and several other analyses.

for $K^0_S K^\pm \pi^\mp$ states (common to both K^0_S categories), and $\texttt{ProbNN}_{K\pi} > 0.15\,(0.20)$ for the $K^0_S K^+ K^-$ DD (LL) configuration. It is also important to mention that all charged tracks, either from the K^0_S or the B meson, have `isMuon` decisions rejecting muon candidates. Protons in the final states are further suppressed by imposing $\texttt{ProbNN}_{hp}$ greater than 0.01 or 0.10 for tracks associated to pions or kaons, respectively.

Finally, the strategy regarding background contribution sources is similar in this analysis to the cases discussed in Sec. 6.2.3. Explicitly, vetoes on J/ψ, $\psi(2S)$ and χ_c charmonia transitions and the D and Λ_c^+ intermediate states are required. Moreover, in order to reduce partially-reconstructed backgrounds to negligible levels, lower bound is placed on the B-candidate invariant mass of 5200 MeV/c^2. This has been verified to remove partially reconstructed backgrounds populating the $K^0_S K^\pm \pi^\mp$ final states, such as $B^0_s \to K^{*0}(K^0_S\pi^0)\overline{K}^{*0}(K^-\pi^+)$, $B^0 \to D^-(K^0_S\pi^-\pi^0)K^+$ and $B^0 \to K^{*0}(K^0_S\pi^0)\rho^0(\pi^+\pi^-)$, where the latter decay also involves the misidentification of one of the pions as a kaon. Therefore, any partially-reconstructed contribution is neglected or accommodated in the combinatorial background in this measurement.

7.2 Mass fit model

Although the purpose of this amplitude analysis is to study exclusively $K^0_S K^\pm \pi^\mp$ final states, it is convenient to utilise the simultaneous `B2KShh` fitting machinery to provide a more robust yield determination. Nonetheless, some improvements have been introduced in order to address the additional categories required by the different running conditions. The fit contains a series of 24 classes corresponding to the final states $K^0_S\pi^+\pi^-$, $K^0_S K^+\pi^-$, $K^0_S K^-\pi^+$ and $K^0_S K^+ K^-$; K^0_S reconstruction categories Down-Down and Long-Long; and trigger operation conditions 2011, 2012a and 2012b. These are parametrised in the mass fit framework and the relevant yields are simultaneously determined from an extended unbinned fit. Notice that the two charged configurations $K^0_S K^\pm \pi^\mp$ are explicitly separated in order to allow possible *CP*-violation studies. It is also important to mention that both signal yields and mass fit regions for $B^0_s \to K^0_S K^+ K^-$ decays are maintained blind for this analysis, in order to avoid conflicts with the ongoing search for this mode.

7.2.1 Signal model

Similarly to the branching ratio measurement, signal distributions are parametrised by a sum of two Crystal Ball functions, which share the same mean and width values

but have different tail parameters. However, since there is a significant increase in the dimension of the parameter space, a series of constraints are mandatory to ensure the robustness of the fit. First, masses of the B^0 and B_s^0 mesons are universal for each of the K_S^0 categories and running periods, and the widths are represented as a ratio with respect to the $K_S^0\pi^+\pi$ final state and common between the years. Furthermore, the parameters for the $K_S^0K^+\pi^-$ and $K_S^0K^-\pi^+$ mass shapes are constrained to be the same. An additional constraint is set in the right-handed tail parameter, which is fixed to be the same for all the years of a given final state and K_S^0 type. This is motivated by the limited statistics available in each year to accommodate properly these stochastic effects and the similarities seen in these parameters. A fit to all simulated samples is performed simultaneously to extract these various parameters and corresponding correlations.

7.2.2 Signal cross-feeds

Possible reflections between the charged final states are described by a double asymmetric Crystal Ball function with a common mean and width. Whilst the mean is shared between the K_S^0 categories and trigger conditions for a given misidentification source, the resolutions are floated individually for each of these contributions. Moreover, the fraction of the second CB is shared between the years. Each cross-feed yield is Gaussian constrained to be equal to the number of signal candidates in its corresponding true spectrum, multiplied by the relevant misidentification and relative selection efficiency.

Although all lineshapes are derived from simulated datasets, cross-feeds shapes receive additional corrections. These consist of event-by-event weights related to the data-driven misidentification efficiency and to the known true-signal Dalitz-plot distribution. Whereas the first is determined using the `PIDCalibTool`, the phase-space correction is obtained from simulation based on results reported from the time-dependent amplitude analyses performed at BaBar, specifically for $B^0 \to K_S^0\pi^+\pi^-$ and $B^0 \to K_S^0K^+K^-$ decays [169, 171]. Since no previous measurements, prior to this analysis, are available for $B_s^0 \to K_S^0K^\pm\pi^\mp$ channels, a simplified model including only $K^*(892)^{(\pm,0)}$ and $K_0^*(1430)^{(\pm,0)}$ resonances is considered. These improvements are of great importance in the parametrisation of the tails that can contribute under the signal region.

7.2.3 Combinatorial background model

The remaining contribution considered in the model originates from combinatorics. An independent exponential shape is included for the combinatorial background for each decay mode, K^0_S category and year. Similarly, scaling factors for different slopes of the $K^0_S K^+ K^-$ and $K^0_S K^\pm \pi^\mp$ modes with respect to $K^0_S \pi^+ \pi^-$ are introduced. Moreover, three additional ratios are considered to accommodate differences between LL and DD slopes for 2011, 2012a and 2012b data conditions. It has been observed that the stability of the fit model requires a constraint on the scaling factor between the slopes of the background in the different signal modes, which is set to be the same and fixed in the data fit.

7.2.4 Fit to the B candidate invariant distribution

The results of the simultaneous fit to data are shown in Figures 7.2 and 7.3 for $K^0_S K^+ \pi^-$ and $K^0_S K^- \pi^+$ final states, respectively. For simplicity the results for the other final states are omitted in this discussion. Although some fluctuations are seen, in particular for the 2011 and 2012a trigger conditions, there is a satisfactory agreement in the whole mass range, as indicated by the residuals.

For the purpose of the amplitude analysis it is relevant to quote the observed yields for signal, background and cross-feeds inside a chosen signal region, hereafter referred to as the $\pm 2.5\,\sigma$ mass window around the B^0_s fitted mass. Explicitly, the events selected within the range $[\mu(B^0_s) - 2.5 \times \sigma(B^0_s \to K^0_S K^\pm \pi^\mp), \mu(B^0_s) + 2.5 \times \sigma(B^0_s \to K^0_S K^\pm \pi^\mp)]$ for each trigger condition and K^0_S category are utilised in the Dalitz-plane fitting. These yields are gathered in Table 7.2. Notice that the only cross-feed relevant for the $K^0_S K^\pm \pi^\mp$ final states come from $B^0 \to K^0_S \pi^+ \pi^-$ decays, which is evident from the mass plots. The distributions of candidates in the signal region over both the standard and square Dalitz plots are shown in Fig. 7.4.

7.3 Dalitz-plot generalities

An introduction to the Dalitz-plane dynamics and underlying interpretation has been already reported in Section 3.2. In the following the description of the likelihood function utilised in the Dalitz-plot fit is revised, including conventions adopted for $B^0_s \to K^0_S K^\pm \pi^\mp$ decays. The amplitude analysis is performed within the `Laura++` [159] framework, which has been developed by members of the University of Warwick elementary particle physics group and used for several BaBar [186–188] and more recently LHCb [189–191] publications.

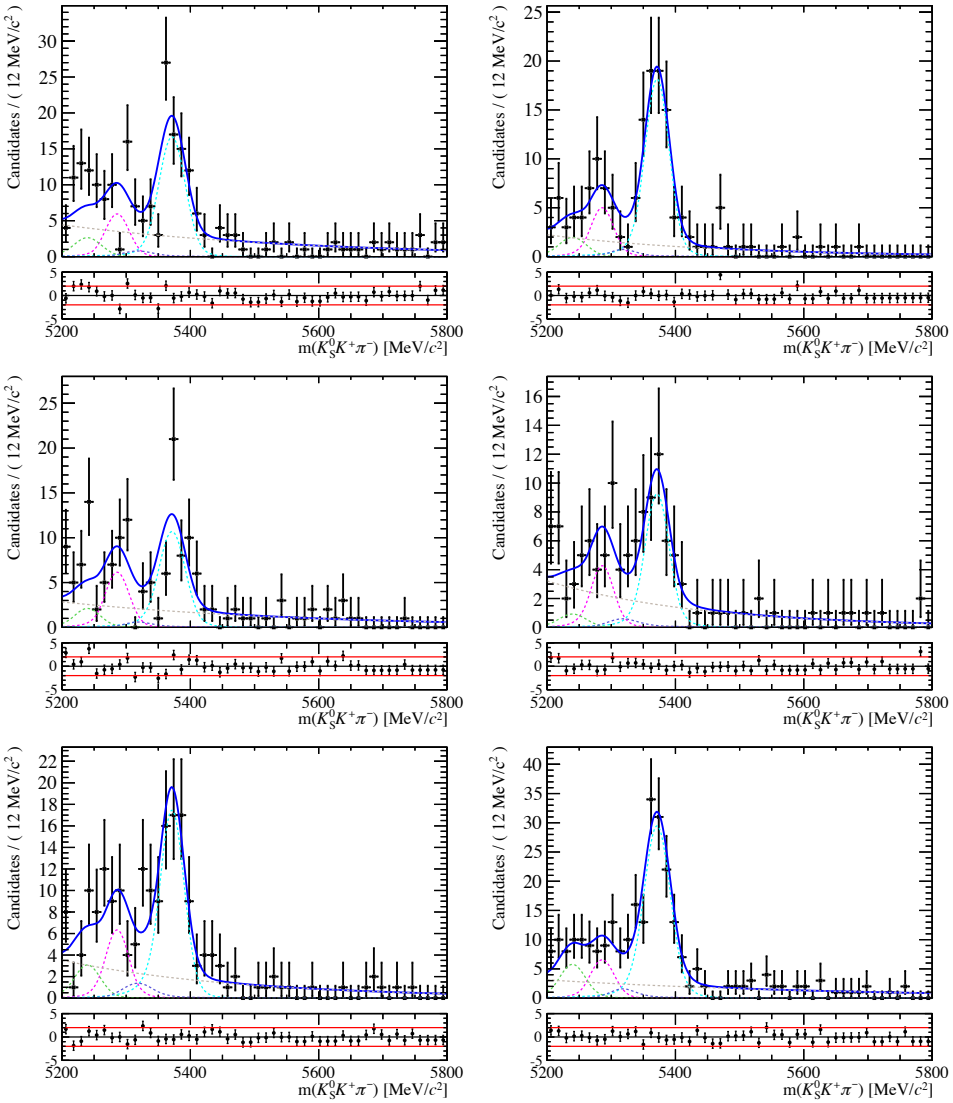

Figure 7.2: Invariant mass data distribution for $K^0_S K^+\pi^-$ final state for the (left) Down-Down and (right) Long-Long K^0_S type, in the (top) 2011, (middle) 2012a and (bottom) 2012b dataset. Each component of the fit model is displayed on the plot: the signal PDFs are represented by the dashed magenta and dotted cyan line for B^0 and B^0_s, respectively; the cross-feeds from $B^0 \to K^0_S\pi^+\pi^-$ and $B^0 \to K^0_S K^+K^-$ decays by the dot-long-dashed purple line and dot-dashed dark green line, respectively; the overall fit is given by the thick blue line; and the combinatorial background by the dash-triple-dotted grey line.

7.3.1 Signal PDF

Due to the inability to distinguish the B^0_s and $\overline{B}^0_s$ amplitudes, as described in Sec. 3.3, a simultaneous untagged decay-time-integrated amplitude analysis is constructed for the $K^0_S K^+\pi^-$ and $K^0_S K^-\pi^+$ final states. The Dalitz-plot amplitudes are formalised

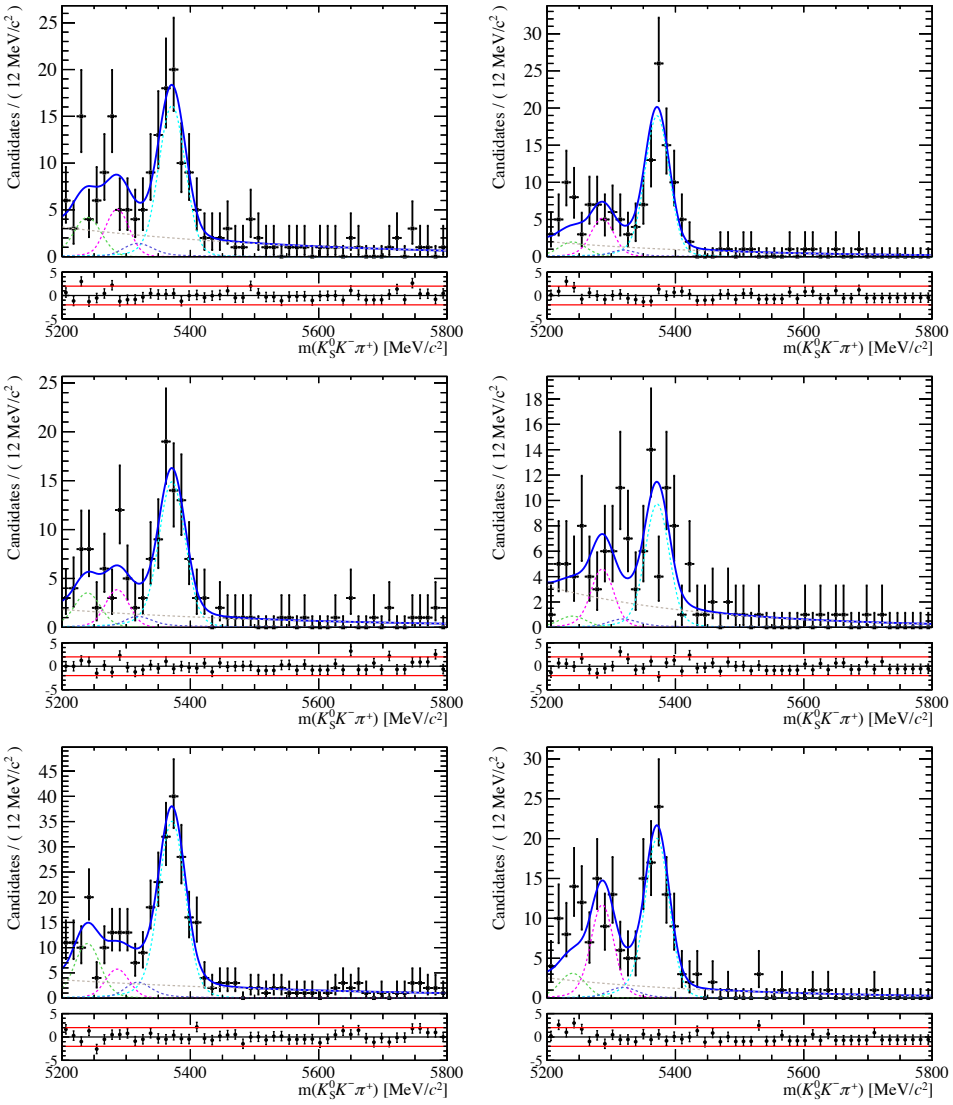

Figure 7.3: Invariant mass data distribution for $K^0_S K^-\pi^+$ final state for the (left) Down-Down and (right) Long-Long K^0_S type, after the full selection in the (top) 2011, (middle) 2012a and (bottom) 2012b dataset. Refer to Fig. 7.2 for components details.

in the isobar model as a sum of individual complex coefficients and dynamical amplitude terms given by Eq. 3.20, explicitly described by $\mathcal{A}_f$ and $\mathcal{A}_{\bar{f}}$. Whilst large contributions from both charged and neutral K^* resonances are expected to dominate, resonances such as $a_2(1320)$ decaying to $K^0_S K^\pm$ should be marginal.[2] As such

[2] A B^0_s decay to such an unflavoured final state must be mediated by exchange or annihilation amplitudes, which are expected to be suppressed. The $B^0_s \to \pi^+\pi^-$ decay has, however, been observed [192] with branching fraction $\mathcal{O}(10^{-6})$.

Table 7.2: Fitted yields for the full range and within $2.5\,\sigma$ of the B_s^0 peak for the B_s^0 signal, combinatorial and $B^0 \to K_S^0\pi^+\pi^-$ cross-feeds, separated into each decay channel, K_S^0 category and year.

			B_s^0-signal		Combinatorial		Cross-feed
Final state	K_S^0	Year	$2.5\,\sigma$	Full fit	$2.5\,\sigma$	Full fit	$2.5\,\sigma$
$K_S^0K^+\pi^-$	DD	2011	72.1	73.6 ± 10.6	22.1	108.3 ± 15.1	1.7
		2012a	45.7	48.2 ± 8.6	14.3	70.1 ± 12.1	1.1
		2012b	130.0	135.3 ± 13.6	17.9	87.4 ± 13.8	3.1
	LL	2011	74.6	76.2 ± 9.8	8.4	44.1 ± 9.8	1.8
		2012a	36.8	38.5 ± 7.7	11.2	58.8 ± 11.2	0.9
		2012b	71.9	73.5 ± 10.6	13.6	71.7 ± 13.1	1.7
$K_S^0K^-\pi^+$	DD	2011	71.4	72.8 ± 10.3	16.1	78.9 ± 12.7	1.3
		2012a	65.2	68.8 ± 9.6	9.5	46.2 ± 9.9	1.2
		2012b	158.6	165.1 ± 15.2	21.3	104.1 ± 15.0	2.9
	LL	2011	75.7	77.3 ± 9.8	7.4	39.0 ± 10.2	1.4
		2012a	38.5	40.3 ± 8.1	11.2	58.9 ± 11.9	0.7
		2012b	80.0	81.7 ± 10.4	9.5	50.1 ± 12.3	1.4

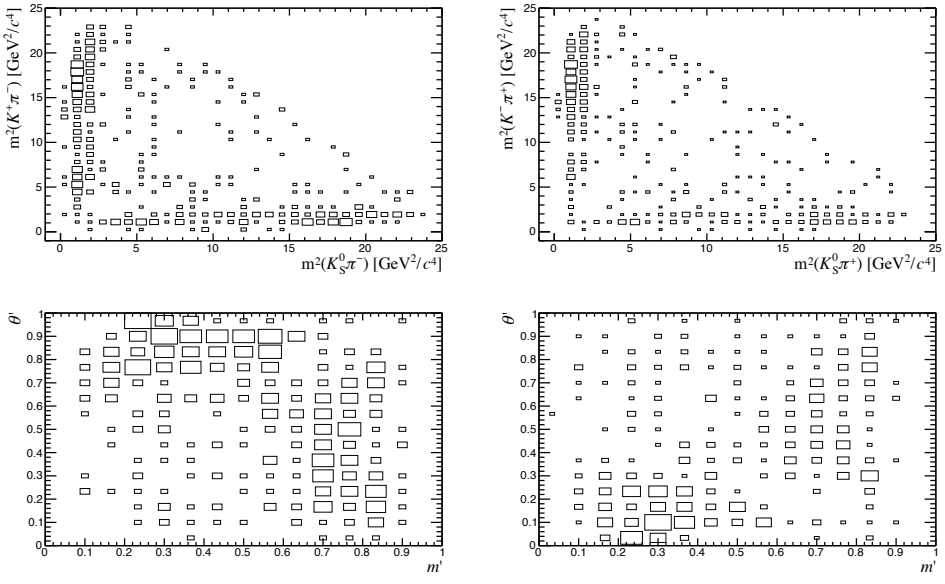

Figure 7.4: Distributions for (left) $K_S^0K^+\pi^-$ and (right) $K_S^0K^-\pi^+$ candidates in the signal region over the (top) standard and (bottom) square Dalitz plot. Note that the value $\theta^{'}$ is reflected about $\theta^{'} = 0.5$ when going from one final state to the other.

the Dalitz-plane is defined in terms of $K^{\pm}\pi^{\mp}$ and $K^0_S\pi^{\mp}$ invariant masses, hereafter designated as s and t, respectively.

The flavour-averaged signal Dalitz-plot likelihood function approximated from Eq. 3.43 can be determined as

$$\mathcal{P}_f^{\text{sig}}(s,t) = \frac{|\mathcal{A}_f(s,t)|^2}{\int\int_{DP} |\mathcal{A}_f(s,t)|^2 \, ds\, dt} \,, \tag{7.1}$$

with a similar expression for the conjugate final state $\mathcal{A}_{\bar{f}}$.

7.3.2 Resonant amplitudes

The resonance dynamics contained within the F_j terms of Eq. 3.20 is explicitly given by the product of the invariant mass and angular distribution probabilities, *i.e.*

$$F_j(L,s,t) = R_j(s) \times F_L(|\vec{p}|\, r) \times F_L(|\vec{q}|\, r) \times T_j(L,\vec{p},\vec{q}) \;, \tag{7.2}$$

where each term is defined as

- $R_j(s)$ is the resonance mass term (*e.g.* Breit–Wigner);
- $T_j(L,\vec{p},\vec{q})$ is the angular probability distribution (Zemach formalism);
- F_L are barrier factors with parameter r shown in Eq. 3.30;
- $\vec{p}$ and $\vec{q}$ are the momenta of the bachelor particle and one of the resonance daughters respectively, both evaluated in the rest frame of the resonance;
- L is the orbital angular momentum between the resonance and the bachelor.

The $F_j(s,t)$ are each normalised such that, over the whole Dalitz plot,

$$\int\int_{DP} |F_j(s,t)|^2 \, dsdt = 1 \;, \tag{7.3}$$

which is calculated using Gauss–Legendre integration methods [193].

Angular distributions

In the previously introduced Zemach tensor formalism, the angular probability distributions for a resonance of spin L are given by

$$L = 0 \quad : \quad T_j = 1\,, \tag{7.4}$$

$$L = 1 \quad : \quad T_j = -2\vec{p}\cdot\vec{q}\,, \tag{7.5}$$

$$L = 2 \quad : \quad T_j = \frac{4}{3}\left[3(\vec{p}\cdot\vec{q})^2 - (|\vec{p}||\vec{q}|)^2\right]\,. \tag{7.6}$$

Note the similarity of these forms to the Legendre polynomials, of the cosine of the angle between $\vec{p}$ and $\vec{q}$. The convention for the resonance daughter $\vec{q}$ is such that the K^0_S is used as reference for both $K^0_S h^+$ and $K^0_S h^-$ resonances whilst h^+ is used for h^+h^- resonances.

Blatt–Weisskopf barrier factors

The penetration barrier form factors are defined in Eq. 3.30, where $z = |\vec{q}\,|\,r$ or $|\vec{p}\,|\,r$, with the radius parameter given by $4.0\,\mathrm{GeV}^{-1} \approx 0.8\,\mathrm{fm}$. Notice that these are calculated for each angular momentum L, with z_0 representing the value of z when the invariant mass is equal to the pole mass of the resonance.

Mass lineshapes

Some of the most relevant resonance mass forms have been already introduced in Section 3.2.2, in particular the Relativistic Breit–Wigner (RBW) and LASS lineshapes given in Eqs. 3.28 and 3.31, respectively. Although the RBW is suitable for narrow isolated resonances such as $K^*(892)$, in the event of more than one overlapping resonances or a significant interference with a nonresonant component, the sum of the contributions in the isobar model violates unitarity. This constitutes a problem for the description of broad resonances, such as the $K^*_0(1430)$ and nonresonant components contributing to the final states of interest. These so-called $K\pi$ S-wave parametrisations are often modelled by the LASS shape, which is used as baseline in this analysis. Alternative descriptions, which are considered when assigning model-related uncertainties, are outlined in Appendix C.

7.3.3 Isobar coefficients

As mentioned in Sec. 7.3.1 the dynamical amplitudes, either resonant or nonresonant, are multiplied by complex coefficients that describe the relative strengths of the components. The chosen parametrisation of the isobar coefficients is in terms of

real and imaginary parts $c_j = x + iy$, introduced for each final state. The preference for this convention is motivated by possible problems with positive definite values in the magnitude and phase approach.

Fit fractions

As the choice of normalisation, phase convention and amplitude formalism may not always be the same for different experiments, fit fractions are presented in addition to amplitude magnitudes to allow a more meaningful comparison of results. The fit fraction is defined as the integral of a single decay amplitude squared divided by the coherent matrix element squared for the complete Dalitz plot

$$FF_j = \frac{\int\int_{DP} |c_j F_j(s,t)|^2 \, dsdt}{\int\int_{DP} |\sum_k c_k F_k(s,t)|^2 \, dsdt} \,. \tag{7.7}$$

Note that the sum of these fit fractions is not necessarily unity due to the potential presence of net constructive or destructive interference. The interference fit fractions for two components i and j is given by

$$FF_{ij} = \frac{\int\int_{DP} 2\mathrm{Re}\left[c_i c_j^* F_i(s,t) F_j^*(s,t)\right] dsdt}{\int\int_{DP} |\sum_k c_k F_k(s,t)|^2 \, dsdt} \,. \tag{7.8}$$

In this definition, $FF_{jj} = 2FF_j$. For the purpose of the branching ratio calculation, it is relevant to define the flavour-averaged fit fraction

$$\widehat{FF}_j = \frac{\int\int_{DP} |c_j F_j(s,t)|^2 \, dsdt + \int\int_{DP'} \left|\bar{c}_j \bar{F}_j(s',t')\right|^2 ds'dt'}{\int\int_{DP} |\sum_k c_k F_k(s,t)|^2 \, dsdt + \int\int_{DP'} \left|\sum_k \bar{c}_k \bar{F}_k(s',t')\right|^2 ds'dt'} \,, \tag{7.9}$$

where bar stands for the conjugate final state under consideration.

Multiple solutions

In case there are overlapping broad resonances, or a broad resonance overlapping with a nonresonant component, in the same partial wave, it is likely that the fit will have multiple solutions. In a simple picture, one can have two large fit fractions and a negative interference fit fraction or two smaller fit fractions with a positive interference term, both giving very similar overall results.

To be sure to find the global minimum, each fit is repeated $\mathcal{O}(100)$ times with randomised starting parameters. The solution with the smallest negative log-likelihood (to which most of the fits should usually converge) is taken as the default

result, but the solutions corresponding to secondary minima are also examined.

Statistical uncertainties

A simple and effective method of determining statistical uncertainties is by using toy simulated samples. Uncertainties can be determined not only on the fitted isobar coefficients, but also on any derived quantities – *i.e.* not only on real and imaginary parts of the amplitude, but also on magnitudes, phases, fit fractions and interference fit fractions. Correlations between these parameters can also be interpreted from the scatter of the distributions found in the toys, rather than the single point estimate of the correlations obtained from `MINUIT` in the fit to data.

7.3.4 Goodness-of-fit criteria

A common practice in high energy physics is to bin a given dataset and evaluate the quality of the fit using a χ^2 calculation. This is a convenient and powerful tool in many scenarios. However, in situations where the bin population is limited (*i.e.* as expected for $B_s^0 \to K_S^0 K^\pm \pi^\mp$ decays), the significance of any discrepancy between the data and the fitted PDF is often overestimated.

In order to examine the suitability of (un)binned approaches, a series of toy simulated studies have been performed with a simple signal model comprised of $K^*(892)$ and $K_0^*(1430)$ resonances. A two-dimensional χ^2/ndf-test along with the unbinned methods [194] referred to as mixed-sample and point-to-point dissimilarity tests are investigated. Although equally populated bins are examined in the χ^2/ndf routine, the anticipated statistics limitation is evident, disfavouring this method for this analysis. Both unbinned approaches are competitive and the toy studies indicate the ranges of the two metrics that correspond to good fits to be used in the data fit evaluation.

7.4 Signal efficiency variation across the Dalitz plot

The variation of efficiency across the Dalitz plane must be included in the amplitude fit. An ideal analysis would select events with equal probability from any region of the phase space, but it has been already shown that the selection favours specific regions. In order to address possible disagreements between the data and simulation the total efficiency determination is built up from several individual contributions

i. Geometrical efficiency obtained from simulated-only samples;

ii. Selection efficiency (trigger, stripping and `SelDP` criteria) are determined from simulated samples and corrected for possible data/simulation differences in the tracking and trigger efficiencies;

iii. Data-driven particle identification efficiencies derived from the `PIDCalib`.

Note that this procedure is implemented for each trigger condition and K^0_S category. Fluctuations due to limited statistics are smoothed out by fitting each efficiency function to a 2D cubic spline across the square Dalitz plot. The total efficiency is then obtained by multiplying together the values of the spline for each contribution at the given phase-space position.

7.4.1 Geometrical efficiency

Generator-level simulated samples produced without any cuts on the daughter particles are utilised to evaluate the geometrical efficiency, defined as the fraction of the total number of events generated that are within the nominal LHCb acceptance. Negligible distinctions are seen between 2011 and 2012 datasets associated to the increase in the beam energy (and hence a change in the B^0_s kinematics). Note that no differences are expected between 2012a/2012b trigger nor K^0_S DD/LL categories. Figure 7.5 shows the resulting 2011 efficiency histogram for $B^0_s \to K^0_S K^+\pi^-$ decays. Uncertainties are due to the simulated statistics and are evaluated using the Clopper-Pearson method as implemented in the `TEfficiency` class [195]. Variations of about 10 % (relative) across the phase space are seen throughout and are considered in the systematics studies.

7.4.2 Selection efficiency

Although many selection requirements have been chosen to minimise efficiency variations across the DP, large non-uniformities are foreseen due to the reconstruction and trigger criteria. In addition, to accurately model these features, weighting factors are applied to account for data/simulation differences in the tracking and `L0` trigger.

Tracking correction

Tracking efficiency data-driven corrections are available as a function of momentum and pseudorapidity for `Long` tracks [196], using 2012 calibration datasets.

Correction-tables are used to weight each simulated B^0_s-daughter track.[3] These simulated ensembles are pre-matched to the true-signal data distribution of p, η and track multiplicity, using $B^0 \to K^0_S\pi^+\pi^-$ data signal samples as proxy modes. This particular choice is motivated by the large available statistics and fair agreement in these control variables amongst the $B^0_{(s)} \to K^0_S h^\pm h'^\mp$ decays modes. The total tracking efficiency correction in bins of the square Dalitz plot is obtained from the event-by-event multiplication of the corrections for each track, which introduce small variations at the percent level. Uncertainties are evaluating by bootstrapping the simulated sample and propagating the statistical uncertainties of the calibration samples.

`L0Hadron TOS` trigger efficiency correction

Further corrections are associated to possible differences in the `L0Hadron TOS` trigger efficiency. Note that these are applied to both simulated candidates passing this line decision and those failing it, here evaluated by separating the samples into mutually exclusive "`L0Hadron TOS`" and "`L0Global TIS` and not `L0Hadron TOS`" categories. Since this division reduces the available statistics, the combined-year dataset is utilised in the method, assuming a constant discrepancy for all running periods.

Data/simulation corrections are obtained from the known absolute data efficiencies [197], which are compared to the simulated results. These are evaluated from the ratio of events passing the examined `L0` criteria in the simulation, and from calibration samples for each track based on the particle type, dipole magnet polarity, the part of the calorimeter that the track hits and the transverse energy deposited. Note that possible cluster overlaps in the calorimeter are also considered in the routine. The data efficiency is calculated as the probability that at least one of the four tracks or none of the tracks pass the `L0Hadron TOS` trigger, respectively for the `TOS` and `TIS`-only categories. Correction histograms are therefore obtained by dividing these efficiencies as a function of the square Dalitz-plane position. Large variations up to 20 % are observed across the phase space, indicating the importance of this source of correction.

Total selection efficiency

The selection efficiency is defined as $\epsilon_{\texttt{TOS||TIS}} = \epsilon_{\texttt{TOS}} + \epsilon_{\texttt{TIS\&\&!TOS}}$, *i.e.* it is the sum (not the average) of the two efficiencies. Therefore, these are combined into a single

[3] A single procedure to quantify potential differences in the K^0_S vertexing and tracking efficiency for both Down-Down and Long-Long categories is under investigation, and therefore, these tracks are removed from this process.

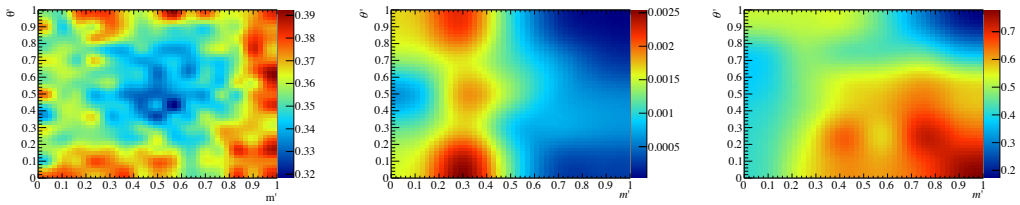

Figure 7.5: Efficiency variation as a function of the $B_s^0 \to K_S^0 K^+ \pi^-$ square Dalitz plot position obtained from 2011 operation conditions examined for the (left) generator-level, (centre) selection and (right) particle identification criteria.

map according to the proportions seen in data as

$$\epsilon_{\texttt{TOS||TIS}} = \frac{f^{\text{data}}_{\texttt{TOS}}}{f^{\text{MC}}_{\texttt{TOS}}} \epsilon_{\texttt{TOS}} + \frac{f^{\text{data}}_{\texttt{TIS\&\&!TOS}}}{f^{\text{MC}}_{\texttt{TIS\&\&!TOS}}} \epsilon_{\text{TIS\&\&!TOS}} \,, \tag{7.10}$$

where the f terms are the fractions of each category in data and simulation, as labelled ($f^{\text{data}}_{\texttt{TOS}} + f^{\text{data}}_{\texttt{TIS\&\&!TOS}} = f^{\text{MC}}_{\texttt{TOS}} + f^{\text{MC}}_{\texttt{TIS\&\&!TOS}} = 1$). Figure 7.5 indicates the representative efficiency variation over the phase space, where all uncertainties are combined in quadrature.

7.4.3 PID efficiency

Particle identification efficiencies are obtained by the usual multibody `PIDCalib` re-weighting technique, evaluated separately by the charge of the track and dipole magnet polarity, as a function of kinematic properties. Figure 7.5 displays the efficiency variation over the Dalitz plane for $B_s^0 \to K_S^0 K^+ \pi^-$ decays. Note that a similar pattern is expected for the conjugate final state mirrored across $\theta' = 0.5$.

7.4.4 Total efficiency

The relevant spline-smoothed total efficiency histograms are obtained from the individual components multiplied altogether. A representative efficiency map is shown in Fig. 7.6, which is used as an input to the Dalitz-plot fit. It is worth mention that has been observed no differences between the years in any of the intermediate steps neither in the overall shape or level of the efficiency.

7.5 Background Dalitz-plot distributions

Another crucial piece of information required for the amplitude fit is the knowledge of the Dalitz-plot distribution of each of the sources of background within the signal

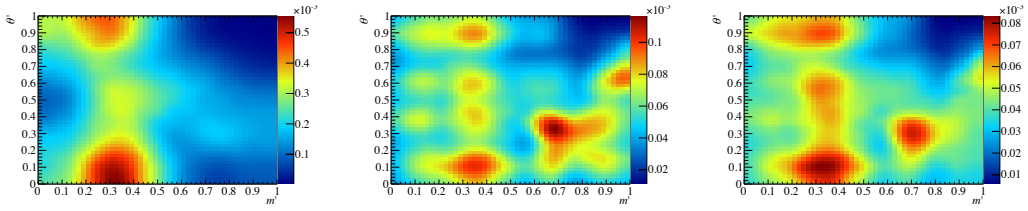

Figure 7.6: Combined efficiency variation (left) and corresponding (middle) upper and (right) lower uncertainties across the $B_s^0 \to K_S^0 K^+\pi^-$ square Dalitz plot, as interpolated from a fit to a 2D cubic spline, for the Down-Down K_S^0 category.

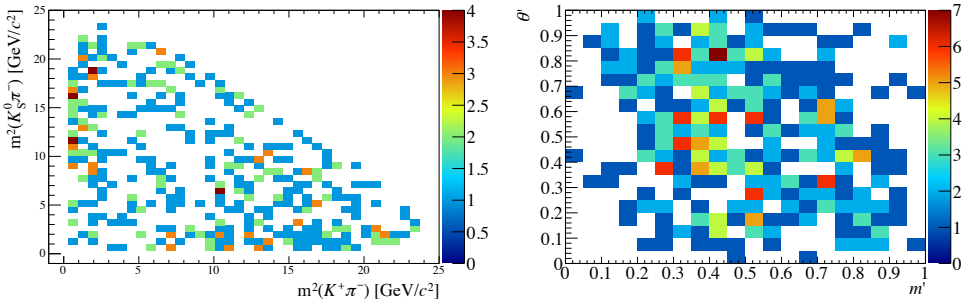

Figure 7.7: High-sideband data distributions for $B_s^0 \to K_S^0 K^+\pi^-$ decays in the loose 2012b `SelDP` selection as a function of the (left) standard and (right) square Dalitz plots.

region. Non-negligible contributions from combinatorial backgrounds and crossfeed from $B^0 \to K_S^0\pi^+\pi^-$ decays reported in Table 7.2 are discussed in the following. Small contributions from other sources are neglected.

7.5.1 Combinatorial background

Combinatorial background distributions are obtained from candidates in a high B_s^0 mass sideband, *i.e.* in the range of $[5400, 5800]$ MeV/c^2. Noticeable structures at the low invariant mass values related to random associations of light resonances (*e.g.* K^*) with a track are observed. In order to improve the resolution in modelling these contributions by enhancing the sample size, the `SelDP` criteria has been loosened. Several validation studies have been performed to verify the robustness of this strategy, and no further non-trivial pattern is seen. Note that in this approach it is assumed and has also been validated, that these distributions are independent of the region of the B candidate invariant mass under consideration. Figure 7.7 depicts an indicative phase-space distribution for the 2012b running period. The distributions of backgrounds are provided as square Dalitz-plane histograms in the amplitude fit.

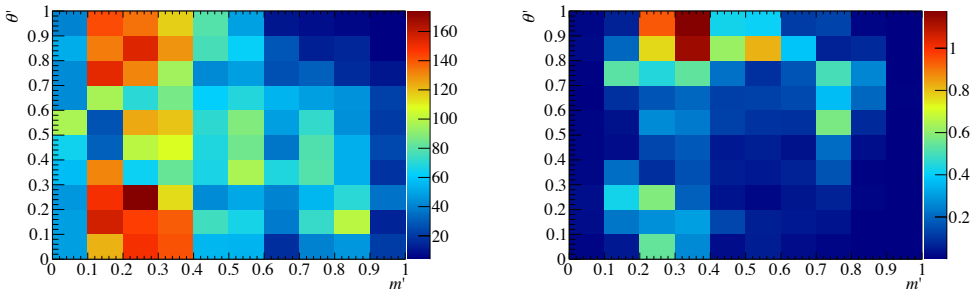

Figure 7.8: Square Dalitz-plot distributions for (left) uncorrected and (right) re-weighted $B^0 \to K^0_S\pi^+\pi^-$ simulated samples. Note that only the relative variation across the phase space is relevant in modelling this contribution.

7.5.2 $B^0 \to K^0_S\pi^+\pi^-$ crossfeeds

Analogously to the mass-fit procedure, phase-space maps for misidentified $B^0 \to K^0_S\pi^+\pi^-$ decays are derived from simulated samples re-weighted by the `PIDCalib` and true-signal Dalitz-plot information. Figure 7.8 shows an example distribution obtained with this approach. Similar behaviour is seen for the remaining trigger and K^0_S conditions.

7.6 Dalitz-plot fitting

The strategy implemented in the determination of the nominal amplitude model and in the evaluation of the data fit results is given as

i. Define a signal window in the B^0_s candidate invariant mass spectrum around the B^0_s signal peak, in order to enhance the purity of the sample entering the DP fit. A window of $\pm 2.5\sigma$ was taken, where σ is the fitted width of the B^0_s peak, which can vary for each K^0_S category and year condition;

ii. Obtain efficiency variation maps across the Dalitz plot;

iii. Determine the DP distribution(s) of background events in the B^0_s signal region;

iv. Identify which resonances must be added to the fit model – the fit is not blind. This is achieved by including contributions that are expected, and then removing those which prove not to be significant;

v. The significance of a given resonant contribution is evaluated by considering the change in the negative log-likelihood values obtained with and without

that resonance included in the fit. [4] Three scenarios are considered

- Contributions that cause a change of less than 9 units of 2ΔNLL are considered not to be significant and are excluded from the model;
- Those that cause a change greater than 25 units of 2ΔNLL are considered to be significant and are included in the model;
- For those that fall between 9 and 25 units, ensembles of simulated pseudo-experiments are generated with parameters corresponding to the best fit for the model excluding the resonance and in the following each toy is fitted with and without that resonance. The distribution of 2ΔNLL from toys is fitted with a χ^2 shape with the number of degrees of freedom floated. From extrapolating the fitted function, the p-value can be calculated from the fraction of toys where the 2ΔNLL is equal or larger than the value obtained from the fits to data. The p-values gives a robust estimate of the true significance;

vi. The goodness-of-fit of the final model is determined from unbinned approaches.

A simultaneous unbinned Dalitz-plot fit based on the JFIT framework [200] is performed for each event i and signal/background k component as

$$\mathcal{L} = \prod_{i}^{N_c} \left[\sum_{k} N_k \mathcal{P}_k \left(m_i^2(K^{\pm}\pi^{\mp}), m_i^2(K^0_S\pi^{\mp}) \right) \right], \tag{7.11}$$

where N_c and N_k are the number of candidates and yields, respectively. These are examined for each final state category: $K^0_S K^+\pi^-$ and $K^0_S K^-\pi^+$ decay channels; DD and LL K^0_S reconstructions; and trigger running periods 2011, 2012a and 2012b. Note that the signal PDFs are multiplied by the appropriate efficiency function for each condition. Although all parameters for a given $K^0_S K^{\pm}\pi^{\mp}$ final state are shared for the K^0_S and year hypotheses, the amplitudes for $K^0_S K^+\pi^-$ and $K^0_S K^-\pi^+$ configurations are considered independently in the model, unless stated otherwise.

7.6.1 Resonant contributions

The nominal fit model includes all of the resonances listed in Table 7.3. Further details on the parametrisations used are given in Sec. 3.2.2.

[4] Note that this so-called stepwise model reduction approach is known to be non optimal [198]. This is related to a choice of a pre-defined threshold significance value and the absence of a mechanism to consider the addition of two interfering amplitudes in the same examination - which is of great relevance for Dalitz-plot analyses [199]. In this work, this standard procedure is nevertheless assumed to be a good approximation.

The $K\pi$ S-wave

Among the several different possibilities to describe the $K\pi$ S-wave described in App. C.1, the LASS parametrisation is found to give the best fit to data. Note however that there are potentially physical reasons to have different values for the LASS parameters of the $\overline{(}\overline{K}^{*}_{0}\overline{)}(1430)^{0}$ and $K^{*}_{0}(1430)^{\pm}$ resonances. In particular, since there are different diagrams involved for the production of each of these components, the ratio between the resonant and nonresonant parts in each case may differ. However, the data sample sizes available in these studies are relatively small, which reduces significantly the ability to float these parameters. Instead, these features are addressed in the systematic uncertainties related to the choice of the model. Additional discussions about the main lineshapes investigated are given in Appendix C.2.

The $K^{0}_{S}K^{\pm}$ invariant mass

The distribution of events in the $K^{0}_{S}K^{\pm}$ invariant mass spectrum does not indicate any obvious contribution. Nonetheless, it is possible that some resonance such as $a_2(1320)^{\pm}$ or even contributions from the tail of $a_0(980)^{\pm}$ states can appear. This has been addressed in the construction of the signal model, from which it is found from data that none of these contributions is significant.

Nonresonant

Nonresonant components have been investigated by including independent contributions in the pairs $m(K^{\pm}\pi^{\mp})$ and $m(K^{0}_{S}\pi^{\mp})$, with the intention to provide a more generic form than the LASS shape for the $K\pi$ S-wave contributions. In other words, these nonresonant terms replace the effective range components in the LASS parametrisation and receive additional isobar parameters. These components are

Table 7.3: List of resonances included in the fit to the data sample and corresponding parameters (and uncertainties) obtained from PDG [28].

Resonance	Spin	Model	Mass (MeV/c^2)	Width (MeV)
$\overline{(}\overline{K}^{*}\overline{)}(892)^{0}$	1	Rel BW	895.81 ± 0.19	47.4 ± 0.6
$K^{*}(892)^{\pm}$	1	Rel BW	891.66 ± 0.26	50.8 ± 0.9
$\overline{(}\overline{K}^{*}_{0}\overline{)}(1430)^{0}$	0	LASS	1425 ± 50	270 ± 80
$K^{*}_{0}(1430)^{\pm}$	0	LASS	1425 ± 50	270 ± 80
$\overline{(}\overline{K}^{*}_{2}\overline{)}(1430)^{0}$	2	Rel BW	1432.4 ± 1.3	109 ± 5
$K^{*}_{2}(1430)^{\pm}$	2	Rel BW	1425.6 ± 1.5	98.5 ± 2.7

described by exponential terms, each controlled by a given parameter α, which may be determined from the fit to data. This alternative model has been investigated and disfavoured in this analysis. Further details are given in Appendix C.2.4.

7.6.2 Results of the data fit

The results of the fit are shown in Tables 7.4 and 7.5 for the $K^0_S K^+\pi^-$ and $K^0_S K^-\pi^+$ final states, respectively. The real and imaginary parts of the amplitudes, which are the fitted parameters, are given along with the fit fractions of each component. The interference fit fractions are given in Tables 7.6 and 7.7. The $K^*(892)^+$ and $K^*(892)^-$ contributions serve as reference amplitudes, with fixed coefficients, in each of the final states. The statistical uncertainties for the real and imaginary parts of the amplitudes are obtained from the uncertainties returned by the fit, while statistical uncertainties for fit fractions are determined using toy simulation. Note that the results for $K^0_S K^+\pi^-$ and $K^0_S K^-\pi^+$ are consistent, indicating that there is no visible *CP* violation at this level of precision.

However, the real and imaginary parameters obtained for the two final states are rather different, which has been further investigated. In particular, potential effects related to the simplification of the amplitude model (Sec. 3.3), *CP* violation and even an instability of the fit could potentially cause such a difference. The ensembles utilised to determine the statistical uncertainties on the fit fractions are used in order to verify the behaviour of the fit. Figure 7.9 shows the resulting complex parameter distributions. The first important feature of these plots is that there is a clear stability in the determination of the fit fraction parameters. It can also be noticed that whilst the relative phases for the charged resonances can be obtained reasonably well, the sensitivity for the neutral ones are significantly affected. Moreover, there is a better precision for the $K^0_S K^-\pi^+$ final states, which could be associated with the slightly larger sample. An alternative scenario has been verified by using the $\overline{(K)}^{*0}(892)$ resonance as a reference amplitude instead of the charged $K^{*\pm}(892)$. Although better precision is achieved for the isobar coefficients, the same fit fractions are obtained. Since this is the only relevant information in this work, the main conclusion is that there is no bias caused by differences seen in the real and imaginary parameters.

Invariant mass distributions of data and toy simulation generated from the fit model can be seen in Fig. 7.10, for both $K^0_S K^+\pi^-$ and $K^0_S K^-\pi^+$ final states. These correspond to the combined K^0_S and year datasets. The fit model appears to fit the data very well in these projections, with only a few points lying away from the blue line. Some noticeable differences between the two final states in each invariant

Table 7.4: Results of the default fit to data in the $K^0_S K^+\pi^-$ Dalitz plot. The statistical uncertainties are evaluated from toy simulation. Note that the sum of the fit fractions need not be 100% due to interference effects (*e.g.* between the two $K^*_0(1430)$ components). Note that the $K^*(892)^-$ resonance is used as reference.

		Isobar model coefficients	
Resonance	Fit fraction (%)	Real part	Imaginary part
$K^*(892)^-$	14.8 ± 2.3	1.00	0.00
$K^*_0(1430)^-$	30.2 ± 3.9	-0.11 ± 0.35	1.42 ± 0.11
$K^*_2(1430)^-$	3.2 ± 1.4	-0.42 ± 0.12	-0.20 ± 0.15
$\overline{K}^*(892)^0$	13.9 ± 2.9	0.40 ± 0.44	-0.88 ± 0.20
$\overline{K}^*_0(1430)^0$	32.7 ± 3.1	0.34 ± 0.58	1.45 ± 0.23
$\overline{K}^*_2(1430)^0$	6.9 ± 2.8	-0.64 ± 0.16	-0.24 ± 0.27
Total fit fraction	102		

Table 7.5: Results of the default fit to data in the $K^0_S K^-\pi^+$ Dalitz plot. The statistical uncertainties are evaluated from toy simulation. Note that the $K^*(892)^+$ resonance is used as reference.

		Isobar model coefficients	
Resonance	Fit fraction (%)	Real part	Imaginary part
$K^*(892)^+$	14.0 ± 1.8	1.00	0.00
$K^*_0(1430)^+$	27.4 ± 3.7	-1.26 ± 0.18	-0.61 ± 0.21
$K^*_2(1430)^+$	5.7 ± 1.9	0.56 ± 0.13	-0.31 ± 0.15
$K^*(892)^0$	19.2 ± 3.0	0.53 ± 0.50	1.04 ± 0.29
$K^*_0(1430)^0$	28.7 ± 4.0	-1.27 ± 0.26	-0.65 ± 0.48
$K^*_2(1430)^0$	6.4 ± 2.3	0.67 ± 0.15	0.04 ± 0.27
Total fit fraction	101		

mass pair are observed. [5] These discrepancies can be potentially associated to *CP* violation effects, which can be addressed by a model-independent analysis but could also show up in a model-dependent fit. Since only the later approach is attempted in this thesis and the interpretation of this behaviour is limited with the given model simplification, no further details on this is given. Furthermore, the distribution of the helicity angle projections in the region of resonant structures are particularly useful to check the agreement between the fit and the data. Figures 7.11 and 7.12 show zooms of the $K^*(892)$ (below $1.0\,\text{GeV}/c^2$) and $K^*(1430)$ (within $[1.1 - 1.6]\,\text{GeV}/c^2$) regions. The first region is very well understood, dominated by the spin-1 $K^*(892)$

[5] A Kolmogorov-Smirnov test has been performed to determine if the corresponding distributions are likely to originate from a common parent distribution or not. The resulting values are 0.004, 0.294 and 0.027 for the $K\pi$, πK^0_S and $K K^0_S$ invariant mass pairs, respectively. Note that since these are three projections of the same data, the values obtained from the Kolmogorov-Smirnov test are correlated.

Table 7.6: Interference fit fractions (%) from the nominal Dalitz plot fit to the $K^0_S K^+\pi^-$ final state. The amplitudes are: (A_0) $K^*(892)^-$, (A_1) $K^*_0(1430)^-$, (A_2) $K^*_2(1430)^-$, (A_3) $\overline{K}^*(892)^0$, (A_4) $\overline{K}^*_0(1430)^0$ and (A_5) $\overline{K}^*_2(1430)^0$.

	A_0	A_1	A_2	A_3	A_4	A_5
A_0	14.8	0.0	0.0	0.4	2.2	−0.9
A_1		30.2	0.0	0.6	0.0	−2.9
A_2			3.2	−0.1	−1.7	0.4
A_3				13.9	0.1	0.0
A_4					32.7	0.0
A_5						6.7

Table 7.7: Interference fit fractions (%) from the nominal Dalitz plot fit to the $K^0_S K^-\pi^+$ final state. The amplitudes are: (A_0) $K^*(892)^+$, (A_1) $K^*_0(1430)^+$, (A_2) $K^*_2(1430)^+$, (A_3) $K^*(892)^0$, (A_4) $K^*_0(1430)^0$ and (A_5) $K^*_2(1430)^0$.

	A_0	A_1	A_2	A_3	A_4	A_5
A_0	14.0	0.0	0.0	0.6	−1.0	0.8
A_1		27.4	0.0	1.3	0.0	−1.3
A_2			5.7	−0.1	−2.2	0.5
A_3				19.2	0.1	0.0
A_4					28.7	0.0
A_5						6.4

resonances. Notice the significant effect of the efficiency on the extremes of the distribution, which are well reproduced by the fit model. The only pronounced discrepancies are observed in the $\cos(K^0_S\pi^-)$ helicity angle in a single bin of the vector region around $[-0.5, -0.4]$ and at low values of $\cos(K^0_S\pi^-)$ in the scalar region. The first effect corresponds to the excesses seen around $2.0 - 2.5$ GeV/c^2 in the $K^+\pi^-$ invariant mass plots, and is consistent with being a statistical effect. The latter effect has been investigated and is found to be related to the fixed parameters of the LASS shape. Variations of these parameters, and hence the discrepancy, are accounted for in the systematic uncertainties. The regions at higher mass, where the $K^*_0(1430)$ and $K^*_2(1430)$ resonances appear, indicate the dominance of the scalar component, which is reflected in the fit fractions of the two components. For completeness, a zoom on this region up to 2.0 GeV/c^2 is shown in Fig. 7.13. The good agreement of the fit model compared to the data in these slices suggests that no significant resonant contribution is missing, and the model represents well the underlying physics.

GoF evaluation

Following the establishment of the baseline model, the series of unbinned GoF methods mentioned in Sec. 7.3.4 are applied and the results are shown in Appendix C. The goodness of the fit values reported lie within the satisfactory range as determined from the toy simulation studies, giving further confidence in the quality of the fit.

Secondary minima

As noted in Sec. 7.3.3, there can often be multiple solutions in Dalitz plot fits. To be sure to find the global minimum, each fit is repeated 100 times with randomised starting parameters. The solution with the smallest negative log-likelihood is taken as the default result, but other secondary minima are found with $2\Delta NLL$ values that are respectively 5.73, 7.72, 8.43 and 9.64 units from the global minimum. Since some of these solutions are not well separated from the global minimum, a series of studies have been performed to investigate this feature. It has been noticed that these provide no further distinct solution, and therefore, these can be neglected as multiple results.

7.7 Systematic uncertainties

There are two categories of systematic uncertainties that may affect the extracted values of the observables in the Dalitz-plot fit: inaccuracy in the experimental inputs used in the fit and the choice of the nominal parametrisation. The systematic uncertainties on the fit fractions are gathered in Table 7.8. Note that the information

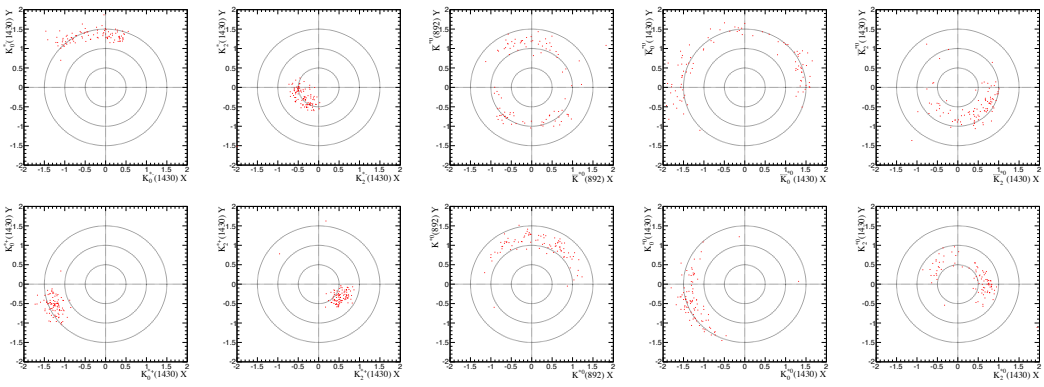

Figure 7.9: Isobar coefficients of the amplitude obtained from toy simulated samples for each resonance in the fit.

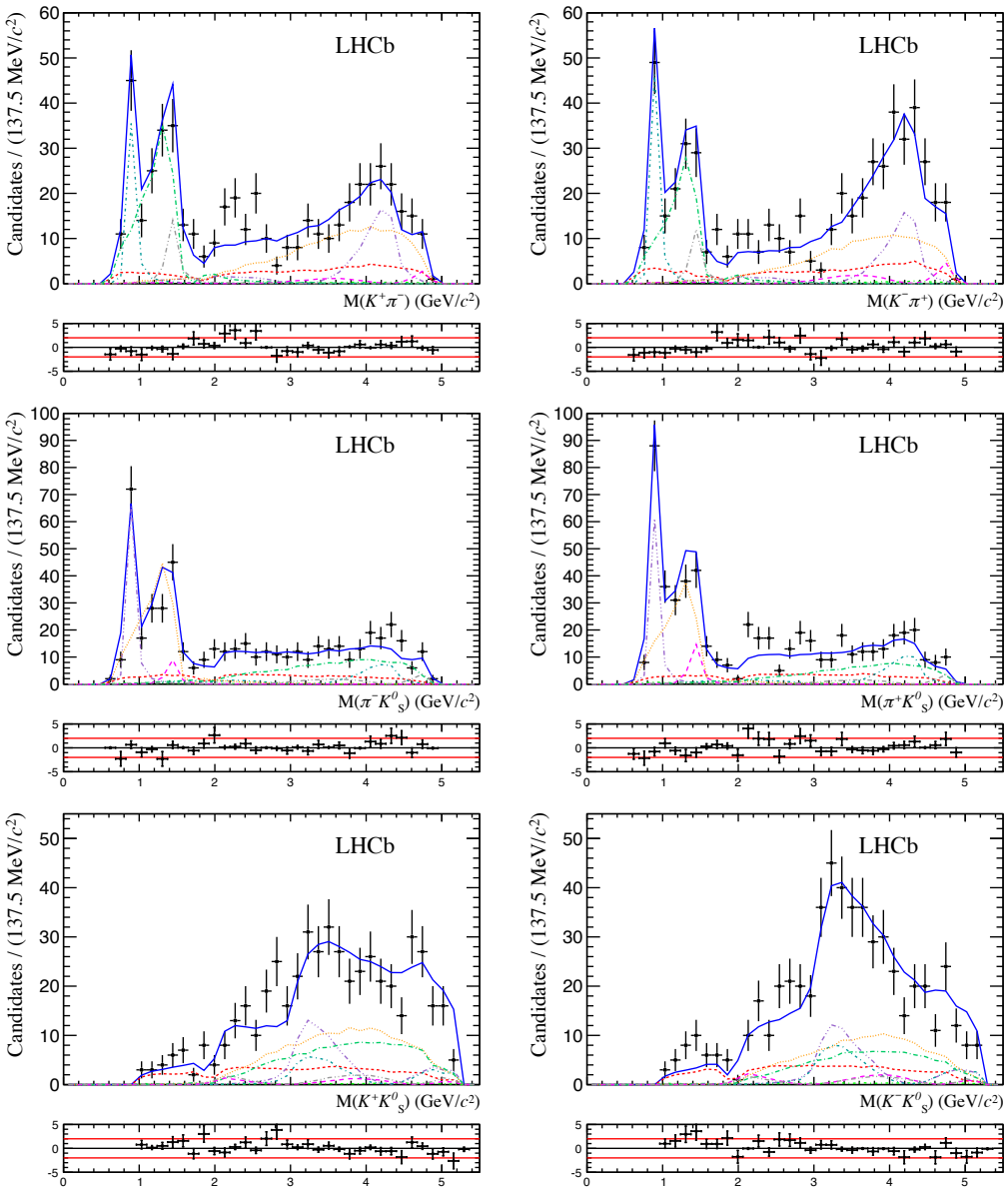

Figure 7.10: Invariant mass distributions of the combined (left) $K^0_S K^+\pi^-$ and (right) $K^0_S K^-\pi^+$ Dalitz plot fits for (top) $m(K^\pm\pi^\mp)$, (middle) $m(K^0_S\pi^\mp)$ and (bottom) $m(K^0_S K^\pm)$. The full fit is shown in blue, background from combinatorics in red, cross-feed from $B^0 \to K^0_S\pi^+\pi^-$ in light green and the data is given in black points. The resonance components are shown for $K^{*\pm}(892)$ in violet dash triple-dotted, $K^{*\pm}_0(1430)$ in orange dotted, $K^{*\pm}_2(1430)$ in magenta long-dashed, $\overset{(-)}{K}{}^{*0}(892)$ in dark cyan dash dotted, $\overset{(-)}{K}{}^{*0}_0(1430)$ in green long-dash dotted and $\overset{(-)}{K}{}^{*0}_2(1430)$ gray long-dash double-dotted.

on the magnitude and phase have been omitted, since only branching fractions are reported as results.

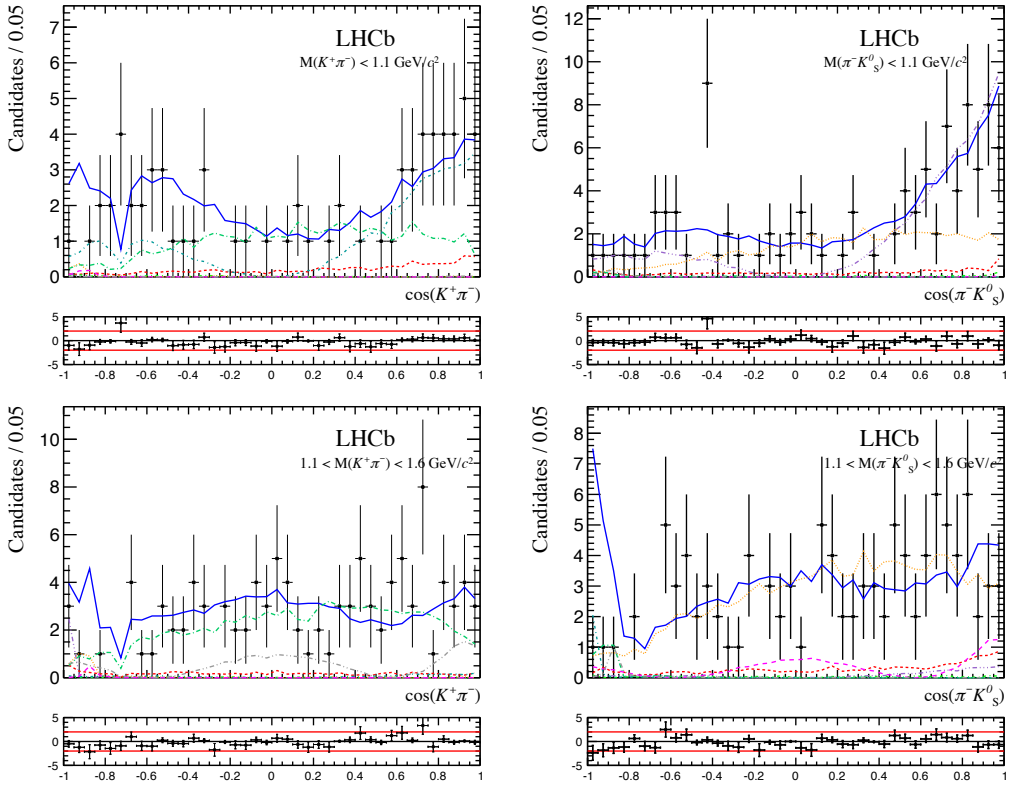

Figure 7.11: Helicity angle projections of the combined $K^0_S K^+\pi^-$ Dalitz plot fit for the (top) $K^*(892)$ and (bottom) $K^*(1430)$ regions in the (left) $m(K^+\pi^-)$ and (right) $m(K^0_S\pi^-)$ pairs. The full fit is shown in blue, background from combinatorics in red, cross-feed from $B^0 \to K^0_S\pi^+\pi^-$ in light green and the data is given in black points. Refer to Fig. 7.10 for resonance components details.

7.7.1 Experimental uncertainties

The experimental systematic uncertainties originate from the imprecision introduced from the external inputs in the Dalitz-plot fit, such as fixed yields and efficiency/background phase-space maps. These are evaluated as follows

i. Uncertainties on the signal and background yields are examined from scaling the errors obtained from the whole mass fit range to the DP fit signal region. While statistical uncertainties are available from the covariance matrix in the nominal result, systematics affecting the yields are extracted similarly as for the branching fraction measurement in Sec. 6.2.6. These are propagated into the amplitude fit by generating a series of ensembles in order to address the uncertainties related to the yield extraction. This is obtained by either the RMS of the fitted quantity over the ensemble or the mean difference to the nominal model.

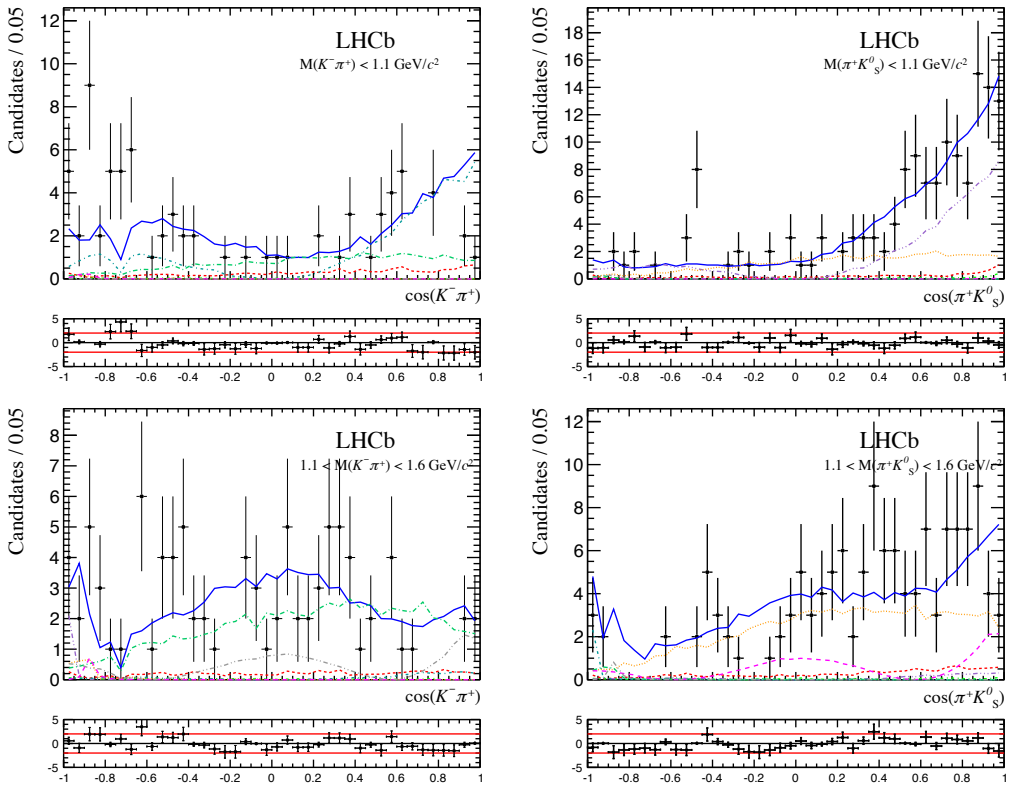

Figure 7.12: Helicity angle projections of the combined $K^0_S K^-\pi^+$ Dalitz plot fit for the (top) $K^*(892)$ and (bottom) $K^*(1430)$ regions in the (left) $m(K^-\pi^+)$ and (right) $m(K^0_S\pi^+)$ pairs. The full fit is shown in blue, background from combinatorics in red, cross-feed from $B^0 \to K^0_S\pi^+\pi^-$ in light green and the data is given in black points. Refer to Fig. 7.10 for resonance components details.

ii. Background variations over the phase space from both combinatorics and cross-feeds are estimated by varying the histograms used to model the shape within their statistical uncertainties to create an ensemble of new histograms. The data is refitted using each new histogram and the systematic uncertainty is taken to be the RMS of the fitted quantity over the ensemble.

iii. Imperfections on the phase-space efficiency modelling are determined by repeating the Dalitz-plot fit using new histograms obtained by varying each bin within its uncertainties, similarly to the background distributions. Moreover, uncertainties related to the `PIDCalib` method are examined by varying the binning scheme choice.

iv. Pseudo-experiments generated from the nominal results are used to quantify any intrinsic bias in the fit procedure. These are evaluated as the sum in

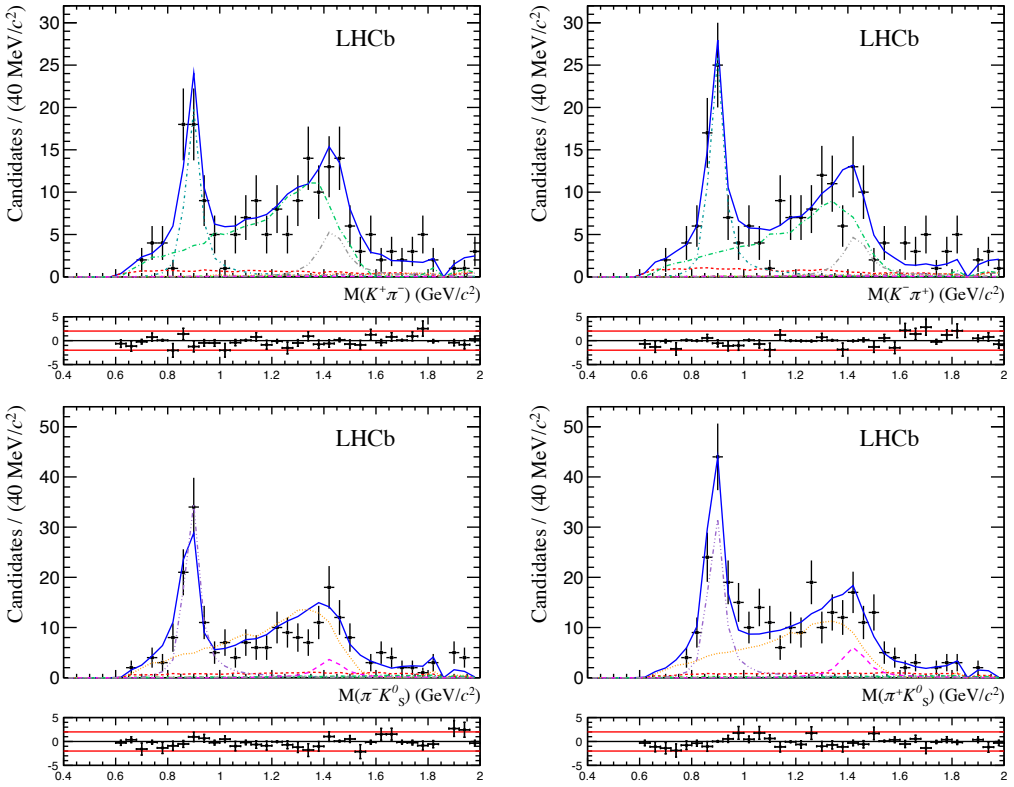

Figure 7.13: Invariant mass distributions of the combined (left) $K^0_S K^+\pi^-$ and (right) $K^0_S K^-\pi^+$ Dalitz plot fits for (top) $m(K^\pm\pi^\mp)$ and (bottom) $m(K^0_S\pi^\mp)$ up to 2.0 GeV/c^2. The full fit is shown in blue, background from combinatorics in red, cross-feed from $B^0 \to K^0_S\pi^+\pi^-$ in light green and the data is given in black points. Refer to Fig. 7.10 for resonance components details.

quadrature of the mean difference between the nominal and sampled values and the corresponding uncertainty.

7.7.2 Model uncertainties

The choice of the nominal model with respect to either the lineshapes or the signal contributions, introduces important uncertainties to the measurement

i. Each resonant contribution has fixed parameters in the Dalitz-plot fit. These include masses and widths, Blatt–Weisskopf radius and the LASS parameters r and a. The fit is repeated many times varying each of these fixed parameters within its uncertainties. The RMS of the distribution of the change in each fitted parameter is taken as the systematic uncertainty.

ii. The baseline LASS parametrisation for the $K\pi$ S-wave modelling is known to

Table 7.8: Summary of the systematic uncertainties on the fit fractions (%). The columns give the contributions from the different sources described in the text.

	Fit fraction (%) uncertainties							
Resonance	Yields	Eff.	Bkg. sqDP	Fit Bias	Add. Res.	Fixed Par.	Model Alt.	Total
$K^*(892)^-$	0.20	0.38	0.20	1.73	0.08	1.20	0.44	2.21
$K_0^*(1430)^-$	0.15	0.65	0.25	8.10	0.08	3.82	9.36	12.97
$K_2^*(1430)^-$	0.18	0.23	0.15	0.06	0.17	1.51	2.76	3.17
$\overline{K}^*(892)^0$	0.29	0.21	0.14	1.39	0.04	1.86	0.77	2.48
$\overline{K}_0^*(1430)^0$	0.21	0.58	0.41	3.00	0.04	3.91	10.40	11.53
$\overline{K}_2^*(1430)^0$	0.11	0.75	0.35	0.63	0.28	4.47	5.05	6.83
$K^*(892)^+$	0.58	0.40	0.13	0.24	0.29	0.79	0.26	1.16
$K_0^*(1430)^+$	0.77	0.49	0.31	2.36	0.39	4.78	26.20	26.76
$K_2^*(1430)^+$	0.09	0.10	0.17	0.07	0.83	3.02	3.38	4.61
$K^*(892)^0$	0.50	0.13	0.23	0.25	0.09	0.75	1.54	1.82
$K_0^*(1430)^0$	0.51	0.41	0.48	0.06	0.47	2.01	6.50	6.87
$K_2^*(1430)^0$	0.15	0.23	0.21	0.32	0.04	0.95	3.43	3.59

be an approximate form, and uncertainties are assigned by evaluating an alternative parametrisation. This is given by the use of the EFKLLM model, as discussed in Appendix C.2.4. These correspond to the largest systematic uncertainties assigned to this measurement.

iii. The effects of including additional signal components in the fit is examined individually for each contribution. Although $K^*(1410)$ and $K^*(1680)$ resonances have been considered as potential missing components, the resulting values are unrealistic and as such are not considered in the evaluation of this uncertainty. The only systematic effects included corresponds to the insertion of the $a_2(1320)^{\pm}$ resonance.

7.8 Results

The fit fractions of the resonant components can be converted into quasi-two-body branching fractions by multiplying by the values reported in the previous chapter of $\mathcal{B}(B_s^0 \to {}^{(}\overline{K}{}^{)0} K^{\pm}\pi^{\mp}) = (73.6 \pm 5.7 \pm 6.9 \pm 3.0) \times 10^{-6}$ [108], using explicitly

$$\mathcal{B}\left(B_s^0 \to K^* K\right) = \widehat{FF}_j \times \mathcal{B}\left(B_s^0 \to {}^{(}\overline{K}{}^{)0} K^{\pm}\pi^{\mp}\right) , \tag{7.12}$$

where $\widehat{FF}_j$ is given in Eq. 7.9. Note that this corresponds to a measurement of the sum of branching fractions for both initial and both final states. The branching

fractions for the modes of interest are determined to be

$$\begin{aligned}
\mathcal{B}\left(B_s^0 \to K^{*\pm}(892)K^{\mp}\right) &= (10.6 \pm 0.99 \pm 1.06 \pm 1.36) \times 10^{-6}\,, \\
\mathcal{B}\left(B_s^0 \to K_0^{*\pm}(1430)K^{\mp}\right) &= (21.2 \pm 2.05 \pm 13.8 \pm 2.72) \times 10^{-6}\,, \\
\mathcal{B}\left(B_s^0 \to K_2^{*\pm}(1430)K^{\mp}\right) &= (3.30 \pm 0.88 \pm 2.86 \pm 0.42) \times 10^{-6}\,, \\
\mathcal{B}\left(B_s^0 \to \overline{(}K\overline{)}^{*0}(892)\,\overline{(}K\overline{)}^{0}\right) &= (12.2 \pm 1.44 \pm 1.38 \pm 1.57) \times 10^{-6}\,, \\
\mathcal{B}\left(B_s^0 \to \overline{(}K\overline{)}_0^{*0}(1430)\,\overline{(}K\overline{)}^{0}\right) &= (22.6 \pm 2.00 \pm 6.42 \pm 2.89) \times 10^{-6}\,, \\
\mathcal{B}\left(B_s^0 \to \overline{(}K\overline{)}_2^{*0}(1430)\,\overline{(}K\overline{)}^{0}\right) &= (4.87 \pm 1.42 \pm 3.84 \pm 1.36) \times 10^{-6}\,,
\end{aligned}$$

where the uncertainties are respectively statistical, systematic and due to the uncertainty on $\mathcal{B}(B_s^0 \to \overline{(}K\overline{)}^0 K^{\pm}\pi^{\mp})$.

The measurements of the previously observed decay modes $B_s^0 \to K^{*\pm}(892)K^{\mp}$ and $B_s^0 \to \overline{(}K\overline{)}^{*0}(892)\,\overline{(}K\overline{)}^{0}$ are in good agreement with, and more precise than, the results reported in Refs. [37] and [38], respectively. Moreover, large systematic uncertainties related to the variation of the $K\pi$ S-wave modelling are observed for the $K_0^{*(0,\pm)}(1430)$ resonances, which limit the first observation of this mode. Notice that larger samples will allow the reduction of both statistical and systematic uncertainties on these results. In particular, flavour tagged approaches should provide appropriate sensitivity to the relative phase and permit *CP* violation measurements for this complex three-body final state.

8 Conclusions

The 2011 and 2012 LHCb dataset, corresponding to an integrated luminosity of 1.0 fb^{-1} and 2.0 fb^{-1} recorded at a centre-of-mass energy of 7 TeV and 8 TeV, respectively, has been analysed in the context of charmless three-body decays of either $B^0_{(s)}$ mesons or beauty baryons with a K^0_S meson in the final state.

As an initial step towards studying the phenomenology of these transitions, a search to establish the signals of $B^0_{(s)} \to K^0_S h^\pm h'^\mp$ decays in the 2011 dataset has been performed. The decays $B^0_s \to K^0_S K^\pm \pi^\mp$ and $B^0_s \to K^0_S \pi^+ \pi^-$ are observed for the first time. The latter is 5.9 standard deviations including statistical and systematic uncertainties, a clear observation, and the former is even more unambiguous. The decay mode $B^0 \to K^0_S K^\pm \pi^\mp$, previously observed by the BaBar experiment, is confirmed. No significant evidence for $B^0_s \to K^0_S K^+ K^-$ decays is obtained, and a 90 % confidence level is placed on the corresponding branching fraction. The first observation of these B^0_s decay modes is an important milestone towards extracting information on the mixing-induced *CP*-violating phase in the B^0_s system and the weak phase γ from these channels. Moreover, the rich structure of the Dalitz plots, particularly for $B^0_{(s)} \to K^0_S K^\pm \pi^\mp$ decays, is another motivation to extend this programme to the amplitude analyses.

Searches for the previously unobserved decays $\Lambda^0_b(\Xi^0_b) \to K^0_S p h^-$ are also performed in the 1.0 fb^{-1} dataset. The decay channel $\Lambda^0_b \to K^0_S p \pi^-$ is observed for the first time, allowing a measurement of its phase-space integrated *CP* asymmetry, which shows no significant deviation from zero. All presented results, except for those of the branching fractions of $\Lambda^0_b \to \Lambda^+_c \pi^-$ and $\Lambda^0_b \to \Lambda^+_c K^-$, are the first to date. The first observation of a charmless hadronic three-body decay of a b baryon opens a new field of possible amplitude analyses and *CP* violation measurements that will be of great interest to study with larger data samples. A future update of this analysis with the full 2011+2012 dataset is therefore of great appeal, and is

currently under development.

Finally, the first untagged decay-time-integrated amplitude analysis of $B_s^0 \to K_S^0 K^\pm \pi^\mp$ decays has been presented. The amplitude model contains a total of six independent components for each of the $K_S^0 K^+ \pi^-$ and $K_S^0 K^- \pi^+$ final states, consisting of the resonance pairs of $K^*(892)^{0,\pm}$, $K_0^*(1430)^{0,\pm}$ and $K_2^*(1430)^{0,\pm}$. The fit fraction results are converted into branching fractions measurements by multiplying them by the $B_s^0 \to K_S^0 K^\pm \pi^\mp$ inclusive branching fraction. The results for the $B_s^0 \to K^{*\pm}(892) K^\mp$ and $B_s^0 \to K^{*0}(892) K^0$ decay modes are in good agreement with, and more precise than, the previous measurements obtained from a smaller data sample collected by LHCb. All other branching fraction results are first reported measurements. Although larger samples will allow the reduction of both statistical and systematic uncertainties on these measurements, flavour tagged approaches are clearly the most appropriate strategy to be pursued in the future, in order to obtain sensitivity to the relative phases and permit *CP* violation measurements for this interesting but complex three-body final state.

A

Searches for $B^0_{(s)} \to J/\psi\, p\bar{p}$ and $B^+ \to J/\psi\, p\bar{p}\pi^+$ decays

A.1 Preamble

The results of searches for $B^0_{(s)} \to J/\psi\, p\bar{p}$ and $B^+ \to J/\psi\, p\bar{p}\pi^+$ decays published in Ref. [201] are reproduced verbatim in the following. The analysis is based on a data sample, corresponding to an integrated luminosity of $1.0\,\text{fb}^{-1}$ of pp collisions, collected with the LHCb detector. Since these channels include charmonium contributions in the final states and have a very distinct topology to $K^0_S h^\pm h'^\mp$ decays, these results have been removed from the main discussion in the dissertation.

A.2 Introduction

The production of baryon-antibaryon pairs in B meson decays is of significant experimental and theoretical interest. For example, in the case of $p\bar{p}$ pair production, the observed decays $B^0 \to \overline{D}^{(*)0} p\bar{p}$ [202, 203], $B^+ \to K^{(*)+} p\bar{p}$ [204–208], $B^0 \to K^{(*)0} p\bar{p}$ [205, 207] and $B^+ \to \pi^+ p\bar{p}$ [205, 206] all have an enhancement near the $p\bar{p}$ threshold.[1] Possible explanations for this behaviour include the existence of an intermediate state in the $p\bar{p}$ system [209] and short-range correlations between p and $\overline{p}$ in their fragmentation [210–212]. Moreover, for each of these decays, the branching fraction is approximately 10 % that of the corresponding decay with $p\bar{p}$ replaced by $\pi^+\pi^-$ [213]. In contrast, the decay $B^0 \to J/\psi\, p\bar{p}$ has not yet been observed; the most restrictive upper limit being $\mathcal{B}(B^0 \to J/\psi\, p\bar{p}) < 8.3 \times 10^{-7}$ at 90 % confidence level [214], approximately fifty times lower than the branching fraction for $B^0 \to J/\psi\, \pi^+\pi^-$ decays [215]. This result is in tension with the theoretical

[1] Throughout this paper, the inclusion of charge-conjugate processes is implied.

prediction of $\mathcal{B}(B^0 \to J/\psi p\overline{p}) = (1.2 \pm 0.2) \times 10^{-6}$ [216]. Improved experimental information on the $B^0 \to J/\psi p\overline{p}$ decay would help to understand the process of dibaryon production.

In this paper, the results of a search for $B^0 \to J/\psi p\overline{p}$ and $B_s^0 \to J/\psi p\overline{p}$ decays are presented. No prediction or experimental limit exists for the branching fraction $\mathcal{B}(B_s^0 \to J/\psi p\overline{p})$, but it is of interest to measure the suppression relative to $B_s^0 \to J/\psi \pi^+\pi^-$ [217]. In addition, a search for the decay $B^+ \to J/\psi p\overline{p}\pi^+$ is performed, for which no published measurement exists. All branching fractions are measured relative to that of the decay $B_s^0 \to J/\psi \pi^+\pi^-$, which is well suited for this purpose due to its similar topology to the signal decays. Additionally, the lower background level and its more precisely measured branching fraction make it a more suitable normalisation channel than the companion B^0 mode.

A.3 Detector and dataset

The LHCb detector [5] is a single-arm forward spectrometer covering the pseudorapidity range $2 < \eta < 5$, designed for the study of particles containing b or c quarks. The detector includes a high precision tracking system consisting of a silicon-strip vertex detector surrounding the pp interaction region, a large-area silicon-strip detector located upstream of a dipole magnet with a bending power of about 4 Tm, and three stations of silicon-strip detectors and straw drift tubes placed downstream. The combined tracking system provides momentum measurement with relative uncertainty that varies from 0.4% at 5 GeV/c to 0.6% at 100 GeV/c, and impact parameter (IP) resolution of 20 µm for tracks with high transverse momentum ($p_{\rm T}$). Charged hadrons are identified using two ring-imaging Cherenkov detectors [218]. Photon, electron and hadron candidates are identified by a calorimeter system consisting of scintillating-pad and preshower detectors, an electromagnetic calorimeter and a hadronic calorimeter. Muons are identified by a system composed of alternating layers of iron and multiwire proportional chambers [219]. The trigger [142] consists of a hardware stage, based on information from the calorimeter and muon systems, followed by a software stage, which applies a full event reconstruction.

The analysis uses a data sample, corresponding to an integrated luminosity of 1.0 fb^{-1} of pp collision data at a centre-of-mass energy of 7 TeV, collected with the LHCb detector during 2011. Samples of simulated events are also used to determine the signal selection efficiency, to model signal event distributions and to investigate possible background contributions. In the simulation, pp collisions are generated using Pythia 6.4 [220] with a specific LHCb configuration [221]. Decays of hadronic

particles are described by EvtGen [222], in which final state radiation is generated using Photos [223]. The interaction of the generated particles with the detector and its response are implemented using the Geant4 toolkit [224] as described in Ref. [225].

A.4 Trigger and selection requirements

The trigger requirements for this analysis exploit the signature of the $J/\psi \to \mu^+\mu^-$ decay, and hence are the same for the signal and the $B_s^0 \to J/\psi\,\pi^+\pi^-$ control channel. At the hardware stage either one or two identified muon candidates are required. In the case of single muon triggers, the transverse momentum of the candidate is required to be larger than $1.5\,\text{GeV}/c$. For dimuon candidates a requirement on the product of the p_T of the muon candidates is applied, $\sqrt{p_{\text{T}1}p_{\text{T}2}} > 1.3\,\text{GeV}/c$. In the subsequent software trigger, at least one of the final state muons is required to have both $p_\text{T} > 1.0\,\text{GeV}/c$ and IP $> 100\,\mu\text{m}$. Finally, the muon tracks are required to form a vertex that is significantly displaced from the primary vertices (PVs) and to have invariant mass within $120\,\text{MeV}/c^2$ of the known J/ψ mass, $m_{J/\psi}$ [213].

The selection uses a multivariate algorithm (hereafter referred to as MVA) to reject background. A neural network is trained on data using the $B_s^0 \to J/\psi\,\pi^+\pi^-$ control channel as a proxy for the signal decays. Preselection criteria are applied in order to obtain a clean sample of the control channel decays. The muons from the J/ψ decay must be well identified and have $p_\text{T} > 500\,\text{MeV}/c$. They should also form a vertex with $\chi^2_\text{vtx} < 12$ and have invariant mass within the range $-48 < m_{\mu^+\mu^-} - m_{J/\psi} < 43\,\text{MeV}/c^2$. The separation of the J/ψ vertex from all PVs must be greater than 3 mm. The pion candidates must be inconsistent with the muon hypothesis, have $p_\text{T} > 200\,\text{MeV}/c$ and have minimum χ^2_IP with respect to any of the PVs greater than 9, where the χ^2_IP is defined as the difference in χ^2 of a given PV reconstructed with and without the considered track. In addition, the scalar sum of their transverse momenta must be greater than $600\,\text{MeV}/c$. The B candidate formed from the J/ψ and two oppositely charged hadron candidates should have $\chi^2_\text{vtx} < 20$ and a minimum χ^2_IP with respect to any of the PVs less than 30. In addition, the cosine of the angle between the B candidate momentum vector and the line joining the associated PV and the B decay vertex (B pointing angle) should be greater than 0.99994.

The mass distribution of candidate $B^0_{(s)} \to J/\psi\,\pi^+\pi^-$ decays remaining after the preselection is then fitted in order to obtain signal and background distributions of the variables that enter the MVA training, using the *sPlot* technique [154]. The

fit model is described in Sec. A.5. The variables that enter the MVA training are chosen to minimise any difference in the selection between the signal and control channels. Different selection algorithms are trained for the $B^0_{(s)} \to J/\psi p\overline{p}$ mode and for the $B^+ \to J/\psi p\overline{p}\pi^+$ mode, with slightly different sets of variables. The variables in common between the selections are the minimum $\chi^2_{\rm IP}$ of the B candidate; the cosine of the B pointing angle; the χ^2 of the B and J/ψ candidate vertex fits; the χ^2 per degree of freedom of the track fit of the charged hadrons; and the minimum IP of the muon candidates. For the $B^0_{(s)} \to J/\psi p\overline{p}$ selection the following additional variables are included: the $p_{\rm T}$ of the charged hadron and J/ψ candidates; the $p_{\rm T}$ of the B candidate; and the flight distance and flight distance significance squared of the B candidate from its associated PV. For the $B^+ \to J/\psi p\overline{p}\pi^+$ selection only the momentum and $p_{\rm T}$ of the muon candidates are included as additional variables.

The MVAs are trained using the NeuroBayes package [226]. Two different figures of merit are considered to find the optimal MVA requirement. The first is that suggested in Ref. [157]

$$\mathcal{Q}_1 = \frac{\epsilon_{\rm MVA}}{a/2 + \sqrt{B_{\rm MVA}}}\,, \tag{A.1}$$

where $a = 3$ and quantifies the target level of significance, $\epsilon_{\rm MVA}$ is the efficiency of the selection of the signal candidates, which is determined from simulated signal samples, and $B_{\rm MVA}$ is the expected number of background events in the signal region; which is estimated by performing a fit to the invariant mass distribution of the data sidebands. The second figure of merit is an estimate of the expected 90 % confidence level upper limit on the branching fraction in the case that no signal is observed

$$\mathcal{Q}_2 = \frac{1.64\,\sigma_{N_{\rm sig}}}{\epsilon_{\rm MVA}}\,, \tag{A.2}$$

where $\sigma_{N_{\rm sig}}$ is the expected uncertainty on the signal yield, which is estimated from pseudo-experiments generated with the background-only hypothesis. The maximum of the first and the minimum of the second figure of merit are found to occur at very similar values. For the $B^0_{(s)} \to J/\psi p\overline{p}$ ($B^+ \to J/\psi p\overline{p}\pi^+$) decay, requirements are chosen such that approximately 50 % (99 %) of the signal is retained while reducing the background to 20 % (70 %) of its level prior to the cut. The background level for the $B^+ \to J/\psi p\overline{p}\pi^+$ decay is very low due to its proximity to threshold, and only a loose MVA requirement is necessary.

The particle identification (PID) selection for the signal modes is optimised in a similar way using Eq. (A.1). It is found that, for the signal channels, placing a tight requirement on the proton with a higher value for the logarithm of the

likelihood ratio of the proton and pion hypotheses [218] and a looser requirement on the other proton results in much better performance than applying the same requirement on both protons. No PID requirements are made on the pion track in the $B^+ \to J/\psi\, p\overline{p}\pi^+$ mode.

The acceptance and selection efficiencies are determined from simulated signal samples, except for those of the PID requirements, which are determined from data control samples to avoid biases due to known discrepancies between data and simulation. High-purity control samples of $\Lambda \to p\pi^-$ ($D^0 \to K^-\pi^+$) decays with no PID selection requirements applied are used to tabulate efficiencies for protons (pions) as a function of their momentum and $p_{\rm T}$. The kinematics of the simulated signal events are then used to determine an average efficiency. Possible variations of the efficiencies over the multibody phase space are considered. The efficiencies are determined in bins of the Dalitz plot, $m^2_{J/\psi h^+}$ vs. $m^2_{h^+h^-}$, where $h = \pi, p$; the J/ψ decay angle (defined as the angle between the μ^+ and the $p\overline{p}$ system in the J/ψ rest frame); and the angle between the decay planes of the J/ψ and the h^+h^- system. The variation with the Dalitz plot variables is the most significant. For the $B^0_s \to J/\psi\,\pi^+\pi^-$ control sample, the distribution of the signal in the phase space variables is determined using the *sPlot*technique and these distributions are used to find a weighted average efficiency.

A number of possible background modes, such as cross-feed from $B^0_{(s)} \to J/\psi\, h^+h'^-$ final states (where $h^{(\prime)} = \pi, K$), have been studied using simulation. None of these are found to give a significant peaking contribution to the B candidate invariant mass distribution once all the selection criteria had been applied. Therefore, all backgrounds in the fits to the mass distributions of $B^0_{(s)} \to J/\psi\, p\overline{p}$ and $B^+ \to J/\psi\, p\overline{p}\pi^+$ candidates are considered as being combinatorial in nature. For the fits to the $B^0_s \to J/\psi\,\pi^+\pi^-$ control channel, some particular backgrounds are taken into account, as described in the following section.

After all selection requirements are applied, 854 and 404 candidates are found in the invariant mass ranges $[5167, 5478]\,{\rm MeV}/c^2$ and $[5129, 5429]\,{\rm MeV}/c^2$ for $B^0_{(s)} \to J/\psi\, p\overline{p}$ and $B^+ \to J/\psi\, p\overline{p}\pi^+$ decays, respectively. The efficiency ratios, with respect to the $B^0_s \to J/\psi\,\pi^+\pi^-$ normalisation channel, including contributions from detector acceptance, trigger and selection criteria (but not from PID) are 0.92 ± 0.16, 0.85 ± 0.12 and 0.17 ± 0.04 for $B^0 \to J/\psi\, p\overline{p}$, $B^0_s \to J/\psi\, p\overline{p}$ and $B^+ \to J/\psi\, p\overline{p}\pi^+$, respectively. In addition, the relative PID efficiencies are found to be 0.78 ± 0.02, 0.79 ± 0.02 and 1.00 ± 0.03 for $B^0 \to J/\psi\, p\overline{p}$, $B^0_s \to J/\psi\, p\overline{p}$ and $B^+ \to J/\psi\, p\overline{p}\pi^+$, respectively. The systematic uncertainties arising from these values are discussed in Sec. A.6.

A.5 Fit model and results

Signal and background event yields are estimated by performing unbinned extended maximum likelihood fits to the invariant mass distributions of the B candidates. The signal probability density functions (PDFs) are parametrised as the sum of two Crystal Ball (CB) functions [174], where the power law tails are on opposite sides of the peak. This form is appropriate to describe the asymmetric tails that result from a combination of the effects of final state radiation and stochastic tracking imperfections. The two CB functions are constrained to have the same peak position, equal to the value fitted in the simulation. The resolution parameters are allowed to vary within a Gaussian constraint, with the central value taken from the simulation and scaled by the ratio of the values found in the control channel data and corresponding simulation. The proximity to threshold of the signal decays provides a mass resolution of 1–3 MeV/c^2, whereas for the normalisation channel it is 6–9 MeV/c^2. The tail parameters and the relative normalisation of the two CB functions are taken from the simulated distributions and fixed for the fits to data.

A second-order polynomial function is used to describe the combinatorial background component in the $B^0_{(s)} \to J/\psi\, p\overline{p}$ spectrum while an exponential function is used for the same component in the $B^+ \to J/\psi\, p\overline{p}\pi^+$ and $B^0_{(s)} \to J/\psi\, \pi^+\pi^-$ channels. The parameters of these functions are allowed to vary in the fits. There are several specific backgrounds that contribute to the $B^0_{(s)} \to J/\psi\, \pi^+\pi^-$ invariant mass spectrum [215], which need to be explicitly modelled. In particular, the decay $B^0 \to J/\psi\, K^+\pi^-$, where a kaon is misidentified as a pion, is modelled by an exponential function. The yield of this contribution is allowed to vary in order to enable a better modelling of the background in the low mass region. Two additional sources of peaking background are considered: partially reconstructed decays, such as $B^0_s \to J/\psi\, \eta'(\rho\gamma)$; and decays where an additional low momentum pion is included from the rest of the event, such as $B^+ \to J/\psi\, K^+$. Both distributions are fitted with a non-parametric kernel estimation, with shapes fixed from simulation. The yields of these components are also fixed to values estimated from the known branching fractions and selection efficiencies evaluated from simulation.

In order to validate the stability of the fit, a series of pseudo-experiments have been generated using the PDFs described above. The experiments are conducted for a wide range of generated signal yields. No significant bias is observed in any of the simulation ensembles; any residual bias being accounted for as a source of systematic uncertainty.

The fits to the data are shown in Figs. A.1 and A.2. The signal yields are

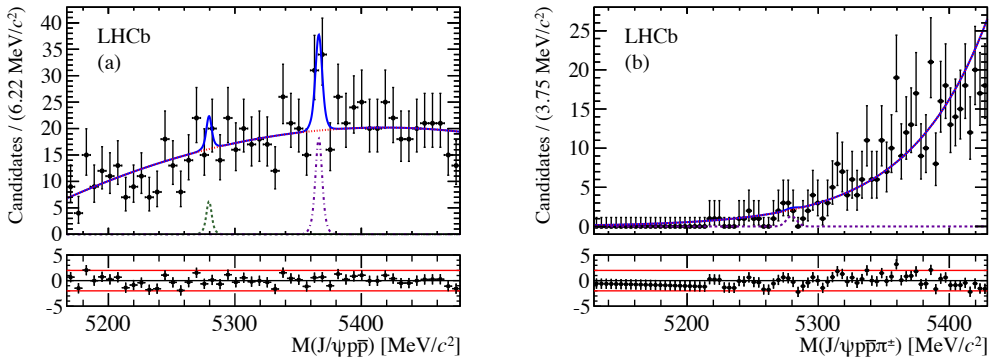

Figure A.1: Invariant mass distribution of (a) $B^0_{(s)} \to J/\psi\, p\overline{p}$ and (b) $B^+ \to J/\psi\, p\overline{p}\pi^+$ candidates after the full selection. Each component of the fit model is displayed on the plot: the signal PDFs are represented by the dot-dashed violet and dashed green line; the combinatorial background by the dotted red line; and the overall fit is given by the solid blue line. The fit pulls are also shown, with the red lines corresponding to $2\,\sigma$. The $B^+ \to J/\psi\, p\overline{p}\pi^+$ yield is multiplied by five in order to make the signal position visible.

$N(B^0 \to J/\psi\, p\overline{p}) = 5.9\ ^{+5.9}_{-5.1} \pm 2.5$, $N(B^0_s \to J/\psi\, p\overline{p}) = 21.3\ ^{+8.6}_{-7.8} \pm 2.6$ and $N(B^+ \to J/\psi\, p\overline{p}\pi^+) = 0.7\ ^{+3.2}_{-2.5} \pm 0.7$, where the first uncertainties are statistical and the second are systematic and are described in the next section. The numbers of events in the $B^0_s \to J/\psi\, \pi^+\pi^-$ normalisation channel are found to be 2120 ± 50 and 4021 ± 76 (statistical uncertainties only) when applying the selection requirements for the $B^0_{(s)} \to J/\psi\, p\overline{p}$ and $B^+ \to J/\psi\, p\overline{p}\pi^+$ measurements, respectively.

The statistical significances of the signal yields are computed from the change in the fit likelihood when omitting the corresponding component, according to $\sqrt{2\ln(L_{\rm sig}/L_0)}$, where $L_{\rm sig}$ and L_0 are the likelihoods from the nominal fit and from the fit omitting the signal component, respectively. The statistical significances are found to be $1.2\,\sigma$, $3.0\,\sigma$ and $0.2\,\sigma$ for the decays $B^0 \to J/\psi\, p\overline{p}$, $B^0_s \to J/\psi\, p\overline{p}$ and $B^+ \to J/\psi\, p\overline{p}\pi^+$, respectively. The statistical likelihood curve is convolved with a Gaussian function of width given by the systematic uncertainty. The resulting negative log likelihood profiles are shown in Fig. A.3. The total significances of each signal are found to be $1.0\,\sigma$, $2.8\,\sigma$ and $0.2\,\sigma$ for the modes $B^0 \to J/\psi\, p\overline{p}$, $B^0_s \to J/\psi\, p\overline{p}$ and $B^+ \to J/\psi\, p\overline{p}\pi^+$, respectively.

A.6 Systematic uncertainties

Many potential sources of systematic uncertainty are reduced by the choice of the normalisation channel. Nonetheless, some factors remain that could still affect the

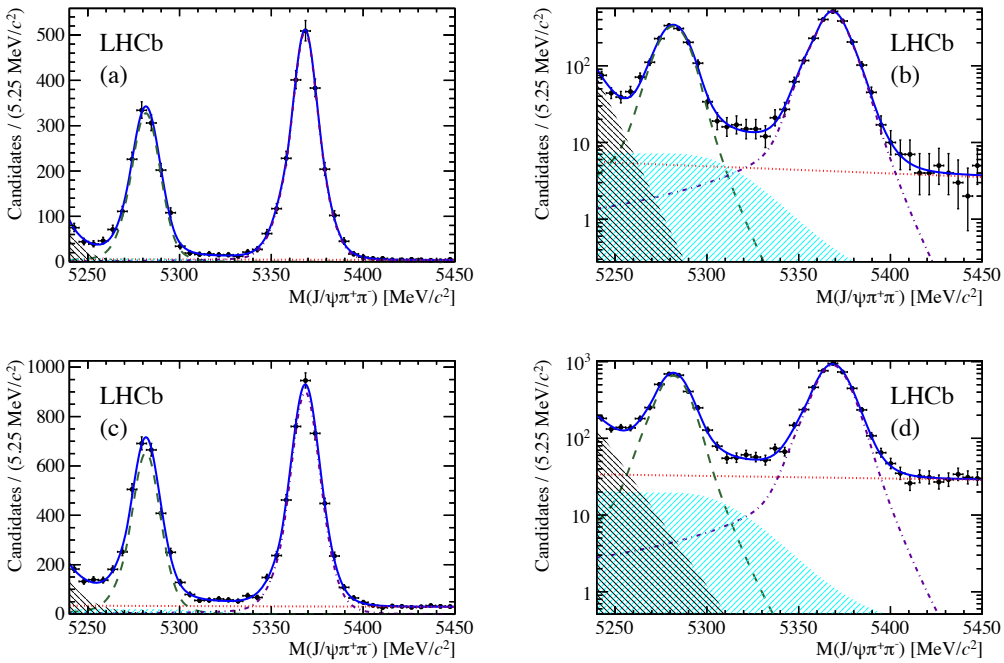

Figure A.2: Invariant mass distribution of $B^0_{(s)} \to J/\psi\pi^+\pi^-$ candidates after the full selection for the (a) $B^0_{(s)} \to J/\psi p\overline{p}$ and (c) $B^+ \to J/\psi p\overline{p}\pi^+$ searches. The corresponding logarithmic plots are shown in (b) and (d). Each component of the fit is represented on the plot: $B^0 \to J/\psi\pi^+\pi^-$ signal (green dashed), $B^0_s \to J/\psi\pi^+\pi^-$ signal (violet dot-dashed), $B^0 \to J/\psi K^+\pi^-$ background (black falling hashed), $B^0_s \to J/\psi\eta'$ background (cyan rising hashed), and combinatorial background (red dotted). The overall fit is represented by the solid blue line.

measurements of the branching fractions. The sources and their values are summarised in Table A.1.

Precise knowledge of the selection efficiencies for the modes is limited both by the simulation sample size and by the variation of the efficiency over the multi-body phase space, combined with the unknown distribution of the signal over the phase space. The simulation sample size contributes an uncertainty of approximately 1 % in each of the channels, and the effect of efficiency variation across the phase space, determined from the spread of values obtained in bins of the relevant variables, is evaluated to be 17 %, 14 % and 23 % for $B^0 \to J/\psi p\overline{p}$, $B^0_s \to J/\psi p\overline{p}$ and $B^+ \to J/\psi p\overline{p}\pi^+$ decays, respectively. The large systematic uncertainties reflect the unknown distribution of signal events across the phase space. In contrast, the uncertainty for the $B^0_s \to J/\psi\pi^+\pi^-$ normalisation channel is estimated by varying the binning scheme in the phase space variables and is found to be only 1% for both the

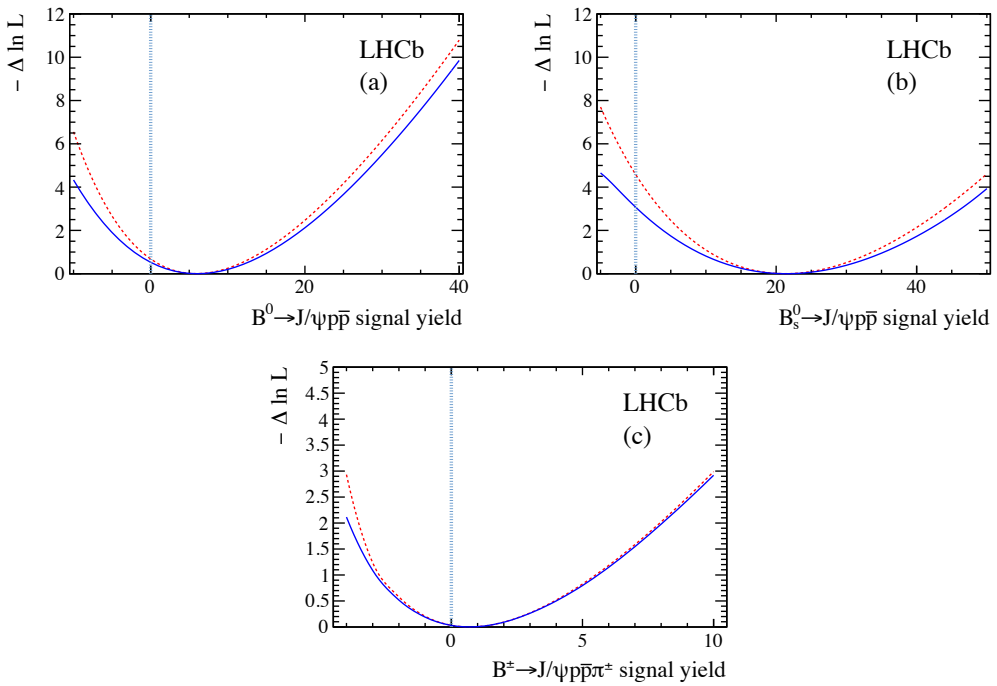

Figure A.3: Negative log-likelihood profiles for the (a) $B^0 \to J/\psi\, p\bar{p}$, (b) $B_s^0 \to J/\psi\, p\bar{p}$, and (c) $B^+ \to J/\psi\, p\bar{p}\pi^+$ signal yields. The red dashed line corresponds to the statistical-only profile while the blue line includes all the systematic uncertainties.

$B^0_{(s)} \to J/\psi\, p\bar{p}$ and $B^+ \to J/\psi\, p\bar{p}\pi^+$ MVA selections. Possible biases due to training the MVA using the control channel were investigated and found to be negligible.

The proton PID efficiency is measured using a high-purity data sample of $\Lambda \to p\pi^-$ decays. By repeating the method with a simulated control sample, and considering the difference with the simulated signal sample, the associated systematic uncertainties are found to be 3 %, 3 % and 2 % for the modes $B^0 \to J/\psi\, p\bar{p}$, $B_s^0 \to J/\psi\, p\bar{p}$ and $B^+ \to J/\psi\, p\bar{p}\pi^+$, respectively. Furthermore, the limited sample sizes give an additional 1 % uncertainty. In the $B^+ \to J/\psi\, p\bar{p}\pi^+$ channel there is an additional source of uncertainty due to the different reconstruction efficiencies for the extra pion track in data and simulation, which is determined to be less than 2 %.

The effect of approximations made in the fit model is investigated by considering alternative functional forms for the various signal and background PDFs. The nominal signal shapes are replaced with a bifurcated Gaussian function with asymmetric exponential tails. The background is modelled with an exponential function for $B^0_{(s)} \to J/\psi\, p\bar{p}$ decays, whereas a second-order polynomial function is

used for $B^+ \to J/\psi p\overline{p}\pi^+$ and the normalisation channel. Combined in quadrature, these sources change the fitted yields by 2.5, 2.6 and 0.7 events, which correspond to 42 %, 12 % and 92 % for the $B^0 \to J/\psi p\overline{p}$, $B_s^0 \to J/\psi p\overline{p}$ and $B^+ \to J/\psi p\overline{p}\pi^+$ modes, respectively. The bias on the determination of the fitted yield is studied with pseudo-experiments. No significant bias is found, and the associated systematic uncertainty is 0.2, 0.3 and 0.2 events (4 %, 1 % and 26 %) for the $B^0 \to J/\psi p\overline{p}$, $B_s^0 \to J/\psi p\overline{p}$ and $B^+ \to J/\psi p\overline{p}\pi^+$ modes, respectively.

Since a B_s^0 meson decay is used for the normalisation, the results for $\mathcal{B}(B^0 \to J/\psi p\overline{p})$ and $\mathcal{B}(B^+ \to J/\psi p\overline{p}\pi^+)$ rely on the knowledge of the ratio of the fragmentation fractions, measured to be $f_s/f_d = 0.256 \pm 0.020$ [176], introducing a relative uncertainty of 8 %. It is assumed that $f_u = f_d$. The uncertainty on the measurement of the $B_s^0 \to J/\psi \pi^+\pi^-$ branching fraction includes a contribution from this source. Hence, to avoid double counting, it is omitted when evaluating the systematic uncertainties on the absolute branching fractions.

A series of cross-checks are performed to test the stability of the fit result. The PID and MVA requirements are tightened and loosened. The fit range is restricted to $[5229, 5416]\,\text{MeV}/c^2$ and $[5129, 5379]\,\text{MeV}/c^2$ for $B^0_{(s)} \to J/\psi p\overline{p}$ and $B^+ \to J/\psi p\overline{p}\pi^+$ decays, respectively. No significant change in the results is observed in any of the cross-checks.

Table A.1: Systematic uncertainties on the branching fraction ratios of the decays $B^0 \to J/\psi p\overline{p}$, $B_s^0 \to J/\psi p\overline{p}$ and $B^+ \to J/\psi p\overline{p}\pi^+$ measured relative to $B_s^0 \to J/\psi \pi^+\pi^-$. The total is obtained from the sum in quadrature of all contributions.

Source	Uncertainty on the branching fraction ratio (%)		
	$B^0 \to J/\psi p\overline{p}$	$B_s^0 \to J/\psi p\overline{p}$	$B^+ \to J/\psi p\overline{p}\pi^+$
Event selection	1	1	1
Efficiency variation	17	14	23
PID simulation sample size	1	1	1
PID calibration method	3	3	2
Tracking efficiency	—	—	2
Fit model	42	12	92
Fit bias	4	1	26
Fragmentation fractions	8	—	8
Total	46	19	98

A.7 Results and conclusions

The relative branching fractions are determined according to

$$\frac{\mathcal{B}(B_q \to J/\psi\, p\overline{p}(\pi^+))}{\mathcal{B}(B_s^0 \to J/\psi\, \pi^+\pi^-)} = \frac{\epsilon^{\rm sel}_{B_s^0 \to J/\psi\, \pi^+\pi^-}}{\epsilon^{\rm sel}_{B_q \to J/\psi\, p\overline{p}(\pi^+)}} \times \quad \frac{\epsilon^{\rm PID}_{B_s^0 \to J/\psi\, \pi^+\pi^-}}{\epsilon^{\rm PID}_{B_q \to J/\psi\, p\overline{p}(\pi^+)}} \times \frac{N_{B_q \to J/\psi\, p\overline{p}(\pi^+)}}{N_{B_s^0 \to J/\psi\, \pi^+\pi^-}} \times \frac{f_s}{f_q}, \quad \text{(A.3)}$$

where $\epsilon^{\rm sel}$ is the selection efficiency, $\epsilon^{\rm PID}$ is the particle identification efficiency, and N is the signal yield. The results obtained are

$$\begin{aligned}
\frac{\mathcal{B}(B^0 \to J/\psi\, p\overline{p})}{\mathcal{B}(B_s^0 \to J/\psi\, \pi^+\pi^-)} &= (1.0\,^{+1.0}_{-0.9}\,\pm 0.5) \times 10^{-3}\,, \\
\frac{\mathcal{B}(B_s^0 \to J/\psi\, p\overline{p})}{\mathcal{B}(B_s^0 \to J/\psi\, \pi^+\pi^-)} &= (1.5\,^{+0.6}_{-0.5}\,\pm 0.3) \times 10^{-2}\,, \\
\frac{\mathcal{B}(B^+ \to J/\psi\, p\overline{p}\pi^+)}{\mathcal{B}(B_s^0 \to J/\psi\, \pi^+\pi^-)} &= (0.27\,^{+1.23}_{-0.95} \pm 0.26) \times 10^{-3}\,,
\end{aligned}$$

where the first uncertainty is statistical and the second is systematic. The absolute branching fractions are calculated using the measured branching fraction of the normalisation channel $\mathcal{B}(B_s^0 \to J/\psi\, \pi^+\pi^-) = (1.98 \pm 0.20) \times 10^{-4}$ [217]

$$\begin{aligned}
\mathcal{B}(B^0 \to J/\psi\, p\overline{p}) &= (2.0\,^{+1.9}_{-1.7}(\text{stat})\ \pm 0.9(\text{syst})\ \pm 0.1\,[\text{norm}]) \times 10^{-7}, \\
\mathcal{B}(B_s^0 \to J/\psi\, p\overline{p}) &= (3.0\,^{+1.2}_{-1.1}(\text{stat})\ \pm 0.6(\text{syst})\ \pm 0.3\,[\text{norm}]) \times 10^{-6}, \\
\mathcal{B}(B^+ \to J/\psi\, p\overline{p}\pi^+) &= (0.54\,^{+2.43}_{-1.89}(\text{stat}) \pm 0.52(\text{syst}) \pm 0.03\,[\text{norm}]) \times 10^{-7},
\end{aligned}$$

where the third uncertainty originates from the control channel branching fraction measurement. The dominant uncertainties are statistical, while the most significant systematic come from the fit model and from the variation of the efficiency over the phase space.

Since the significances of the signals are below $3\,\sigma$, upper limits at both 90 % and 95 % confidence levels (CL) are determined using a Bayesian approach, with a prior that is uniform in the region with positive branching fraction. Integrating the likelihood (including all systematic uncertainties), the upper limits are found to be

$$\begin{aligned}
\frac{\mathcal{B}(B^0 \to J/\psi\, p\overline{p})}{\mathcal{B}(B_s^0 \to J/\psi\, \pi^+\pi^-)} &< 2.6\ (3.0) \times 10^{-3} \quad \text{at}\ \ 90\,\%\ (95\,\%)\ \text{CL}\,, \\
\frac{\mathcal{B}(B_s^0 \to J/\psi\, p\overline{p})}{\mathcal{B}(B_s^0 \to J/\psi\, \pi^+\pi^-)} &< 2.4\ (2.7) \times 10^{-2} \quad \text{at}\ \ 90\,\%\ (95\,\%)\ \text{CL}\,, \\
\frac{\mathcal{B}(B^+ \to J/\psi\, p\overline{p}\pi^+)}{\mathcal{B}(B_s^0 \to J/\psi\, \pi^+\pi^-)} &< 2.5\ (3.1) \times 10^{-3} \quad \text{at}\ \ 90\,\%\ (95\,\%)\ \text{CL}\,,
\end{aligned}$$

and the absolute limits are

$$\begin{aligned}
\mathcal{B}(B^0 \to J/\psi\, p\overline{p}) &< 5.2\ (6.0) \times 10^{-7} \quad \text{at}\ \ 90\,\%\ (95\,\%)\ \text{CL}\,, \\
\mathcal{B}(B_s^0 \to J/\psi\, p\overline{p}) &< 4.8\ (5.3) \times 10^{-6} \quad \text{at}\ \ 90\,\%\ (95\,\%)\ \text{CL}\,, \\
\mathcal{B}(B^+ \to J/\psi\, p\overline{p}\pi^+) &< 5.0\ (6.1) \times 10^{-7} \quad \text{at}\ \ 90\,\%\ (95\,\%)\ \text{CL}\,.
\end{aligned}$$

In summary, using the data sample collected in 2011 by the LHCb experiment corresponding to an integrated luminosity of $1.0\,\text{fb}^{-1}$ of pp collisions at $\sqrt{s} = 7\,\text{TeV}$, searches for the decay modes $B^0 \to J/\psi\, p\overline{p}$, $B_s^0 \to J/\psi\, p\overline{p}$ and $B^+ \to J/\psi\, p\overline{p}\pi^+$ are performed. No significant signals are seen, and upper limits on the branching fractions are set. A significant improvement in the existing limit for $B^0 \to J/\psi\, p\overline{p}$ decays is achieved and first limits on the branching fractions of $B_s^0 \to J/\psi\, p\overline{p}$ and $B^+ \to J/\psi\, p\overline{p}\pi^+$ decays are established. The limit on the $B^0 \to J/\psi\, p\overline{p}$ branching fraction is in tension with the theoretical prediction [216]. The significance of the $B_s^0 \to J/\psi\, p\overline{p}$ signal is $2.8\,\sigma$, which motivates new theoretical calculations of this process as well as improved experimental searches using larger datasets.

B

Probing *CP* violation in $B_s^0 \to K_S^0\pi^+\pi^-$ decays

B.1 Preamble

In addition to the discussion in Sec. 3.3 about the possible sensitivity to *CP* violation in $B_s^0 \to K_S^0 K^\pm \pi^\mp$ decays, a series of studies have been performed using the $B_s^0 \to K_S^0\pi^+\pi^-$ channel. These results have been presented at the 37^{th} International Conference on High Energy Physics (ICHEP 2014) [227], and are reproduced verbatim in the following.

B.2 Abstract

The three-body charmless hadronic decay $B_s^0 \to K_S^0\pi^+\pi^-$ provides a number of novel possibilities to search for *CP* violation effects and test the Standard Model of particle physics. These include fits to the Dalitz-plot distributions of the decay-time-integrated final state, decay-time-dependent (but without initial state flavour tagging) fits to the Dalitz-plot distribution, as well as full decay-time-dependent and flavour tagged fits. The relative sensitivities of these different approaches are investigated.

B.3 Introduction

The search for a new source of *CP* violation in addition to that predicted by the CKM matrix [23,25] is among the main goals of current particle physics research. In the quark sector, a number of important tests have been performed by experiments

such as BaBar, Belle and LHCb [32, 228–231]. This line of investigation will be continued by Belle II [232] and the upgraded LHCb experiment [233, 234].

One of the most interesting approaches to search for new sources of *CP* violation is by studying the decay-time distribution of neutral B meson decays to hadronic final states mediated by the loop ("penguin") $b \to s$ amplitude. As-yet undiscovered particles can contribute in the loops and cause the observables to deviate from their expected values in the Standard Model (SM) [33–36]. Studies of B^0 decays to $\phi K^0_{\rm S}$, $\eta' K^0_{\rm S}$, $K^0_{\rm S} K^0_{\rm S} K^0_{\rm S}$ and various other final states have been performed for this reason. The latest results are consistent with the SM predictions, but improved measurements are needed to be sensitive to small deviations.

Experience from previous experiments has shown that full decay-time-dependent Dalitz-plot analysis of a three-body decay (for example $B^0 \to K^0_{\rm S}\pi^+\pi^-$) is more sensitive than a "quasi-two-body" approach (in this example, considering only the $K^0_{\rm S}\rho^0$ contribution). This is particularly notable in the case that broad resonances contribute, since interference causes effects to which quasi-two-body approaches have no sensitivity [45–47]. Several methods have been proposed to exploit such interferences in $b \to s$ transitions to allow determination of underlying parameters such as the CKM phase γ with reduced theoretical uncertainty [43, 44, 48, 235, 236]. Full decay-time-dependent Dalitz-plot analyses of $B^0 \to K^0_{\rm S}\pi^+\pi^-$ [168, 169] and $B^0 \to K^0_{\rm S} K^+ K^-$ [170, 171] have been performed by BaBar and Belle, but similar studies of B^0_s meson decays have not yet been possible.

First results from LHCb on decays of the B^0_s meson via hadronic $b \to s$ amplitudes have, however, recently become available. Decay-time-dependent analyses of $B^0_s \to K^+K^-$ [237] and $B^0_s \to \phi\phi$ [238] have already been performed. The first observations of $B^0_s \to K^0_{\rm S} K^\pm \pi^\mp$ and $B^0_s \to K^0_{\rm S}\pi^+\pi^-$ have also been reported [108], including information on contributing K^* resonances [37], suggesting that it will be possible to study *CP* violation in these modes in the future.

One interesting feature of the $B^0_s \to K^0_{\rm S}\pi^+\pi^-$ decays is that an asymmetry in the time-integrated yields across the mirror line of the Dalitz plot is a signature of *CP* violation [239–241]. This can be exploited to search for *CP* asymmetry with either model-independent or model-dependent approaches. Another important aspect of the B^0_s system, with regard to *CP* violation searches, is the non-zero width difference $\Delta\Gamma_s$ between the mass eigenstates. Compared to the situation for B^0 decays, the decay-time distribution receives additional terms that do not vanish when integrated over the initial flavour of the B meson. This implies that information about *CP* violation parameters can be obtained from analyses that do not tag the initial flavour, through so-called effective lifetime measurements [58, 59]. Although

analyses that include flavour tagging information will always be more sensitive, this method may still be of interest for analyses based on small event samples, since it is difficult to achieve high effective tagging efficiency at hadron collider experiments such as LHCb.

The purpose of this paper is to investigate the comparative sensitivity of different methods to search for *CP* violation in $B^0_s \to K^0_S\pi^+\pi^-$ decays. The methods that are considered are (i) untagged, decay-time-integrated; (ii) untagged, decay-time-dependent; (iii) tagged, decay-time-dependent. Only model-dependent methods are included. The study is based on a simple toy model for the decays, including contributions only from $K^*(892)$, $K^*_0(1430)$, $\rho(770)$, and $f_0(980)$ resonances, implemented with the `Laura++` Dalitz-plot fitting package [159].

B.4 Formalism

The decay-time distribution for the decays of mesons, initially produced as $\overline{B}^0_s$ and B^0_s flavour eigenstates, to a final state f can be written [31]

$$\begin{aligned}\frac{d}{dt}\Gamma_{\overline{B}^0_s\to f}(t) = \frac{\mathcal{N}_f\, e^{-t/\tau(B^0_s)}}{2\tau(B^0_s)}\Big[\cosh\left(\tfrac{\Delta\Gamma_s t}{2}\right) + S_f\sin(\Delta m_s t) - \\ C_f\cos(\Delta m_s t) + A_f^{\Delta\Gamma_s}\sinh\left(\tfrac{\Delta\Gamma_s t}{2}\right)\Big]\,,\end{aligned} \tag{B.1}$$

and

$$\begin{aligned}\frac{d}{dt}\Gamma_{B^0_s\to f}(t) = \frac{\mathcal{N}_f\, e^{-t/\tau(B^0_s)}}{2\tau(B^0_s)}\Big[\cosh\left(\tfrac{\Delta\Gamma_s t}{2}\right) - S_f\sin(\Delta m_s t) + \\ C_f\cos(\Delta m_s t) + A_f^{\Delta\Gamma_s}\sinh\left(\tfrac{\Delta\Gamma_s t}{2}\right)\Big]\,,\end{aligned} \tag{B.2}$$

where the mass and width differences between the light (L) and heavy (H) B^0_s physical eigenstates are defined as $\Delta m_s = m_{\rm H} - m_{\rm L}$ and $\Delta\Gamma_s = \Gamma_{\rm L} - \Gamma_{\rm H}$, and the B^0_s lifetime is $\tau(B^0_s) = \left(\frac{\Gamma_{\rm L}+\Gamma_{\rm H}}{2}\right)^{-1}$ (units with $\hbar = c = 1$ are used). The coefficients of the $\sin(\Delta m_s t)$, $\cos(\Delta m_s t)$ and $\sinh\left(\frac{\Delta\Gamma_s t}{2}\right)$ terms are often expressed as

$$S_f \;\equiv\; \frac{2\,\Im(\lambda_f)}{1+|\lambda_f|^2}\,, C_f \;\equiv\; \frac{1-|\lambda_f|^2}{1+|\lambda_f|^2}\,, A_f^{\Delta\Gamma_s} \;\equiv\; -\frac{2\ \mathrm{Re}(\lambda_f)}{1+|\lambda_f|^2}\,, \tag{B.3}$$

where the parameter λ_f encodes information about *CP* violation and is given by $\lambda_f = \frac{q}{p}\frac{\bar{\mathcal{A}}_f}{\mathcal{A}_f}$ where $\bar{\mathcal{A}}_f$ and $\mathcal{A}_f$ are the amplitudes for $\overline{B}^0_s$ and B^0_s decay to the final state f and q and p define the physical eigenstates in terms of their flavour components

$$|B^0_{s\,\rm L}\rangle = p|B^0_s\rangle + q|\overline{B}^0_s\rangle\,, \qquad |B^0_{s\,\rm H}\rangle = p|B^0_s\rangle - q|\overline{B}^0_s\rangle\,, \tag{B.4}$$

with $|p|^2 + |q|^2 = 1$. Note that, by definition,

$$(S_f)^2 + (C_f)^2 + \left(A_f^{\Delta\Gamma_s}\right)^2 = 1\,. \tag{B.5}$$

In the remainder of this work, it will be assumed that $|q/p| = 1$ (*i.e.* absence of *CP* violation in mixing).

By requiring that the integral over t from zero to infinity of the sum of Eq. (B.1) and Eq. (B.2) is equal to $|\mathcal{A}_f|^2 + \left|\bar{\mathcal{A}}_f\right|^2$, the normalisation factor is found to be

$$\mathcal{N}_f = \left(|\mathcal{A}_f|^2 + \left|\bar{\mathcal{A}}_f\right|^2\right) \frac{1-y^2}{1+yA_f^{\Delta\Gamma_s}}\,, \tag{B.6}$$

where $y = \tau(B_s^0)\Delta\Gamma_s/2$. The correction involving y is the origin of the difference between branching fractions calculated at $t = 0$ or after integration over decay time [109].

The discussion above is appropriate for any final state f, including two-body decays. For multibody decays described by the isobar model [96–98], the total amplitude is obtained from a sum of amplitudes from resonant or nonresonant decay channels,

$$\mathcal{A}_f = \sum_{j=1}^{N} c_j F_j(f)\,, \quad \bar{\mathcal{A}}_f = \sum_{j=1}^{N} \bar{c}_j F_j(f)\,, \tag{B.7}$$

where $F_j(f)$ are dynamical amplitudes that contain the lineshape and spin-dependence of the hadronic part of the amplitude labelled by j evaluated at the point in phase space given by f, and c_j are complex coefficients describing the relative magnitude and phase of the different decay channels. Since the $F_j(f)$ terms describe strong dynamics only, they are *CP* conserving. By contrast, the c_j terms can be *CP* violating, which is manifested when $\bar{c}_j$ differs from c_j in either magnitude or phase – typically this can occur when the amplitude j has contributions from both "tree" and "loop" (or "penguin") amplitudes.

The above discussion makes clear how different forms of *CP* violation may be manifest in different types of analysis:

i. Untagged, decay-time-integrated Dalitz plot:
   In the absence of all forms of *CP* violation, there is a symmetry between the mirror line in the $K^0_S\pi^+\pi^-$ phase-space. This can be broken, for example, by *CP* violation in decay to flavour-specific final states, such as $K^{*\pm}\pi^{\mp}$, since the B_s^0 and $\overline{B}_s^0$ decays populate different regions of the Dalitz plot. In general one would expect to find larger asymmetries in some local regions of the phase space, and either model-dependent or model-independent methods could be used to search

for such effects. A model-dependent fit can determine the C_f parameters of Eq. B.1 and B.2.

ii. Untagged, decay-time-dependent Dalitz plot:
The $A_f^{\Delta\Gamma_s}$ terms of Eq. B.1 and B.2 can be determined, and therefore more information is obtained compared to the decay-time-integrated case.

iii. Tagged, decay-time-dependent Dalitz plot:
All terms, including the S_f parameters, can be determined. This method therefore provides additional sensitivity to the model parameters, in particular to the relative phase between B_s^0 and $\overline{B}_s^0$ decay amplitudes.

This general discussion does not answer the question of how much additional sensitivity is obtained as the analysis is made increasingly more complex. That will be addressed in the next sections.

B.5 Method to generate toy samples

Several ensembles of Monte Carlo pseudoexperiments are generated to investigate *CP* violation effects in $B_s^0 \to K_S^0\pi^+\pi^-$ decays. The simulation is performed without any experimental effects, such as background, acceptance, resolution or imperfect flavour tagging. The toy model contains the $\rho^0(770)$, $f_0(980)$, $K^{*\pm}(892)$ and $K_0^{*\pm}(1430)$ resonances. All mass terms are described by the relativistic Breit-Wigner (RBW) function, apart from the $K_0^{*\pm}(1430)$ lineshape which is modelled by the LASS shape [104]. The parametrisation of complex coefficients is given by

$$\overset{(-)}{c_j} = (x_j \pm \Delta x_j) + i(y_j \pm \Delta y_j)\,, \tag{B.8}$$

where Δx_j and Δy_j are *CP*-violating parameters. Table B.1 summarises the baseline model used to generate events, with decay-time distribution given in Eq. B.1 and B.2. Values of $\tau(B_s^0) = 1.517$ ps, $\Delta m_s = 17.76$ ps^{-1} and $y = 0.058$ are used.

In the fit, the $\overset{(-)}{c_j}$ coefficients are measured relative to the $\rho^0(770)$ resonance contribution. Each pseudoexperiment is fitted many times with randomised initial values of the parameters in order to find the global minimum of the negative log likelihood function. Asymmetries are calculated as

$$\mathcal{A}_{CP\,j} = \frac{|\bar{c}_j|^2 - |c_j|^2}{|\bar{c}_j|^2 + |c_j|^2} = \frac{-2(x_j\Delta x_j + y_j\Delta y_j)}{x_j^2 + \Delta x_j^2 + y_j^2 + \Delta y_j^2}\,. \tag{B.9}$$

CP violation can also be manifest in a difference between the phase of the B_s^0 and

Table B.1: Benchmark parameters for the baseline Dalitz plot model used as input in the generation.

Resonance	x_j	Δx_j	y_j	Δy_j
$\rho^0(770)$	1.0	0.0	0.0	0.0
$f_0(980)$	$0.4\cos(5\pi/4)$	0.0	$0.4\sin(5\pi/3)$	0.0
$K^{*\pm}(892)$	$1.2\cos(\pi/3)$	0.0	$1.2\sin(\pi/3)$	0.0
$K_0^{*\pm}(1430)$	$1.7\cos(\pi/3)$	0.0	$1.7\sin(\pi/3)$	0.0

$\overline{B}{}^0_s$ decay amplitudes,

$$\Delta\delta_j = \arg\left(\frac{\bar{c}_j}{c_j}\right) = \tan^{-1}\left(\frac{y_j + \Delta y_j}{x_j + \Delta x_j}\right) - \tan^{-1}\left(\frac{y_j - \Delta y_j}{x_j - \Delta x_j}\right). \tag{B.10}$$

The baseline model is modified in various ways to introduce *CP* violation. Interference between the B^0_s-$\overline{B}{}^0_s$ oscillation and decay amplitudes is incorporated through the *CP* violation weak phase ϕ_s. While the SM predicts $\phi_s^{\rm SM} = -2\beta_s \equiv -2\arg(-V_{ts}V_{tb}^*/V_{cs}V_{cb}^*) = -0.036\pm0.002$ rad, contributions from physics beyond the SM could lead to much larger values. Three different scenarios are generated: $\phi_s = 0$, $\phi_s = -2\beta_s$ and $\phi_s = -20\beta_s$. In addition, *CP* violation in the decay of each resonance is examined: *CP* violation in the magnitude, with $\mathcal{A}_{CP} = 5\%$, 10%, 20% and 50%; *CP* violation due to the difference in the relative phase in steps of $\pi/4$ from 0 to 2π; and *CP* violation in both magnitude and phase difference. Pseudoexperiments are generated with sample size corresponding roughly to the anticipated yields available at LHCb by the end of the LHC Run II (2000 events). Ensembles with other sample sizes are also generated to test the scaling of the uncertainties. Only a representative subset of the results obtained are presented here due to space constraints.

B.6 Results

Figure B.1 shows the results for various scenarios of *CP* violation in the $K^{*\pm}(892)$ amplitude, with yields corresponding to LHC Run I+II. The fitted values of the isobar coefficients in each pseudoexperiment are represented by the points in the Argand plane, with the ellipses illustrating the central values and $1\,\sigma$ contour boundaries from the ensemble. The colour schemes for B^0_s and $\overline{B}{}^0_s$ coefficients are represented respectively by: blue and cyan for method i; light and dark green for method ii; and red and magenta for method iii.

It is immediately clear that the magnitude of the amplitude is determined

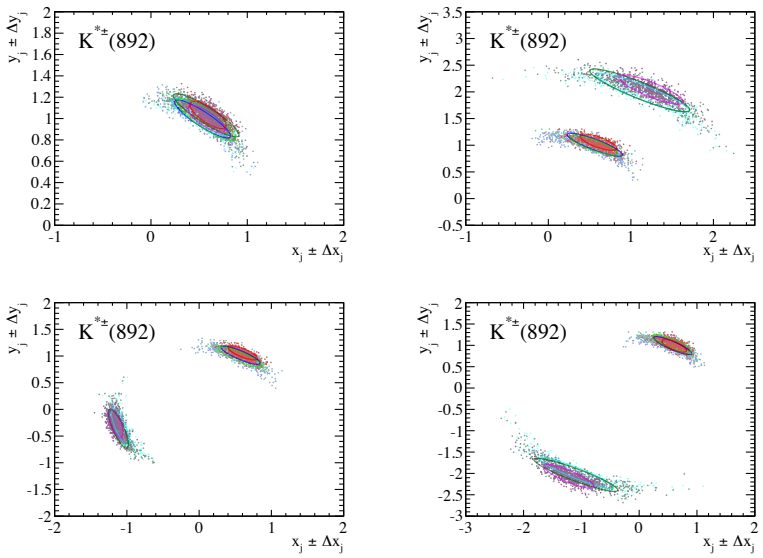

Figure B.1: Fitted values of the $K^{*\pm}(892)$ isobar coefficients plotted in the Argand plane. The points are the values determined from individual pseudoexperiments while the ellipses illustrate the mean value and 68% confidence level contour from the corresponding ensemble. The results for c_j ($\bar{c}_j$) are shown for method i in blue (cyan), for method ii in green (dark green) and for method iii in red (magenta). All experiments are generated with 2000 signal events and $\phi_s = -2\beta_s$ and the following scenarios: (top left) no *CP* violation, (top right) $\mathcal{A}_{CP} = 50\%$, (bottom left) $\Delta\delta = 3\pi/4$ and (bottom right) $\mathcal{A}_{CP} = 50\%$ and $\Delta\delta = \pi$.

much more precisely than the phase, leading to the arc-like distribution of points. Table B.2 compares the precision of the different fitting methods for each of the *CP* violation scenarios. The results indicate that the generated asymmetries are retrieved in all scenarios with good precision and without significant bias. The untagged methods give statistical uncertainties that are only slightly larger, due to the fact that the K^* resonances from the decay of B_s^0 and $\overline{B}_s^0$ populate different regions of the Dalitz plot. In addition, the very similar uncertainties given by the two untagged approaches suggests that the $A_f^{\Delta\Gamma_s}$ term does not provide a significant amount of extra sensitivity. Further studies with realistic experimental effects are necessary to determine the exact sensitivities achievable. An extrapolation of the precision estimated here suggests that such measurements appear to be feasible, albeit with large uncertainty, with the LHCb Run I dataset that is already in hand.

A further study is performed to investigate the sensitivity to the ϕ_s observable. Figure B.2 compares the results from methods ii and iii (such a determination is not possible with method i). It is clear that it is possible to determine the weak phase with both improved precision and greater accuracy when tagging is applied. With perfect tagging, the precision on ϕ_s shows an order of magnitude

Table B.2: Comparison of the uncertainties on the $K^{*\pm}(892)$ *CP*-violating parameters determined using the different fitting methods. The results are quoted in terms of the polar co-ordinates $c_j = a_j e^{i\delta_j}$, $\bar{c}_j = \bar{a}_j e^{i\bar{\delta}_j}$. The relative uncertainties for method iii are quoted (the central values of the parameters correspond to the values given in Table B.1, modified according to the *CP* violation parameters), together with comparisons of the uncertainties with the different Dalitz plot fit methods. The typical uncertainty on the relative precision is ± 0.1.

CP-violation parameters			σ(method iii) (%)				$\frac{\sigma(\text{method ii})}{\sigma(\text{method iii})}$				$\frac{\sigma(\text{method i})}{\sigma(\text{method iii})}$			
$\mathcal{A}_{CP}$	$\Delta\delta$	ϕ_s	a_j	$\bar{a}_j$	δ_j	$\bar{\delta}_j$	a_j	$\bar{a}_j$	δ_j	$\bar{\delta}_j$	a_j	$\bar{a}_j$	δ_j	$\bar{\delta}_j$
20%	0	0	4.6	3.7	12.3	11.6	1.1	1.2	1.8	1.8	1.0	1.0	1.7	1.8
50%	0	$2\beta_s$	5.1	3.3	15.0	12.2	1.0	1.1	1.6	1.8	0.9	1.1	1.5	1.8
0%	$\pi/4$	0	4.2	4.3	12.2	7.7	1.0	1.1	1.8	1.6	1.0	0.9	1.6	1.5
0%	$3\pi/4$	$2\beta_s$	4.2	4.0	12.4	4.7	1.0	1.2	1.6	1.8	1.0	1.1	1.5	1.8
5%	$\pi/4$	0	4.5	3.9	11.4	8.3	1.0	1.1	1.8	1.4	0.9	1.0	1.8	1.5
50%	π	$2\beta_s$	5.2	3.6	14.5	7.1	1.0	1.1	1.6	1.7	1.1	0.9	1.6	1.7

improvement. Using a more realistic tagging power of $\sim 5\%$, as achieved recently by LHCb [112, 113], still provides a factor ~ 2.5 better sensitivity to ϕ_s than the untagged case. Alternatively one can fix the value of $\phi_s = -2\beta_s$ in the fit and float the Δy_j parameter of the $\rho^0(770)$ resonance in order to measure the relative phase between the B_s^0 and $\overline{B}_s^0$ decay to this state. This approach is also illustrated in Fig. B.2 and shows the same behaviour comparing methods ii and iii.

B.7 Summary

The recent observation of B_s^0 decays to charmless three-body final states marks the start of a new and interesting field of *CP* violation investigation. In this note, a comparative sensitivity study for different approaches to Dalitz plot analysis has been performed for $B_s^0 \to K_S^0\pi^+\pi^-$ decays. It has been demonstrated that good precision for the phase difference between B_s^0 and $\overline{B}_s^0$ decays to $K^{*\pm}(892)\pi^{\mp}$ can be achieved with untagged analysis approaches (e.g. for the LHC Run I and II). Flavour tagging is, however, needed to determine ϕ_s (i.e. the relative phase in $B_s^0(\overline{B}_s^0) \to K_S^0\rho^0(770)$ decays). These results indicate directions for possible amplitude analyses that can be pursued in future by Belle II and LHCb.

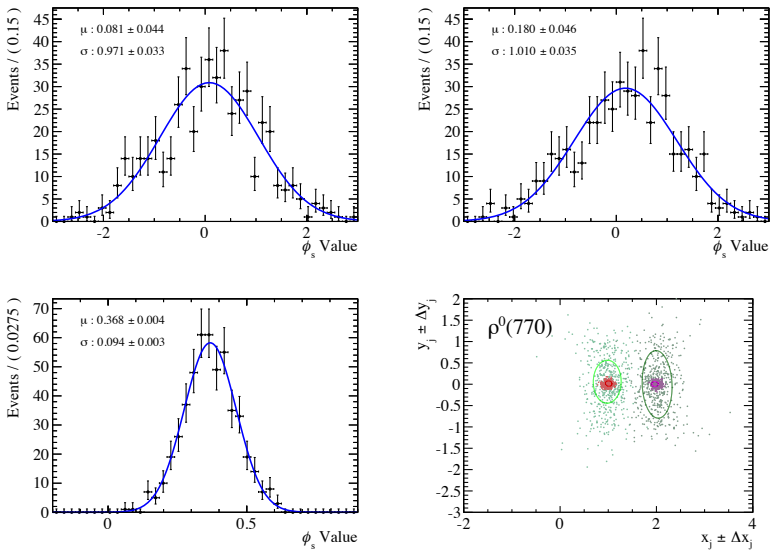

Figure B.2: Fitted values of ϕ_s for (top left) method ii with $\phi_s = -2\beta_s$, (top right) method ii with $\phi_s = -20\beta_s$ and (bottom left) method iii with $\phi_s = -20\beta_s$. The (bottom right) Argand plot displays the fitted coefficient values for the $\rho^0(770)$ resonance with fixed $\phi_s = -2\beta_s$ and $\mathcal{A}_{CP} = 50\%$.

C

Alternative models of the $K\pi$ S-wave

C.1 Lineshapes definition

C.1.1 kappa

One possible parameterisation of the $K\pi$ S-wave is to simply use a Flatté shape for the $K_0^*(1430)$ and include the κ resonance at low $m(K\pi)$. Since the κ is extremely broad, it is necessary to use a modified description of the mass-dependent width [242]

$$R_j(m) = \frac{m_0\Gamma(m)}{m_0^2 - m^2 - im_0\Gamma(m)}\,, \tag{C.1}$$

where the terms have their usual definition and the width is given as

$$\Gamma(m) = \rho\left(\frac{m^2 - s_A}{m_0^2 - s_A}\right) f(m) \exp\left(\frac{-(m^2 - m_0^2)}{A}\right). \tag{C.2}$$

Here $\rho = 2q/m$ is a phase-space factor, $f(m) = b_2 m^2 + b_1$, where b_1 and b_2 are constants, A is also a constant and s_A is the referred to as Adler zero. [1]

The Flatté lineshape has the same form as the κ but the mass dependent width is given by

$$\Gamma(m) = \left(\frac{m^2 - s_A}{m_0^2 - s_A}\right)\left(g_1\rho_{K\pi}(m) + g_2\rho_{K\eta'}(m)\right). \tag{C.3}$$

where $\rho_{K\pi}$ and $\rho_{K\eta'}$ are phase-space factors for the $K\pi$ and $K\eta'$ channels respectively and $g_{1,2}$ parameterise the coupling to these two channels. This lineshape

[1] The values of these constants are extracted from the BES data as $b_1 = 24.49\,\mathrm{GeV}/c, b_2 = 0.0\,\mathrm{GeV}/c, A = 2.5\,\mathrm{GeV}^2/c^4$ and $m_0 = 3.3\,\mathrm{GeV}/c^2$. In addition, $s_A = 0.234\,\mathrm{GeV}^2/c^4$, calculated as $m_K^2 - 0.5m_\pi^2$ [242].

accounts for the $\rho_{K\eta'}$ channel opening close to the $K_0^*(1430)$ pole mass. [2]

C.1.2 EFKLLM model

An alternative model for the $K\pi$ S-wave has been introduced in Ref. [243]. This model implements the following to model the S-wave contribution

$$R_j(m) = F(m)\left(\frac{c_0}{m^2} + c_1\right), \tag{C.4}$$

where $F(m)$ is a form factor which is given in Ref. [243]. It is given as a magnitude and phase at each value of $m(K\pi)$ – these values are themselves obtained from LASS data. The terms $c_{0,1}$ are complex numbers to be determined by the fit.

C.1.3 Breit–Wigner and nonresonant terms

Another approach, albeit one that violates unitarity, consists in the use of a Breit–Wigner shape for the $K_0^*(1430)$ and an exponential form factor (EFF) in m_{ij} to describe the nonresonant component. Such a form factor is given by

$$R_j(m) = e^{-\alpha m^2}, \tag{C.5}$$

where α is a shape parameter that must be determined from the data by floating it in the fit. This functional form was introduced in Ref. [244], and therefore, is referred to as the Belle parametrisation. Note that these parametrisations depend on one of the invariant mass combinations, so that "$K^0_S\pi^\mp$ nonresonant" and "$K^\pm\pi^\mp$ nonresonant" can receive different terms.

C.2 Fit results

Modelling properly the $K\pi$ S-wave is one the most challenging features of this amplitude analysis. This section describes the main results considering alternative parametrisations to the nominal one. A summary comparing the main results for these many models is given in Tables C.1 and C.2, and discussed in the following.

C.2.1 LASS shape

The LASS lineshape is useful to model the physical behaviour of a $K_0^*(1430)$ resonance interfering strongly with a nonresonant term. However, the benchmark imple-

[2] The values of these constants are taken from Ref. [242], and are found to be $m_0 = 1.513\,\text{GeV}/c^2, g_1 = 0.304\,\text{GeV}/c^2, g_2 = 0.380\,\text{GeV}/c^2, s_A = 0.234\,\text{GeV}^2/c^4$.

Table C.1: Summary of the agreement between the fit and data for the different parametrisations of the $K\pi$ S-wave discussed below. Note that some initial GoF compatibility results for each model are provided: mean value from the mixed sample test (MS) examined by varying the the number of data entries in the mixed sample, the number of toy entries and the number of nearest neighbours considered, respectively; and point to point dissimilarity method (P2P) χ^2. The number of solutions within $\Delta\text{NLL} = 25$ is also shown.

	Final state	NLL	nPar	MS(100,10,10) μ	MS(200,10,10) μ	P2P χ^2	Sol.
Model [i]	$K^0_S K^+\pi^-$	1463.38	10	1.359 ± 0.059	3.296 ± 0.058	1.21	12
	$K^0_S K^-\pi^+$	–	10	1.096 ± 0.050	2.631 ± 0.054	1.73	–
Model [v]	$K^0_S K^+\pi^-$	1416.81	14	1.432 ± 0.052	3.422 ± 0.054	1.77	24
	$K^0_S K^-\pi^+$	–	14	0.966 ± 0.049	2.445 ± 0.055	1.54	–
κ-model	$K^0_S K^+\pi^-$	1529.52	14	3.167 ± 0.057	5.391 ± 0.070	3.38	10
	$K^0_S K^-\pi^+$	–	14	2.450 ± 0.060	4.521 ± 0.061	2.79	–
EFKLLM	$K^0_S K^+\pi^-$	1413.23	14	2.028 ± 0.054	4.434 ± 0.059	0.63	27
	$K^0_S K^-\pi^+$	–	10	1.394 ± 0.050	3.392 ± 0.054	1.41	–
BW+Belle	$K^0_S K^+\pi^-$	1397.90	16	0.725 ± 0.046	2.121 ± 0.057	2.20	41
	$K^0_S K^-\pi^+$	–	16	0.665 ± 0.049	1.952 ± 0.051	2.12	–
BW+Flat	$K^0_S K^+\pi^-$	1419.07	12	1.308 ± 0.050	3.099 ± 0.054	1.07	26
	$K^0_S K^-\pi^+$	–	12	0.849 ± 0.049	2.416 ± 0.051	3.02	–

mentation has applied a cut-off at around the charm mass, which limits the extrapolation for the whole invariant mass region. Hence, five possible LASS descriptions have been studied

i. Default lineshape with all parameters fixed [245, 246];

ii. No cut-off at the charm threshold, with both masses, widths, r and a parameters floating independently for $K_0^*(1430)^\pm$ and $\overline{(K)}{}_0^*(1430)^0$ resonances (but the same between the two final states);

iii. No cut-off at the charm threshold, with masses and widths floating but constrained to be the same between $K_0^*(1430)^\pm$ and $\overline{(K)}{}_0^*(1430)^0$, but r and a parameters are independently floated;

iv. No cut-off at the charm threshold, with masses and widths Gaussian constrained to the nominal values independently for $K_0^*(1430)^\pm$ and $\overline{(K)}{}_0^*(1430)^0$, and r and a parameters are also independently floated;

v. No cut-off at the charm threshold, with masses and widths fixed to the nominal values, and r and a parameters are independently floated for $K_0^*(1430)^\pm$ and $\overline{(K)}{}_0^*(1430)^0$ resonances.

There is an overall good agreement between the results for all hypotheses, and hence, further information are necessary to distinguish these figures. This can

Table C.2: Summary of the fit fractions (%) for the different parametrisations of the $K\pi$ S-wave.

	Fit fractions (%)					
Resonance	Model [i]	Model [v]	κ-model	EFKLLM	BW+Belle	BW+Flat
$K^*(892)^-$	14.8	12.8	13.8	15.2	14.7	11.6
$(K\pi)_0^-$ Res	30.2	37.1	9.7	35.7	35.9	34.1
$(K\pi)_0^-$ NonRes	–	–	5.4	51.1	63.7	–
$(K\pi)_0^-$ Inter	–	–	0.4	−47.2	−31.5	–
$(K\pi)_0^-$ Tot	30.2	37.1	15.5	39.6	68.1	34.1
$K_2^*(1430)^-$	3.2	0.3	2.5	0.4	0.9	1.2
$\overline{K}^*(892)^0$	13.9	18.4	23.0	13.2	17.8	17.9
$\overline{(K\pi)}_0^0$ Res	32.7	52.0	25.1	17.0	35.9	19.4
$\overline{(K\pi)}_0^0$ NonRes	–	–	11.6	43.1	61.5	21.6
$\overline{(K\pi)}_0^0$ Inter	–	–	1.8	−37.8	2.9	11.3
$\overline{(K\pi)}_0^0$ Tot	32.7	52.0	38.5	22.3	100.3	52.3
$\overline{K}_2^*(1430)^0$	6.9	3.0	12.5	1.8	1.1	3.8
$K^*(892)^+$	14.0	16.5	19.4	13.8	12.9	16.5
$(K\pi)_0^+$ Res	27.4	31.9	18.1	30.0	10.0	32.6
$(K\pi)_0^+$ NonRes	–	–	6.1	7.6	92.1	–
$(K\pi)_0^+$ Inter	–	–	1.0	16.1	4.0	–
$(K\pi)_0^+$ Tot	27.4	31.9	25.2	53.7	106.1	32.6
$K_2^*(1430)^+$	5.7	0.7	1.8	2.3	1.0	2.2
$K^*(892)^0$	19.2	21.7	24.7	17.7	21.9	20.5
$(K\pi)_0^0$ Res	28.7	40.4	18.5	33.9	7.7	13.0
$(K\pi)_0^0$ NonRes	–	–	16.2	38.9	96.1	30.0
$(K\pi)_0^0$ Inter	–	–	−1.4	−50.6	0.9	7.7
$(K\pi)_0^0$ Tot	28.7	40.4	33.3	22.2	104.7	50.7
$K_2^*(1430)^0$	6.4	2.8	9.2	3.0	0.2	0.02

be obtained by studying the floating LASS parameters shown in Table C.3. A noticeable feature in these results is that at the same time that for the charged $K_0^*(1430)$ resonance the mass and widths obtained are in agreement with the current measurements, the neutral terms are in quite disagreement. In particular, there is a trend to move the mass to much lower values whilst large values for the width are found. These are obviously non physical regions, which disfavour these implementations. The main conclusion is that with the given statistics it is not possible to float these parameters and it is more appropriate to rely on the results obtained from other experiments with larger statistics.

Therefore, the only remaining implementations are the ones that keep the masses and widths constant, which are models [i] and [v]. In order to provide a more detailed picture for these, Table C.1 gathers the main GoF results in each case. There is a fair agreement between the GoF methods investigated for these

Table C.3: Floated shape parameteres from the fit to data (statistical uncertainties only) for the different LASS parametrisation of the $K\pi$ S-wave. See text for definition.

		Fitted Values (GeV)	
	Parameter	$\overline{(K}_0^*(1430)^0$	$K^*(892)^\pm$
Model [ii]	m_0	1.250 ± 0.029	1.430 ± 0.021
	Γ_0	0.370 ± 0.051	0.252 ± 0.053
	a	0.352 ± 0.083	4.530 ± 1.160
	r	0.000 ± 0.000	1.480 ± 0.372
Model [iii]	m_0	1.313 ± 0.035	–
	Γ_0	0.418 ± 0.046	–
	a	0.218 ± 0.052	1.069 ± 0.312
	r	0.000 ± 0.000	1.926 ± 0.341
Model [iv]	m_0	1.294 ± 0.023	1.435 ± 0.019
	Γ_0	0.335 ± 0.041	0.258 ± 0.046
	a	0.295 ± 0.071	4.018 ± 1.103
	r	0.000 ± 0.000	1.648 ± 0.396
Model [v]	a	0.171 ± 0.041	1.892 ± 0.560
	r	0.000 ± 0.000	2.282 ± 0.330

two approaches, with a significant change in the NLL in model [v], which has also a larger number of free parameters. Although there are potential differences between the resonant and nonresonant terms in the LASS shape in the $K_0^*(1430)^\pm$ and $\overline{(K}_0^*(1430)^0$ resonances, it has been noticed that a large number of irreducible multiple solutions appear close to the nominal value for model [v]. This feature is mainly related to the limited statistics available, indicating that it is more reliable to fix the LASS parameters to the results from other experiments. Therefore, the nominal fixed LASS model [i] has been chosen as the baseline parametrisation.

C.2.2 κ model

The first of the alternatives to the LASS parametrisation considered in this analysis is to use the Flatté lineshape for the $K_0^*(1430)$ at the same time as adding the κ resonance to the model. Two scenarios have been investigated with respect to the definition reported in Sec. C.1.1: fixed values to the nominal measurements; floating the κ parameters. The results for both scenarios have significantly worse consistency with the data, noticeable by the large ΔNLL with respect to the nominal fit results. Therefore, these approaches are not considered reasonable models, and are not used further in the analysis [247].

C.2.3 EFKLLM model

Another interesting alternative to the LASS parametrisation is provided in the EFKLLM model. The results for its implementation are also reported in Table C.1. It has been found that this alternative provides the best NLL value for the lowest number of multiple solutions. Since a reasonable agreement for the $K_0^*(1430)$ contribution is seen in data, this has been considered as an alternative approach used to evaluate systematic uncertainty due to the $K\pi$ S-wave model.

C.2.4 Breit–Wigner and nonresonant model

In order to evaluate an alternative to the LASS lineshape where the resonant and nonresonant terms are disentangled, two approaches have been investigated: Relativistic BW with either the Belle nonresonant term of or a flat term. The results for both models are shown in Table C.1. In addition, the exponential terms controlled by the α parameters are found to be 0.119 ± 0.036 and 0.079 ± 0.026 for the $K^{\pm}\pi^{\mp}$ and ${}^{(\overline{\ })}K^0_S\pi^{\mp}$ pairs, respectively. Both approaches are disfavoured with respect to the LASS lineshape, in particular due to the fact it does not respect unitarity.

Bibliography

[1] A. Sakharov, *Violation of CP invariance, c asymmetry, and baryon asymmetry of the Universe*, Pisma Zh. Eksp. Teor. Fiz. **5** (1967) 32.

[2] J. Christenson, J. Cronin, V. Fitch, and R. Turlay, *Evidence for the 2π decay of the K_2^0 Meson*, Phys. Rev. Lett. **13** (1964) 138.

[3] BaBar, B. Aubert *et al.*, *The BaBar detector*, Nucl. Instrum. Meth. **A479** (2002) 1, arXiv:hep-ex/0105044.

[4] A. Abashian *et al.*, *The Belle Detector*, Nucl. Instrum. Meth. **A479** (2002) 117.

[5] LHCb Collaboration, A. A. Alves Jr. *et al.*, *The LHCb detector at the LHC*, JINST **3** (2008) S08005.

[6] R. Dalitz, *On the analysis of tau-meson data and the nature of the tau-meson*, Phil. Mag. **44** (1953) 1068.

[7] I. Bediaga *et al.*, *On a CP anisotropy measurement in the Dalitz plot*, Phys. Rev. **D80** (2009) 096006, arXiv:0905.4233.

[8] M. Williams, *Observing CP violation in many-body decays*, Phys. Rev. **D84** (2011) 054015, arXiv:1105.5338.

[9] T. Lee and C.-N. Yang, *Question of parity conservation in weak interactions*, Phys. Rev. **104** (1956) 254.

[10] C. Wu *et al.*, *Experimental test of parity conservation in beta decay*, Phys. Rev. **105** (1957) 1413.

[11] CPLEAR Collaboration, A. Angelopoulos *et al.*, *First direct observation of time reversal noninvariance in the neutral kaon system*, Phys. Lett. **B444** (1998) 43.

[12] BaBar Collaboration, J. Lees *et al.*, *Observation of time reversal violation in the B^0 meson system*, Phys. Rev. Lett. **109** (2012) 211801, arXiv:1207.5832.

[13] L. Landau, *On the conservation laws for weak interactions*, Nucl. Phys. **3** (1957) 127.

[14] BaBar Collaboration, B. Aubert *et al.*, *Observation of CP violation in the B^0 meson system*, Phys. Rev. Lett. **87** (2001) 091801, arXiv:hep-ex/0107013.

[15] P. Harris *et al.*, *New experimental limit on the electric dipole moment of the neutron*, Phys. Rev. Lett. **82** (1999) 904.

[16] S. Glashow, *Partial symmetries of weak interactions*, Nucl. Phys. **22** (1961) 579.

[17] S. Weinberg, *A model of leptons*, Phys. Rev. Lett. **19** (1967) 1264.

[18] A. Salam, *Weak and electromagnetic interactions*, Conf. Proc. **C680519** (1968) 367.

[19] F. Englert and R. Brout, *Broken symmetry and the mass of gauge vector mesons*, Phys. Rev. Lett. **13** (1964) 321.

[20] P. W. Higgs, *Broken symmetries and the masses of gauge bosons*, Phys. Rev. Lett. **13** (1964) 508.

[21] ATLAS Collaboration, G. Aad *et al.*, *Observation of a new particle in the search for the Standard Model Higgs boson with the ATLAS detector at the LHC*, Phys. Lett. **B716** (2012) 1, `arXiv:1207.7214`.

[22] CMS Collaboration, S. Chatrchyan *et al.*, *Observation of a new boson at a mass of 125 GeV with the CMS experiment at the LHC*, Phys. Lett. **B716** (2012) 30, `arXiv:1207.7235`.

[23] N. Cabibbo, *Unitary symmetry and leptonic decays*, Phys. Rev. Lett. **10** (1963) 531.

[24] S. Glashow, J. Iliopoulos, and L. Maiani, *Weak interactions with lepton-hadron symmetry*, Phys. Rev. **D2** (1970) 1285.

[25] M. Kobayashi and T. Maskawa, *CP violation in the renormalizable theory of the weak interaction*, Prog. Theor. Phys. **49** (1973) 652.

[26] L.-L. Chau and W.-Y. Keung, *Comments on the parametrization of the Kobayashi-Maskawa matrix*, Phys. Rev. Lett. **53** (1984) 1802.

[27] L. Wolfenstein, *Parametrization of the Kobayashi-Maskawa matrix*, Phys. Rev. Lett. **51** (1983) 1945.

[28] Particle Data Group, K. Olive *et al.*, *Review of Particle Physics*, Chin. Phys. **C38** (2014) 090001.

[29] LHCb Collaboration, R. Aaij *et al.*, *Precision measurement of CP violation in $B^0_s \to J/\psi K^+K^-$ decays*, Phys. Rev. Lett. **114** (2015) 041801, arXiv:1411.3104.

[30] CKMfitter Group, J. Charles *et al.*, *CP violation and the CKM matrix: Assessing the impact of the asymmetric B factories*, Eur. Phys. J. **C41** (2005) 1, arXiv:hep-ph/0406184.

[31] I. Dunietz, R. Fleischer, and U. Nierste, *In pursuit of new physics with B^0_s decays*, Phys. Rev. **D63** (2001) 114015, arXiv:hep-ph/0012219.

[32] Heavy Flavor Averaging Group, Y. Amhis *et al.*, *Averages of b-hadron, c-hadron, and τ-lepton properties as of early 2012*, arXiv:1207.1158, updated results and plots available at: http://www.slac.stanford.edu/xorg/hfag/.

[33] Y. Grossman and M. P. Worah, *CP asymmetries in B decays with new physics in decay amplitudes*, Phys. Lett. **B395** (1997) 241, arXiv:hep-ph/9612269.

[34] R. Fleischer, *CP violation and the role of electroweak penguins in nonleptonic B decays*, Int. J. Mod. Phys. **A12** (1997) 2459, arXiv:hep-ph/9612446.

[35] D. London and A. Soni, *Measuring the CP angle β in hadronic $b \to s$ penguin decays*, Phys. Lett. **B407** (1997) 61, arXiv:hep-ph/9704277.

[36] M. Ciuchini *et al.*, *CP violating B decays in the standard model and supersymmetry*, Phys. Rev. Lett. **79** (1997) 978, arXiv:hep-ph/9704274.

[37] LHCb Collaboration, R. Aaij *et al.*, *Observation of $B^0_s \to K^{*\pm}K^{\mp}$ and evidence for $B^0_s \to K^{*-}\pi^+$ decays*, New J. Phys. **16** (2014), no. 12 123001, arXiv:1407.7704.

[38] LHCb Collaboration, R. Aaij *et al.*, *Search for the $B^0_{(d,s)} \to K^{*0}(892)K^0_{\rm S}$ decays at LHCb*, LHCb-PAPER-2015-018, In preparation.

[39] Y. Nir and H. R. Quinn, *Measuring CKM parameters with CP asymmetry and isospin analysis in $B \to \pi K$*, Phys. Rev. Lett. **67** (1991) 541.

[40] M. Gronau, *Elimination of penguin contributions to CP asymmetries in B decays through isospin analysis*, Phys. Lett. **B265** (1991) 389.

[41] M. Gronau and J. L. Rosner, *Weak phase gamma from ratio of $B \to K\pi$ rates*, Phys. Rev. **D57** (1998) 6843, arXiv:hep-ph/9711246.

[42] M. Gronau and J. L. Rosner, *The role of $B_s \to K\pi$ in determining the weak phase γ*, Phys. Lett. **B482** (2000) 71, arXiv:hep-ph/0003119.

[43] M. Ciuchini, M. Pierini, and L. Silvestrini, *New bounds on the CKM matrix from $B \to K\pi\pi$ Dalitz plot analyses*, Phys. Rev. **D74** (2006) 051301, arXiv:hep-ph/0601233.

[44] M. Ciuchini, M. Pierini, and L. Silvestrini, *Hunting the CKM weak phase with time-integrated Dalitz analyses of $B_s \to K\pi\pi$ decays*, Phys. Lett. **B645** (2007) 201, arXiv:hep-ph/0602207.

[45] A. E. Snyder and H. R. Quinn, *Measuring CP asymmetry in $B \to \rho\pi$ decays without ambiguities*, Phys. Rev. D **48** (1993) 2139.

[46] J. Charles *et al.*, *$B^0_d(t) \to DPP$ time dependent dalitz plots, CP-violating angles 2β, $2\beta + \gamma$, and discrete ambiguities*, Phys. Lett. **B425** (1998) 375, arXiv:hep-ph/9801363.

[47] T. Latham and T. Gershon, *A method to measure* $\cos(2\beta)$ *using time-dependent Dalitz Plot analysis of $B^0 \to D_{CP}\pi^+\pi^-$*, J. Phys. **G36** (2009) 025006, arXiv:0809.0872.

[48] M. Gronau, D. Pirjol, A. Soni, and J. Zupan, *Improved method for CKM constraints in charmless three-body B and B(s) decays*, Phys. Rev. **D75** (2007) 014002, arXiv:hep-ph/0608243.

[49] M. Gronau, *U spin symmetry in charmless B decays*, Phys. Lett. **B492** (2000) 297, arXiv:hep-ph/0008292.

[50] A. Soni and D. A. Suprun, *Determination of γ from charmless $B \to M_1 M_2$ decays using U-spin*, Phys. Rev. **D75** (2007) 054006, arXiv:hep-ph/0609089.

[51] R. Fleischer, *New strategies to extract β and γ from $B_d \to \pi^+\pi^-$ and $B^0_s \to K^+K^-$*, Phys. Lett. **B459** (1999) 306, arXiv:hep-ph/9903456.

[52] R. Fleischer, *Extracting CKM phases from angular distributions of $B_{d,s}$ decays into admixtures of CP eigenstates*, Phys. Rev. **D60** (1999) 073008, arXiv:hep-ph/9903540.

[53] S. Descotes-Genon, J. Matias, and J. Virto, *Exploring $B_{d,s} \to KK$ decays through flavour symmetries and QCD-factorisation*, Phys. Rev. Lett. **97** (2006) 061801, arXiv:hep-ph/0603239.

[54] R. Fleischer, *CP violation in the B system and relations to $K \to \pi\nu\bar{\nu}$ decays*, Phys. Rept. **370** (2002) 537, arXiv:hep-ph/0207108.

[55] M. Ciuchini, M. Pierini, and L. Silvestrini, *$B_s \to K^{(*)0}\overline{K}^{(*)0}$ decays: The golden channels for new physics searches*, Phys. Rev. Lett. **100** (2008) 031802, arXiv:hep-ph/0703137.

[56] H.-Y. Cheng and C.-K. Chua, *Charmless three-body decays of B_s mesons*, Phys. Rev. **D89** (2014) 074025, arXiv:1401.5514.

[57] Y. Li, *Branching Fractions and Direct CP Asymmetries of $\bar{B}_s^0 \to K^0 h^+ h'^-(h^{(\prime)} = K, \pi)$ Decays*, Sci. China Phys. Mech. Astron. **58** (2015), no. 3 031001, arXiv:1401.5948.

[58] I. Dunietz, *$B_s - \bar{B}_s$ mixing, CP violation and extraction of CKM phases from untagged B_s data samples*, Phys. Rev. **D52** (1995) 3048, arXiv:hep-ph/9501287.

[59] R. Fleischer and R. Knegjens, *Effective lifetimes of B_s decays and their constraints on the B_s^0-$\bar{B}_s^0$ mixing parameters*, Eur. Phys. J. **C71** (2011) 1789, arXiv:1109.5115.

[60] S. Weinberg, *Phenomenological lagrangians*, Physica **A96** (1979) 327.

[61] W. Skiba, *TASI lectures on effective field theory and precision electroweak measurements*, arXiv:1006.2142.

[62] D. J. Gross and F. Wilczek, *Asymptotically free gauge theories. i*, Phys. Rev. D **8** (1973) 3633.

[63] H. D. Politzer, *Asymptotic freedom: an approach to strong interactions*, Phys. Rept. **14** (1974) 129.

[64] D. J. Gross, *Twenty five years of asymptotic freedom*, Nucl. Phys. Proc. Suppl. **74** (1999) 426, arXiv:hep-th/9809060.

[65] K. G. Wilson and W. Zimmermann, *Operator product expansions and composite field operators in the general framework of quantum field theory*, Communications in mathematical physics **24** (1972), no. 2 87.

[66] G. Buchalla, A. J. Buras, and M. E. Lautenbacher, *Weak decays beyond leading logarithms*, Rev. Mod. Phys. **68** (1996) 1125, arXiv:hep-ph/9512380.

[67] G. Branco, L. Lavoura, and J. Silva, *CP Violation*, International series of monographs on physics, Clarendon Press, 1999.

[68] K. G. Wilson, *Renormalization group and strong interactions*, Phys. Rev. D **3** (1971) 1818.

[69] A. J. Buras, *Theoretical review of B physics*, Nucl. Instrum. Meth. **A368** (1995) 1, arXiv:hep-ph/9509329.

[70] A. J. Buras, *Operator product expansion, renormalization group and weak decays*, Lect. Notes Phys. **558** (2000) 65, arXiv:hep-ph/9901409.

[71] E. Stueckelberg and A. Petermann, *Normalization of constants in the quanta theory*, Helv. Phys. Acta **26** (1953) 499.

[72] M. Gell-Mann and F. E. Low, *Quantum electrodynamics at small distances*, Phys. Rev. **95** (1954) 1300.

[73] E. Witten, *Short distance analysis of weak Interactions*, Nucl. Phys. **B122** (1977) 109.

[74] M. Beneke, G. Buchalla, M. Neubert, and C. T. Sachrajda, *QCD factorization in $B \to \pi K$, $\pi\pi$ decays and extraction of Wolfenstein parameters*, Nucl. Phys. **B606** (2001) 245, arXiv:hep-ph/0104110.

[75] M. Beneke, G. Buchalla, M. Neubert, and C. T. Sachrajda, *QCD factorization for exclusive, nonleptonic B meson decays: general arguments and the case of heavy light final states*, Nucl. Phys. **B591** (2000) 313, arXiv:hep-ph/0006124.

[76] D.-s. Du, J.-f. Sun, D.-s. Yang, and G.-h. Zhu, *Charmless two-body B decays: a global analysis with QCD factorization*, Phys. Rev. **D67** (2003) 014023, arXiv:hep-ph/0209233.

[77] M. Neubert, *Aspects of QCD factorization*, AIP Conf. Proc. **602** (2001) 168, arXiv:hep-ph/0110093.

[78] C. W. Bauer, S. Fleming, and M. E. Luke, *Summing Sudakov logarithms in $B \to X_s\gamma$ in effective field theory*, Phys. Rev. **D63** (2000) 014006, arXiv:hep-ph/0005275.

[79] D. Fakirov and B. Stech, *F and D decays*, Nucl. Phys. **B133** (1978) 315.

[80] N. Cabibbo and L. Maiani, *Two-body decays of charmed mesons*, Phys. Lett. **B73** (1978) 418.

[81] J. D. Bjorken, *Topics in B physics*, Nucl. Phys. Proc. Suppl. **11** (1989) 325.

[82] M. Beneke, G. Buchalla, M. Neubert, and C. T. Sachrajda, *QCD factorization for $B \to \pi\pi$ decays: Strong phases and CP violation in the heavy quark limit*, Phys. Rev. Lett. **83** (1999) 1914, arXiv:hep-ph/9905312.

[83] Y.-Y. Keum, H.-n. Li, and A. Sanda, *A novel PQCD approach in charmless B meson decays*, AIP Conf. Proc. **618** (2002) 229, arXiv:hep-ph/0201103.

[84] J.-P. Lee, *Taming the end-point singularities in heavy-to-light decays*, Phys. Rev. **D75** (2007) 031501, arXiv:hep-ph/0612083.

[85] M. Nagashima and H.-n. Li, *k(T) factorization of exclusive processes*, Phys. Rev. **D67** (2003) 034001, arXiv:hep-ph/0210173.

[86] J. C. Collins, *Sudakov form-factors*, Adv. Ser. Direct. High Energy Phys. **5** (1989) 573, arXiv:hep-ph/0312336.

[87] C.-H. Chen, Y.-Y. Keum, and H.-n. Li, *Perturbative QCD analysis of $B \to \phi K$ decays and power counting*, Phys. Rev. D **64** (2001) 112002.

[88] C. W. Bauer, S. Fleming, D. Pirjol, and I. W. Stewart, *An effective field theory for collinear and soft gluons: heavy to light decays*, Phys. Rev. **D63** (2001) 114020, arXiv:hep-ph/0011336.

[89] D. Pirjol, *Theory of hadronic B decays*, Nucl. Phys. Proc. Suppl. **156** (2006) 81, arXiv:hep-ph/0502141.

[90] C.-W. Chiang and Y.-F. Zhou, *Flavor symmetry analysis of charmless $B \to VP$ decays*, JHEP **0903** (2009) 055, arXiv:0809.0841.

[91] M. Beneke and M. Neubert, *QCD factorization for $B \to PP$ and $B \to PV$ decays*, Nucl. Phys. **B675** (2003) 333, arXiv:hep-ph/0308039.

[92] H.-Y. Cheng and C.-K. Chua, *QCD factorization for charmless hadronic B_s decays revisited*, Phys. Rev. **D80** (2009) 114026, arXiv:0910.5237.

[93] A. Ali *et al.*, *Charmless non-leptonic B_s decays to PP, PV and VV final states in the pQCD approach*, Phys. Rev. **D76** (2007) 074018, arXiv:hep-ph/0703162.

[94] W. Wang, Y.-M. Wang, D.-S. Yang, and C.-D. Lu, *Charmless two-body $B_{(s)} \to VP$ decays In soft-collinear-effective-theory*, Phys. Rev. **D78** (2008) 034011, arXiv:0801.3123.

[95] BaBar Collaboration, B. Aubert *et al.*, *An amplitude analysis of the decay* $B^{\pm} \to \pi^{\pm}\pi^{\pm}\pi^{\mp}$, Phys. Rev. **D72** (2005) 052002, arXiv:hep-ex/0507025.

[96] G. N. Fleming, *Recoupling effects in the isobar model. 1. General formalism for three-pion scattering*, Phys. Rev. **135** (1964) B551.

[97] D. Morgan, *Phenomenological analysis of* $I = 1/2$ *single-pion production processes in the energy range 500 to 700 MeV*, Phys. Rev. **166** (1968) 1731.

[98] D. Herndon, P. Soding, and R. Cashmore, *A generalised isobar model formalism*, Phys. Rev. **D11** (1975) 3165.

[99] S. Mandelstam, *Determination of the pion-nucleon scattering amplitude from dispersion relations and unitarity. general theory*, Phys. Rev. **112** (1958) 1344.

[100] R. G. Newton, *Optical theorem and beyond*, American Journal of Physics **44** (1976) 639.

[101] N. A. Tornqvist, *The scalar* $q\bar{q}$ *nonet and confirmation of the broad* $\sigma(\approx 500)$ *meson*, arXiv:hep-ph/9608464.

[102] I. Aitchison, *K-Matrix formalism for overlapping resonances*, Nucl. Phys. **A189** (1972) 417.

[103] J. M. Blatt and V. F. Weisskopf, *Theoretical nuclear physics*, John Wiley & Sons, New York, 1952.

[104] D. Aston *et al.*, *A Study of* $K^-\pi^+$ *scattering in the reaction* $K^-p \to K - \pi^+$ *at 11-GeV/c*, Nucl. Phys. **B296** (1988) 493.

[105] C. Zemach, *Determination of the spins and parities of resonances*, Phys. Rev. **140** (1965) B109.

[106] LHCb Collaboration, R. Aaij *et al.*, *First evidence of direct CP violation in charmless two-body decays of* B_s^0 *mesons*, Phys. Rev. Lett. **108** (2012) 201601, arXiv:1202.6251.

[107] LHCb collaboration, R. Aaij *et al.*, *Observation of overlapping spin-1 and spin-3* $\bar{D}^0 K^-$ *resonances at mass* $2.86\text{GeV}/c^2$, Phys. Rev. Lett. **113** (2014) 162001, arXiv:1407.7574.

[108] LHCb collaboration, R. Aaij *et al.*, *Study of* $B^0_{(s)} \to K^0_S h^+ h'^-$ *decays with first observation of* $B^0_s \to K^0_S K^{\pm}\pi^{\mp}$ *and* $B^0_s \to K^0_S \pi^+\pi^-$, JHEP **1310** (2013) 143, arXiv:1307.7648.

[109] K. De Bruyn *et al.*, *Branching ratio measurements of B_s^0 decays*, Phys. Rev. **D86** (2012) 014027, arXiv:1204.1735.

[110] BaBar Collaboration, J. Lees *et al.*, *Amplitude analysis of $B^0 \to K^+\pi^-\pi^0$ and evidence of direct CP violation in $B \to K^*\pi$ decays*, Phys. Rev. **D83** (2011) 112010, arXiv:1105.0125.

[111] Belle Collaboration, A. Garmash *et al.*, *Dalitz analysis of three-body charmless $B^0 \to K^0\pi^+\pi^-$ decay*, Phys. Rev. **D75** (2007) 012006, arXiv:hep-ex/0610081.

[112] LHCb Collaboration, R. Aaij *et al.*, *Measurement of CP asymmetry in $B_s^0 \to D_s^\mp K^\pm$ decays*, JHEP **1411** (2014) 060, arXiv:1407.6127.

[113] LHCb Collaboration, R. Aaij *et al.*, *Measurement of the CP-violating phase ϕ_s in $\bar{B}_s^0 \to D_s^+ D_s^-$ decays*, Phys. Rev. Lett. **113** (2014) 211801, arXiv:1409.4619.

[114] L. Evans and P. Bryant, *LHC Machine*, JINST **3** (2008) S08001.

[115] R. Assmann, M. Lamont, and S. Myers, *A brief history of the LEP collider*, Nucl. Phys. Proc. Suppl. **109B** (2002) 17.

[116] F. Marcastel, *CERN's accelerator complex. La chaîne des accélérateurs du CERN*, OPEN-PHO-CHART-2013-001 (2013), General Photo.

[117] ATLAS Collaboration, G. Aad *et al.*, *The ATLAS experiment at the CERN Large Hadron Collider*, JINST **3** (2008) S08003.

[118] CMS Collaboration, S. Chatrchyan *et al.*, *The CMS experiment at the CERN LHC*, JINST **3** (2008) S08004.

[119] ALICE Collaboration, K. Aamodt *et al.*, *The ALICE experiment at the CERN LHC*, JINST **3** (2008) S08002.

[120] LHCb collaboration, *LHCb $b\bar{b}$ production angle public plots*, http://lhcb.web.cern.ch/lhcb/speakersbureau/html/bb_ProductionAngles.html.

[121] R. Lindner, *LHCb layout schema*, LHCb Collection, Feb, 2008.

[122] F. Follin and D. Jacquet, *Implementation and experience with luminosity levelling with offset beam*, arXiv:1410.3667.

[123] LHCb Collaboration, B. Adeva *et al.*, *LHCb: Technical Proposal*, Tech. Rep. CERN-LHCC-98-004, Geneva, 1998.

[124] LHCb Collaboration, *LHCb magnet: technical design report*, Tech. Rep. CERN-LHCC-2000-007, 2000.

[125] M. Vesterinen, *Considerations on the LHCb dipole magnet polarity reversal*, Tech. Rep. LHCb-PUB-2014-006. CERN-LHCb-PUB-2014-006, CERN, Geneva, Apr, 2014.

[126] S. Lochner and M. Schmelling, *The Beetle reference manual - chip version 1.3, 1.4 and 1.5*, Tech. Rep. LHCb-2005-105. CERN-LHCb-2005-105, CERN, Geneva, Nov, 2006.

[127] A. Affolder *et al.*, *Radiation damage in the LHCb Vertex Locator*, JINST **8** (2013) P08002, arXiv:1302.5259.

[128] R. Aaij *et al.*, *Performance of the LHCb Vertex Locator*, JINST **9** (2014) 09007, arXiv:1405.7808.

[129] LHCb Collaboration, *LHCb technical design report: Reoptimized detector design and performance*, Tech. Rep. CERN-LHCC-2003-030, 2003.

[130] J. Gassner, M. Needham, and O. Steinkamp, *Layout and Expected Performance of the LHCb TT Station*, Tech. Rep. LHCb-2003-140, CERN-LHCb-2003-140, 2004.

[131] E. Rodrigues, *Performance and Operational Aspects of LHCb's VELO and ST*, PoS **Vertex2013** (2013) 003.

[132] LHCb collaboration, *St material for publications*, http://lhcb.physik.uzh.ch/ST/public/material/index.php.

[133] LHCb Collaboration, *LHCb: Inner tracker technical design report*, Tech. Rep. CERN-LHCC-2002-029, 2002.

[134] *LHCb Collaboration: Outer tracker technical design report*, Tech. Rep. CERN-LHCC-2001-024, 2001.

[135] LHCb Outer Tracker group, R. Arink *et al.*, *Performance of the LHCb Outer Tracker*, JINST **9** (2014), no. 01 P01002, arXiv:1311.3893.

[136] R. Frühwirth, *Application of Kalman filtering to track and vertex fitting*, Nucl. Instrum. Meth. **A262** (1987) 444.

[137] LHCb Collaboration, R. Aaij *et al.*, *LHCb detector performance*, Int. J. Mod. Phys. **A30** (2015), no. 07 1530022, arXiv:1412.6352.

[138] LHCb Collaboration, *LHCb: RICH technical design report*, Tech. Rep. CERN-LHCC-2000-037, 2000.

[139] LHCb RICH Group, M. Adinolfi *et al.*, *Performance of the LHCb RICH detector at the LHC*, Eur. Phys. J. **C73** (2013) 2431, arXiv:1211.6759.

[140] LHCb Collaboration, I. Machikhiliyan, *Current status and performance of the LHCb electromagnetic and hadron calorimeters*, J. Phys. Conf. Ser. **293** (2011) 012052.

[141] LHCb Collaboration, *LHCb calorimeters: Technical design report*, Tech. Rep. CERN-LHCC-2000-036, 2000.

[142] R. Aaij *et al.*, *The LHCb Trigger and its performance in 2011*, JINST **8** (2013) P04022, arXiv:1211.3055.

[143] LHCb HLT project, J. Albrecht, V. Gligorov, G. Raven, and S. Tolk, *Performance of the LHCb High Level Trigger in 2012*, J. Phys. Conf. Ser. **513** (2014) 012001, arXiv:1310.8544.

[144] A. Puig, *The LHCb trigger in 2011 and 2012*, Tech. Rep. LHCb-PUB-2014-046. CERN-LHCb-PUB-2014-046, CERN, Geneva, Nov, 2014.

[145] V. Gligorov, C. Thomas, and M. Williams, *The HLT inclusive B triggers*, Tech. Rep. LHCb-PUB-2011-016, CERN-LHCb-PUB-2011-016, LHCb-INT-2011-030, CERN, Geneva, 2011.

[146] M. Williams *et al.*, *The HLT2 Topological Lines*, Tech. Rep. LHCb-PUB-2011-002, CERN-LHCb-PUB-2011-002, CERN, Geneva, 2011.

[147] V. V. Gligorov and M. Williams, *Efficient, reliable and fast high-level triggering using a bonsai boosted decision tree*, JINST **8** (2013) P02013, arXiv:1210.6861.

[148] LHCb collaboration, R. Aaij *et al.*, *Branching fraction and CP asymmetry of the decays* $B^+ \to K^0_S\pi^+$ *and* $B^+ \to K^0_S K^+$, Phys. Lett. **B726** (2013) 646, arXiv:1308.1277.

[149] J. Brehmer, J. Albrecht, and P. Seyfert, *Ghost probability: an efficient tool to remove background tracks*, Tech. Rep. LHCb-INT-2012-025. CERN-LHCb-INT-2012-025, CERN, Geneva, Sep, 2012.

[150] M. Needham, *Clone Track Identification using the Kullback-Liebler Distance*, Tech. Rep. LHCb-2008-002. CERN-LHCb-2008-002. LPHE-2008-002, CERN, Geneva, Jan, 2008.

[151] F. Archilli *et al.*, *Performance of the Muon Identification at LHCb*, JINST **8** (2013) P10020, arXiv:1306.0249.

[152] L. Breiman, J. H. Friedman, R. A. Olshen, and C. J. Stone, *Classification and regression trees*, Wadsworth international group, Belmont, California, USA, 1984.

[153] R. E. Schapire and Y. Freund, *A decision-theoretic generalization of on-line learning and an application to boosting*, Jour. Comp. and Syst. Sc. **55** (1997) 119.

[154] M. Pivk and F. R. Le Diberder, *sPlot: a statistical tool to unfold data distributions*, Nucl. Instrum. Meth. **A555** (2005) 356, arXiv:physics/0402083.

[155] L. Breiman, J. Friedman, R. Olshen, and C. Stone, *Classification and Regression Trees*, Wadsworth and Brooks, Monterey, CA, 1984.

[156] B. P. Roe *et al.*, *Boosted decision trees as an alternative to artificial neural networks for particle identification*, Nuclear Instruments and Methods in Physics Research A **543** (2005) 577, arXiv:physics/0408124.

[157] G. Punzi, *Sensitivity of searches for new signals and its optimization*, in *Statistical Problems in Particle Physics, Astrophysics, and Cosmology* (L. Lyons, R. Mount, and R. Reitmeyer, eds.), p. 79, 2003. arXiv:physics/0308063.

[158] T. Gershon, T. Latham, and R. Silva Coutinho, *Selection optimisation for Dalitz-plot analyses*, CERN-LHCb-INT-2015-003; LHCb-INT-2015-003. in preparation.

[159] Laura++ Dalitz plot fitting package, University of Warwick, http://laura.hepforge.org/.

[160] A. Stuart, O. K, and S. Arnold, *Kendall's advanced theory of statistics*, vol. 2: Classical Inference and Relationship, Oxford University Press Inc., New York, 6th ed., 1999.

[161] L. Lyons, *Statistics for nuclear and particle physicists*, vol. ISBN-9780521379342, Cambridge University Press, 1986.

[162] R. Fisher, *On the mathematical foundations of theoretical Statistics*, Phil. Trans. Roy. Soc. Lond. **A222** (1922) 309.

[163] LHCb Collaboration, R. Aaij *et al.*, *Searches for Λ_b^0 and Ξ_b^0 decays to $K^0_S p\pi^-$ and $K^0_S pK^-$ final states with first observation of the $\Lambda_b^0 \to K^0_S p\pi^-$ decay*, JHEP **1404** (2014) 087, arXiv:1402.0770.

[164] S. Wilks, *The large-sample distribution of the likelihood ratio for testing composite hypotheses*, The Annals of Mathematical Statistics **9** (1938) 6062.

[165] L. Lyons, D. Gibaut, and P. Clifford, *How to combine correlated estimates of a single physical quantity*, Nucl. Instrum. Meth. **A270** (1988) 110.

[166] A. Valassi, *Combining correlated measurements of several different physical quantities*, Nucl. Instrum. Meth. **A500** (2003) 391.

[167] G. J. Feldman and R. D. Cousins, *A unified approach to the classical statistical analysis of small signals*, Phys. Rev. **D57** (1998) 3873, arXiv:physics/9711021.

[168] Belle Collaboration, J. Dalseno *et al.*, *Time-dependent Dalitz Plot measurement of CP parameters in $B^0 \to K^0_S\pi^+\pi^-$ decays*, Phys. Rev. **D79** (2009) 072004, arXiv:0811.3665.

[169] BaBar Collaboration, B. Aubert *et al.*, *Time-dependent amplitude analysis of $B^0 \to K^0_S\pi^+\pi^-$*, Phys. Rev. **D80** (2009) 112001, arXiv:0905.3615.

[170] BELLE Collaboration, Y. Nakahama *et al.*, *Measurement of CP violating asymmetries in $B^0 \to K^0_S K^+K^-$ decays with a time-dependent Dalitz approach*, Phys. Rev. **D82** (2010) 073011, arXiv:1007.3848.

[171] BaBar collaboration, J. Lees *et al.*, *Study of CP violation in Dalitz-plot analyses of $B^0 \to K^+K^-K^0_S$, $B^+ \to K^+K^-K^+$, and $B^+ \to K^0_S K^0_S K^+$*, Phys. Rev. **D85** (2012) 112010, arXiv:1201.5897.

[172] BaBar Collaboration, P. del Amo Sanchez *et al.*, *Observation of the Rare Decay $B^0 \to K^0_S K^\pm\pi^\mp$*, Phys. Rev. **D82** (2010) 031101, arXiv:1003.0640.

[173] LHCb Collaboration, *Branching fraction measurements of $B^0_{d,s}$ decays to $K^0_S h^\pm h'^\mp$ final states, including first observation of $B^0_s \to K^0_S K^\pm\pi^\mp$*, , Link to LHCb-ANA-2012-026.

[174] T. Skwarnicki, *A study of the radiative cascade transitions between the Upsilon-prime and Upsilon resonances*, PhD thesis, Institute of Nuclear Physics, Krakow, 1986, DESY-F31-86-02.

[175] ARGUS collaboration, H. Albrecht *et al.*, *Exclusive hadronic decays of B mesons*, Z. Phys. **C48** (1990) 543.

[176] LHCb collaboration, R. Aaij *et al.*, *Measurement of the fragmentation fraction ratio f_s/f_d and its dependence on B meson kinematics*, JHEP **04** (2013) 1, arXiv:1301.5286.

[177] H. Dong and Z.-T. Liang, *Hyperon polarization in different inclusive production processes in unpolarized high-energy hadron hadron collisions*, Phys. Rev. **D70** (2004) 014019, arXiv:hep-ph/0403041.

[178] LHCb collaboration, R. Aaij *et al.*, *Study of beauty baryon decays to D^0ph^- and $\Lambda_c^+h^-$ final states*, Phys. Rev. **D89** (2014) 032001, arXiv:1311.4823.

[179] LHCb collaboration, R. Aaij *et al.*, *Measurements of the branching fractions of the decays $B_s^0 \to D_s^{\mp}K^{\pm}$ and $B_s^0 \to D_s^-\pi^+$*, JHEP **06** (2012) 115, arXiv:1204.1237.

[180] LHCb collaboration, R. Aaij *et al.*, *Measurements of the $\Lambda_b^0 \to \Lambda J/\psi$ decay amplitudes and the Λ_b^0 baryon production polarisation in pp collisions at $\sqrt{s} =$ 7 TeV*, Phys. Lett. **B724** (2013) 27, arXiv:1302.5578.

[181] LHCb collaboration, R. Aaij *et al.*, *Precision measurement of the Λ_b^0 baryon lifetime*, Phys. Rev. Lett. **111** (2013) 102003, arXiv:1307.2476.

[182] CDF Collaboration, T. Aaltonen *et al.*, *Observation of the Ω_b^- baryon and measurement of the properties of the Ξ_b^- and Ω_b^- baryons*, Phys. Rev. **D80** (2009) 072003, arXiv:0905.3123.

[183] LHCb collaboration, R. Aaij *et al.*, *Measurement of b hadron production fractions in* 7 TeV *pp collisions*, Phys. Rev. **D85** (2012) 032008, arXiv:1111.2357.

[184] LHCb collaboration, R. Aaij *et al.*, *Study of the kinematic dependences of Λ_b^0 production in pp collisions and a measurement of the $\Lambda_b^0 \to \Lambda_c^+\pi^-$ branching fraction*, JHEP **08** (2014) 143, arXiv:1405.6842.

[185] M. Baalouch *et al.*, *Search for the decay $B_s^0 \to K_S^0K^+K^-$*, LHCb-ANA-2014-043.

[186] BaBar collaboration, B. Aubert *et al.*, *Evidence for direct CP violation from Dalitz-plot analysis of* $B^{\pm} \to K^{\pm}\pi^{\mp}\pi^{\pm}$, Phys. Rev. **D78** (2008) 012004, arXiv:0803.4451.

[187] BaBar collaboration, B. Aubert *et al.*, *Dalitz Plot analysis of* $B^{\pm} \to \pi^{\pm}\pi^{\pm}\pi^{\mp}$ *Decays*, Phys. Rev. **D79** (2009) 072006, arXiv:0902.2051.

[188] BaBar collaboration, P. del Amo Sanchez *et al.*, *Dalitz-plot analysis of* $B^0 \to \bar{D}^0\pi^+\pi^-$, PoS **ICHEP2010** (2010) 250, arXiv:1007.4464.

[189] LHCb collaboration, R. Aaij *et al.*, *Observation of overlapping spin-*1 *and spin-*3 $\bar{D}^0K^-$ *resonances at mass* 2.86 GeV/c^2, Phys. Rev. Lett. **113** (2014) 162001, arXiv:1407.7574.

[190] LHCb collaboration, R. Aaij *et al.*, *Dalitz plot analysis of* $B_s^0 \to \bar{D}^0K^-\pi^+$ *decays*, Phys. Rev. **D90** (2014) 072003, arXiv:1407.7712.

[191] LHCb collaboration, R. Aaij *et al.*, *First observation of the* $B^- \to D^+K^-\pi^-$ *decay and study of its Dalitz plot structure*, LHCb-PAPER-2015-007, in preparation.

[192] LHCb collaboration, R. Aaij *et al.*, *Measurement of b-hadron branching fractions for two-body decays into charmless charged hadrons*, JHEP **10** (2012) 037, arXiv:1206.2794.

[193] W. H. Press, S. A. Teukolsky, W. T. Vetterling, and B. P. Flannery, *Numerical Recipes in C*, Cambridge University Press, Cambridge, 1998.

[194] M. Williams, *How good are your fits? Unbinned multivariate goodness-of-fit tests in high energy physics*, JINST **5** (2010) P09004, arXiv:1006.3019.

[195] R. Brun and F. Rademakers, *ROOT: An object oriented data analysis framework*, Nucl. Instrum. Meth. **A389** (1997) 81.

[196] M. De Cian *et al.*, *Measurement of the track finding efficiency*, Tech. Rep. LHCb-PUB-2011-025. CERN-LHCb-PUB-2011-025, CERN, Geneva, Apr, 2012. More details can be found here: https://twiki.cern.ch/twiki/bin/view/LHCb/LHCbTrackingEfficiencies.

[197] A. Martin Sanchez, P. Robbe, and M.-H. Schune, *Performances of the LHCb L0 Calorimeter Trigger*, Tech. Rep. LHCb-PUB-2011-026. CERN-LHCb-PUB-2011-026, CERN, Geneva, Jun, 2012. More details can be

found here: https://twiki.cern.ch/twiki/bin/viewauth/LHCbPhysics/CalorimeterObjectsToolsGroupDOC#L0_Hadron_trigger_efficiencies.

[198] F. Harrell, *Regression Modeling Strategies: With Applications to Linear Models, Logistic Regression, and Survival Analysis*, Graduate Texts in Mathematics, Springer, 2001.

[199] B. Guegan, J. Hardin, J. Stevens, and M. Williams, *Model selection for amplitude analysis*, arXiv:1505.0513.

[200] E. Ben-Haim, R. Brun, B. Echenard, and T. E. Latham, *JFIT: a framework to obtain combined experimental results through joint fits*, arXiv:1409.5080.

[201] LHCb, R. Aaij *et al.*, *Searches for $B^0_{(s)} \to J/\psi p\bar{p}$ and $B^+ \to J/\psi p\bar{p}\pi^+$ decays*, JHEP **1309** (2013) 006, arXiv:1306.4489.

[202] Belle Collaboration, K. Abe *et al.*, *Observation of $\overline{B}^0 \to D^{(*)0}p\bar{p}$*, Phys. Rev. Lett. **89** (2002) 151802, arXiv:hep-ex/0205083.

[203] BaBar collaboration, P. del Amo Sanchez *et al.*, *Observation and study of the baryonic B-meson decays $B \to D^{(*)}p\bar{p}(\pi)(\pi)$*, Phys. Rev. **D85** (2012) 092017, arXiv:1111.4387.

[204] BaBar collaboration, B. Aubert *et al.*, *Measurement of the $B^+ \to p\bar{p}K^+$ branching fraction and study of the decay dynamics*, Phys. Rev. **D72** (2005) 051101(R), arXiv:hep-ex/0507012.

[205] BaBar collaboration, B. Aubert *et al.*, *Evidence for the $B^0 \to p\bar{p}K^{*0}$ and $B^+ \to \eta_c K^{*+}$ decays and study of the decay dynamics of B meson decays into $p\bar{p}h$ final states*, Phys. Rev. **D76** (2007) 092004, arXiv:0707.1648.

[206] Belle Collaboration, J.-T. Wei *et al.*, *Study of $B^+ \to p\bar{p}K^+$ and $B^+ \to p\bar{p}\pi^+$*, Phys. Lett. **B659** (2008) 80, arXiv:0706.4167.

[207] Belle Collaboration, J.-H. Chen *et al.*, *Observation of $B^0 \to p\bar{p}K^{*0}$ with a large K^{*0} polarization*, Phys. Rev. Lett. **100** (2008) 251801, arXiv:0802.0336.

[208] LHCb collaboration, R. Aaij *et al.*, *Measurements of the branching fractions of $B^+ \to p\bar{p}K^+$ decays*, Eur. Phys. J. **C73** (2013) 2462, arXiv:1303.7133.

[209] C.-K. Chua, W.-S. Hou, and S.-Y. Tsai, *Possible hints and search for glueball production in charmless rare B decays*, Phys. Lett. **B544** (2002) 139, arXiv:hep-ph/0204186.

[210] C.-K. Chua, W.-S. Hou, and S.-Y. Tsai, *Charmless three-body baryonic B decays*, Phys. Rev. **D66** (2002) 054004, arXiv:hep-ph/0204185.

[211] B. Kerbikov, A. Stavinsky, and V. Fedotov, *Model independent view on the low mass proton anti-proton enhancement*, Phys. Rev. **C69** (2004) 055205, arXiv:hep-ph/0402054.

[212] H.-Y. Cheng and K.-C. Yang, *Charmless exclusive baryonic B decays*, Phys. Rev. **D66** (2002) 014020, arXiv:hep-ph/0112245.

[213] Particle Data Group, J. Beringer *et al.*, *Review of particle physics*, Phys. Rev. **D86** (2012) 010001.

[214] Belle Collaboration, Q. Xie *et al.*, *Observation of $B^- \to J/\psi \Lambda \overline{p}$ and searches for $B^- \to J/\psi \Sigma^0 \overline{p}$ and $B^0 \to J/\psi p \overline{p}$ decays*, Phys. Rev. **D72** (2005) 051105(R), arXiv:hep-ex/0508011.

[215] LHCb collaboration, R. Aaij *et al.*, *Analysis of the resonant components in $\overline{B}^0 \to J/\psi \pi^+ \pi^-$*, Phys. Rev. **D87** (2013) 052001, arXiv:1301.5347.

[216] C.-H. Chen, H.-Y. Cheng, C. Geng, and Y. Hsiao, *Charmful three-body baryonic B decays*, Phys. Rev. **D78** (2008) 054016, arXiv:0806.1108.

[217] LHCb collaboration, R. Aaij *et al.*, *Analysis of the resonant components in $\overline{B}^0_s \to J/\psi \pi^+ \pi^-$*, Phys. Rev. **D86** (2012) 052006, arXiv:1204.5643.

[218] M. Adinolfi *et al.*, *Performance of the LHCb RICH detector at the LHC*, Eur. Phys. J. **C73** (2013) 2431, arXiv:1211.6759.

[219] A. A. Alves Jr *et al.*, *Performance of the LHCb muon system*, JINST **8** (2013) P02022, arXiv:1211.1346.

[220] T. Sjöstrand, S. Mrenna, and P. Skands, *PYTHIA 6.4 physics and manual*, JHEP **05** (2006) 026, arXiv:hep-ph/0603175.

[221] I. Belyaev *et al.*, *Handling of the generation of primary events in* Gauss*, the LHCb simulation framework*, Nuclear Science Symposium Conference Record (NSS/MIC) **IEEE** (2010) 1155.

[222] D. J. Lange, *The EvtGen particle decay simulation package*, Nucl. Instrum. Meth. **A462** (2001) 152.

[223] P. Golonka and Z. Was, *PHOTOS Monte Carlo: a precision tool for QED corrections in Z and W decays*, Eur. Phys. J. **C45** (2006) 97, arXiv:hep-ph/0506026.

[224] Geant4 collaboration, J. Allison *et al.*, *Geant4 developments and applications*, IEEE Trans. Nucl. Sci. **53** (2006) 270; Geant4 collaboration, S. Agostinelli *et al.*, *Geant4: a simulation toolkit*, Nucl. Instrum. Meth. **A506** (2003) 250.

[225] M. Clemencic *et al.*, *The LHCb simulation application,* GAUSS*: design, evolution and experience*, J. Phys.: Conf. Ser. **331** (2011) 032023.

[226] M. Feindt and U. Kerzel, *The NeuroBayes neural network package*, Nucl. Instrum. Meth. **A559** (2006) 190.

[227] T. Gershon, T. Latham, and R. S. Coutinho, *Probing CP violation in* $B_s^0 \to K_S^0\pi^+\pi^-$ *decays*, arXiv:1411.2018.

[228] M. Antonelli *et al.*, *Flavor Physics in the Quark Sector*, Phys. Rept. **494** (2010) 197, arXiv:0907.5386.

[229] Belle Collaboration, J. Brodzicka *et al.*, *Physics achievements from the Belle experiment*, PTEP **2012** (2012) 04D001, arXiv:1212.5342.

[230] BaBar and Belle Collaborations, A. Bevan *et al.*, *The Physics of the B Factories*, Eur. Phys. J. **C74** (2014), no. 11 3026, arXiv:1406.6311.

[231] LHCb Collaboration, R. Aaij *et al.*, *Implications of LHCb measurements and future prospects*, Eur. Phys. J. **C73** (2013), no. 4 2373, arXiv:1208.3355.

[232] T. Aushev *et al.*, *Physics at Super B Factory*, arXiv:1002.5012.

[233] LHCb collaboration, *Letter of Intent for the LHCb Upgrade*, CERN-LHCC-2011-001. LHCC-I-018.

[234] LHCb collaboration, *Framework TDR for the LHCb Upgrade*, CERN-LHCC-2012-007. LHCB-TDR-012.

[235] M. Gronau, D. Pirjol, A. Soni, and J. Zupan, *Constraint on* $\bar{\rho}, \bar{\eta}$ *from* $B \to K^*\pi$, Phys. Rev. **D77** (2008) 057504, arXiv:0712.3751.

[236] I. Bediaga, G. Guerrer, and J. M. de Miranda, *Extracting the quark mixing phase* γ *from* $B^\pm \to K^\pm\pi^+\pi^-$, $B^0 \to K_S\pi^+\pi^-$, *and* $\bar{B}^0 \to K_S\pi^+\pi^-$, Phys. Rev. **D76** (2007) 073011, arXiv:hep-ph/0608268.

[237] LHCb Collaboration, R. Aaij *et al.*, *First measurement of time-dependent CP violation in $B_s^0 \to K^+K^-$ decays*, JHEP **1310** (2013) 183, arXiv:1308.1428.

[238] LHCb Collaboration, R. Aaij *et al.*, *First measurement of the CP-violating phase in $B_s^0 \to \phi\phi$ decays*, Phys. Rev. Lett. **110** (2013) 241802, arXiv:1303.7125.

[239] G. Burdman and J. F. Donoghue, *B meson CP violation without flavor identification*, Phys. Rev. **D45** (1992) 187.

[240] S. Gardner, *Direct CP violation in untagged B meson decays*, Phys. Lett. **B553** (2003) 261, arXiv:hep-ph/0203152.

[241] S. Gardner and J. Tandean, *Observing direct CP violation in untagged B meson decays*, Phys. Rev. **D69** (2004) 034011, arXiv:hep-ph/0308228.

[242] D. Bugg, *Comments on the sigma and kappa*, Phys. Lett. **B572** (2003) 1.

[243] B. El-Bennich *et al.*, *CP violation and kaon-pion interactions in $B \to K\pi^+\pi^-$ decays*, Phys. Rev. **D79** (2009) 094005, arXiv:0902.3645.

[244] Belle Collaboration, A. Garmash *et al.*, *Dalitz analysis of the three-body charmless decays $B^+ \to K^+\pi^+\pi^-$ and $B^+ \to K^+K^+K^-$*, Phys. Rev. **D71** (2005) 092003, arXiv:hep-ex/0412066.

[245] BaBar Collaboration, B. Aubert *et al.*, *Ambiguity-free measurement of $\cos(2\beta)$: Time-integrated and time-dependent angular analyses of $B \to J/\psi K\pi$*, Phys. Rev. **D71** (2005) 032005, arXiv:hep-ex/0411016.

[246] BaBar Collaboration, B. Aubert *et al.*, *Dalitz-plot analysis of the decays $B^\pm \to K^\pm\pi^\mp\pi^\pm$*, Phys. Rev. **D72** (2005) 072003, arXiv:hep-ex/0507004.

[247] P. Dauncey, M. Kenzie, N. Wardle, and G. Davies, *Handling uncertainties in background shapes: the discrete profiling method*, JINST **10** (2015), no. 04 P04015, arXiv:1408.6865.